

DISSERTATION

submitted to the
Combined Faculty of Natural Sciences and Mathematics
of the Ruperto Carola University Heidelberg, Germany
for the degree of
Doctor of Natural Sciences

Presented by
Romina Virginia Celada (Lic. Chem.)
born in Rosario, Argentina

Date of oral examination:

**Target identification studies for SC83288:
a novel drug for the treatment of severe malaria**

Referees:

Prof. Dr. Michael Lanzer

Prof. Dr. Marcel Deponte

To my family

In memory of Elon, our beloved cat

Ich erkläre hiermit, dass ich die vorliegende Doktorarbeit selbständig unter Anleitung verfasst und keine anderen als die angegebenen Quellen und Hilfsmittel benutzt habe.

Ich erkläre hiermit, dass ich an keiner anderen Stelle ein Prüfungsverfahren beantragt bzw. die Dissertation in dieser oder anderer Form bereits anderweitig als Prüfungsarbeit verwendet oder einer anderen Fakultät als Dissertation vorgelegt habe.

Die vorliegende Arbeit wurde am Department für Infektiologie, Abteilung Parasitologie des Universitätsklinikum Heidelberg in der Zeit von Dezember 2018 bis Mai 2022 unter der Leitung von Prof. Dr. Michael Lanzer ausgeführt.

.....

Datum

.....

Romina Virginia Celada

Acknowledgements

I would like to thank Prof. Dr. Michael Lanzer for opening the doors of his laboratory and giving me the opportunity to work on this project, as challenging as exciting, for my PhD thesis. I would also like to thank the members of my TAC committee, Prof. Dr. Marcel Deponde and Prof. Dr. Christian Klein for their valuable feedback during our yearly meetings. I am also grateful for the predisposition of Prof. Dr. F. Nina Papavasiliou and Prof. Dr. Gert Fricker to participate in my PhD examination committee.

I would also like to thank Dr. Cecilia Sanchez, Dr. Nicole Kilian, Marina Müller and Atdhe Kernaja for their help and advice. I am grateful for the support, brainstorming sessions, discussions, and all the fun I had with my lab mates over the years, Monika, Britta, Sophia, Marianne, Fiona, Guillermo, and Violeta, and all the students that joined the group for their practical work as well as BSc and MSc theses. I also want to say thanks to Anne Lorenz and Maren Gehringer for their contributions to this work and their undying motivation.

Thanks to Miriam Griesheimer and Sandra Niebel for guiding me through countless administration procedures, always happy and patient despite my infinite questions.

Thanks to the Parasitology Department of the Center for Infectious Diseases, for their constant feedback and fruitful discussions during the department seminars.

A great thank you to all the collaborator scientists, whose contributions were essential for the development of this work. Thanks to Dr. Marie Hoarau, Dr. Sumalee Kamchonwongpaisan and her team at the NTSDA/BIOTEC in Thailand; Isabelle Becher and Per Haberkant from the Savitski team at EMBL Heidelberg; Erin Manson and Prof. Dr. Michael Barrett from the University of Glasgow. Thanks to Dr. Ariane Nunes Alves from the TU Berlin for her good predisposition, help and advice. A special thanks to Dr. Jerzy Dziekan for bringing in his expertise to this project and for his contributions, that constituted a turning point in my thesis. Thanks to Michal Kucharski and Prof. Dr. Zbynek Bozdech from the NTU Singapore. Thanks to Dr. Markus Ganter and Severina Klaus for all the advice, brainstorming and support as well as their experimental contribution. Thanks to Dr. Maëlle Duffey for her help and advice.

Thanks to HBIGS for all the training opportunities, and for giving me the chance to come to Germany to build up my career.

Thanks to Martina Galvan, Rolf Lutz and Sandra Martini for always welcoming me with a smile and for their help as a PhD student and during my time as a Student Speaker. Thanks to Usama, Amel and Bianca for all the fun we had together.

Gracias a mi familia, Mamá, Papá y Denise por apoyarme incondicionalmente en este sueño loco que fue mi doctorado en el exterior, y mi vida en Alemania. Gracias a la Universidad Nacional de Rosario y especialmente a la Facultad de Ciencias Bioquímicas y Farmacéuticas, por brindarme una formación científica amplia que me permitió extender mis bases de conocimiento en química hacia la biología molecular. Gracias a la gente que me ha acompañado a la distancia todos estos años, gracias a Nati, Lula, Gus y Lu por la motivación, el apoyo y el cariño.

Thanks to my favorite person in the world, Alex, for the infinite amounts of support, motivation, encouraging words and love during the ups and downs of research. Thanks for all the fun, for all the walks to relax from work and for always pushing me in the right direction when I feel down.

Last but not least, thanks to the cats for always cheering me up.

Table of Contents

LIST OF ABBREVIATIONS	1
SUMMARY	7
ZUSAMMENFASSUNG	9
1. INTRODUCTION	11
1.1 Malaria	11
1.1.1 Origin	11
1.1.2 Disease characteristics	11
1.1.3 Fight against malaria: a battle yet to be won	12
1.2 Biology of <i>Plasmodium falciparum</i>	16
1.2.1 Life cycle of <i>P. falciparum</i> parasites	16
1.2.2 Asexual reproduction of parasites: schizogony	17
1.2.3 Metabolism of nucleotides in <i>P. falciparum</i> parasites	18
1.3 A brief history of antimalarial drugs	20
1.3.1 A look into the past	20
1.3.2 Antimalarials currently in use	22
1.3.3 The malaria treatment of tomorrow	25
1.4 SC83288, a promising novel drug candidate	25
1.5 Target identification strategies	27
1.6 Aim of the study	29
2. MATERIALS AND METHODS	31
2.1 Materials	31
2.1.1 Equipment	31
2.1.2 Consumables	32
2.1.3 Chemicals	33
2.1.4 Reagent Kits	33
2.1.5 Biological material	34
2.1.5.1 Enzymes	34
2.1.5.2 Molecular weight/size markers and loading dyes	34
2.1.5.3 Parasite strains	34
2.1.5.4 Bacteria strains	34
2.1.5.5 Plasmids	35
2.1.5.6 Primers for PCR	36
2.1.5.7 Other biological material	36
2.1.6 Buffers, media, and solutions	37
2.1.7 Software and Databases	40

2.2 Methods	41
2.2.1 Cell culture of <i>Plasmodium falciparum</i> parasites	41
2.2.1.1 In vitro culture conditions	41
2.2.1.2 Morphological examination of parasites and parasitemia determination	41
2.2.1.3 Cryopreservation and thawing of parasites	42
2.2.1.4 Parasite cultures synchronization with D-sorbitol	42
2.2.1.5 Magnetic purification of late-stage parasites	43
2.2.1.6 Heat-inactivation of human serum for growth medium preparation	43
2.2.2 Microbiology and Molecular Biology	43
2.2.2.1 Preparation of electro-competent PMC 103 <i>E. coli</i> bacteria	43
2.2.2.2 Transformation of electro-competent PMC 103 <i>E. coli</i> bacteria	44
2.2.2.4 Isolation of plasmid DNA from bacteria (Maxiprep)	44
2.2.2.5 Genomic DNA isolation from <i>P. falciparum</i> parasites	45
2.2.2.6 Polymerase chain reaction (PCR)	45
2.2.2.7 Agarose gel electrophoresis of nucleic acids	46
2.2.2.8 Agarose gel extraction and purification	46
2.2.2.9 Photometric determination of DNA concentration	46
2.2.2.10 Restriction enzymes digestion of DNA	47
2.2.3 Protein Biochemistry	47
2.2.3.1 Preparation of <i>P. falciparum</i> protein extract	47
2.2.3.2 SDS polyacrylamide gel electrophoresis (SDS-PAGE) of proteins	48
2.2.3.3 Coomassie blue staining for protein visualization	48
2.2.3.4 Protein concentration measurement via Bradford assay	48
2.2.3.5 Thermal proteome profiling of <i>P. falciparum</i> cell lysates	49
2.2.3.6 Intact-cell Cellular Thermal Shift Assay	49
2.2.3.7 <i>In vitro</i> determination of DHFR activity	50
2.2.3.8 <i>In vitro</i> determination of DHPS activity	51
2.2.3.9 <i>In vitro</i> determination of HPPK activity	51
2.2.3.10 Kinase enzymatic activity determination	51
2.2.4 DNA binding studies	52
2.2.4.1 Preparation of salmon sperm DNA fragments	52
2.2.4.2 Preparation of <i>P. falciparum</i> DNA fragments	52
2.2.4.3 Trichloroacetic acid DNA precipitation for [³ H]-SC83288 binding assay	52
2.2.4.4 DNA-binding dyes characterization	53
2.2.4.5 Fluorescence quenching assay	55
2.2.5 Growth inhibition assay and determination of IC ₅₀ values	55
2.2.5.1 Modifications for the measurement of the IC ₅₀ value of sulfadoxine	57
2.2.6 <i>In vitro</i> drug combination assays	58
2.2.7 Untargeted metabolomics	59
2.2.8 Chemical rescue assays	62
2.2.8.1 Growth assay under hypoxanthine supplementation	62
2.2.8.2 Growth assay under S-adenosylmethionine (AdoMet) supplementation	62
2.2.9 Sodium-dependent swelling assay	63

2.2.10 Live cell imaging	64
2.2.11 RNAseq transcriptomics perturbation profiling	66
2.2.12 Data analysis	67
3. RESULTS	69
3.1 SC83288 displays structural similarities with Omecamtiv Mecarbil, but they show no <i>in vitro</i> interaction	69
3.2 SC83288 interacts with antifolates without sharing their target	70
3.3 Untargeted metabolomics analysis shows disruptions in methionine recycling and phospholipids metabolism	74
3.4 SC83288 does not interact with DNA molecules through binding	82
3.5 Intracellular localization strategies	84
3.5.1 SC83288 does not possess relevant fluorescent properties	84
3.5.2 Click chemistry-based approach gives clues about resistance mechanism	85
3.6 SC83288 does not cause a swollen appearance of parasite cells	87
3.7 Untargeted metabolomics analysis of SC83288 resistant parasites	89
3.8 Lower orotate basal levels do not constitute a coping mechanism against antifolates	92
3.9 DBP9 is not a potential target of SC83288	93
3.10 SC83288 causes membrane disruptions in <i>P. falciparum</i> cells	96
3.11 Proteomics approaches	99
3.11.1 Thermal proteome profiling of <i>P. falciparum</i> lysates	100
3.11.2 Intact-cell CETSA reveals the interaction of SC83288 with <i>P. falciparum</i> DNA replication licensing factor MCM2 and fumarase among other proteins	100
3.11.2.1 Fumarate hydratase (PF3D7_0927300)	104
3.11.2.2 Activator of Hsp90 ATPase, putative (PF3D7_0308500, PFC0360w)	105
3.11.2.3 Serine repeat antigen 5 (PF3D7_0207600)	105
3.11.2.4 DNA replication licensing factor MCM2 (PF3D7_1417800)	106
3.11.2.5 Ribosomal protein of the 40S subunit eS17 (PF3D7_1242700)	107
3.11.2.6 CCO copper chaperone Cox17 (PF3D7_1025600)	107
3.11.2.7 Subtilisin-like protease 2 (PF3D7_1136900)	108
3.11.2.8 1-Cys peroxiredoxin, PfAOP (PF3D7_0729200)	108
3.11.2.9 Cytosolic Fe-S protein assembly protein 1 (PF3D7_1209400)	109
3.11.2.10 Isoleucine tRNA ligase, putative (PF3D7_1225100)	109
3.11.2.11 Prolyl 4-hydroxylase subunit α , putative (PF3D7_0829400)	110
3.11.2.12 Cyt-b ₅ -like heme/steroid binding protein (PF3D7_0918100)	110
3.11.2.13 Carbamoyl phosphate synthetase (PF3D7_1308200)	111
3.11.2.14 <i>Plasmodium</i> exported protein PHISTc (PF3D7_0424000)	111
3.11.2.15 Casein kinase 2 subunit α (PF3D7_1108400)	112
3.11.2.16 AP-4 complex subunit ϵ , putative (PF3D7_0904100)	112
3.12 SC83288 induces major downregulation of transcription	113

4. DISCUSSION	119
5. CONCLUSION AND OUTLOOK	129
6. REFERENCES	131
7. APPENDIX I: RESULTS FROM GO ENRICHMENT ANALYSIS	149

List of abbreviations

°C	degrees Celsius
Δ	change
ε	molar extinction coefficient
λ_{exc}	excitation wavelength
λ_{em}	emission wavelength
μ	micro-
Σ	sum
2SC	S-(2-succinyl)cysteine
A	adenine or alanine
Abs	absorbance
ACC	1-aminocyclopropane-1-carboxylic acid
ACS	1-aminocyclopropane-1-carboxylate synthase
ACT	artemisinin combination therapy
ADA	adenosine deaminase
AdoMet	S-adenosylmethionine
AdS	adenylosuccinate
ADP	adenosine diphosphate
ADSS	adenylosuccinate synthetase
AGC	automatic gain control
AMP	adenosine monophosphate
ANOVA	analysis of variance
AOP	antioxidant protein
AP	adaptor protein complexes
api-IRS	apicoplast isoleucine tRNA synthetase
APS	ammonium persulfate
AQ	amodiaquine
Art	artemisinin
ATP	adenosine triphosphate
ATP4	ATPase 4
ATP6	ATPase 6
AU	arbitrary units
AUC	area under the curve
BCE	before common era
bp	base pair(s)
BS	biosynthesis
BSA	bovine serum albumin
C	cytosine or cysteine
CAC	citric acid cycle, tricarboxylic acid cycle, Krebs' cycle
CCO	cytochrome-c oxidase complex
CCT	CTP-phosphocholine cytidyltransferase
CEPT	choline/ethanolamine-phosphotransferase
CETSA	cellular thermal shift assay
CH ₂ -THF	methylenetetrahydrofolate
CIA	cytoplasmic iron-sulfur cluster protein assembly
CK	choline kinase
CK2	casein kinase 2

CPS	carbamoyl phosphate synthetase
CRT	chloroquine resistance transporter
CQ	chloroquine
CuAAC	copper-catalysed azide-alkyne cycloaddition
Cyt	cytochrome
D	aspartic acid
Da	Dalton
DAPI	4,6-diamidino-2-phenylindole
DARTS	drug affinity responsive target stability
DBP9	DEAD box protein 9
dd	double distilled
DEG	differentially expressed genes
DHF	dihydrofolate
DHFR	dihydrofolate reductase
DHPS	dihydropteroate synthase
DIFO	difluorinated cyclooctyne
dil	dilution factor
DINIES	Drug-target Interaction Network Inference Engine based on Supervised analysis
DMSO	dimethyl sulfoxide
DNA	deoxyribonucleic acid
dNTP	deoxyribonucleoside triphosphate
DRTP	drug-dose response transcriptional profiling
DTT	dithiothreitol, Cleland's reagent
E	glutamic acid
<i>E. coli</i>	<i>Escherichia coli</i>
EBI GOA	European Bioinformatics Institute's Gene Ontology Annotation database
EC	Enzyme Commission (number)
ECT	CTP-phosphoethanolamine cytidyltransferase
EDTA	ethylenediaminetetracetate
EK	ethanolamine kinase
EMBL	European Molecular Biology Laboratory
ENT4	equilibrative nucleoside transporter 4
ER	endoplasmic reticulum
<i>et al.</i>	<i>et alia</i> (and others)
F	phenylalanine
FDR	false discovery rate
FH	fumarate hydratase
for	forward
g	gram
<i>g</i>	<i>g</i> force (relative centrifugal force)
GFP	green fluorescent protein
GMP	guanosine monophosphate
GO	gene ontology
GR	glutathione reductase
GSF	succinated glutathione
GSH	glutathione
GSSG	glutathione disulfide, glutathione dimer

GTS	Global Technical Strategy for Malaria 2016-2030
h	hour or human
HEPES	(4-(2-hydroxyethyl)-1-piperazineethanesulfonic acid)
HGPRT	hypoxanthine-guanine phosphoribosyltransferase
HGXPRTase	hypoxanthine-guanine-xanthine phosphoribosyl transferase
HILIC	hydrophilic interaction liquid chromatography
HMDP (-PP)	6-hydroxymethyl-7,8-dihydropterin (-diphosphate)
hpi	hours post invasion
HPPK	6-hydroxymethyl-7,8-dihydropterin pyrophosphokinase
Hsp90	heat shock protein 90
IC ₅₀	half of maximal inhibitory concentration
IMP	inosine monophosphate
iRBC	infected red blood cell(s)
ITDR	isothermal dose-response
IVIEWGA	<i>in vitro</i> evolution and whole genome analysis
kb	kilobase pair
kDa	kilodalton
KEGG	Kyoto encyclopedia of genes and genomes
<i>l</i>	optical path length
L	liter
LB	Luria Bertani
LDH	lactate dehydrogenase
m	milli- or meter
M	molar
MAD	median absolute deviation
MB	methylene blue
MCM	minichromosome maintenance
MDR	multi-drug resistance
MDR-1 (-2)	multi-drug resistance transporter 1 (or 2)
MDT	minimal dose threshold
min	minute
mL	milliliter
mm	millimeter
MMV	Medicines for Malaria Venture
MPMP	malaria parasite metabolic pathways project
MQ	mefloquine
MQO	malate:quinone oxidoreductase
MS	mass spectrometry
MTA	5'-methylthioadenosine
MTR	5'-methylthioribose
MTR1P	5'-methylthioribose-1-phosphate
m/z	mass to charge ratio
n	nano-
NADPH	reduced nicotinamide adenine dinucleotide phosphate
NBD-Cl	4-chloro-7-nitrobenzofurazan
NEB	New England Biolabs
NFM	no-folate medium, folate free medium
niRBC	non-infected red blood cells
NLS	nuclear localization signal

nm	nanometer
NMDG	N-methyl-D-glucamine
NP-40	Tergitol-type NP-40, nonylphenoxyethoxyethanol
NPPs	new permeation pathways
NRPs	non-ribosomal peptides
NT1	nucleoside transporter 1
OAA	oxaloacetate
OD	optical density
OM	Omecamtiv mecarbil
p	pico-
P4H	prolyl-4-hydroxylase
pABA	para-aminobenzoic acid
PAGE	polyacrylamide gel electrophoresis
Pb	<i>Plasmodium berghei</i>
PBS	phosphate buffered saline
PC	phosphatidylcholine
PCD	programmed cell death
PCNA	proliferating cell nuclear antigen
PCR	polymerase chain reaction
PDB	protein data bank
PE	phosphatidylethanolamine
Pf	<i>Plasmodium falciparum</i>
PFA	paraformaldehyde
pH	potential of hydrogen
PHIST	Plasmodium helical interspersed subtelomeric proteins
Pi	phosphate
PKs	polyketides
PMT	phosphoethanolamine methyltransferase
PPi	pyrophosphate
PRPP	phosphoribosyl pyrophosphate
PS	phosphatidylserine
PSD	phosphatidylserine decarboxylase
PSM	peptide spectral matches
PSS/PSS2	phosphatidylserine synthase
PV	parasitophorous vacuole
px	pixel
Pyr	pyrimethamine
QD	quinidine
QM	quadruple mutant
QN	quinine
R ²	coefficient of determination, goodness of fit
RBC	red blood cell
rev	reverse
RNA	ribonucleic acid
ROS	reactive oxygen species
rpm	revolutions per minute
RPMI	Roswell Park Memorial Institute
RT	room temperature
SAMP	adenylosuccinate

SAR	structure-activity relationship
SB	super broth
SD	standard deviation, serine decarboxylase
SDS	sodium dodecylsulfate
SDX	sulfadoxine
sec	second
SEM	standard error of the mean
SERA	serine-repeat antigen
SM	secondary metabolites
snoRNP	small nucleolar ribonucleoprotein particle
SOB	super optimal broth
SOC	super optimal broth with catabolite repression
STEVOR	Subtelomeric Variable Open Reading frame (protein)
SUB2	subtilisin-like protease 2
T	thymine or threonine
TAE	Tris-acetate EDTA
Taq	<i>Thermus aquaticus</i>
TCA	trichloroacetic acid
TCEP	Tris-(2-carboxyethyl)phosphine hydrochloride
TE	Tris-EDTA
TEMED	tetramethyl ethylenediamine
TES	N-Tris(hydroxymethyl)methyl-2-aminoethanesulfonic acid
TP3	TO-PRO-3 iodide
TPP	thermal proteome profiling
Tris	Tris(hydroxymethyl)-aminomethane
TRX	thioredoxin
U	unit
UHPLC	ultra high-performance liquid chromatography
UN	United Nations
Uni PEP	unique peptides identified
UPR	unfolded protein response
USA	United States of America
UTR	untranslated region
UV	ultraviolet
V	volt
vs	versus
v/v	volume to volume
w/v	weight to volume
WHO	World Health Organization
WT	wild type
X	times
Y	tyrosine
YMDB	yeast metabolome database

Summary

Despite global efforts for its elimination, malaria continues to be a major infectious disease worldwide. In 2020, more than 240 million cases and more than 600 000 deaths were reported. This represents a setback in the progress observed in the past decades, which had also reached a plateau in the past few years. This data also shows that the milestones set in the World Health Organization's Global Technical Strategy for Malaria 2016-2030, a plan adopted by the United Nations, have not been met. With an increase in mosquito resistance to insecticides and parasite resistance to antimalarial therapies as main biological threats to malaria control, there is a dire need of new medicines with novel modes of action that are refractory to resistance development. SC83288 is a promising clinical candidate for the treatment of severe malaria that has a novel structure. With high *in vitro* activity against multiple *P. falciparum* strains and no evidence of cross-resistance with other known antiplasmodial drugs, the compound appears to have a novel mode of action as well.

The main objective of this doctoral thesis was to gain a better understanding of the antimalarial mechanism of SC83288 and to identify its molecular targets. To this end, a wide range of methodologies were employed. The analysis of the potential relationship of the compound with antifolates led to the observation that it has an affinity for ATP-binding sites, such as those present in kinases. An untargeted metabolomics study revealed that upon treatment with SC83288, parasites accumulated products of the metabolism of AdoMet through a pathway that has not been reported before in *P. falciparum*. In addition, treated parasites presented lower levels of phosphatidylserine lipids and intermediates of the Kennedy pathway for the synthesis of phosphatidylethanolamine. Live cell imaging showed that early-treated parasites were not able to undergo DNA replication and displayed membrane disruptions accompanied by cell death. A label-free proteomic approach revealed that SC83288 interacts with a number of parasite proteins, from which four were identified as potential targets: fumarate hydratase, protein kinase CK2, DNA replication licensing factor MCM2 and cytosolic [Fe-S] protein assembly protein CIA1. An analysis of the transcriptional response of *P. falciparum* to SC83288 revealed a major downregulation of transcription, and a correlation to the gene transcription profile elicited by methylene blue. Taken together, these results led to the formulation of the hypothesis that the main target of SC83288 is the plasmodial enzyme fumarate hydratase. It is additionally proposed that the compound has multiple targets, which may include CK2, MCM2 and CIA1.

Although further experimental evidence is needed to validate this hypothesis, the results represent a substantial leap towards the elucidation of the mode of action of SC83288.

Zusammenfassung

Malaria ist trotz globaler Bemühungen zur Ausrottung nach wie vor eine der häufigsten Infektionskrankheiten weltweit. Im Jahr 2020 wurden mehr als 240 Millionen Fälle und mehr als 600 000 Todesfälle gemeldet. Dies bedeutet einen Rückschritt der in den letzten Jahrzehnten erreichten Fortschritte bei der Bekämpfung von Malaria, welche in den Jahren zuvor bereits ein Plateau erreicht hatte. Der Anstieg der Fallzahlen führte dazu, dass die festgelegten Meilensteine der globalen technischen Malaria-Strategie 2016-2030 der Weltgesundheitsorganisation (WHO), einem von den Vereinten Nationen angenommenen Plan, nicht erreicht wurden. Aufgrund der Zunahme an Resistenzen von Moskitos gegenüber Insektiziden und Ausbildung von Resistenzen der Parasiten gegenüber Antimalaria-Therapien, besteht ein dringender Bedarf an neuen Arzneimitteln mit neuartigen Wirkmechanismen, welche die Fähigkeit besitzen Resistenzen zu umgehen. SC83288 ist ein vielversprechender Kandidat für die Therapie von schwerer Malaria, welcher eine neue Strukturklasse aufweist. Mit einer hohen in-vitro Aktivität gegenüber mehreren *P. falciparum*-Stämmen und ohne Hinweise auf Kreuzresistenzen mit bereits bekannten antiplasmodischen Medikamenten, scheint der Wirkstoff auch einen neuartigen Wirkmechanismus zu besitzen.

Das Ziel dieser Doktorarbeit war es, das Verständnis für den antimalariatischen Wirkmechanismus von SC83288 zu erweitern und seine molekularen Ziele zu identifizieren. Zu diesem Zweck wurde eine breite Palette von Methoden eingesetzt. Die Analyse der potenziellen Beziehung des Wirkstoffs zu Antifolaten führte zu der Beobachtung, dass eine Affinität für ATP-Bindungsstellen, wie sie in Kinasen vorhanden sind, existiert. Eine ungezielte Metabolismus-Studie ergab, dass die Parasiten nach der Behandlung mit SC83288 Produkte des AdoMet-Stoffwechsels über einen Weg akkumulierten, welcher für *P. falciparum* bisher unbekannt war. Darüber hinaus wiesen die behandelten Parasiten geringere Mengen an Phosphatidylserin-Lipiden und Zwischenprodukten des Kennedy-Stoffwechselwegs für die Synthese von Phosphatidylethanolamin auf. Bildgebende Verfahren in lebenden Zellen zeigten, dass früh behandelte Parasiten nicht in der Lage waren eine DNA-Replikation durchzuführen. Zusätzlich wiesen sie Störungen der Membranen auf, die mit dem Zelltod einhergingen. Ein markierungsfreies proteomisches Experiment zeigte, dass SC83288 mit einer Reihe von Parasitenproteinen interagiert, von denen vier als potenzielle Ziele identifiziert wurden: Fumarat-Hydratase, Proteinkinase CK2, DNA-Replikationslizenzierungsfaktor MCM2 und das zytosolische [Fe-S]-Protein-Assembly-Protein CIA1.

Eine Analyse der Transkriptionsreaktion von *P. falciparum* für SC83288 ergab eine erhebliche Herabregulierung der Transkription und eine Korrelation mit dem durch Methylenblau hervorgerufenen Gentranskriptionsprofil. Zusammengenommen führten diese Ergebnisse zu der Hypothese, dass es sich bei dem Hauptziel von SC83288 um das plasmodiale Enzym Fumarat-Hydratase handelt. Darüber hinaus deuten die Ergebnisse darauf hin, dass der Wirkstoff mehrere Ziele hat, zu denen CK2, MCM2 und CIA1 gehören könnten. Obwohl mehr experimentelle Daten nötig wären, um die Hypothese zweifelsfrei zu bestätigen, konnte durch diese Arbeit ein wertvoller Schritt für die Aufklärung des Wirkmechanismus von SC83288 geleistet werden.

1. Introduction

1.1 Malaria

1.1.1 Origin

Malaria is a potentially lethal infectious disease, which can be tracked back in recorded human history as far back as 2700 BCE [1]. However, it was not until 1890 that humankind began to understand its causes. Before 1880, and the germ theory of infection introduced by Pasteur and Koch, the idea that malaria was caused by miasmas was widely accepted. Miasma is an ancient Greek word for “pollution”, and it was used to describe a poisonous vapour emerging from swamps and decomposing matter. In 1880, a French army doctor named Charles Louis Alphonse Laveran discovered the true pathogens behind malaria [2, 3]. His findings, however, needed several years of further study and the use of newly developed techniques to be fully accepted. By 1890, it was understood that the causing agents of malaria were protozoan parasites of at least three different species, which invade and multiply in red blood cells through a multiple-stage developmental cycle [1]. During the following years, investigations were carried out with the purpose of uncovering how malaria was transmitted to humans. Theories involving mosquitoes as vectors for the disease gained popularity, and they were proven by the British army doctor Ronald Ross in 1897, although for the avian malaria parasite *Proteosoma relictum* (now known as *Plasmodium relictum*). Ross proposed that human malaria was transmitted in the same fashion [4-6], which led to other studies proving his theory [1]. In 1902, Ross was recognized with the Nobel Prize in Physiology or Medicine, and in 1907 Laveran was awarded the same prize [7].

1.1.2 Disease characteristics

Human malaria can be caused by at least six *Plasmodium* species: *P. falciparum*, *P. vivax*, *P. ovale curtisi*, *P. ovale wallikeri*, *P. malariae* and *P. knowlesi*, although the last one is primarily responsible for monkey infections with Macaques as their natural hosts [8, 9]. *Plasmodium falciparum* is the most prevalent globally with its main occurrence in Africa, a region where 95% of total malaria cases are reported [10, 11]. Furthermore, complications in *P. falciparum* infections are responsible for 95% of deaths related to malaria [12].

After an infection with *P. falciparum* parasites, symptoms can take up to 10-14 days to appear, and can present in the form of uncomplicated or severe malaria. Uncomplicated malaria has unspecific symptoms such as fever, chills, body-aches, headache, cough, and diarrhoea.

Outside endemic regions, diagnosis relies on the consideration of patient’s travel history and consequent analysis of stained blood smears using light microscopy [13]. The progression of the disease to severe (and potentially fatal) falciparum malaria depends on the level of immunity (innate or acquired) of the patient and the treatment received, both in its timing and efficacy. The symptoms of severe malaria vary in relationship with the age of the individual as well as their geographical location. The median age of patients is inversely proportional to the intensity of transmission. In areas with stable high transmission throughout the year, severe anaemia is the most common complication, especially among infants and young children. Meanwhile, in regions where transmission is less intense or follows a seasonal pattern, cerebral malaria in children takes the lead. Severe manifestations of falciparum malaria in adults and children include impaired consciousness, respiratory distress (acidotic breathing), multiple convulsions, prostration, shock, pulmonary oedema (confirmed radiologically), abnormal bleeding, jaundice, severe anaemia, hypoglycemia, acidosis, hyperlactatemia, acute kidney failure, and hyperparasitemia [14].

1.1.3 Fight against malaria: a battle yet to be won

Despite constant efforts against it, malaria still constitutes a major burden on global health. A decreasing trend in the global number of cases and deaths was observed from 2000 to 2015 (Table 1-1), but the progress reached a plateau in the following years. Moreover, an increase has been seen in the data from 2020. These global values correspond not only to falciparum malaria but also to the cases caused by the other potentially lethal parasite, *P. vivax*, although they represent less than 2% of total cases. Vivax malaria is, however, especially important outside the African continent [11].

Table 1-1. Global estimated malaria cases and deaths in selected years over 2000-2020. Estimated cases and deaths are shown with 95% upper and lower confidence intervals. Adapted from [11].

Year	Number of cases (x1 000)				Number of deaths		
	Point	Lower bound	Upper bound	<i>P. vivax</i> (%)	Point	Lower bound	Upper bound
2000	241 000	226 000	260 000	7.7	896 000	854 000	942 000
2005	246 000	228 000	271 000	8.1	778 000	733 000	838 000
2010	244 000	225 000	269 000	6.7	698 000	650 000	764 000
2015	224 000	207 000	243 000	4.5	562 000	524 000	619 000
2020	241 000	218 000	269 000	1.9	627 000	583 000	765 000

To analyse the progress in the battle against malaria, it is important to consider the incidence (number of cases per 1 000 population at risk), which was reduced from 81 in 2000 to 59 in 2015, and to 56 in 2019.

The decrease in incidence together with a number of cases following a consistent or even slightly increasing pattern reflects the growth in population at risk, which is a factor that makes data interpretation a much more complex task. The increase in incidence and case numbers for the year 2020 can be attributed to disruptions caused by the COVID-19 pandemic [11, 15].

The distribution of malaria cases and fatalities around the globe can be seen in the maps from the Malaria Atlas Project [16, 17]. The decrease in falciparum malaria achieved in the period from 2000 to 2019 is recognizable in the maps shown in the figures Figure 1-1 and Figure 1-2. Here, the sustained malaria burden on the African continent is especially notable, together with the rising number of cases in the Bolivarian Republic of Venezuela. As mentioned earlier, most of the malaria cases (95%) are concentrated on the African continent, as well as deaths (96%) from which around 80% correspond to children under the age of five [11].

In 2015, the United Nations (UN) adopted the World Health Organization's (WHO) Global Technical Strategy for Malaria 2016-2030 (GTS), with the aim to reduce malaria incidence and mortality rates by at least 90% from the levels registered in 2015. As of 2021, the milestones set in the GTS have in general not been met [18]. Key obstacles in the fight against malaria are not only of financial nature but also biological, parasite resistance to currently used antimalarial therapies and mosquito resistance to insecticides are major threats to malaria elimination.

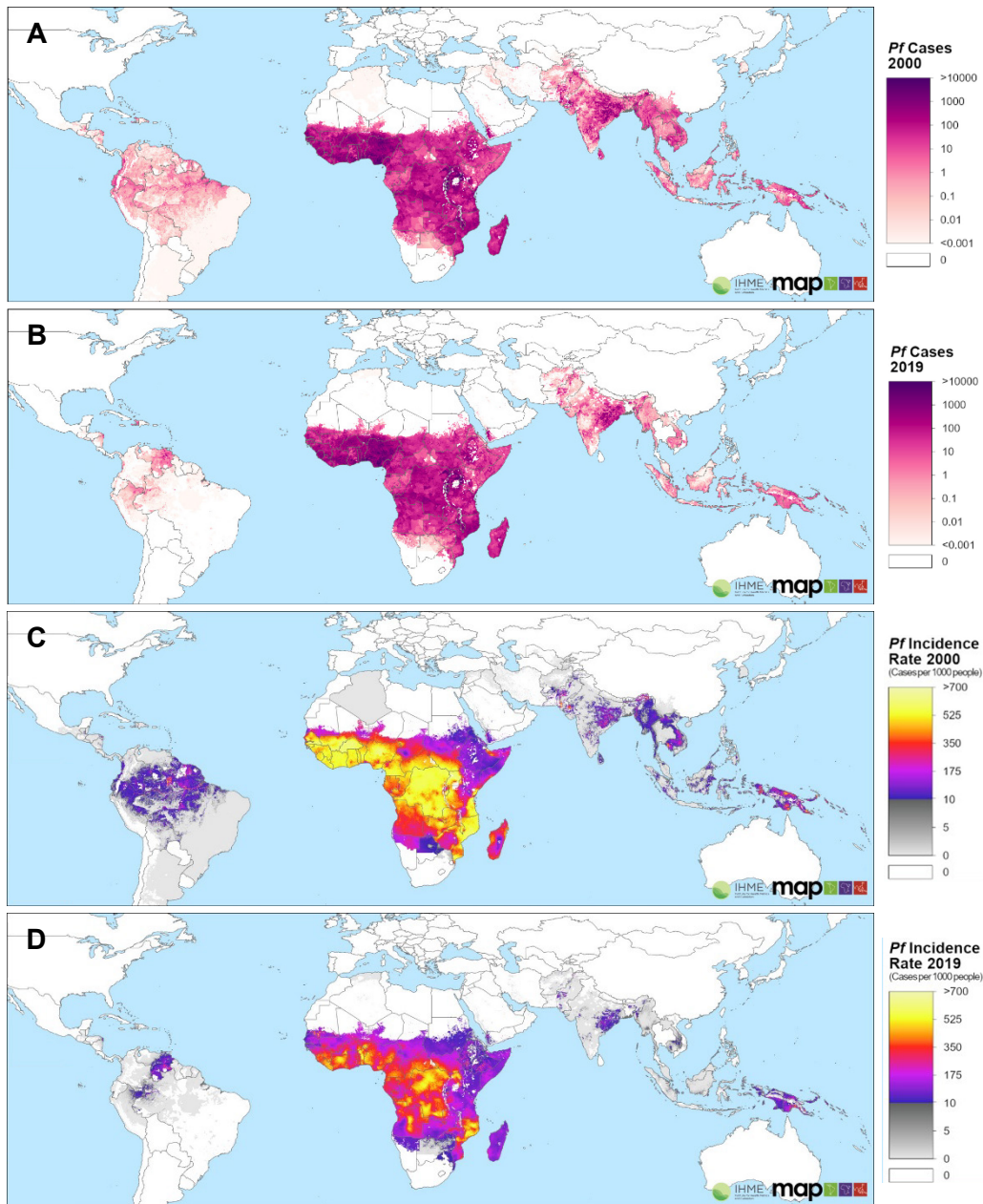


Figure 1-1. Distribution of the global burden of *P. falciparum* malaria cases in the years 2000 and 2019. (A-B) Total estimated falciparum malaria cases worldwide in the year 2000 (A) and 2019 (B). (C-D) Incidence rates (cases per 1 000 people) of falciparum malaria worldwide in the year 2000 (C) and 2019 (D). Note the colour scaling is split to better differentiate within low endemic areas, with one linear scale between rates of zero and ten cases per 1000 (grey shades) and a second linear scale between 10 and 1 000 (colours from purple to yellow). Adapted from the Malaria Atlas Project [16, 17] under the Creative Commons Attribution 3.0 Unported License (CC BY 3.0).

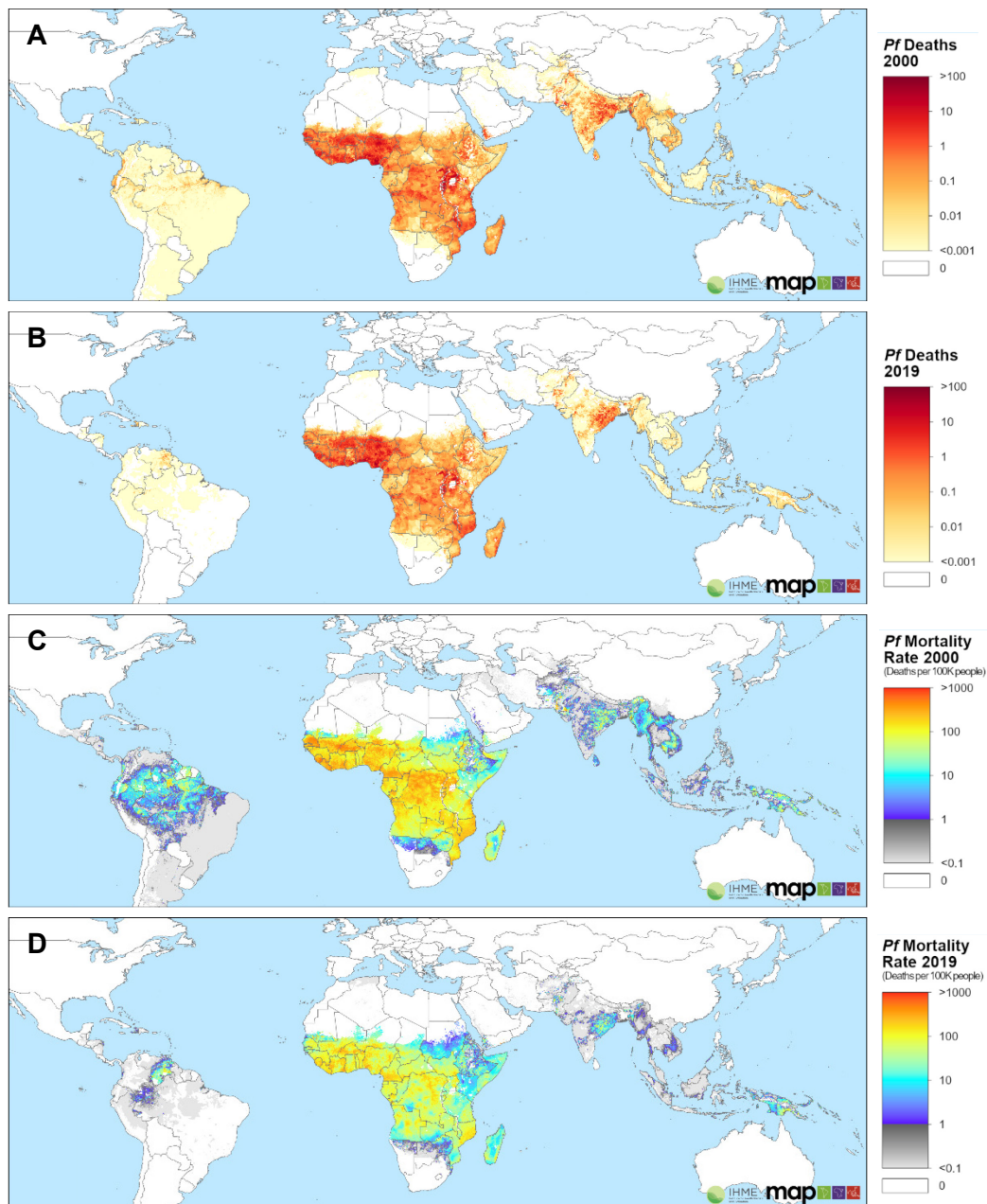


Figure 1-2. Distribution of the global burden of *P. falciparum* malaria deaths in the years 2000 and 2019. (A-B) Total estimated falciparum malaria deaths worldwide in the year 2000 (A) and 2019 (B). (C-D) Mortality rates (deaths per 100 000 people) of falciparum malaria worldwide in the year 2000 (C) and 2019 (D). Note the colour scaling is split to better differentiate within low endemic areas, with one linear scale between rates lower than 0.1 and 1 death per 100 000 people (grey shades) and a second linear scale between 1 and higher than 1 000 (colours from blue to orange). Adapted from the Malaria Atlas Project [16, 17] under the Creative Commons Attribution 3.0 Unported License (CC BY 3.0).

1.2 Biology of *Plasmodium falciparum*

1.2.1 Life cycle of *P. falciparum* parasites

The apicomplexan parasite *Plasmodium falciparum* develops through a complex life cycle that involves humans and mosquitoes as host organisms. When an infected female Anopheles mosquito takes a blood meal (Figure 1-3, A), *P. falciparum* sporozoites enter the human host and infect liver cells (Figure 1-3, B). After the successful infection of a hepatocyte, a parasitophorous vacuole is formed around the sporozoite, which undergoes a liver stage development for about ten days. Then, the parasite, which has the form of a merozoite, is able to release merozoites into the bloodstream. From now on, the parasites enter an asexual replicative cycle that involves erythrocytes as host cells (Figure 1-3, C). Each iteration of this cycle lasts approximately 48 hours and starts with the invasion of red blood cells by the merozoites. The parasites go through three developmental stages: rings, trophozoites and schizonts. In the last stage, parasites undergo schizogony, a cell division process that culminates with the formation of merozoites, that are released from the infected erythrocyte to infect new host cells and initiate a new cycle. The asexual development cycle of these apicomplexan parasites is responsible for the clinical manifestations of malaria. A proportion of cells differentiate in their development and instead of going through another replicative cycle, they commit to sexual development for the formation of female or male gametocytes (Figure 1-3, D). For this, the parasite goes through five stages in about 15 days. Fully developed gametocytes are then taken up by female Anopheles mosquitoes during a blood meal. In the mosquito midgut, a macro- and a microgamete (originated from a female and a male gametocyte) form a zygote through sexual reproduction (Figure 1-3, E). This zygote transforms into an ookinete that migrates through the midgut epithelium to form an oocyst. A 17-days sporogonic cycle inside the oocyst (Figure 1-3, F) allows the formation of sporozoites, which will in turn migrate to the mosquito salivary glands, enabling malaria transmission. The life cycle is then complete and ready for transmission to a new host during the next blood meal [19].

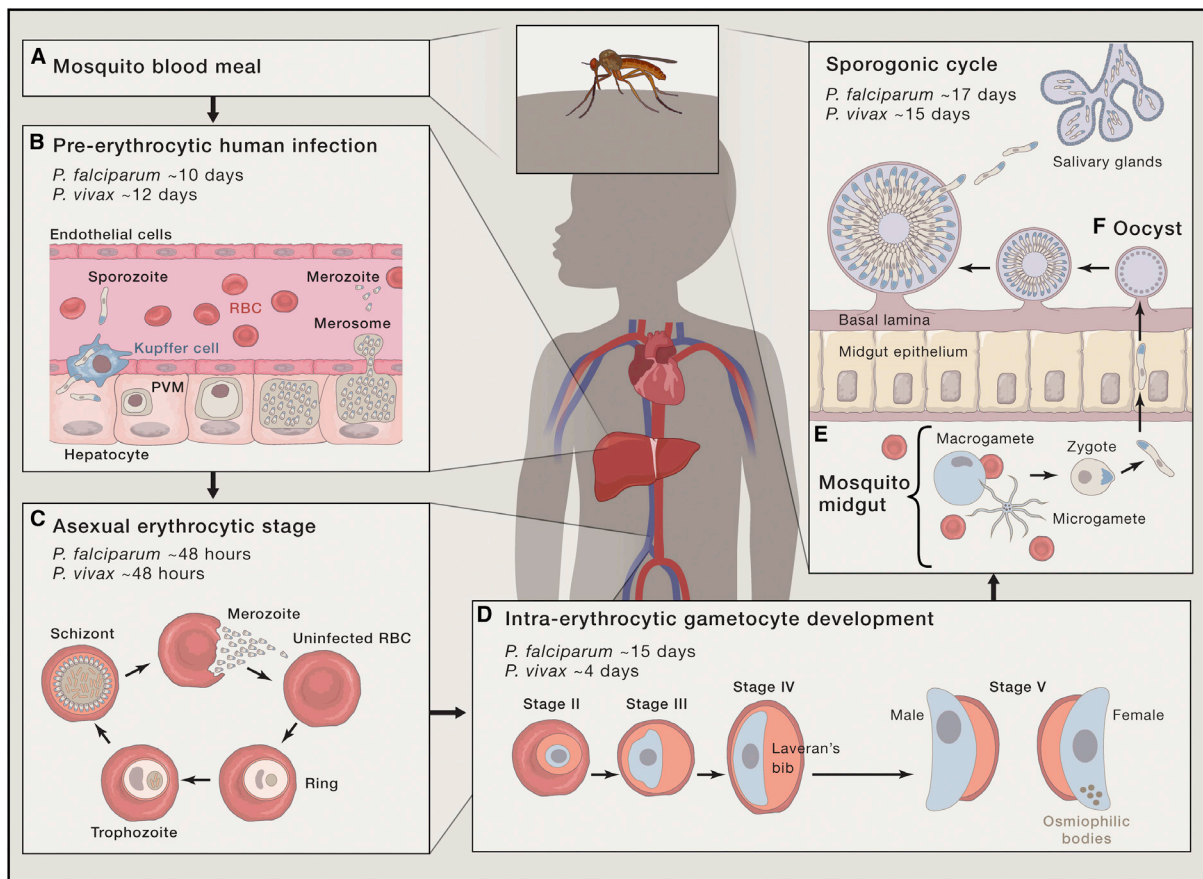


Figure 1-3. Life cycle of *P. falciparum* parasites. (A) The cycle starts when an infected female *Anopheles* mosquito takes a blood meal, and sporozoites enter the human host. (B) Sporozoites reach the liver and invade hepatocytes. Through schizogony, the parasite replicates and releases tens of thousands of merozoites into the bloodstream. (C) Merozoites invade erythrocytes, where an asexual development cycle takes place. (D) A portion of merozoites escape the asexual cycle and commit to gametocytogenesis. (E) Gametocytes are taken up by a mosquito during a blood meal and develop into extracellular female and male gametes in the midgut. (F) After mating, the formed zygote develops into an oocyst, where asexual sporogonic replication occurs. Released sporozoites reach the salivary glands and are then ready for the invasion of a human host during the next blood meal. Figure from the work of Cowman *et al.* [19], reproduced with authorization from the publisher.

1.2.2 Asexual reproduction of parasites: schizogony

In general, the cell cycle of eukaryotes can be described roughly as a series of steps in which the cell grows, duplicates its genome and divides. For apicomplexans, and specifically for *P. falciparum*, this process is different and allows the generation of a higher number of daughter cells. During intraerythrocytic stages up to around 16 merozoites can be released from an infected red blood cell, and although not all merozoites can achieve a new infection, they produce parasite multiplication rates of up to 11-fold per asexual development cycle [20]. *P. falciparum* parasites follow asexual reproduction by schizogony, a process in which the cell undergoes multiple rounds of asynchronous DNA replication and nuclear division conserving an intact nuclear envelope and becoming a multinucleated cell before fragmentation and formation of merozoites takes place [21].

The daughter cells are then released and, after successful erythrocyte invasion, transform to rings that develop into mononucleated trophozoites. Around 30 hours post invasion (hpi) the DNA replication process starts and a new round of schizogony takes place [22].

Plasmodium parasites possess DNA replication machinery conserved across eukaryotes, such as DNA polymerases, proliferating cell nuclear antigen (PCNA), and minichromosome maintenance proteins (MCMs). However, some elements of the origin recognition complex (ORC), that binds to DNA and promotes the initiation of replication, could not be identified by homology [20].

The cell cycle of these parasites is highly complex and in order to succeed it must be tightly regulated. Although some agents involved in the regulation have been characterized, the details of this process remain largely elusive [20].

1.2.3 Metabolism of nucleotides in *P. falciparum* parasites

The development of *P. falciparum* parasites through schizogony requires the steady provision of purine and pyrimidine nucleotides for their use as building blocks for the synthesis of DNA as well as the RNA necessary for gene transcription. While they cannot synthesize purines, they are able to import various metabolites from the host cell and incorporate them into a recycling pathway (Figure 1-4) to generate dATP, ATP, GTP and dGTP. Through PfNT1-mediated (*P. falciparum* nucleoside transporter 1) transport, hypoxanthine, xanthine, guanine, adenine and adenosine are imported from the infected erythrocyte and incorporated to the salvage route [23]. In addition, parasites can use AMP as an alternative purine source, although its uptake involves a transporter that remains unknown [24]. The uptake of adenine and 2'-deoxyadenosine can also occur through PfENT4 (*P. falciparum* equilibrative nucleoside transporter type 4) [25].

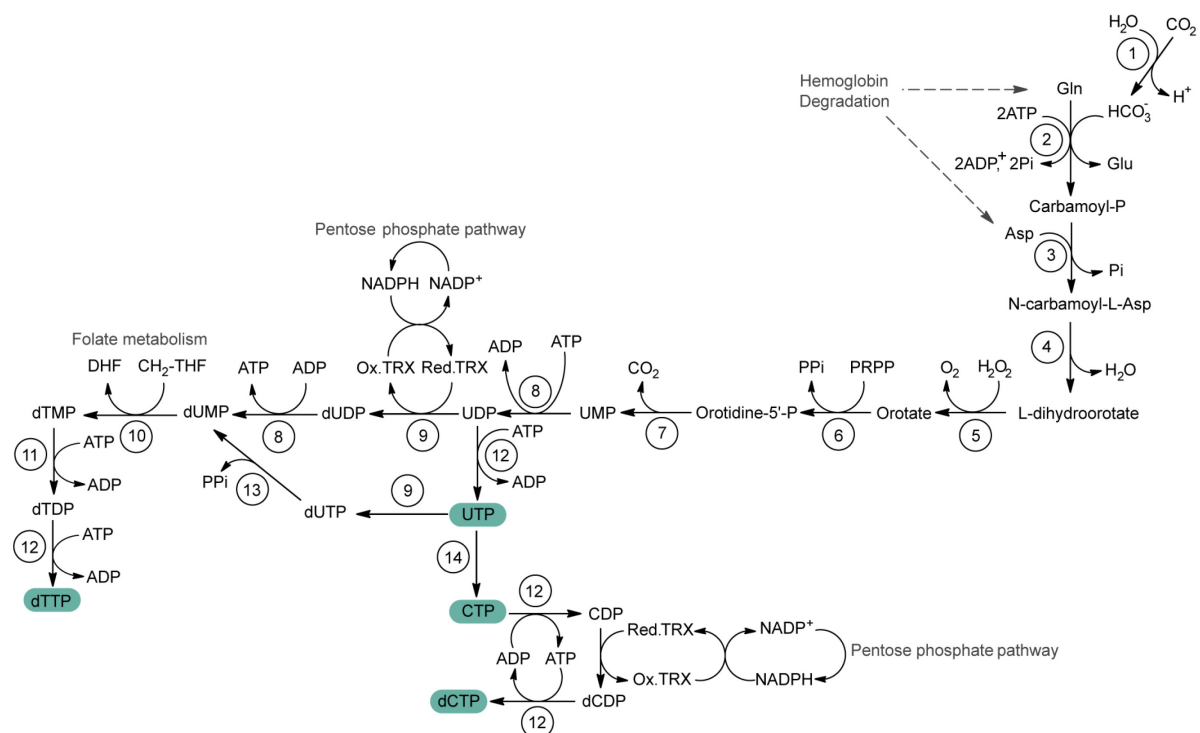


Figure 1-5. Pathway for the synthesis de novo of pyrimidine nucleotides in *P. falciparum* parasites. The products of this route are dTTP, UTP, dCTP and CTP (highlighted in green). Enzymes: (1) Carbonic anhydrase, (2) Carbamoyl-P synthetase, (3) Aspartate carbamoyltransferase, (4) Dihydroorotase, (5) Dihydroorotate dehydrogenase, (6) Orotate phosphoribosyltransferase, (7) Orotidine-5'-phosphate decarboxylase, (8) Cytidylate kinase, (9) Ribonucleotide reductase, (10) Thymidylate synthetase, (11) dTMP kinase, (12) Nucleotide diphosphate kinase, (13) dUTP diphosphatase, (14) CTP synthase. Abbreviations: TRX, thioredoxin; DHF, dihydrofolate; CH₂-THF, methylenetetrahydrofolate. This metabolic route scheme was built following the website of the MPMP project (Malaria Parasite Metabolic Pathways) [26] and the work from H. Ginsburg [27].

1.3 A brief history of antimalarial drugs

The history of medicines used to treat malaria is extensive and in the last two hundred years the efforts that have been dedicated to eradicating (or at least fighting against) the disease are reflected in the number of therapies developed. To this day, new drugs are being investigated and needed, since the emergence of resistance is a major threat to the progress in malaria elimination [11]. An overview of how antimalarials have evolved over time is presented in the following sections.

1.3.1 A look into the past

The known history of antimalarials goes as far back as the 17th century, when bark from the cinchona tree, was used in Peru to treat malaria. Then called “Jesuits’ Bark” or “sacred bark”, it was dried, finely grounded and mixed into wine for its consumption. After almost 200 years, in 1820, quinine (QN, Figure 1-6, A) was extracted from the bark and purified by Pierre Joseph Pelletier and Joseph Caventou.

Quinine was the main antimalarial for another hundred years, until the development of more effective synthetic alternatives [29]. In 1909, almost a century after the isolation of QN, its correct structure was reported by Paul Rabe [30]. However, before the structure was fully elucidated, William Henry Perkin attempted to synthesize the compound, which led to the discovery of the first aniline dye. This was the beginning of a synthetic dye industry that would develop more chemotherapeutic agents against a range of diseases including malaria [31]. Although the mode of action of QN is not fully understood, purine nucleoside phosphorylase was recently identified as a target [32]. Currently, the use of this drug (in combination with doxycycline) is only recommended by the WHO for the management of severe malaria when an artemisinin combination therapy (ACT) is not available [33].

Quinacrine (also known as mepacrine or atabrine, Figure 1-6, B), was one of the many synthetic compounds developed by the dye industry to replace QN in response to the shortages experienced during end of the First World War and following decades. It was widely used during the Second World War, but the posterior rise of chloroquine led to its replacement [34]. The effects of quinacrine are mainly attributed to DNA intercalation and regulation of nuclear proteins, and efforts are currently directed to repurpose quinacrine for anticancer therapy [35].

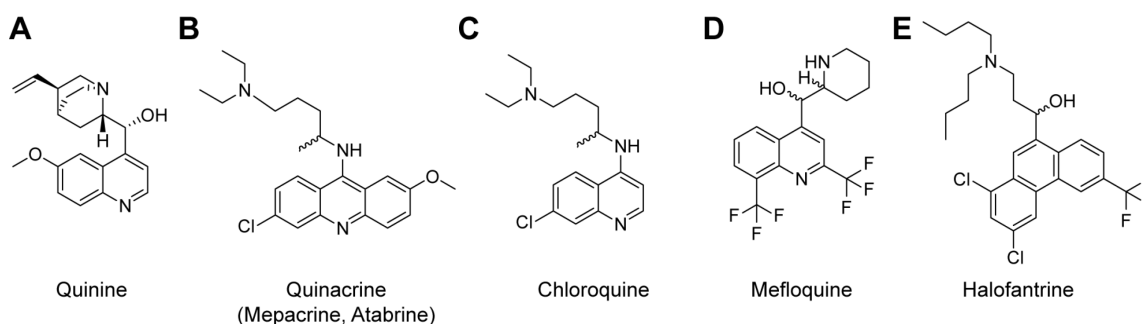


Figure 1-6. Antimalarials from the past. Structure of antimalarial medicines of importance that were discovered or developed between the 17th century and the 1980s. Register of quinine-containing bark from the cinchona tree usage dates back to the 17th century, although the isolation of the alkaloid was achieved in 1820. Resistance has reduced partially or completely the effectiveness of some of these drugs, which have been replaced with other therapies.

Another compound that originated in the German dye industry during the interwar period is Resochin (also known as SN 7618) which was first synthesized in 1934 [34]. Soon after, its development was abandoned after it was mistakenly considered too toxic for clinical use [34]. During the Second World War, US American researchers continued investigations on SN 7618, now known as Chloroquine (CQ, Figure 1-6, C) [34, 36]. The drug was an excellent antimalarial, used massively worldwide.

However, in less than two decades resistant strains started spreading, limiting the use of CQ for malaria treatment [37]. The mode of action of CQ involves the interaction with β -hematin crystals surfaces, leading to the inhibition of crystallization and heme detoxification in parasites [38]. In order to exert this toxic effect over *P. falciparum* cells, CQ accumulates in the parasite digestive vacuole [39, 40]. Resistance is mediated by mutant versions PfCRT (*P. falciparum* Chloroquine Resistance Transporter), a membrane protein located in the digestive vacuole that is able to transport the drug out of the organelle [41-46]. Currently, CQ is only recommended for the treatment of *P. vivax* infection and for prophylaxis in central America for vivax malaria [33].

Mefloquine (MQ, Figure 1-6, D) was developed for the treatment of chloroquine resistant malaria by the US Army after the Vietnam War, in the 1970s [47, 48]. The mode of action of MQ is related to that of other quinoline antimalarials, as the previously described CQ, and involves the inhibition of heme detoxification [38]. After less than ten years in the market for the treatment of uncomplicated malaria, resistance to MQ emerged, mediated by PfMDR1 (*P. falciparum* multidrug-resistant transporter 1) [49, 50]. Despite controversy regarding toxicity over the nervous system and side effects, which were deemed rare by later studies [47, 51, 52], MQ is used for treatments in combination with artesunate, while it is recommended for chemoprevention purposes as a standalone therapeutic [33]. Halofantrine (Figure 1-6, E) was also developed by the US Army, and was first reported as effective against multi-drug resistant malaria in 1982 [53]. Mainly due to cardiotoxicity and other side effects, it is no longer recommended for treatment or prophylaxis, although it may be used in extreme cases where both the patient has no cardiac disease and the manifestations of malaria are not only severe but also caused by a multi-resistant strain [47, 48].

1.3.2 Antimalarials currently in use

The latest Model List of Essential Medicines from the WHO [33] lists 16 drugs for the treatment of malaria. They have to be used as combination therapies, with only three exceptions. Artemether (Figure 1-7, A) is indicated for the management of severe malaria, CQ, can be used alone to treat *P. vivax* infections, and primaquine shall be used alone to achieve a radical cure *P. vivax* and *P. ovale* infections in a 14-days treatment. In addition, six formulations are listed for antimalarial chemoprophylaxis: amodiaquine-sulfadoxine-pyrimethamine, CQ (only in central America for vivax malaria), doxycycline, MQ, proguanil-CQ and sulfadoxine-pyrimethamine.

Artemisinin (first called qinghaosu) origins go back to more than 2000 years in the past [54]. It is a natural product present in the leaves of *Artemisia annua*, which was used in Chinese traditional medicine against fevers. The discovery of its antimalarial properties happened in the late 1960s, amidst a rather complex political context in China [55, 56]. The isolation of artemisinin was carried out by the research group of Prof. Youyou Tu in 1972 [54], and after the great impact it had in the fight against malaria, she was awarded the Nobel Prize in Physiology or Medicine in 2015 [7]. Although ACTs have been a key success factor in the progress towards malaria elimination, their role as gold standard therapy is endangered by the spread of parasite resistance [57-61]. Studies on the mode of action and resistance of artemisinin have been controversial [62]. As a general overview, artemisinin and its derivatives are activated by heme, generating free radicals that inflict protein damage [63, 64], while they are also involved in the up regulation of the unfolded protein response (UPR) pathways [65]. Resistance to artemisinin is associated with mutations in the Kelch-type propeller domain of the parasite protein PfK13 [66], which are thought to help parasites cope with the UPR up regulation by altering ubiquitination patterns [67] enhancing their survival rate. The project that resulted in the discovery of artemisinin was also the origin of other antimalarials, such as lumefantrine (also called benflumetol, discovered in 1976) and pyronaridine (in 1973), which are partner drugs in ACTs (Figure 1-7, A) [68] and interfere with β -hematin formation [48, 69].

Combination therapies, such as artemether-lumefantrine, artesunate-pyronaridine, artesunate-amodiaquine, artesunate-mefloquine, and dihydroartemisinin-piperaquine (Figure 1-7, A) [48], consist one of three fast acting and more bioavailable artemisinin derivatives with a partner drug that has a different mode of action and a longer half-life. This is highly efficient and avoids recrudescence, since the partner drug eliminates the parasite charge that persists after the artemisinin derivative concentration has significantly decreased [70].

Amodiaquine and piperaquine (Figure 1-7, A) are ACTs partner drugs structurally related to CQ. The first is a 4-aminoquinoline first synthesized in 1948, while the latter is a bulkier bisquinoline discovered in China in the 1960s. They inhibit the process of heme digestion and detoxification, sharing their mode of action with other quinoline-based drugs [48, 71, 72].

Antifolate antimalarials target either the enzyme dihydropteroate synthase (PfdHPS, class I antifolates) or dihydrofolate reductase (PfdHFR, class II antifolates). Proguanil (Figure 1-7, B) is a prodrug that targets DHFR after its metabolization to cycloguanil and was reported in 1945 as the first antimalarial of this type [73]. In the last decades, it was used for chemoprophylaxis and treatment of uncomplicated malaria in combination with atovaquone, an inhibitor of the plasmodial mitochondrial electron transport, under the name of Malarone [74]. Currently, the use of Malarone is no longer recommended by the WHO, but proguanil in combination with CQ is advised for chemoprophylaxis [33]. Pyrimethamine is a class II antifolate developed in the 1950s, and it is the most widely used antimalarial compound of this kind. It has been used alone, but mostly in combination with sulfadoxine (a class I antifolate with origin in the 1960s) [73]. Pyrimethamine and sulfadoxine (Figure 1-7, C) are among the recommended drugs used for chemoprophylaxis, together and in a triple combination with amodiaquine, while for curative treatments they are only advised for their use in combination with artesunate [33].

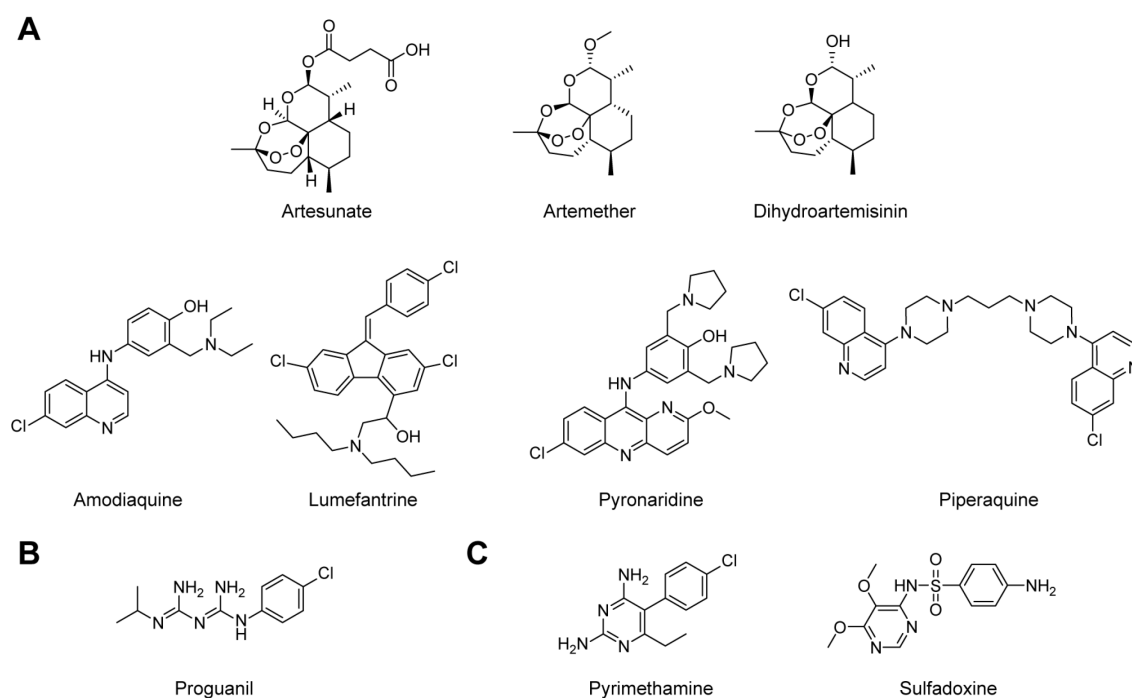


Figure 1-7. Structure of antimalarials in use. Structure of compounds are grouped according to their use in combination. (A) Artemisinin derivatives and partner drugs: artemether-lumefantrine, artesunate-pyronaridine, artesunate-amodiaquine, artesunate-mefloquine (MQ structure is shown in Figure 1-6), and dihydroartemisinin-piperaquine are used ACTs. (B) Proguanil, one of the first antifolates for the treatment of malaria, is used for chemoprophylaxis in combination with CQ. (C) The antifolate combination pyrimethamine-sulfadoxine, commonly sold under the name Fansidar.

1.3.3 The malaria treatment of tomorrow

New medicines are needed for the battle against malaria, which have to fulfil specific requirements depending on the ultimate objective of the fight: control and case management, elimination, or chemoprevention to prevent re-introduction of the disease. The spread of resistance to artemisinin-based therapies increased the demand for new drugs with novel modes of action effective against resistant strains, which should ideally also be effective with a short and simple treatment [75]. Currently, the antimalarial pipeline has a substantial number of compounds across the different stages of drug development, which were recently reviewed in detail by Tse *et al.* [48]. Additionally, an updated overview of the development projects supported by the international consortium Medicines for Malaria Venture (MMV) can be found on their website [76]. It is important to remark that despite the growth of new antimalarial candidates in the last years it is necessary to continuously provide a strong supply of new molecules into the pipeline, due to attrition and failure in later development stages [77].

1.4 SC83288, a promising novel drug candidate

SC83288 is the product of years of work in lead optimization efforts from a new class of antimalarials: sulfonyl-phenyl-ureido benzamidines (Figure 1-8) [78]. These originated from the chemical optimization of an *in silico* high throughput screening of a virtual library of small molecules interacting with the structure of *P. falciparum* lactate dehydrogenase (LDH). While sulfonyl-phenyl-ureido benzamidines display low *in vitro* activity as inhibitors of PfLDH, they produce a strong inhibition of parasite growth [79]. SC83288 possesses a strong *in vitro* antiparasitic activity (in the nanomolar range) against a wide spectrum of *P. falciparum* strains, including those resistant to known antimalarials (Table 1-2). Remarkably, when evaluating a short-term exposure of parasites, it showed to be more active against trophozoite and schizont stages [78]. Additionally, it has shown no interaction with artemisinins [80].

SC83288 is sensitive to structural changes, which is reflected in the results from the structure activity relationship (SAR) study reported by Pegoraro *et al.* [78]. Furthermore, the compound was found to be stable and therefore not metabolized by parasites or erythrocytes over the course of six hours [78]. These findings remark the importance of all the moieties present in the molecule and suggest that it interacts as a whole with its main target.

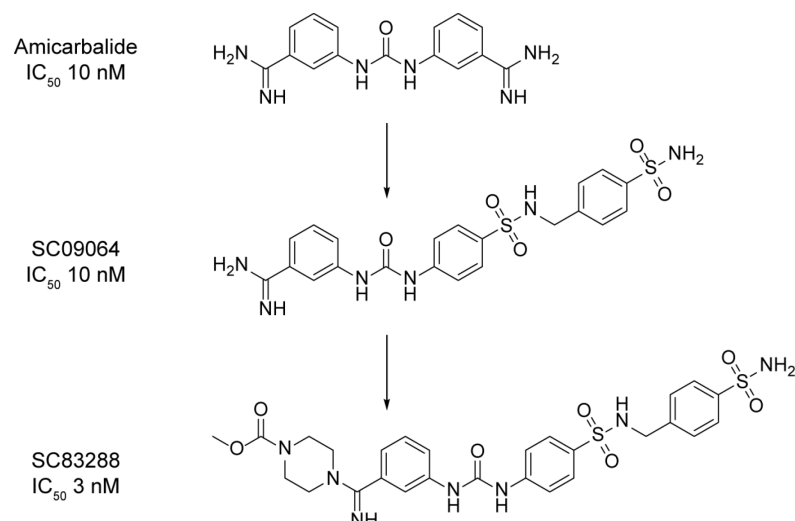


Figure 1-8. Structures and *in vitro* antimalarial activity of hit and lead compounds. IC₅₀ values correspond to measurements of *in vitro* growth inhibition assays using *P. falciparum* Dd2 parasites. Adapted from [78].

Table 1-2. Susceptibility of several *P. falciparum* strains to SC83288 and selected antimalarials. IC₅₀ values are expressed as mean ± SEM of three independent determinations. Abbreviations: n.d., not determined; CQ, chloroquine; QN, quinine; QD, quinidine; MQ, mefloquine; Pyr, pyrimethamine; AQ, amodiaquine; Art, artemisinin. The presented values were reported in [78].

Strain	IC ₅₀ (nM)							
	SC83288	CQ	QN	QD	MQ	Pyr	AQ	Art
Dd2	3 ± 1	135 ± 21	100 ± 1	15 ± 1	4 ± 0.1	22000 ± 1700	7 ± 1	2 ± 0.1
D10	5 ± 1	11 ± 3	58 ± 5	16 ± 1	1 ± 0.1	11 ± 2	7 ± 2	9 ± 0.4
3D7	8 ± 2	3 ± 1	14 ± 2	14 ± 1	4 ± 0.1	16 ± 3	8 ± 1	8 ± 0.3
FCR3	6 ± 1	25 ± 4	182 ± 27	32 ± 6	4 ± 0.6	31 ± 8	8 ± 0.4	5 ± 1
K1	5 ± 1	70 ± 14	46 ± 4	12 ± 3	1 ± 0.2	> 15000	9 ± 1	3 ± 1
Thai19	4 ± 1	74 ± 17	62 ± 1	22 ± 5	1 ± 0.1	> 15000	9 ± 1	3 ± 1
7G8	10 ± 1	30 ± 7	70 ± 17	16 ± 4	2 ± 0.1	> 15000	7 ± 2	1 ± 0.3
NF54	2 ± 1	n.d.	n.d.	n.d.	n.d.	n.d.	n.d.	n.d.

Throughout preclinical studies, SC83288 showed to be a promising clinical candidate for the treatment of severe malaria, presenting a favourable pharmacokinetic profile and the ability to cure *P. falciparum* infections in humanized mice [78].

An *in vitro* evolution and whole genome analysis (IVIEWGA) approach was carried out in an initial attempt to understand the mode of action of the drug. The generation of parasite lines resistant to SC83288 was possible, but it required increasing drug pressure from 50 nM to 1 µM over the course of more than eight months. Genome sequencing of these resistant strains revealed alterations in the genes encoding the multi-drug resistance transporter 2 (PfMDR2), the putative RNA helicase DBP9, and the calcium pump PfATP6 [78].

A later study showed that a single amino acid mutation on PfATP6, substituting a phenylalanine residue for a tyrosine at the position 972 was sufficient to produce a decrease of three orders of magnitude in parasite susceptibility to SC83288, reflected on a higher IC₅₀ value. However, during the same study, PfATP6 was found to play a role only in resistance to the drug and not on its mode of action [81]. Further experiments have been carried out in an attempt to characterize the mechanism in which the drug exerts its antiplasmodial activity but, so far, no molecular targets have been identified.

1.5 Target identification strategies

The identification of the molecular targets of a small molecule, alongside the elucidation of its mode of action is a complex, cost- and time-intensive task. Furthermore, this process can increase tremendously in difficulty if the compound has multiple targets. In such cases, decades of research work can go by without leading to clear answers, as can be learned from the history of suramin [82]. There is a wide range of approaches that can be used for this purpose, and their use may not only be limited by the access to specific equipment or associated costs but also by specific characteristics of the bioactive compound. Therefore, there is no “one fits all” standard path for target identification. The combined application of complementary methods suitable for the molecule under study, allows for the construction of a model for its mode of action. This is done from a big-picture perspective that takes into consideration the interactions of the molecule with cellular components and its effects from different points of view (e.g. metabolomics, proteomics, transcriptomics, bioinformatics analysis). Then, the model can be tested in order to validate the proposed targets or to modify the underlying hypothesis.

Experimental target identification approaches can be roughly divided into those that require a labelling or modification of the bioactive molecule, and label-free methods. The first ones are widely used, with affinity-based proteomics (also referred to as pulldown methods) being the most remarkable example [83]. However, it is not always possible to synthesize an adequate probe that retains the bioactivity of the studied molecule or that is able to interact in the same way with cellular components. Such is the case for SC83288, whose antimalarial activity is greatly affected by structural changes. Label-free technologies are therefore the tool of choice. Among these we can find approaches without direct detection of drug-target interaction but of the cellular responses to treatment, such as untargeted metabolomics, transcriptome profiling and the observation of cellular parameters or characteristics such as the integrity of intracellular structures through electron microscopy.

The intracellular localization of the compound can also be helpful in target elucidation, although it is only possible to carry it out in a label-free setting when the compound properties are adequate, i.e. it is fluorescent. A genomics approach extensively used is IVIEWGA, where sublethal doses of the compound are administered to cultured cells over long periods of time in order to obtain cell lines resistant to the compound. The genomes of the resulting resistant clones are then sequenced to identify differences to the wild-type strain, which are usually associated with the mode of action of the drug [84]. There are also proteomics methods that do not require a functionalization of the small molecule of interest, such as CETSA (Cellular Thermal Shift Assay) and DARTS (Drug Affinity Responsive Target Stability), among others [85, 86]. These two techniques are based on the differential properties of proteins when they are bound to ligands such as small active molecules. DARTS takes advantage of the lower susceptibility of bound proteins to the action of proteases, allowing for the identification of SDS-PAGE gel bands that do not show a decrease in intensity (and therefore concentration) when digested in the presence of the drug under study [87]. CETSA exploits the differential thermal stability of proteins bound to ligands, allowing the detection of differences in the soluble fraction of protein at denaturing temperatures [32, 88]. The detection can be carried out using mass spectrometry for identification, as well as western blot for validation purposes [85].

Overall, a plethora of methods for target identification, each with its own advantages and downfalls, can be combined for the unveiling of the mode of action of a molecule with known bioactivity properties. The choice of technique is related to a number of factors, such as the characteristics of the drug, the organism towards which it is active, already known information about possible molecular targets, and available equipment. As new technologies are developed, the obstacles for this process are slowly broken down, but it remains cost- and time-intensive. Although not a strict requirement for drug approval, target identification is of great importance [89]. Especially for molecules with novel structures, such as SC83288, efforts for the elucidation of their mode of action can lead to the discovery of new antimalarial targets and a better understanding of the biology of *P. falciparum* parasites.

1.6 Aim of the study

This doctoral thesis is focused on the elucidation of the molecular targets of SC83288, as well as the understanding of its mode of action. The aim of this work is then to contribute to further development of the drug, uncovering possibilities for its optimization and increasing the chances of success of future clinical trials as well as to aid in the identification of potential interactions with other drugs or within patients, which may or not be desired.

2. Materials and Methods

2.1 Materials

2.1.1 Equipment

Equipment	Company
Analytical scale	Kern and Sohn, Balingen, Germany
Autoclave Systec 2540	Tuttnauer, Wettenberg, Germany
Camera S6X11	Rainbow CCTV, Irvine, CA, USA
Centrifuge Biofuge Fresco/Pico	Heraeus Instruments, Hanau, Germany
Centrifuge J2-MC	Beckman, Krefeld, Germany
Centrifuge Megafuge 1.0 R/2.0 R	Heraeus Instruments, Hanau, Germany
Centrifuge RC5BPlus	Sorvall, Langenselbold, Germany
Centrifuge rotors JA20.2, JA20.1	Beckman Instruments, Palo Alto, CA, USA
Centrifuge rotors SS-34, GS-3, SM24	DuPont Instruments, Bad Homburg, Germany
Confocal microscope Axiovert 100M	Zeiss, Jena, Germany
Digital camera DC120 Zoom	Kodak, New York, USA
Electroporator Gene Pulser II	Bio-Rad, München, Germany
Freezer -20 °C LGex3410 MedLine	Liebherr, Biberach, Germany
Freezer -80 °C HERAfreeze	Thermo Fisher Scientific, Dreieich, Germany
Fridge LKexv 3910 MedLine	Liebherr, Biberach, Germany
Gas burner gasprofi 1 micro	WLD-TEC
Gel imaging equipment, INTAS	Science Imaging Instruments, Göttingen, Germany
Heat block, NeoBlock Mono I	NeoLab, Heidelberg, Germany
Hot plate with magnetic stirring	Heidolph, Schwabach, Germany
Hot plate with magnetic stirring	IKA, Staufen, Germany
Ice machine	Ziegra, Isernhagen, Germany
Incubator Heraeus B12/UB12	Thermo Fisher Scientific, Dreieich, Germany
Light optical microscope Axiolab.A1	Zeiss, Jena, Germany
Liquid nitrogen tank	Air Liquide, Ludwigshafen, Germany
Liquid nitrogen tank Cryosystem 6000	MVE Biological Solutions, GA, USA
Liquid nitrogen tank LS 6000	Taylor-Wharton, Husum, Germany
Liquid nitrogen tank RS series	Taylor-Wharton, Husum, Germany
Liquid scintillation counter Tri-Carb 4910TR	Perkin Elmer, Waltham, USA
Magnetic sorter VarioMACS	Miltenyi Biotec, Bergisch Gladbach, Germany
Microscope camera ODC 825	Kern & Sohn, Balingen, Germany
Microwave oven	AEG, Nürnberg, Germany
MilliQ water system Purist ultrapure	Rephile, Germany

Equipment	Company
Multichannel pipette Biohit Mline m100	Sartorius AG, Göttingen, Germany
Neubauer chamber, improved	Roth, Karlsruhe, Germany
pH-meter pH 7110	WTW, Weilheim, Germany
Pipetman Gilson P10, P200, P1000	Abimed, Langenfeld, Germany
Pipettus Forty/Standard	Hirschmann Labortechnik, Eberstadt, Germany
Plate reader FLUOstar OPTIMA	BMG Labtech, Ortenberg, Germany
Plate reader Cytation3	BioTEK, Bad Friedrichshall, Germany
Point laser scanning confocal microscope, enhanced resolution, Airyscan 2 LSM900	Zeiss, Jena, Germany
Power supply Power Pac 200/300	Bio-Rad, München, Germany
Power supply EPS 1001/3501	Amersham Biosciences, München, Germany
Printer hp LaserJet 1300	Hewlett Packard, Heidelberg, Germany
Quartz precision cells	Hellma, Müllheim, Germany
SDS-PAGE XCell SureLock Mini-Cell	Thermo Fisher Scientific, Dreieich, Germany
Shaker incubator Innova 4000/4300	New Brunswick, Wesseling-Berzdorf, Germany
Shaker KS 501 digital	IKA, Staufen, Germany
Sonicator Sonopuls HD 2070	Bandelin, Berlin, Germany
Spectrophotometer UVIKON 923	Kontron Instruments, München, Germany
Sterile workbench HeraSafe	Heraeus Instruments, Hanau, Germany
Sterile workbench SterilGard Class II	The Baker Company, Stanford, ME, USA
Stopwatch	Roth, Karlsruhe, Germany
Test tube rotator	Hartenstein, Würzburg, Germany
Thermocycler Labcycler	Sensoquest, Göttingen, Germany
UV Transilluminator TFX-35M	Vilber Lourmat, Eberhardzell, Germany
Vortex Genie 2	Roth, Karlsruhe, Germany
Water bath Julabo 7A	Julabo, Seelbach, Germany

2.1.2 Consumables

Consumable	Company
8-well μ -Slide (1.5 polymer coverslip)	ibidi GmbH, Gräfelfing, Germany
96-/6-/12-well plates, black/clear	Greiner Bio-One, Frickenhausen, Germany
Aluminium foil	Roth, Karlsruhe, Germany
Coverslips, 20x20 mm	Roth, Karlsruhe, Germany
Cryovials, 2 mL	Nalgene, Wiesbaden, Germany
Cuvettes, semi-micro, 3 mL	Sarstedt, Nümbrecht, Germany
Electroporation cuvettes Gene Pulser	Bio-Rad, München, Germany
Filters system 0.2 μ m, 500 mL	Corning, Kaiserslautern, Germany
Filters Millex GS 0.2 μ m	Merck Millipore, Darmstadt, Germany

Consumable	Company
Glass microfiber filter GF/C 25 mm Whatman	GE Healthcare Life Sciences, München, Germany
Immersion oil	Zeiss, Jena, Germany
MACS CS column	Miltenyi Biotec, Bergisch Gladbach, Germany
Microcentrifuge tubes, 1.5/2 mL	Sarstedt, Nümbrecht, Germany
Nitrile gloves, TouchNTuff	Ansell, München, Germany
Object slides	Marienfeld, Lauda-Königshofen, Germany
Parafilm	Bemis, Londonerry, UK
PCR soft tubes, 0.25 mL	Biozym Scientific, Hessisch Oldendorf, Germany
PCR strip tubes and domed caps	BioMedical Instruments, Zoellnitz, Germany
Petri dishes, 100 mm/140 mm diameter	Greiner Bio-One, Frickenhausen, Germany
Pipette tips	Corning Corporation, Bodenheim, Germany
Plastic vials for scintillation counting, Midi	Perkin Elmer, Waltham, USA
Polypropylene centrifuge tubes (15/50 mL)	Greiner Bio-One, Frickenhausen, Germany
Serological pipettes (1/2/5/10/25/50 mL)	Corning Corporation, Bodenheim, Germany

2.1.3 Chemicals

The compounds used in this study were obtained from the companies indicated for each case, or from AppliChem (Darmstadt, Germany), BIORON Diagnostics (Römerberg, Germany), c.c.pro (Oberdorla, Germany), Honeywell Fluka (Charlotte, NC, USA), Jacobus Pharmaceuticals (Princeton, NJ, USA), Merck (Darmstadt, Germany), Roth (Karlsruhe, Germany), Sigma-Aldrich (Burlington, MA, USA), Serva Electrophoresis (Heidelberg, Germany), Thermo Fisher Scientific (Dreieich, Germany), or Roche (Basel, Switzerland). Orders were carried out directly through the vendors or through the Heidelberg Medical Facility, unless stated otherwise. All compounds were used without further purification unless stated otherwise.

The SC-compounds, namely SC83288 and SC106879 were provided by 4SC AG, München, Germany.

2.1.4 Reagent Kits

Reagent Kit	Company
DNeasy Blood & Tissue Kit	Qiagen, Hilden, Germany
EnzyChrom Kinase Assay Kit	BioAssay Systems, CA, USA
QIAquick Gel Extraction Kit	Qiagen, Hilden, Germany
Plasmid MaxiPrep Kit	Qiagen, Hilden, Germany

2.1.5 Biological material

2.1.5.1 Enzymes

Restriction enzymes used in this study were purchased from New England Biolabs (Frankfurt am Main, Germany). For the polymerase chain reactions (PCR), EconoTaq DNA Polymerase was purchased from BioCat (Heidelberg, Germany) and Phusion High-Fidelity DNA polymerase from Thermo Fisher Scientific (Dreieich, Germany).

2.1.5.2 Molecular weight/size markers and loading dyes

Molecular weight markers, size markers and loading dyes were purchased from Thermo Fisher Scientific (Dreieich, Germany), namely 6X DNA loading buffer, Gene Ruler 1 Kb plus DNA ladder and Page Ruler plus prestained protein ladder.

2.1.5.3 Parasite strains

Strain	Origin
<i>P. falciparum</i> 3D7	The Netherlands [90]
<i>P. falciparum</i> 3D7 PfATP6 ^{F972Y}	Generated by Dr. Maëlle Duffey [81]
<i>P. falciparum</i> 3D7 Nina10	Provided by Prof. Jude Przyborski, Heidelberg, Germany
<i>P. falciparum</i> 3D7 NLS-mCherry PCNA1-GFP	Generated by Severina Klaus [21]

2.1.5.4 Bacteria strains

Strain	Origin
<i>E. coli</i> PMC 103	Provided by Prof. Alan Cowman [91]

2.1.5.5 Plasmids

For the preparation of *P. falciparum* DNA fragments to be used in DNA binding studies the pARL-stevor¹⁻⁸⁰-GFP plasmid [92], shown in Figure 2-1 was used as a source for the 5' UTR PfCRT promoter as described in Section 2.2.4.2.

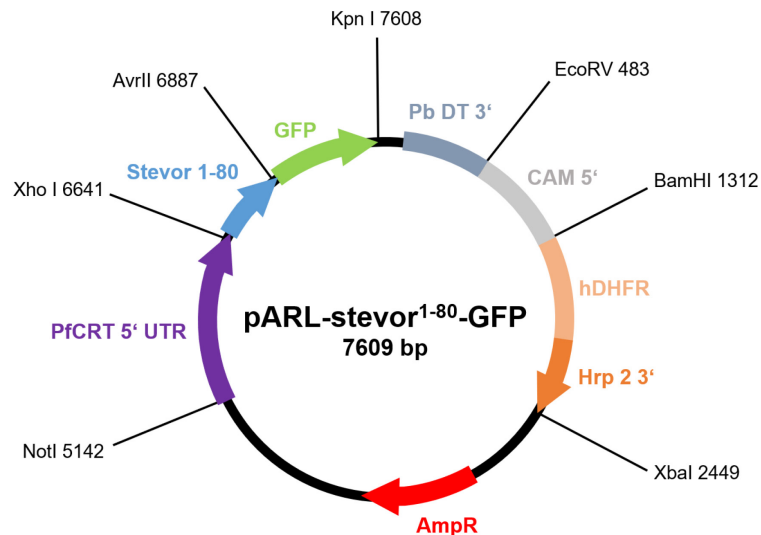


Figure 2-1. Schematic representation of the plasmid pARL-stevor¹⁻⁸⁰-GFP. Restriction sites of interest are marked with black lines and their position indicated next to the name of the enzyme that recognizes the site.

The parasite strain denominated *P. falciparum* 3D7 Nina10 which carries the plasmid shown in Figure 2-2 was generated in the group of Prof. Dr. Jude Przyborski and was kindly provided for this study.

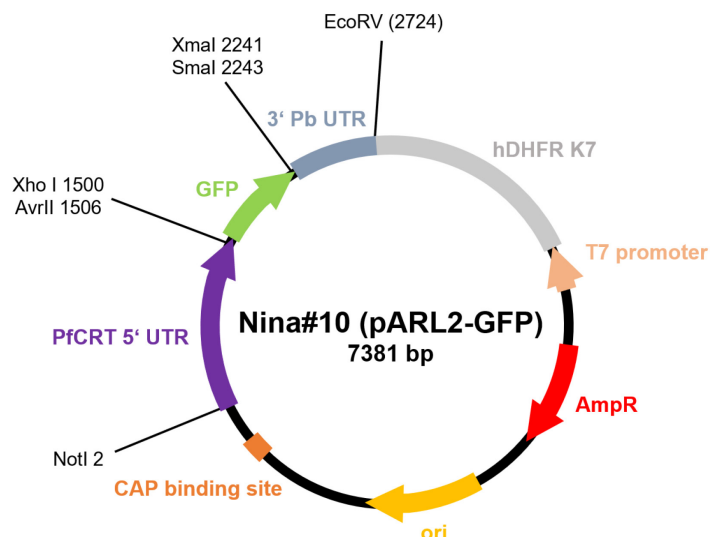


Figure 2-2. Schematic representation of the plasmid Nina#10 (pARL2-GFP). Restriction sites of interest are marked with black lines and their position indicated next to the name of the enzyme that recognizes the site.

The plasmid pL6-CS (Figure 2-3) was kindly provided by Dr. José Juan Lopez Rubio [93]. It was used in this study as a positive control in PCR reactions for the detection of *hDHFR*.

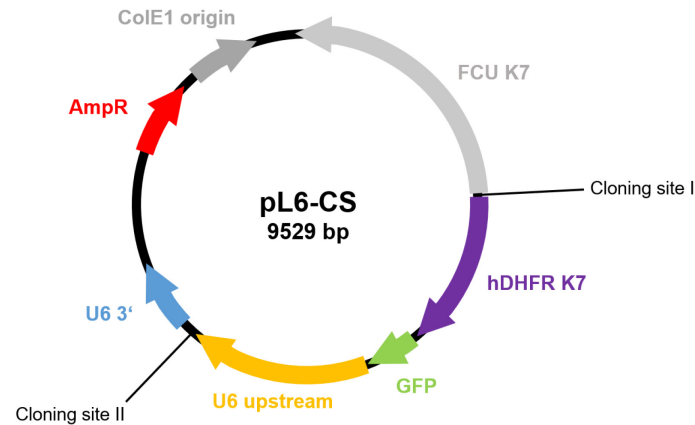


Figure 2-3. Schematic representation of the plasmid pL6-CS. The position of cloning sites is marked with black lines.

2.1.5.6 Primers for PCR

The primers used in this study were purchased from Eurofins (Luxembourg) or Thermo Fisher Scientific (Dreieich, Germany).

Name	Sequence (5' → 3')
PfDHPS-1400-for	AACCTAAACGTGCTGTTCAAAG
PfDHPS-2100-rev	TTCATTTTGTGTTTCATCATG
hDHFR-1-for	ATGCATGGTTCGCTAAACTGC
hDHFR-700-rev	ATTCTTCTCATATACTTCAAATTTG
PfCRT-1-SpeI-for	GGACTAGTATGAAATTCGCAAGTAAAAAATAATC
PfCRT-540-BssHII-rev	TTGGCGCGCTTTGAATTTCCCTTTTATTTC

2.1.5.7 Other biological material

For the culture of *P. falciparum* parasites *in vitro*, a fresh A+ erythrocyte concentrate was used, which was obtained from the blood bank in Heidelberg on a weekly basis. Human A+ serum, required for medium formulation, was also purchased from the blood bank in Heidelberg and heat-inactivated in our laboratory.

Salmon sperm DNA was purchased from Sigma-Aldrich, and its solutions were prepared by overnight dissolution in Tris-EDTA (TE) buffer at 4 °C to achieve concentrations of around 10 mg/mL. The resulting solutions were stored at -20 °C until further processing.

2.1.6 Buffers, media, and solutions

Unless otherwise specified, buffers, media, and solutions were stored at room temperature (RT). Filter sterilization was carried out using 0.2 μm filters, chosen from those mentioned in the table of consumables (Section 2.1.2) according to the solution volume.

Buffer/Medium/Solution	Composition
Acetate buffer	2 mM sodium acetate, 9.3 mM sodium chloride, 0.1 mM EDTA, pH was adjusted to 5
Agarose solution for DNA electrophoresis gel	1% agarose in 1X TAE buffer, boiled for complete dissolution and stored at 56 °C
Albumax II	5% (w/v) Albumax II in RPMI 1640 (with 25 mM HEPES and L-Glutamine, Gibco), filter sterilised, stored at -20 °C
Ampicillin stock, 1000X	100 mg/mL ampicillin in sterile H ₂ O _{dd} , freshly prepared
Cell culture media	
Complete	10% (v/v) human serum, 0.2 $\mu\text{g}/\mu\text{L}$ gentamycin, 0.2 mM hypoxanthine, in RPMI 1640 (with 25 mM HEPES and L-Glutamine, Gibco), stored at 4 °C
Complete without serum	0.5% (v/v) Albumax II, 0.2 $\mu\text{g}/\mu\text{L}$ gentamycin, 0.2 mM hypoxanthine, in RPMI 1640 (with 25 mM HEPES and L-Glutamine, Gibco or Capricorn Scientific supplemented with 25 mM HEPES in our laboratory), stored at 4 °C
Folate free (NFM)	0.5% (v/v) Albumax II, 0.2% (w/v) glucose, 0.2 mM hypoxanthine, 0.2 $\mu\text{g}/\mu\text{L}$ gentamycin, 25 mM HEPES pH 7.3, in RPMI 1640 (with L-Glutamine, without folate, Gibco), stored at 4 °C
Low folate	Folate free cell culture medium, 100 ng/mL folic acid (from 100 $\mu\text{g}/\text{mL}$ stock), stored at 4 °C
Carbonate free	RPMI 1640 (with 25 mM HEPES and L-glutamine, carbonate free, powdered, Gibco) dissolved in H ₂ O _{dd} , pH adjusted to 7.2 at 37 °C, filter sterilised and stored at 4 °C
Phenol red-free, for imaging	25 mM HEPES pH 7.3, 0.2 mM hypoxanthine, 0.2 $\mu\text{g}/\mu\text{L}$ gentamycin, 0.5 % (v/v) Albumax II, in RPMI 1640 (with L-Glutamine, without phenol red, PAN-Biotech), freshly prepared
Concanavalin A solution	5 mg/mL concanavalin A in H ₂ O _{dd} , filter sterilized and stored in 1 mL aliquots at -20 °C
Coomassie staining solution	50% (v/v) methanol, 10% (v/v) acetic acid, 0.5% (w/v) Coomassie Blue R-250 in H ₂ O _{dd}
D-Sorbitol	5% (w/v) D-sorbitol in H ₂ O _{dd} , autoclaved and stored at 4 °C

Buffer/Medium/Solution	Composition
DHFR assay buffer, 1X	50 mM TES pH 7.0, 75 mM β -mercaptoethanol, 1 mg/ml BSA
DHPS activity buffer	100 mM Tris pH 9, 100 mM β -mercaptoethanol, 10 mM magnesium sulfate
Fixation solution	4% paraformaldehyde, 0.0075% glutaraldehyde, in PBS
Folic acid stock solution	100 μ g/mL folic acid, 1 M sodium hydrogencarbonate, filter sterilized
Freezing solution	6.2 M glycerol, 0.14 M sodium lactate, 0.5 mM potassium chloride, in H ₂ O _{dd} , pH adjusted to 7.2 with 0.5 M sodium hydrogencarbonate, filter sterilised, stored at 4 °C
IC ₅₀ lysis buffer	20 mM Tris base, 5 mM EDTA, 0.008% (w/v) saponin, 0.08% (v/v) Triton X-100, in H ₂ O _{dd} , pH adjusted to 7.4 with 1 M hydrochloric acid
LB-Lennox medium	1% (w/v) tryptone, 0.5% (w/v) yeast extract, 0.5% (w/v) sodium chloride, in H ₂ O _{dd} , autoclaved
LB-Lennox agar medium	1% (w/v) tryptone, 0.5% (w/v) yeast extract, 0.5% (w/v) NaCl, 1.5% (w/v) agar, in H ₂ O _{dd} , autoclaved
Lysis buffer (samples for kinase activity assay)	10 mM magnesium chloride, 5 mM β -glycerophosphate, 0.1 mM sodium orthovanadate, 1 mM PMSF, 1X protease inhibitor cocktail (Roche), prepared fresh in PBS
Lysis buffer A (TPP of parasite lysates)	PBS, 5 mM β -glycerophosphate, 0.1 mM sodium orthovanadate, 10 mM magnesium chloride, 2 mM DTT, protease inhibitors added before use: 250 μ g/mL aprotinin, 10 μ g/mL leupeptin, 1 mM PMSF (from 100 mM stock in isopropanol, stored at -20 °C)
Lysis buffer B (TPP of parasite lysates)	8.8% NP-40, 2.75 U/ μ L benzonase, 16.5 mM magnesium chloride, 1X cOmplete protease inhibitor cocktail (Roche), 1X phosphatase inhibitor PhosStop (Roche)
Lysis buffer, 2X (CETSA)	100 mM HEPES, 10 mM β -glycerophosphate, 0.2 mM sodium orthovanadate, 20 mM magnesium chloride (buffer stock stored at 4°C). Before using a buffer aliquot, 2 μ L/mL EDTA-free protease inhibitor cocktail and 2 μ L/mL 1 M TCEP were added
MACS buffer	2 mM EDTA in PBS, autoclaved. 0.5% (w/v) BSA added before use
Master mix HPPK activity	100 mM Tris pH 9, 10 mM β -mercaptoethanol, 10 mM magnesium sulfate, 0.01% w/v BSA, 10 μ M HMDP and 10 μ M ATP
NEB 2.1 buffer, 1X	50 mM sodium chloride, 10 mM Tris-HCl, 10 mM magnesium chloride, 100 μ g/mL BSA, pH 7.9 at 25 °C

Buffer/Medium/Solution	Composition
NMDG saline	5 mM potassium chloride, 1 mM magnesium chloride, 20 mM glucose, 25 mM HEPES, 125 mM NMDG, in H ₂ O _{dd} , pH adjusted to 7.4, filter sterilised and stored at 4 °C
PBS, 1X	1 tablet (Sigma-Aldrich) dissolved in 200 mL H ₂ O _{dd} , autoclaved
Permeabilization solution	0.1% (v/v) Triton X-100 in PBS
Physiological saline	125 mM sodium chloride, 5 mM potassium chloride, 1 mM magnesium chloride, 20 mM glucose, 25 mM HEPES, pH adjusted to 7.4, filter sterilised and stored at 4 °C
Protein loading buffer (SDS-PAGE)	3% (w/v) SDS, 250 mM Tris, 20% (v/v) glycerol, 0.1% (w/v) bromophenol blue, pH adjusted to 6.8. 3% (v/v) β-mercaptoethanol added before use
Quenching solution	0.1 M glycine in PBS
SDS-PAGE running buffer	25 mM Tris, 250 mM glycine, 0.1% (w/v) SDS, in H ₂ O _{dd}
SOB medium	2% (w/v) tryptone/peptone, 0.5% (w/v) yeast extract, 0.05% (w/v) sodium chloride, 0.5% magnesium sulfate, in H ₂ O _{dd} , autoclaved
SOC medium	SOB medium, 20 mM sterile glucose, stored at -20 °C
Sodium orthovanadate (stock solution)	200 mM sodium orthovanadate in H ₂ O _{dd} , pH was adjusted to 10 (yellow coloured solution) and then boiled until the solution was clear. The pH was readjusted to 10 after the solution had cooled down to RT and the process was repeated until the solution was clear at pH 10. Aliquots of 500 μL were stored at -20 °C
Super broth (SB) medium	3.5% (w/v) tryptone/peptone, 3% (w/v) yeast extract, 0.5% (w/v) sodium chloride, in H ₂ O _{dd} , autoclaved
TAE buffer, 1X	4 mM Tris-acetate, 1 mM EDTA, in H ₂ O _{dd} , pH adjusted to 8
TE buffer, 1X	10 mM Tris, 1 mM EDTA, in H ₂ O _{dd} , pH adjusted to 8 with hydrochloric acid, autoclaved
Thawing solution I	12% (w/v) sodium chloride in H ₂ O _{dd} , autoclaved, stored at 4 °C
Thawing solution II	1.6% (w/v) sodium chloride in H ₂ O _{dd} , autoclaved, stored at 4 °C
Thawing solution III	0.9% (w/v) sodium chloride, 0.2% (w/v) glucose, in H ₂ O _{dd} , filter sterilised and stored at 4 °C
WR99210, stock solution	10 mM WR99210, 20% (v/v) DMSO, in H ₂ O _{dd} , long term stored at -20 °C
WR99210, working solution	20 μM WR99210 in RPMI 1640 (with 25 mM HEPES and L-Glutamine, Gibco), stored long term at -20 °C (or at 4 °C for a maximum of two weeks)

2.1.7 Software and Databases

Software/Database	Company/Source
BEDTools	Quinlan Laboratory, University of Utah, USA https://bedtools.readthedocs.io [94]
DINIES	https://www.genome.jp/tools/dinies/ [95]
FIJI Image Analysis	http://fiji.sc/Fiji [96]
Glide (Schrödinger Suite)	Schrödinger Inc., New York, USA [97-99]
HISAT2	University of Texas Southwestern Medical Center, Dallas, USA; and John Hopkins University Center for Computational Biology, Baltimore, USA http://daehwankimlab.github.io/hisat2/ [100]
IDEOM	http://mzmatch.sourceforge.net/ideom.html [101]
KEGG	https://www.genome.jp/kegg/ [102]
Microscope VIS	Kern & Sohn, Balingen, Germany
Malaria Parasite Metabolic Pathways	https://mpmp.huji.ac.il/ [26]
MetaCyc	https://metacyc.org/ [103]
MS Office 365	Microsoft Corporation, CA, USA
MZMatch	http://mzmatch.sourceforge.net [104]
PhenoPlasm	http://phenoplasm.org/ [105]
Phyre2	www.sbg.bio.ic.ac.uk/phyre2/ [106]
PlasmoDB	http://plasmodb.org/plasmo/ [107]
Prism 8.0.2	GraphPad Software, CA, USA
Protein Data Bank	http://rcsb.org/pdb/home/home.do
R software environment	https://www.r-project.org/
Serial Cloner 2.6	http://serialbasics.free.fr/Serial_Cloner.html
SigmaPlot 13.0	Systat Software Inc., Chicago, IL, USA
SnapGene Viewer 2.8.2	GSL Biotech LLC, Chicago, IL, USA
SuSPect	http://www.sbg.bio.ic.ac.uk/~suspect/ [108]
TDR Targets	https://tdrtargets.org [109]
TRIMGALORE	Babraham Bioinformatics, Babraham Institute, Cambridge, UK [110]
YMDB	http://www.ymdb.ca/ [111]
UniProt	https://www.uniprot.org/ [112]
XCMS	The Scripps Research Institute, La Jolla, USA [113]
ZEN Blue 3.1	Zeiss, Jena, Germany

2.2 Methods

2.2.1 Cell culture of *Plasmodium falciparum* parasites

2.2.1.1 In vitro culture conditions

Asexual stages of *P. falciparum* were maintained in continuous blood culture following the standard method of Trager and Jensen [114]. Cultures were kept in an incubator under an atmosphere of 5% O₂, 3% CO₂, 92% N₂ and 95% relative humidity at 37 °C. Parasites were grown in complete RPMI 1640 medium in 100 mm (14 mL) or 140 mm (35 mL) diameter petri dishes, accordingly. Human A+ erythrocytes were used to achieve hematocrit levels between 2-4%. Parasitemia and hematocrit were adjusted depending on the experiment, while for regular culture maintenance parasitemia was kept around 1-5%. Detailed culture media composition is described in Section 2.1.6. Cultures were examined regularly using thin blood smears, which were fixed with methanol and stained with Giemsa. If needed, media was exchanged to avoid accumulation of toxic metabolites, or cultures were diluted with fresh erythrocytes to decrease parasitemia.

2.2.1.2 Morphological examination of parasites and parasitemia determination

Parasite cultures were monitored using Giemsa-stained thin blood smears. This allowed the identification of the different asexual development stages as well as morphological alterations, and the determination of the parasitemia. Thin blood smears were prepared using approximately 20 µL of settled erythrocytes from the cultures on a microscope slide, which was then let dry at RT. The smears were fixed on pure methanol for at least 30 seconds, air dried and then stained in a 10% Giemsa solution for 10 to 30 minutes. After staining, the slides were washed with water and gently dried with a tissue before analysing them under a light microscope using an oil immersion 100X objective. The approximate age and stage of parasites were assessed following literature examples [115, 116]. For parasitemia determination, the number of both infected and total red blood cells were counted on ten consecutive fields (ca. 1 000 total cells) and the following formula (Eq. 2-1) was used:

$$\text{Parasitemia (\%)} = \frac{\text{Number of infected erythrocytes}}{\text{Number of erythrocytes}} \times 100 \quad (\text{Eq. 2-1})$$

2.2.1.3 Cryopreservation and thawing of parasites

Ring-stage cultures of at least 5% parasitemia were used for cryopreservation. The selected cultures were transferred to 15 mL centrifuge tubes and centrifuged (900 *g*, 2 min, RT) while the supernatants were discarded. The resulting pellets were carefully resuspended in 200 μ L of freezing solution and incubated for 5 min at RT. Then, 600 μ L of freezing solution were added dropwise and mixed slowly. The resulting suspensions were transferred into cryogenic vials and frozen at -80 °C. For long term storage, the vials were kept at -196 °C in liquid nitrogen.

To thaw cryopreserved parasites, the frozen cryovial was warmed up at 37 °C until its contents were liquid, when 200 μ L of warm thawing solution I were added. After mixing, the suspension was transferred to a 15 mL centrifuge tube and 9 mL of thawing solution II (pre-warmed at 37 °C) were added dropwise and carefully mixed. The sample was centrifuged (900 *g*, 2 min, RT) and the supernatant discarded. Finally, 7 mL of thawing solution III (pre-warmed at 37 °C) were added dropwise, carefully mixed and the cells were centrifuged (900 *g*, 2 min, RT). The supernatant was discarded, and the pellet resuspended in 14 mL of complete cell culture medium (previously warmed up at 37 °C), then transferred to a 100 mm diameter petri dish containing 500 μ L of fresh erythrocytes. The cultures were monitored after 48 h to assess their revival rate and either exchange the growth medium or dilute the culture with fresh red blood cells to decrease parasitemia. Parasites were deemed adequate for their use in experiments after at least 7 days of being in culture, or when their multiplication rate was stabilized.

2.2.1.4 Parasite cultures synchronization with D-sorbitol

Parasite cultures were synchronized to ring stage using D-sorbitol [117]. For synchronization, a parasite culture was resuspended and transferred to a 15 mL centrifuge tube and then centrifuged (900 *g*, 2 min, RT). The supernatant was discarded, and the pellet resuspended with 10 mL of 5% D-sorbitol (pre-warmed at 37 °C) and incubated for 5 min at 37 °C. The sample was then centrifuged (900 *g*, 2 min, RT) and the supernatant discarded. The cell pellet was resuspended in 14 mL of complete cell culture medium (pre-warmed at 37 °C) and transferred to a 100 mm diameter petri dish. Parasitemia level and parasite age was evaluated after at least one hour using a Giemsa-stained thin blood smear.

2.2.1.5 Magnetic purification of late-stage parasites

Late intraerythrocytic parasite stages present hemozoin crystals in their food vacuoles, which are formed as a product of hemoglobin catabolism and possess paramagnetic properties [118]. Based on this characteristic, *P. falciparum* trophozoite- and schizont-stage parasites can be purified from ring-stage parasites and uninfected erythrocytes and concentrated using the magnetic activated cell sorting (MACS) system [119, 120]. For the purification, the MACS CS column was washed twice with MACS buffer (pre-warmed at 37 °C) and inserted into the VarioMACS separator. The parasite culture was resuspended and loaded into the column, and the elution rate was adjusted to one drop every 3 seconds. After eluting the culture, the column was washed with MACS buffer until a clear flow-through was achieved. The column was then removed from the separator and the late-stage infected erythrocytes were eluted with 10 mL of MACS buffer into a 15 mL centrifuge tube. The cells were centrifuged (900 g, 2 min, RT) and the pellet was resuspended in the appropriate solution according to the experiment to be performed.

2.2.1.6 Heat-inactivation of human serum for growth medium preparation

Human serum, required for cell culture medium preparation, was acquired from the blood bank in Heidelberg and stored at -20 °C until its heat inactivation procedure was carried out. For this, A+ human serum bags were thawed in water at RT and transferred into a sterile flask. The serum was treated with 30 mM calcium chloride (using a 1 M sterile stock solution in H₂O_{dd}) and quickly aliquoted in 50 mL centrifuge tubes. The treated serum was allowed to solidify in a water bath at 37 °C and then stored overnight at 4 °C. On the next day, they were centrifuged (2 600 g, 60 min, RT) and heat inactivated by incubation in a water bath at 56 °C for 30 min. Finally, the heat-inactivated serum aliquots were stored at -20 °C until use.

2.2.2 Microbiology and Molecular Biology

2.2.2.1 Preparation of electro-competent PMC 103 *E. coli* bacteria

For the preparation of electro-competent PMC 103 *E. coli* cells, a starter culture was produced by inoculating 10 mL of super broth (SB) medium with bacterial cells scraped from a frozen glycerol stock and incubating overnight under shaking (37 °C, 200 rpm). After approximately 16 h, 600 mL of SB were inoculated with 6 mL of the starter culture and incubated for 3.5 h under shaking (37 °C, 200 rpm). The cells were harvested by centrifugation (6 000 g, 15 min, 4 °C) and the supernatant was discarded. All the following steps were carried out on an ice bath using solutions at 4 °C.

The bacterial pellet was resuspended in an equal volume of sterile water and centrifuged (6 000 g, 15 min, 4 °C), the washing step was repeated twice. The resulting pellet was resuspended in an equal volume of sterile 10% (v/v) glycerol in H₂O_{dd} and centrifuged (6 000 g, 15 min, 4 °C). The supernatant was discarded, and the pellet resuspended in 1.2 mL of sterile 10% (v/v) glycerol in H₂O_{dd} and distributed in 50 µL aliquots in 1.5 mL microcentrifuge tubes. The aliquots were snap frozen in an ethanol/dry ice bath and stored at -80 °C until further use.

2.2.2.2 Transformation of electro-competent PMC 103 *E. coli* bacteria

Plasmid DNA was introduced into bacterial cells by electroporation. For this, the previously described 50 µL aliquots of electrocompetent PMC 103 *E. coli* bacteria were thawed on ice and mixed with 150 µL of 10% (v/v) glycerol in H₂O_{dd}. 10 µL of plasmid DNA were added to the cells and the mixture was transferred to a cold electroporation cuvette. Electroporation was performed at 2 500 V. Immediately after, 1 mL of SOC medium (pre-warmed to 37 °C) was added to the cuvette. The sample was then transferred to a 15 mL centrifugation tube and incubated for one hour under shaking (37 °C, 200 rpm). Finally, the cell suspension was plated onto selective LB-Lennox agar plates and grown overnight at 37 °C.

2.2.2.4 Isolation of plasmid DNA from bacteria (Maxiprep)

The isolation of plasmid DNA was performed using the Plasmid Maxi Kit (Qiagen) according to manufacturer's instructions. A single bacterial colony was used to inoculate 3 mL of LB-Lennox medium (supplemented with the appropriate selection antibiotic, i.e. ampicillin 100 µg/mL) and grown for six to eight hours under shaking (37 °C, 200 rpm). This starter culture was diluted 1:1 000 in LB-Lennox medium (i.e. 400 µL in 400 mL medium) and incubated overnight with shaking (37 °C, 200 rpm). After approximately 16 h, cells were harvested by centrifugation (6 000 g, 15 min, 4 °C), mixed with resuspension buffer and lysed by 5 min incubation at RT with lysis buffer. The lysis was stopped by the addition of cold neutralization buffer, followed by 20 min incubation on ice. Samples were centrifuged (15 000 g, 30 min, 4 °C), the supernatant containing plasmid DNA was loaded into pre-equilibrated columns and eluted by gravity flow. After several washing steps, DNA was eluted, precipitated with isopropanol, and centrifuged (15 000 g, 30 min, 4 °C). The pellet was washed with cold 70% ethanol and centrifuged (15 000 g, 20 min, 4 °C). The supernatant was removed, and the DNA pellet was left to air dry at RT before being resuspended in 50 to 150 µL of H₂O_{dd} and stored at -20 °C.

2.2.2.5 Genomic DNA isolation from *P. falciparum* parasites

In order to obtain genomic DNA from *P. falciparum*, the intraerythrocytic parasites were extracted from their host cells. For this, 14 mL of trophozoite- and schizont-stage culture of at least 5% parasitemia were transferred to a 15 mL centrifuge tube and centrifuged (900 g, 2 min, RT). The supernatant was removed, cells were washed with PBS and then resuspended in 10 mL of PBS. 100 µL of a 10% (w/v) saponin solution in PBS were added and mixed by inversion, followed by a 5 min incubation on ice to allow the complete lysis of erythrocytes. The sample was centrifuged (2 600 g, 10 min, 4 °C), the pellet was washed with PBS and then resuspended in 200 µL of PBS and transferred to a 1.5 mL microcentrifuge tube. The genomic DNA was isolated using the DNeasy Blood & Tissue Kit (Qiagen) following the manufacturer's instructions. The parasite suspension was lysed with 200 µL of AL buffer in presence of 20 µL of proteinase K, vortexed and incubated at 56 °C in a heat block for 10 min. Afterwards, 200 µL of 99% ethanol were added and the mixture was vortexed thoroughly, then transferred to a DNeasy spin column and centrifuged (6 000 g, 1 min, RT). The eluate was discarded and 500 µL of AW1 buffer were added, followed by a centrifugation (6 000 g, 1 min, RT). Again, the eluate was discarded and 500 µL of AW2 buffer were added, followed by a centrifugation (17 000 g, 3 min, RT). The column was then transferred to a fresh 1.5 mL microcentrifuge tube. To elute the DNA, 50 µL of H₂O_{dd} were loaded to the membrane and incubated 1 min at RT, followed by a centrifugation (6 000 g, 1 min, RT). The genomic DNA solution was stored at -20 °C.

2.2.2.6 Polymerase chain reaction (PCR)

The amplification of DNA fragments of interest was performed using either the EconoTaq DNA Polymerase (for identification or amplification purposes) or Phusion High-Fidelity DNA polymerase (for sequencing purposes). The PCR reaction mix and thermocycling conditions were as follows:

Master Mix		Thermocycling conditions		
Buffer 10X	2.5 µL	Initial denaturation	94 °C	10 min
dNTPs 2 mM	2.5 µL	Denaturation Annealing Elongation	94 °C <i>x</i> °C* 68 °C	45 sec 45 sec 1 min/kb
MgCl ₂ 50 mM	1.25 µL			
Forward primer 50 µM	0.5 µL			
Reverse primer 50 µM	0.5 µL			
DNA template	2 µL			
DNA Polymerase	0.25 µL	Final elongation	68 °C	10 min
H ₂ O _{dd}	15.5 µL	Hold	4 °C	
Final volume	25 µL	* <i>x</i> = T _m of primers – 5 °C		

2.2.2.7 Agarose gel electrophoresis of nucleic acids

Agarose gel electrophoresis was used for the separation of DNA molecules according to their size and charge ratio. The concentration of agarose was either 1% or 2%, depending on the needed resolution. Gels were prepared by dissolving agarose in 1X TAE buffer by boiling. After it cooled down to 56 °C, ethidium bromide was added in a 1:10 000 dilution and the agarose was poured into a cast. Immediately after, combs were inserted to create wells and the gel was left to solidify at RT. Then, the gels were transferred to an electrophoresis chamber filled with 1X TAE buffer, connected to a power supply. DNA samples were mixed with 6X loading buffer and loaded into the wells of the gels. As a size marker, Gene Ruler 1kb plus (Thermo Fisher Scientific), was run alongside the samples. Electrophoresis was carried out at RT at the constant voltage of 140 V for 60 min. DNA bands were visualized using a table UV transilluminator and captured using a DC120 Zoom Digital Camera (Kodak).

2.2.2.8 Agarose gel extraction and purification

The extraction and purification of specific DNA fragments from an agarose gel was carried out using the QIAquick Gel Extraction Kit (Qiagen) according to the manufacturer's instructions. Briefly, selected DNA bands were cut out from the agarose gel and dissolved in QG buffer (1:3 w/v ratio) by incubating for 10 min at 50 °C. Then, isopropanol was added to precipitate the DNA and the sample was loaded into a QIAquick spin column and centrifuged (17 000 g, 15 sec, RT). DNA bound to the column membrane was washed with PE buffer and then eluted with 20 µL of H₂O_{dd} into a 1.5 mL microcentrifuge tube. Samples were stored at -20 °C.

2.2.2.9 Photometric determination of DNA concentration

The concentration of nucleic acid samples was measured using the spectrophotometer UVIKON 923 (Kontron Instruments). The absorbance of diluted samples at 260 nm was analysed, assuming that an Abs₂₆₀ of 1 corresponds to 50 µg/mL of double stranded DNA [121].

2.2.2.10 Restriction enzymes digestion of DNA

DNA can be cleaved by restriction endonucleases, enzymes that recognize short sequences and catalyse a hydrolytic break in the backbone of the DNA molecule. These digestion reactions were carried out following the reagent mixtures shown below, which were then incubated for at least two hours at the optimal temperature indicated by the supplier for each individual enzyme or combination of enzymes (New England Biolabs). The final reaction volume was either 10 or 100 μL depending on the purpose, and the DNA used was fixed to either 1 or 100 μg , respectively. To achieve the final volume, the amount of water added to the reagent mix was variable (indicated in the tables below with an x) according to the volume of DNA solution necessary based on the concentration.

Control digestion		Plasmid digestion (DNA binding sample)	
NEB Buffer	1 μL	NEB Buffer	10 μL
DNA	1 μg	DNA	100 μg
Enzymes	0.4 μL of each	Enzymes	1 μL of each
H ₂ O _{dd}	x μL	H ₂ O _{dd}	x μL
Total volume	10 μL	Total volume	100 μL

2.2.3 Protein Biochemistry

2.2.3.1 Preparation of *P. falciparum* protein extract

Protein extracts for the measurement of kinase activity were prepared from parasite cultures as follows. Approximately 150 mL of trophozoite-stage cultures (24-38 hpi) were purified using MACS, and the pellet obtained was exposed to a saponin treatment for red blood cell lysis (1 mL of 0.07 % (w/v) saponin and 1 mM PMSF in PBS, 30 sec incubation at 37 °C). Free parasites were spun down (17 000 g , 1 min, 4 °C) and washed twice with 1 mM PMSF in PBS. Then, the pellet was resuspended in 150 μL of lysis buffer (see composition in Section 2.1.6.) and subjected to three freezing/thawing cycles in N₂/37 °C water bath. The samples were subsequently treated with a probe sonicator (Sonopuls HD 2070, Bandelin), using two rounds of 8 pulses at 2 x 10% with minimum power. Between rounds, samples were incubated on ice for at least one minute. Lysates were then centrifuged (17 000 g , 1 h, 4 °C) and the supernatants were aliquoted, flash frozen in liquid nitrogen and stored at -80 °C.

2.2.3.2 SDS polyacrylamide gel electrophoresis (SDS-PAGE) of proteins

Protein samples were analysed by SDS-PAGE electrophoresis. Before being loaded on the SDS-PAGE gel, samples were mixed with loading buffer and heated at 95 °C for 5 min. The molecular weight marker Page Ruler pre-stained plus (Thermo Fisher Scientific) was loaded on the gels alongside the samples and used as a protein ladder. Each gel was run at 40 mA and 200 V for 45 to 60 min in SDS-PAGE running buffer. Depending on the resolution needs, the percentage of acrylamide was chosen, and the gels were prepared as indicated below:

	Resolving gel			Stacking gel	
	8%	10%	12%	5%	
H ₂ O _{dd}	4.68 mL	3.96 mL	3.35 mL	H ₂ O _{dd}	3.46 mL
1.5 M tris pH 8.6	2.50 mL	2.50 mL	2.50 mL	1 M tris pH 6.8	630 µL
10% SDS	100 µL	100 µL	100 µL	10% SDS	50 µL
30% acrylamide	2.66 mL	3.33 mL	4.00 mL	30% acrylamide	830 µL
10% APS	100 µL	100 µL	100 µL	10% APS	50 µL
TEMED	6 µL	6 µL	6 µL	TEMED	5 µL
Total volume	10 mL	10 mL	10 mL	Total volume	5 mL

2.2.3.3 Coomassie blue staining for protein visualization

For the visualization of protein bands in the SDS-PAGE gel, the gels were incubated in Coomassie staining solution for 5 to 10 min under shaking (100 rpm, RT). Then, the staining solution was removed, and the gel was washed several times with distilled water before letting it de-stain in distilled water under shaking (100 rpm, RT) overnight or until the protein bands were clearly distinguishable.

2.2.3.4 Protein concentration measurement via Bradford assay

Protein sample concentration was measured using the Bradford assay [122]. For this, Bio-Rad Dye Reagent Concentrate (Bio-Rad) was used according to the manufacturer's instructions, using a stock solution of BSA in H₂O_{dd} as standard. A standard curve composed of five concentrations (0, 1, 2.5, 5 and 10 µg of BSA) in a total volume of 800 µL were prepared in duplicates. Then, 200 µL of dye reagent concentrate were added, and the samples were vortexed. After 5 min of incubation at RT, absorbance was measured at 595 nm. Protein sample dilutions were prepared in the same fashion and their concentrations were calculated using the fresh standard curve.

2.2.3.5 Thermal proteome profiling of *P. falciparum* cell lysates

Trophozoite-stages cultures of 3D7 WT *P. falciparum* parasites of around 24-32 hpi and parasitemia levels higher than 5% were subjected to MACS purification. The obtained infected red blood cell pellets were lysed using 1 mL of 0.07% saponin in PBS with protease inhibitors (250 µg/mL aprotinin, 10 µg/mL leupeptin, 1 mM PMSF) for 30 sec at 37 °C. After centrifuging at 17 000 *g* for 1 min at 4 °C, the supernatant was discarded, and the pellet was washed with cold PBS with protease inhibitors. The parasite pellet was then resuspended in less than 1 mL of lysis buffer A (see Section 2.1.6), and cells were lysed using three freeze/thaw cycles (liquid nitrogen/37 °C water bath). After a final centrifugation at 17 000 *g* for 10 min at 4 °C, the supernatant was stored at -80 °C after taking aliquots for the measurement of protein concentration using a Bradford assay and for an integrity check of the samples using an SDS-PAGE gel.

Crude lysates were further processed at the laboratory of Dr. Mikhail Savitski and the Proteomics Core Facility at EMBL Heidelberg, by Per Haberkant and Isabelle Becher. After adjusting the protein concentration of lysates to 3.5 mg/mL, 550 µL aliquots were subjected to drug or control treatment for 10 min at 25 °C. The drug treatment consisted of 2.5X, 25X, 125X or 375X the IC₅₀ of SC83288 (8 nM), while the control was 0.5% DMSO. The treated lysate was then distributed in 50 µL aliquots into ten PCR tubes in order to challenge them to the following temperatures for 3 min in a thermocycler: 37, 40.4, 44, 46.9, 49.8, 52.9, 55.5, 58.6, 62 and 66.3 °C. Afterwards, the tubes were incubated for another 3 min at room temperature before being placed on ice. A second lysis step was carried out subsequently, by adding 5 µL of lysis buffer B (see Section 2.1.6) and incubating for one hour at 4 °C under shaking at 500 rpm. A posterior removal of aggregates through filtration was not needed due to the samples being clear. Samples were finally centrifuged at 100 000 *g* for 20 min at 4 °C.

Mass spectrometry was carried out as previously described [123], by our collaborators at EMBL Heidelberg.

2.2.3.6 Intact-cell Cellular Thermal Shift Assay

Samples for intact-cell isothermal dose-response (ITDR) cellular thermal shift assay (CETSA) were prepared according to Dziekan *et al.* [124]. Briefly, a 150 mL trophozoite-stage culture (26-32 hpi) of around 10% parasitemia was subjected to MACS purification under sterile conditions. Here, warm culture medium was used instead of MACS buffer, and the eluate was re-incorporated into the column 2-3 times before washing the column with warm medium.

After centrifugating at 1 200 *g* for 5 min at room temperature, the supernatant was replaced with fresh warm medium, and the culture was allowed to recover for 1 h in the incubator at 37 °C. The number of cells recovered and the level of parasitemia were measured using a hemocytometer and a Giemsa-stained thin blood smear, respectively. This experimental procedure shields enough amount of sample for the exposure of ten drug treatment samples to two different thermal challenge temperatures, which requires a minimum of 400x10⁶ cells. After the recovery step, the culture was centrifuged at 1 200 *g* for 5 min at room temperature. The supernatant was discarded, and the concentration was adjusted to 10x10⁶ cells/mL. Subsequently, 4 mL aliquots of the cell suspension were treated with serial dilutions of SC83288 (covering a range from 7 pM to 3 μM, and a DMSO control). Samples were incubated for 1 h at 37 °C. Each sample was centrifuged at 1 200 *g* for 5 min at room temperature and supernatant was removed before resuspension in 100 mL of room-temperature PBS. A 50 μL aliquot of each sample was added to a separate well of two different 96-well PCR plates (20 x 10⁶ cells per well). The plates were then placed in two thermocyclers, one with the 37 °C control temperature and the other with a denaturing condition (e.g. 50, 55 or 60 °C) and subjected to the thermal challenge for 3 min. Finally, 50 μL of 2X lysis buffer were added to each sample and mixed by pipetting. Posterior analysis, including the steps of peptide sample preparation, tandem mass tag labelling, offline fractionation, and mass spectrometry analysis, were also carried out by Dr. Jerzy Dziekan in the lab of our collaborator Prof. Zbynek Bozdech in NTU Singapore, following their aforementioned publication [124].

2.2.3.7 *In vitro* determination of DHFR activity

The inhibitory activity of SC83288 over DHFR was measured *in vitro* by our collaborators from the Protein-Ligand Engineering and Molecular Biology Research Team (Sumalee Kamchonwongpaisan, Thanaya Saeyang, Jarunee Vanichtanankul and Yongyuth Yuthavong, NTSDA/BIOTEC, Thailand). SC83288 was dissolved in DMSO at 10 mM stock and serially diluted with DMSO. Enzyme inhibition assay was performed in a 96-well plate as previously described [125]. The final concentration of each component in the reaction was 100 μM NADPH, 100 μM DHF, and the sample in 1X DHFR assay buffer (see Section 2.1.6). The kinetic reaction was initiated by an appropriate amount of 5-20 nM DHFR enzyme (PfDHFR-WT, PfDHFR-QM or Human DHFR). The kinetic reaction was followed by recording the optical density at 340 nm (OD₃₄₀) for 1 min using a microplate reader (MULTISKAN GO, Thermo Scientific). The results were expressed as 50% inhibition concentration (IC₅₀) or percentage of inhibition at the highest concentration of samples.

2.2.3.8. *In vitro* determination of DHPS activity

The activity of wild-type PfDHPS was measured by Dr. Marie Hoarau at the Protein-Ligand Engineering and Molecular Biology Research Team (NTSDA/BIOTEC, Thailand) using a procedure previously established in their lab (unpublished, manuscript in preparation by their group). Briefly, activity buffer (100 mM Tris, pH 9, 100 mM β -mercaptoethanol, 10 mM magnesium sulfate) was mixed with HMDP-PP and pABA to a final concentration of 100 μ M. The reaction was initiated by addition of enzyme, and was incubated at 37 °C for 20 min. The reaction was then stopped by incubation at 95 °C for 5 min, followed by a 5 min incubation on ice. The samples were then centrifuged, filtered, and analyzed by Ultra High-Performance Liquid Chromatography (UHPLC) using a 0-50% ACN gradient in 0.1% formic acid in water over 10 min.

2.2.3.9. *In vitro* determination of HPPK activity

A PfHPPK-GFP inhibition assay was carried out by Dr. Marie Hoarau at the Protein-Ligand Engineering and Molecular Biology Research Team (NTSDA/BIOTEC, Thailand) using the KinaseGlo Plus kit (Promega). Test compounds (1 μ L of a 50 mM DMSO stock) and master mix (100 mM Tris pH 9, 10 mM β -mercaptoethanol, 10 mM magnesium sulfate, 0.01% w/v BSA, 10 μ M HMDP and 10 μ M ATP) were dispensed in a white 96-well plate. The reaction was initiated by addition of 2 μ g of PfHPPK-GFP enzyme, reaching a total volume of 50 μ L, and was allowed to proceed for 20 min at RT under shaking at 300 rpm. The reaction was then quenched by addition of 50 μ L KinaseGlo reagent and allowed to equilibrate for 10 min at RT under shaking at 300 rpm. Luminescence was recorded on a Biotek synergy H1 plate reader using an integration time of 1 sec per well. The percentage of inhibition was calculated in relation to positive control (no enzyme added) and negative control (no inhibitor added) measurements. This protocol is part of a manuscript in preparation by the Protein-Ligand Engineering and Molecular Biology Research Team.

2.2.3.10 Kinase enzymatic activity determination

Global kinase enzymatic activity of parasite lysates was determined in presence of different concentrations of SC83288 to observe the potential effect caused by the drug. This was carried out using the reagent kit EnzyChrom (BioAssay Systems), which involves the incubation of the samples with a working reagent. Then, ADP is enzymatically converted to ATP and pyruvate, and this is measured using a fluorometric assay method. For each drug concentration (0, 0.01, 0.1, 1 and 10 μ M) two samples were measured, both containing 5 μ g of protein, one of them being heat inactivated (10 min incubation at 95 °C in heat block) before the assay.

Protein samples were combined with the drug and assay buffer to a final volume of 16 μ L in a well of a black 96-well plate. Then, 4 μ L of a 1 mM ATP stock solution were added to each well and the reactions were incubated at 37 °C for 30 min. Finally, 40 μ L of working reagent were added to each well and fluorescence ($\lambda_{exc} = 530$ nm, $\lambda_{em} = 590$ nm) was measured in the plate reader FLUOstar Optima (BMG Labtech). Fluorescence values of heat inactivated samples were subtracted from those of untreated samples and compared according to the drug treatment received.

2.2.4 DNA binding studies

2.2.4.1 Preparation of salmon sperm DNA fragments

Salmon sperm DNA was used as a standard for binding experiments, for which fragments of around 1 to 2 kb were used. In order to prepare them, 50 mg of salmon sperm DNA were dissolved overnight in 5 mL of 1X TE buffer at 4 °C, to obtain a final concentration of 10 mg/mL. The solution was sonicated to break down the DNA into the desired fragments. Sonication shears DNA by hydrodynamic processes: due to cavitation forces caused by ultrasound, DNA molecules collide several times and as a consequence is sheared [126]. Salmon sperm DNA samples were sonicated three times for 30 sec under 75% power and 2x10% cycles using the probe sonicator Sonopuls HD 2070 (Bandelin). In between rounds of sonication, the samples were allowed to rest on ice for one minute.

2.2.4.2 Preparation of *P. falciparum* DNA fragments

The PfCRT promoter (5' UTR, ca. 1.5 kb) was chosen as a representative standard for *P. falciparum* DNA in binding studies. It was obtained by digestion (see Section 2.2.2.10) of a pARL vector plasmid (see Section 2.1.5.5) using the restriction enzymes NotI and XhoI (New England Biolabs). The digestion products were run on a 1% agarose gel and the 1.5 kb band corresponding to the PfCRT promoter was cut for DNA extraction (see Section 2.2.2.8).

2.2.4.3 Trichloroacetic acid (TCA) DNA precipitation for [³H]-SC83288 binding assay

One of the approaches for the study of the DNA binding properties of SC83288 involved the incubation of DNA samples with [³H]-SC83288 and posterior precipitation of DNA with TCA. After filtration and washing, the count rate (detection rate of ionization events) of the precipitate stuck to the filter paper was measured using a liquid scintillation counter. Therefore, if DNA binding occurred, increasing counts should be observed for increasing amounts of DNA until reaching a saturation point.

DNA fragments, varying in size from 1 to 2 kb, from salmon sperm or *P. falciparum* parasites were used on a range from 0 to 5 µg. Samples were prepared in a total volume of 50 µL, containing the corresponding amount of DNA, 0.5 µM of [³H]-SC83288 and buffer NEB 2.1 (final concentration 1X, from 10X stock solution, see buffer composition in Section 2.1.6), and incubated for 30 min at RT. Then, 50 µL of 20% TCA were added to the samples, which were then incubated for 30 min on ice. The precipitate was filtered through Whatman glass microfiber filters, washed with 10% TCA and then with ethanol, and let air dry for at least 10 min under a fume hood. Dry filters were placed in plastic scintillation counter vials, to which 2 mL of Ultima Gold (Perkin Elmer) liquid scintillation cocktail were added. Samples were measured then in the Tri-Carb 4910 TR liquid scintillation counter (Perkin Elmer). The proportion (expressed in percentage) of [³H]-SC83288 bound to DNA was calculated in relationship to the total counts corresponding to the treatment concentration (0.5 µM) and the total volume of radiolabelled compound to which DNA samples were exposed.

2.2.4.4 DNA-binding dyes characterization

A fluorescence-based DNA binding assay was carried out following the work of Williams *et al.* [127]. The DNA-binding dyes used for this assay were characterised as described in this section in a setup preliminary step, and then were used for the fluorescence quenching assay described in the next section.

DAPI (4,6-diamidino-2-phenylindole, a minor groove binder) and TP3 (TO-PRO-3 iodide, an intercalator) were purchased from Invitrogen (Thermo Fisher Scientific) and 100 µM stock solutions were prepared. In order to measure the dye's DNA binding parameters and compare them with previously reported values, a dye-DNA titration was carried out and from this data a dose-response curve and a Scatchard plot were built.

For the titration curve, the fluorescence of a dye solution was measured upon addition of salmon sperm DNA aliquots. The measurements were carried out in triplicates using a black 96-well plate. First, 198 µL of buffer (acetate buffer for DAPI, TE buffer for TP3, see compositions in Section 2.1.6) were added to the wells and background fluorescence was measured. Then, the dye was added to a final concentration of 1 µM and fluorescence of the free dye was recorded. DNA aliquots from a 1.7 µg/µL solution were added subsequently, incorporating 1 µg on each step until 15 µg, and following each addition fluorescence was measured. Due to the available excitation and emission filters, DAPI fluorescence was measured using the plate reader FLUOstar Optima (BMG Labtech), and for TP3 the Cytation3 Reader (BioTEK) was used.

Excitation and emission wavelengths were: $\lambda_{exc} = 358$ nm, $\lambda_{em} = 461$ nm (gain 1 380), for DAPI; and $\lambda_{exc} = 633$ nm, $\lambda_{em} = 661$ nm (gain 100) for TP3. Each titration curve was repeated independently three times.

Background fluorescence (buffer alone) was subtracted for each data point and the values were further corrected for dilution as follows (Eq. 2-2), where F_{corr} is the corrected fluorescence intensity value, F is the measured value, 200 is the volume in microliters of the free dye solution, and x is the increase in volume as a product of DNA additions.

$$F_{corr} = \frac{F(200 + x)}{200} \quad (\text{Eq. 2-2})$$

For the construction of a Scatchard plot, the parameter f (fraction of dye bound to DNA) was defined as described in (Eq. 2-3), where F_D is the fluorescence intensity of the free dye, $F_{max,corr}$ is the corrected fluorescence corresponding to the highest amount of DNA.

$$f = \frac{F_{corr} - F_D}{F_{max,corr} - F_D} \quad (\text{Eq. 2-3})$$

The DNA concentration was calculated in M(bp) after the law of Beer-Lambert (Eq. 2-4), where Abs_{260} is the absorbance of salmon sperm DNA at 260 nm, ϵ is the molar extinction coefficient of the DNA (assumed to be $12824 \text{ M(bp)}^{-1}\text{cm}^{-1}$ [127]), l is the optical path length in cm and dil is the dilution factor of the DNA sample. The DNA concentration was corrected for the dilution in the titration curve samples, calculating it for each fluorescence determination in the well as shown in (Eq. 2-5), where x is the cumulative added volume of DNA solution.

$$DNA[M(bp)] = \frac{dil * Abs_{260}}{\epsilon * l} \quad (\text{Eq. 2-4})$$

$$DNA_{well}[M(bp)] = \frac{x * DNA[M(bp)]}{200 + x} \quad (\text{Eq. 2-5})$$

The Scatchard plot was then obtained by plotting $(DNA_{well}[M(bp)]/f)$ as a function of $(1-f)^{-1}$. The data points were then be fitted to a curve with the equation shown in (Eq. 2-6). Here, two parameters were defined: N is the number of base pairs per bound molecule of dye, and K_b corresponds to the dye-DNA binding constant. The concentration of dye was considered to stay constant at $1 \mu\text{M}$ throughout the measurements.

$$\frac{DNA_{well}[M(bp)]}{f} = \frac{N}{K_b} (1 - f)^{-1} + N[dye] \quad (\text{Eq. 2-6})$$

The linear curve from (Eq. 2-6) can be generally described as (Eq. 2-7), allowing for the calculation of the binding parameters as shown in (Eq. 2-8). These values can then be compared with those previously reported in the literature [127], to ensure a correct experimental setup.

$$y = y_0 + a * x \quad (\text{Eq. 2-7})$$

$$y = \frac{DNA_{well}[M(bp)]}{f}; \quad x = (1 - f)^{-1}; \quad y_0 = \text{y-intercept of the linear curve}$$

$$N = \frac{y_0}{[dye]}; \quad K_b = \frac{N}{a} \quad (\text{Eq. 2-8})$$

2.2.4.5 Fluorescence quenching assay

For the quenching assay, the fluorescence intensity of a solution containing fixed amounts of dye (2 μM) and salmon sperm DNA (4 μg) was measured upon addition of SC83288 aliquots from a stock solution. First, 189.2 μL of buffer (acetate buffer for DAPI, TE buffer for TP3) were added to selected wells in a black 96-well plate and background fluorescence was measured as described in the previous section. After addition of dye and DNA to their final concentrations, fluorescence intensity was measured again. Then, 3 μL aliquots of a 300 μM SC83288 stock solution were added, recording fluorescence intensity after each addition. The concentration range covered in this assay was 0 to 55.1 μM . In addition, another assay covering a lower drug concentration range (0 to 50 nM) was carried out, where 3 μL aliquots of a 166 nM SC83288 stock solution were added stepwise. Each assay was carried out in triplicates and repeated independently three times. In order to evaluate the fluorescence corresponding to SC83288 in the assay conditions, control samples containing 200 μL of buffer and either 10 or 30 μL of a 166 nM, 0.3 mM, or 3 mM SC83288 stock solution were measured. However, no significant fluorescence intensity was detected.

2.2.5 Growth inhibition assay and determination of IC_{50} values

Antimalarial activity is commonly measured by measuring the growth inhibition caused by the active compound(s) of interest over *P. falciparum* intraerythrocytic stages. It is expressed as IC_{50} values, which indicate the concentration needed to inhibit multiplication of parasites by 50% over a specific period of time. Growth inhibition assays were carried out following a standard procedure based on the detection of parasitic DNA by staining with the fluorescent dye SYBR Green I [128].

Briefly, a ring-stage culture was incubated for 72 h in serial dilutions of the compound of interest in a black 96-well plate. In each well, the final volume was 100 μ L, parasitemia was 0.5% and hematocrit 2%. Incubation was carried out under normal culture conditions (5% O₂, 3% CO₂, 92% N₂ and 95% humidity at 37 °C).

For the experiment setup, a *P. falciparum* culture was synchronized by sorbitol treatment and, after allowing the parasites to recover for at least 2 h, the parasitemia was adjusted to 0.5% and the hematocrit to 4%. In parallel, a 4% hematocrit solution was prepared with uninfected erythrocytes in complete cell culture medium and used as a negative control. Drug solutions were prepared as working solutions (6X starting concentration) in cell culture medium from stock solutions. The starting concentration was selected in a way such that the IC₅₀ value would fall around the middle point of the serial dilutions tested, based on previously reported IC₅₀ values or preliminary measurements.

Growth inhibition assays were set up according to the plate scheme shown on Figure 2-4. First, 50 μ L of complete cell culture medium were added to each well. Then, drug serial dilutions were prepared by adding 25 μ L of the corresponding working solution to each well on the 11th column of the plate. To avoid potential sources of error caused by evaporation, the wells on the edges of the plate were only filled with medium and not used for samples. After thoroughly mixing, 25 μ L of the 11th column wells were transferred to the wells on the 10th column, mixed again, and the process was repeated until reaching the wells on the 4th column. The 25 μ L from the final column were discarded. This way, a 1:3 serial dilution consisting of 8 points was obtained for each row. The 2nd column was reserved for the non-infected erythrocytes solution that serves as a negative control, and 50 μ L of it were added to each well. The 3rd column was allocated for the positive control, where no drug is present. In the 3rd to 11th columns, 50 μ L of the previously prepared *P. falciparum* culture were added to each well. After this, the plate was covered with a clear lid, labelled, and incubated for 72 h. Three days later, the plate was wrapped in aluminium foil and stored at -80 °C until further processing in order to obtain a complete erythrocyte lysis (at least 2 hours).

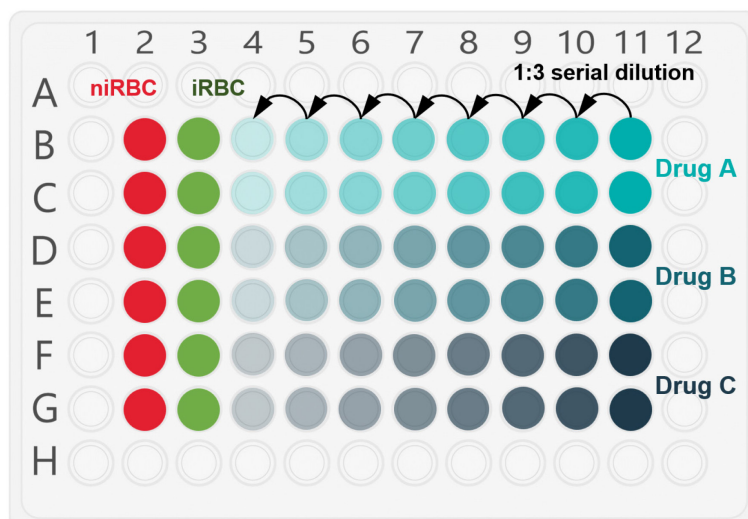


Figure 2-4. Schematic plate for standard 72 h growth inhibition assay. Abbreviations: niRBC, non-infected red blood cells (negative control); iRBC, infected red blood cells (positive control).

At the moment of measuring, aluminium foil was removed from the plate, which was left to thaw at room temperature for at least 1.5 h. Then, 100 μ L of a 1:10 000 dilution of SYBR Green I in lysis buffer (see composition in Section 2.1.6) were added to each sample well. The plate was then shaken for 1 min at 400 rpm and incubated in the dark for 1h at RT. Fluorescence was measured in the FLUOstar Optima plate reader (BMG Labtech) ($\lambda_{exc} = 485 \text{ nm}$, $\lambda_{em} = 520 \text{ nm}$, gain 1380, 10 flashes/well, top optic).

For the calculation of IC_{50} values, the fluorescence intensity of non-infected red blood cells was deducted from that of infected erythrocytes for all conditions. This corrected value for untreated parasites represents a 100% growth and served as basis for the calculation of the percentage of growth of treated parasites. Growth percentages and drug concentrations used for treatment were plotted as a dose-response curve using SigmaPlot, and IC_{50} values were calculated by the software using a sigmoid curve fit (Hill function, four parameters).

2.2.5.1 Modifications for the measurement of the IC_{50} value of sulfadoxine

In vitro determinations of sulfadoxine IC_{50} values are characterized by poor reproducibility and extreme variability in historically reported values [129]. In order to avoid inconsistencies, the modified method described by Wang *et al.* [130] was used in this study. Briefly, parasite cultures were adapted to low folate concentrations using the corresponding cell culture medium described in Section 2.1.6 (low folate). This adaptation period lasted for about two weeks, until cell growth was normal and high parasitemia was easily achievable.

Adapted ring-stage parasites were subjected to synchronization with sorbitol and transferred to a folate free medium (see Section 2.1.6). Two days later, the growth inhibition assay was carried out as previously described, using folate free medium.

2.2.6 *In vitro* drug combination assays

The *in vitro* interaction between two compounds was studied using the fixed ratio isobologram method [131]. For this, the IC₅₀ values of the individual drugs were initially measured, and then the measurements were done over a range of drug combinations. The changes in the IC₅₀ value of a drug combination in comparison with the value of the drugs individually show the nature of the drug-drug interaction: synergistic, antagonistic, or additive (no interaction). The data can be analysed arithmetically (using the mean sum of the fractional IC₅₀s as a parameter to classify the nature of the interaction) or graphically (using isobolograms).

The experiment was very similar to the growth inhibition assays described previously (Section 2.2.5), although the drug working solutions were now drug combinations. Starting drug concentrations were selected in such a way that the IC₅₀ value of the individual drugs fell around the middle of the serial dilutions. The combinations for the study of the interaction of omecamtiv mecarbil (OM) with SC83288 (SC) were prepared as shown below.

OM:SC Ratio	10:0	9:1	8:2	7:3	6:4	5:5	4:6	3:7	2:8	1:9	0:10
Starting [OM] (μM)	105	94.5	84	73.5	63	52.5	42	31.5	21	10.5	0
Starting [SC] (μM)	0	0.1	0.2	0.3	0.4	0.5	0.6	0.7	0.8	0.9	1

For the data analysis, the fractional IC₅₀ (FIC₅₀) was calculated, according to the following definition (Eq. 2-9).

$$FIC_{50\ drug} = \frac{IC_{50\ of\ combination}}{IC_{50\ of\ drug\ alone}} \quad (\text{Eq. 2-9})$$

For the arithmetical analysis, the sum of FIC₅₀ for each combination (ΣFIC₅₀) was calculated, and the mean value of the 11 ΣFIC₅₀ was obtained. A mean value of 0.7 or less was considered a synergistic interaction and a value of 1.3 or higher an antagonistic interaction between both drugs. Any intermediate value was considered an indifferent interaction.

Graphical analysis was performed using isobolograms, where pairs of FIC_{50} values were plotted for each drug combination (Figure 2-5). According to the shape of the curve, the interaction can be described as one of three types. A lack of interaction, or additive effect is inferred from a straight diagonal line, while synergism is indicated by a concave curve towards the origin of the axes, and a convex curve towards the opposite side suggests an antagonistic interaction.

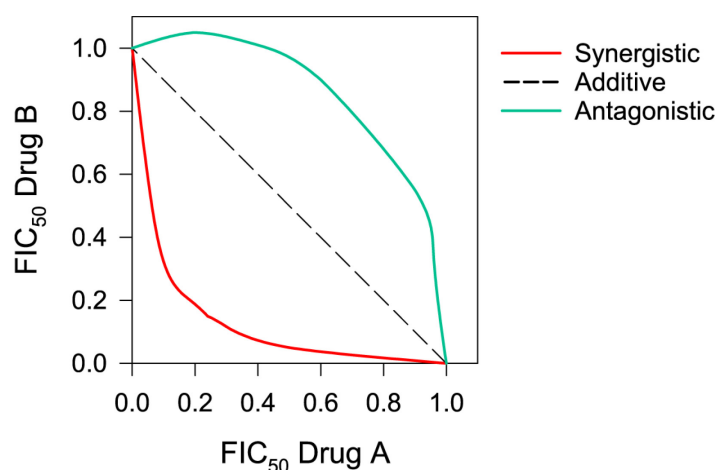


Figure 2-5. Schematic isobologram example, showing characteristic isoboles for *in vitro* drug-drug interaction types. An additive effect, i.e. no interaction between drugs is seen as a straight diagonal curve (dark grey). Synergism is characterised by a concave curve towards the origin of the axes (green), while antagonism is observed as a convex curve towards the opposite (red).

2.2.7 Untargeted metabolomics

Samples for untargeted metabolomics analysis were prepared by Dr. Maëlle Duffey as described in her doctoral dissertation [81] in two rounds. The first round included 4 independent replicates of 3D7 WT and 8 independent replicates of 3D7 PfATP6^{F972Y}, while the second round consisted of 4 new 3D7 WT independent replicates. Second round samples were analysed by mass spectrometry (MS) in parallel with 3D7 WT samples from the first round. All replicates include a control and a sample treated with SC83288.

Mass spectrometry analysis of the samples was carried out by Erin Manson at the research group of Prof. Michael Barrett in the Glasgow Polyomics Center (College of Medical, Veterinary & Life Sciences, University of Glasgow). Hydrophilic interaction liquid chromatography (HILIC) was carried out on a Dionex UltiMate 3000 RSLC system (Thermo Fisher Scientific, Hemel Hempstead, UK) using a ZIC-pHILIC column (150 mm × 4.6 mm, 5 μm column, Merck Sequant).

The column was maintained at 30 °C and samples were eluted with a linear gradient (20 mM ammonium carbonate in water and acetonitrile) over 26 min (24 min for second round) at a flow rate of 0.3 mL/min as follows:

Time (min)	20 mM (NH ₄) ₂ CO ₃ (%)	CH ₃ CN (%)
0	20	80
15	80	20
15	95	5
18 (17)	95	5
18 (17)	20	80
26	20	80

The injection volume was 10 µL and samples were maintained at 5 °C prior to injection. For the MS analysis, an Orbitrap Fusion and a Thermo Orbitrap QExactive (Thermo Fisher Scientific, Hemel Hempstead, UK) were operated for the first and second round, respectively, in polarity switching mode and the MS settings were as follows:

Setting	Orbitrap Fusion	Orbitrap QExactive
Resolution	120 000	70 000
Automatic gain control (AGC)	2 x 10 ⁵	1 x 10 ⁶
m/z range	70-1 000	70-1 050
Sheath gas	40	40
Auxiliary gas	5	5
Sweep gas	1	1
Probe temperature	150 °C	150 °C
Capillary temperature	325 °C	320 °C

For the Orbitrap Fusion, the source voltage for positive mode ionisation was +4.3 kV. For negative mode ionisation it was -3.2 kV. The S-Lens RF level was 30.00%. The instrument was calibrated to standard operating parameters prior to sample run. To enhance calibration stability, lock-mass correction was also applied to each analytical run: a positive mode lock mass (m/z) of 144.9821 and a negative mode lock mass (m/z) of 135.971. For the Thermo Orbitrap QExactive, the source voltage for positive ionisation was +3.8 kV, S-Lens RF Level 30.00%, S-Lens Voltage -25.00 V, Skimmer Voltage -15.00 V, Inject Flatpole Offset -8.00 V, Bent Flatpole DC -6.00 V. For negative mode ionisation the source voltage was -3.8 kV. The calibration mass range was extended to cover small metabolites by inclusion of low mass calibrants with the standard Thermo calmix masses (below m/z 138), butylamine for positive ion electrospray ionisation mode (m/z 74.096426) and trifluoromethanol for negative ion electrospray ionisation mode (m/z 84.9906726). To enhance calibration stability, lock-mass correction was also applied to each analytical run: positive mode lock masses (m/z) 83.0604, 149.0233 and 445.1200; negative mode lock mass (m/z) 89.0244.

Data transformation was also carried out by the research group of Prof. Michael Barrett, instrument raw files were converted to positive and negative ionisation mode mzXML files. These files were then analysed using the XCMS [113]/MZMatch [104]/IDEOM [101] pipeline to produce an IDEOM file.

Statistical analysis and interpretation of the data were done by me for the present study. To be able to compare metabolite accumulation patterns, raw intensity signals from MS data were transformed to Z-scores as previously described [132]. The Z-score for each replicate of each metabolite (Z_i) was calculated as follows (Eq. 2-10), where x_i corresponds to the raw intensity of the given metabolite and, \bar{x} and s are the mean and standard deviation, respectively, of raw intensities of the replicates of the control line (being it either the untreated sample or 3D7 WT):

$$Z_i = \frac{(x_i - \bar{x})}{s} \quad (\text{Eq. 2-10})$$

For every metabolite, Z-scores were compared by condition (treated vs untreated, or mutant line vs WT) using a two-tailed homoscedastic t-test. In order to get an overview of metabolism pathways affected by treatment, metabolites were classified into compound families or categories using the maps assigned to them in the IDEOM file. Then, for each compound category the mean raw intensity of each replicate was calculated, and the Z-scores were determined as described before.

A second filter for the identification of metabolites significantly affected by treatment is to present the data in a volcano plot, where the significance (represented by $-\log_{10}(\text{mean of all P-values/individual P-value})$, or LOD score, significant when higher than 1) is displayed vs the $\log_2(\text{fold change})$. Here, not only statistically significant affected metabolites are highlighted, but also those that have an absolute fold change higher than two ($\log_2(\text{fold change})$ higher than 1 or lower than -1) and therefore are more meaningful for our analysis. In this analysis, the P-value of each metabolite corresponds to the significance of a Pearson correlation and is obtained by locating the corresponding t-value in a two-tailed Student's t-distribution table (*degrees of freedom* = $n-2$). The t-values are calculated as shown in (Eq. 2-11), where n is the number of observations and r is the Pearson correlation coefficient that is obtained by (Eq. 2-12). There, y are the individual raw intensities and \bar{y} is the mean of the observations, while x takes the value zero for control samples and one for treated samples, and \bar{x} corresponds to the mean of these values.

$$t = \frac{r\sqrt{n-2}}{\sqrt{1-r^2}} \quad (\text{Eq. 2-11})$$

$$r = \frac{\sum(x - \bar{x})(y - \bar{y})}{\sqrt{\sum(x - \bar{x})^2 \sum(y - \bar{y})^2}} \quad (\text{Eq. 2-12})$$

As an example, the values are displayed below for 5-methylthioadenosine (approximated values for y are shown), where the Pearson correlation coefficient r takes is equal to 0.699, the t-value is 3.661, and corresponding P-value is 0.003.

	3D7 WT control								3D7 WT treated							
	r1	r2	r3	r4	r5	r6	r7	r8	r1	r2	r3	r4	r5	r6	r7	r8
x	0	0	0	0	0	0	0	0	1	1	1	1	1	1	1	1
y	1.12E+7	7.04E+6	2.80E+6	6.33E+6	1.83E+7	1.01E+7	9.37E+6	1.03E+7	4.36E+7	3.14E+7	3.79E+6	1.61E+7	3.51E+7	5.99E+7	3.86E+7	2.92E+7

2.2.8 Chemical rescue assays

For the examination of the effects of medium supplementation with key metabolites over parasite susceptibility to SC83288, classical growth inhibition assays were carried out as described previously (Section 2.2.5) with the modifications presented next.

2.2.8.1 Growth assay under hypoxanthine supplementation

In this case, the growth inhibition assay was modified by replacing the drug serial dilutions with hypoxanthine serial dilutions, using a starting concentration of 500 μM . The stock solution concentration was limited by the low solubility of hypoxanthine in the neutral pH range required for parasite culture. SC83288 was added to the culture medium to achieve final fixed concentrations of 5 or 10 nM and a control was run in parallel without drug addition. Parasite growth for each hypoxanthine concentration was evaluated in relation to that of parasites not exposed to SC83288.

2.2.8.2 Growth assay under S-adenosylmethionine (AdoMet) supplementation

For the study of the effect of supplementation with S-adenosylmethionine, the growth inhibition assay and IC_{50} determination were carried out as previously described (Section 2.2.5) using modified cell culture medium. This medium included 1 mM AdoMet and was prepared immediately before use by dissolving the corresponding amount of solid S-adenosylmethionine chloride in complete cell culture medium and using a 0.2 μm syringe filter for its sterilization. The IC_{50} values of SC83288 measured under these conditions were then compared to those of standard complete cell culture medium.

2.2.9 Sodium-dependent swelling assay

In order to evaluate a potential Na⁺-dependent swelling phenotype of intraerythrocytic *P. falciparum* cells, an assay was set up and carried out with 3D7 wild-type as well as SC83288-resistant 3D7 PfATP6^{F972Y} parasites. A 7 mL aliquot of a 5% parasitemia trophozoite-stage (22-26 hpi) culture was washed once, and then resuspended in 5 mL of either a sodium free medium (NMDG saline) or a sodium containing medium (carbonate-free RPMI 1640 or physiological saline). A microscope slide was prepared at this point with 10 µL of the sample. The suspension was then divided into 5 samples in 1.5 mL microcentrifuge tubes and 1 µL of a SC83288 stock solution was added to each tube to achieve final concentrations of 0.01, 0.15, 1.5 and 15 µM. One of the samples was treated with 1 µL of DMSO and used as a negative control. In addition, the suspensions were supplemented with 10 µL of a 10 mM glucose solution (prepared in the adequate medium and stored at -20 °C). The cells were then incubated for 1 h at 37 °C in a water bath and samples were taken at t = 15, t = 30 and t = 60 min for the preparation of microscope slides. The slides were examined immediately under the light microscope and pictures of cells under each condition were recorded using the microscope camera ODC 825 (Kern & Sohn).

Cell size of *P. falciparum* parasites at each timepoint of the different treatments was analysed using the software Microscope VIS (Kern & Sohn). First, images were cut into squares of 500x500 px containing infected erythrocytes to facilitate further processing. Then, a polygon was drawn on top of each parasite cell marking its perimeter as precisely as possible, and each polygon's perimeter and area was calculated by the software and reported next to the drawing (Figure 2-6). All parasite cell area measurements were collected in a spreadsheet and the values were normalized to the mean of the area of untreated parasites at time zero (before the start of the experiment). Then, for each condition, cell sizes were compared across time to evaluate a possible swelling. Data was analysed performing One Way ANOVA tests (or, in the case of absence of normal data distribution, Kruskal-Wallis tests) using SigmaPlot.

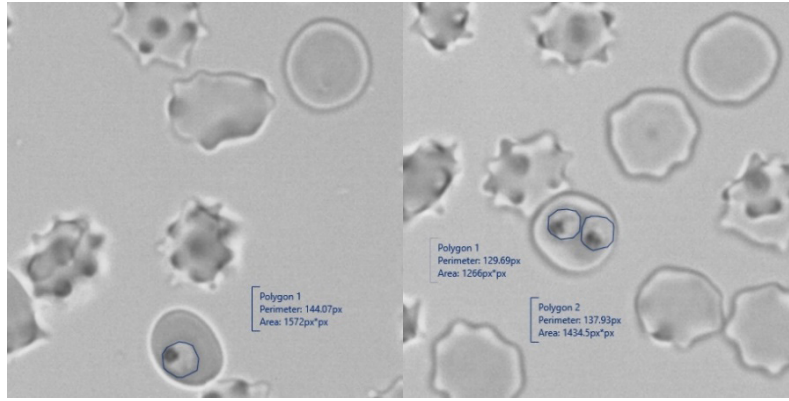


Figure 2-6. Examples of measurement of parasite cell area using polygons in Microscope VIS software.

2.2.10 Live cell imaging

Asexual *P. falciparum* 3D7 parasites episomally expressing 3xNLS-mCherry and PCNA1-GFP [21] were cultured in unwashed 0+ peripheral red blood cells (RBCs) under 25 mM WR99210 and 10 ng/mL blasticidin selection at a 4% hematocrit in complete cell culture medium without serum. Parasites were synchronized via 5% sorbitol treatment and subsequently incubated with 50 U/mL heparin to prevent invasion. 30-32 h after sorbitol synchronization, cultures were washed twice with cell culture medium to remove heparin and permit invasion. Then, 42-46 h after removal of heparin, late-stage parasites were isolated via MACS purification, supplemented with 100-200 μ L fresh RBCs and left to invade in 5 mL complete cell culture medium without serum for 2 h at 60 rpm. After invasion, the remaining late-stage parasites were removed through 5% sorbitol treatment and the resulting ring-stage culture was distributed equally into 5 wells of a 24-well plate. At 6 ± 1 hpi, 2 samples were treated with 80 nM SC83288, 2 samples with an equal volume of DMSO as a vehicle control (0.1% DMSO) and 1 sample remained untreated. At 22 ± 1 hpi, parasites were seeded in the middle four wells of an 8-well glass bottom ibidi dish following Grüring et. al. [133] with minor modifications. Briefly, each well was covered with 100 μ L of 5 mg/mL concanavalin A and left to incubate for 20 min at 37 °C, before removal of concanavalin A. Subsequently, the wells were vigorously washed 3 times with 1X PBS before addition of a cell suspension. To prepare the cell suspension, 500 μ L of resuspended culture from a well containing a culture with the desired treatment was pelleted by centrifugation and the supernatant removed and kept. Cells were washed 2X with incomplete cell culture medium without serum and without Albumax II before resuspension and transfer to the microscopy dish. Cells were left to settle for 10 min at 37 °C before unattached RBCs were removed by careful washing. Finally, the RBC monolayer was covered with the previously reserved medium containing SC83288 or DMSO and returned to the incubator. At 28 ± 1 hpi the microscopy dish was removed from

the incubator and the medium exchanged to 750 μ l phenol red-free imaging medium supplemented with 80 nM SC83288 or DMSO. The dish was tightly closed, sealed with parafilm and imaging immediately performed. One well containing either DMSO or SC83288 treated cells was imaged per session.

Point laser scanning confocal microscopy was performed on a Zeiss LSM900 microscope equipped with an Airyscan detector, using a Plan-Apochromat 63x/1,4 oil immersion objective. Live-cell imaging was performed at 37 °C. Images were acquired at multiple positions using an automated stage and the Definite Focus module for focus stabilization with a time-resolution of 10 min/stack for 10 h. Multichannel images were acquired sequentially in the line scanning mode using 488 nm and 561 nm diode lasers for GFP and mCherry imaging, respectively. GFP and mCherry emission detection was configured to 490-650 nm using variable dichroic mirrors. The Airyscan detector was used with the gain adjusted to 900V, offset was not adjusted (0%). Brightfield images were obtained from a transmitted light photomultiplier tube detector after excitation with 640 nm laser. Sampling of a 6 μ m stack was Nyquist-optimised in xy (~ 50nm) and 600 nm in z, scanning bidirectionally with a pixel dwell time of 0.73 μ s and 2x line averaging. Subsequently, the ZEN Blue 3.1 software was used for the post-2D Airyscan processing with automatically determined default Airyscan Filtering strength.

For analysis, cells at individually acquired positions were manually inspected using the ZEN Blue 3.1 software. Nuclear morphology and DNA replication was analysed using maximum z-projections of the mCherry and GFP channel respectively. Parasite position, health and size, hemozoin movement and intactness of the RBC were investigated using single z-slices of the brightfield channel. The following parameters were noted down for every individual parasite: Parasite death and approximate time of death (defined as either complete loss of nuclear mCherry signal, parasite or RBC lysis), cause of death, occurrence and time of first DNA replication, intactness of the iRBC at the end of imaging, hemozoin morphology and movement. Gametocytes were excluded from analysis.

To visualize unspecific parasite death via DMSO, unsynchronized parasites episomally expressing 3xNLS-mCherry and PCNA1-GFP were used. Untreated cells were seeded as described above. Directly before imaging, the medium covering the RBC monolayer was exchanged to 750 μ l imaging medium containing 5% DMSO. Parasites selected for imaging were aged-matched to previous experiments by appearance (parasite size, nucleus number and hemozoin size) and imaged and analysed as described above.

2.2.11 RNAseq transcriptomics perturbation profiling

A 200 μ L aliquot of a 2% hematocrit and 5% parasitaemia culture of tightly synchronized 3D7 (MR4) trophozoites (25 ± 3 hpi) was exposed to SC83288 or a vehicle control (DMSO) for 4.5 h. Drug concentrations used for treatment corresponded to 5, 10, or 20 nM. Post-treatment, 190 μ L of the culture were transferred to a new hard-shell 96-well PCR plate (Bio-Rad). Plates were centrifuged for 1 min at 1 000 g and the supernatant was aspirated and discarded. Then, 60 μ L of TRIzol reagent (Invitrogen) was added to 4 μ L of remaining infected packed red blood cells. Plates were sealed and vortexed at 7 000 rpm for 1 min. Subsequently, plates were centrifuged for 1 min at 2 000 g and 50 μ L of supernatant were aspirated and transferred to a new 2 mL 96-deep well plate (Corning). The RNA content was extracted using ZYMO DirectZol-96 MagBead RNA kit (ZYMO) following manufacturer instructions with minor modifications. Briefly, 50 μ L of 100% ethanol (Merck) was added to the supernatant and mixed by shaking at 1500 rpm for 30 sec. Then, 10 μ L of beads were added to each sample and incubated for 10 min with shaking. Beads were separated on the magnet (Alpaqua) and after the cleared supernatant was discarded, beads were washed with 500 μ L of each wash buffer following manufacturer instructions. The RNA was eluted in 17 μ L of RNase/DNase free water, and its purity was assessed by spectrometry on a Nanodrop (ThermoScientific). RNA concentration was estimated using RNA-specific Qubit fluorometric assays (Invitrogen) and RNA integrity was assessed on a Bioanalyzer RNA Nano Chip (Agilent). RNA quality cut-off metrics were as follow: 260/280 ratio ≥ 1.8 , 260/230 ratio ≥ 1.5 , RIN ≥ 8 , RNA concentration ≥ 5 ng/ μ L, and only the samples that passed quality metrics were sequenced. All steps were automated on a Hamilton STAR liquid handling platform (Hamilton Robotics).

25 ng of total RNA were reverse-transcribed and amplified using polyA-specific primer as previously described [134]. The resulting cDNA was processed using the Nextera XT library prep kit (Illumina) to obtain short sequence reads according to manufacturer instructions, with minor modifications. Briefly, 0.25 ng of cDNA was fragmented and amplified using downscaled library preparation protocol with 1/4 volume of the recommended reagents. PCR amplification cycles were increased from 12 to 15 cycles. The PCR reactions were purified using 0.6X volumes of AMPure XP magnetic beads (Beckman Coulter) following manufacturer instructions on a Hamilton STAR liquid handling platform. Samples were eluted in 17 μ L of 10 mM Tris-Cl, pH 8.5 (Qiagen) and average library sizes were estimated on Bioanalyzer High Sensitivity chips (Agilent).

Library molarity was assessed with qPCR and libraries were pooled in equimolar ratios and sequenced on a Novaseq S4 platform (Illumina) with pair-end 150 bp long reads protocol, generating on average 2.5 Gb of data per sample (Novogene Co.).

Raw reads obtained from the sequencer were first checked for overall quality and trimmed to remove adapters, amplification primers and low-quality bases from 3'-ends using TRIMGALORE [110]. HISAT2 aligner was used to perform alignment to the genome [100]. Paired reads with proper orientation mapped to unique locations of genome were considered for counting [135]. Gene specific read counts were calculated using BEDTools [94]. Normalized counts TPM were then calculated and used for further analysis. Downstream data analysis was conducted in R environment using transcripts detected in at least 80% of samples. The dataset was filtered, removing top 7% and bottom 3% of transcripts based on expression, as well as 5% transcripts with the highest expression variance between the replicates. \log_2 (fold-change in expression) was calculated for each gene per treatment condition relative to the vehicle control-treated samples (n = 22). Differentially expressed genes were identified using FDR-adjusted student t-test values ($p < 0.05$).

2.2.12 Data analysis

All the data analysis and display were performed using SigmaPlot 13.0, except where otherwise indicated, and with the following additional exceptions: parasite cell area measurement from slides images were carried out using Microscope VIS and dot density plots were produced using Prism 8.0.2, while Z-scores and LOD scores for the metabolomics data were calculated using Microsoft Excel.

3. Results

3.1 SC83288 displays structural similarities with Omecamtiv Mecarbil, but they show no *in vitro* interaction

SC83288 has a novel structure and therefore limited results, or none at all, can be expected from a structural similarity analysis. Nevertheless, I came across omecamtiv mecarbil (OM) using the search function from DINIES (Drug-target Interaction Network Inference Engine based on Supervised analysis, [95]). The similarity score between SC83288 and OM is only 0.43. Although a value under 0.8 is usually deemed not significant, I considered relevant to carry out an interaction study given that the structure of OM is very close to the west side of SC83288 (Figure 3-1, A). Omecamtiv mecarbil is a known selective cardiac myosin activator [136, 137], and its antimalarial activity is very low when compared with that of SC83288 (IC_{50} of $20 \pm 2 \mu\text{M}$, Figure 3-1, B). This considerable difference in activity is a factor that influences the shape of the drug-interaction isobologram (Figure 3-1, C) where a mild antagonism can be observed, but data points cluster on one end. The mean ΣFIC_{50} (see analysis description in Section 2.2.6) has a value of 1.45 ± 0.16 and falls below the cut-off value of 1.5, which indicates an indifferent drug-drug interaction [80]. The asymmetry and the mean ΣFIC_{50} are enough to deem the observed mild antagonism not significant. Therefore, the modes of action of OM and SC83288 are not related.

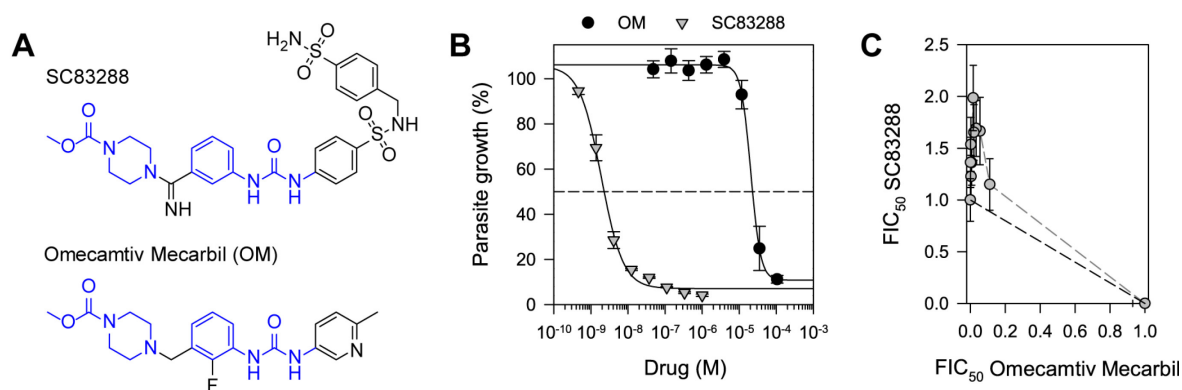


Figure 3-1. Omecamtiv mecarbil has structural similarities with SC83288 but presents a non-significant interaction profile. (A) Structures of SC83288 and Omecamtiv mecarbil (OM), common fragments are shown in blue. (B) *P. falciparum* 3D7 WT parasites *in vitro* susceptibility to SC83288 (grey triangles) and OM (black circles), mean \pm SEM of ten independent replicates. Measured IC_{50} values are 1.9 ± 0.2 nM for SC83288 and $20 \pm 2 \mu\text{M}$ for OM. (C) Isobologram showing the interaction profile between SC83288 and OM, which suggests a mild antagonism. Mean \pm SEM of 4 to 10 replicates. Mean ΣFIC_{50} is 1.45 ± 0.16 (mean \pm SD), indicating (together with the asymmetry of the curve) that the interaction is indifferent.

3.2 SC83288 interacts with antifolates without sharing their target

Sulfadoxine (SDX) and pyrimethamine (Pyr) are antifolate drugs, which were extensively used in combination under the name of Fansidar to treat malaria in the 1960s until the rapid emergence of resistance. They target the parasite enzymes dihydropteroate synthase (DHPS) and dihydrofolate reductase (DHFR), respectively [138]. Both SC83288 and SDX contain sulfonamide groups (Figure 3-2, A, marked in red), while SC83288 has no structural similarities with Pyr. Although the activity of SC83288 is also sensitive to structural changes on the opposite side of the molecule, I explored its potential relationship with antifolates to get insights on the role of the sulfonamide groups. The first step for an *in vitro* drug-drug interaction study is the measurement of the activity of each compound separately. Historically, the determination of the susceptibility of *P.falciparum* parasites to SDX has been characterized by poor reproducibility and a wide range of reported IC₅₀ values for strains considered sensitive. I used a method described by Wang *et al.* [130] for the measurements, which takes into account the interferences caused by folate and other medium components, such as human serum and p-aminobenzoic acid (pABA). Therefore, I adapted the 3D7 parasite culture to grow in a low folate environment before switching to a folate-free medium for the *in vitro* growth inhibition assay. However, I observed a resistant phenotype, without a significant reduction in parasite growth upon treatment with up to 0.158 mM of SDX (Figure 3-2, B). The folate adaptation method had no significant effect on the susceptibility of parasites to SC83288 (Mann-Whitney rank sum test, P = 0.653). The IC₅₀ value reported by Wang *et al.* is 235 ± 170 nM, so I proceeded to check if our parasite strain had any mutation in DHPS that differentiated it from the one used in their publication [129]. Nevertheless, the DHPS sequence of our 3D7 strain encodes the reported amino acids residues (Figure 3-3), including the mutation A437G that causes a significant decrease in susceptibility in comparison with the sensitive strain HB3 [129].

It was decided to continue the analysis with Pyr, which due to its synergism with SDX should interact in the same fashion with SC83288 as SDX would do. The interaction profile, derived from measurements carried out by Dr. Maëlle Duffey, indicates a strong antagonism (Figure 3-2, C). The nature of the interaction can be explained as a product of the competition for a common target. This is, however, not the case of SC83288 and Pyr, as the first has no relevant effect over the enzymatic activity of DHFR (Table 3-1) as confirmed by the team of Dr. Sumalee Kamchonwongpaisan (NTSDA/BIOTEC, Thailand).

Furthermore, the activity of WT DHPS is not affected by SC83288, that achieves a mere 2.4 ± 0.8 % of inhibition at a drug concentration of 1 mM (Table 3-2), as measured by Dr. Marie Hoarau.

The antagonism could then be understood not as a result of target competition, but in terms of a balancing effect, in the case that SC83288 targets a biological process complementary to folate metabolism [139].

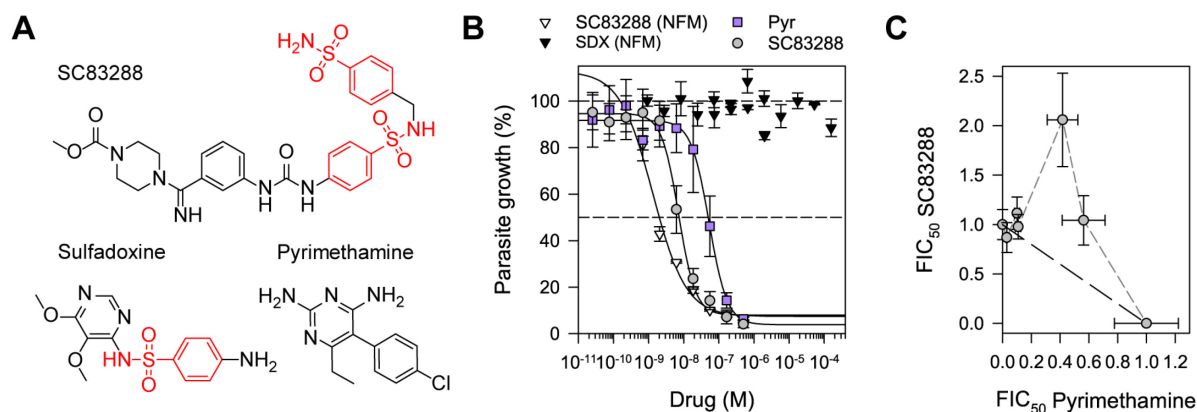


Figure 3-2. SC83288 has similarities with antifolates and is a pyrimethamine antagonist. (A) Structures of SC83288, sulfadoxine and pyrimethamine. Common fragments (sulfonamide group) are shown in red. (B) *P. falciparum* 3D7 parasites *in vitro* susceptibility to SC83288 (white triangles in folate free medium-NFM, grey circles in complete cell culture medium), pyrimethamine (Pyr, purple squares), and sulfadoxine (SDX, in NFM, black triangles). SDX and SC83288 were assayed using a modified *in vitro* assay that involves the previous adaptation of parasites to low folate environments and the posterior assay being carried out in NFM. Mean \pm SEM of 2 to 4 independent replicates. The data for SC83288 (in complete cell culture medium) and Pyr, associated with the study shown in panel (C), were provided by Dr. Maëlle Duffey. Measured IC_{50} values: SC83288 (NFM) 1.3 ± 0.4 nM, Pyr 52.9 ± 8.3 nM, SC83288 7.1 ± 0.8 nM. Mean \pm SEM of 2 to 4 independent replicates. (C) Isobologram showing the antagonistic interaction between SC83288 and Pyr, mean \pm SEM of 4 independent replicates. Data provided by Dr. Maëlle Duffey.

amplified		MINEGASVIDIGGES	SGPFVIPNPKISERDLVVPVLQLFQKEWNDIKNKIVKCDAKPIIS
reported	421	MINEGASVIDIGGES	SGPFVIPNPKISERDLVVPVLQLFQKEWNDIKNKIVKCDAKPIIS
		*****	*****
amplified		IDTINYNVFKECVDNDLVDI	LNDISACTNNPEI IKLLKKNKFYSVVLHMKRGNPHTMDK
reported	481	IDTINYNVFKECVDNDLVDI	LNDISACTNNPEI IKLLKKNKFYSVVLHMKRGNPHTMDK
		*****	*****
amplified		LTNYDNLVYDIKNYLEQRLN	FVNLNGIPRYRILFDIGLGF AKKHDQS IKLLQNIHVYDEY
reported	541	LTNYDNLVYDIKNYLEQRLN	FVNLNGIPRYRILFDIGLGF AKKHDQS IKLLQNIHVYDEY
		*****	*****
amplified		PLFIGYSRKRFIA	HCMNDQKCCN-----
reported	601	PLFIGYSRKRFIA	HCMNDQNVVINTQQKLHDEQQNENKNIVDKSHNWMFQMNMRKDKDQ
		*****	*****

Figure 3-3. Sequence of a fragment of PfDHPS of the 3D7 strain containing residues involved in SDX resistance. A fragment of PfDHPS was amplified using primers described in the Section 2.1.5.6 and genomic DNA from the 3D7 WT *P. falciparum* strain used for this work as a template. After isolation of the amplified fragment through a gel extraction purification step, it was sequenced by Eurofins Genomics. The sequence was then compared to the one reported for the strain in PlasmoDB [107, 140]. In the alignment shown, the highlighted amino acid residues correspond to those associated with resistance to sulfadoxine: Ser436, Gly437, Ala581 and Ala613 [129]. These key residues are identical in our strain as well as their surroundings, and therefore the apparent resistance phenotype observed cannot be attributed to mutations in the *dhps* gene.

In *P. falciparum* parasites, DHPS is actually part of a bifunctional enzyme: PfDHPS-HPPK (HPPK being 6-hydroxymethyl-7,8-dihydropterin pyrophosphokinase). The function of HPPK is to phosphorylate 6-hydroxymethyl-7,8-dihydropterin through an ATP-dependent reaction, to generate the substrate that is then condensed with pABA by DHPS [141]. Interestingly, the function of PfHPPK is impaired by SC83288, reaching an inhibition of $31.5 \pm 2.9\%$ at a drug concentration of 1 mM. This inhibition level is comparable with that of compounds designed at the Protein-Ligand Engineering and Molecular Biology Research Team (NTSDA/BIOTEC, Thailand) which are around 45% (Table 3-2), although it is clear that PfHPPK does not constitute the main target of SC83288. Even when the drug accumulates inside parasites, a concentration of 1 mM is far higher than the nanomolar concentrations that are enough to exert antimalarial activity.

Table 3-1. Effect of SC83288 and known inhibitors over *P. falciparum* DHFR and human DHFR. The enzyme inhibition assay was carried out as described in the Section 2.2.3.7 and, by the Protein-Ligand Engineering and Molecular Biology Research Team (Sumalee Kamchonwongpaisan, Thanaya Saeyang, Jarunee Vanichtanankul and Yongyuth Yuthavong, NTSDA/BIOTEC, Thailand). The results are expressed as 50% inhibition concentration (IC_{50}) or %inhibition at the highest concentration of samples. PfDHFR-QM carries four mutations (N51I, C59R, S108N and I164L) responsible for antifolate resistance. At high concentrations, SC83288 showed precipitation. Mean \pm SD of three determinations.

Compound	IC_{50} (nM)		
	PfDHFR-WT	PfDHFR-QM	Human DHFR
Pyrimethamine	6.34 ± 0.08	334.35 ± 24.57	1951.98 ± 138.72
WR9210	5.59 ± 0.35	5.41 ± 0.50	434.85 ± 21.13
Methotrexate	3.45 ± 0.17	8.22 ± 0.77	291.52 ± 10.43
SC83288	35% inhibition at 100 μ M	8537.50 ± 0.30	No inhibition at 100 μ M

Moreover, the inhibition of PfHPPK does not explain the observed antagonism with Pyr, which is most likely associated with the main mode of action of SC83288. However, the observed inhibition could be analysed further to gain more insights on the main target of the compound. As shown in Figure 3-4, SC83288 has possible binding modes with the ATP binding site of PfHPPK. A molecular docking study carried out by Dr. Marie Hoarau using Glide (Schrodinger suite) with the structure of the apoenzyme (Figure 3-4, A, WT enzyme, PDB ID: 6JWQ) and holoenzyme (Figure 3-4, B, WT enzyme complexed with pterate, PDB ID: 6JWR) version of PfHPPK [142] revealed the possible binding mode, where the drug has major interactions with the residues Asn312, Ser317, Arg326 and Lys185. The inhibition observed can be attributed to the hydrogen bonds formed with Ser317 and Asn312, present for both structures, which lead to binding competition with the substrate ATP.

This suggests that SC83288 could also have an affinity for other ATP binding sites in *P. falciparum* proteome. Thus, the main target of the compound could be an ATP-dependent protein, such as a kinase.

Table 3-2. Effect of SC83288 and known inhibitors over *P. falciparum* DHPS and HPPK. The enzyme inhibition assays were carried out as described in the Sections 2.2.3.8 and 2.2.3.9 by Dr. Marie Hoarau at the Protein-Ligand Engineering and Molecular Biology Research Team, NTSDA/BIOTEC, Thailand. The results are expressed as the percentage of enzyme inhibition for a treatment with 1 mM of either SC83288, a known sulfa inhibitor of DHPS, or compounds developed in their laboratory (i.e. B364 and B098, unpublished, manuscript in preparation by the Protein-Ligand Engineering and Molecular Biology Research Team). Mean \pm SEM of 3 to 4 independent replicates. The abbreviation n.d. stands for not determined.

Compound	% Inhibition at 1 mM drug	
	PfDHPS	PfHPPK
SC83288	2.4 \pm 0.8	31.5 \pm 2.9
Sulfadoxine	45.7 \pm 0.3	n.d.
Sulfathiazole	92.3 \pm 1.7	n.d.
Sulfamethoxazole	70.1 \pm 0.6	n.d.
B364	n.d.	46.0 \pm 4.4
B098	n.d.	43.8 \pm 2.6

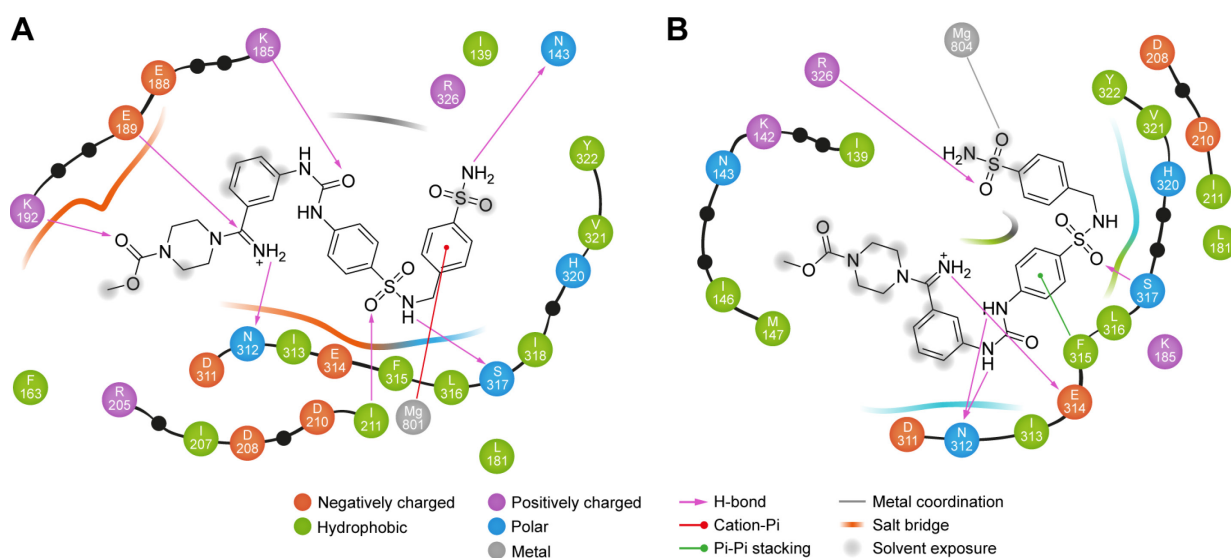


Figure 3-4. Possible binding mode of SC83288 in PfHPPK pocket. Results from a molecular docking study carried out by Dr. Marie Hoarau using Glide (Schrodinger suite) with (A) the structure of the apo-enzyme (WT enzyme, PDB ID: 6JWQ) and (B) holo-enzyme (WT enzyme complexed with pteroylpyruvate, PDB ID: 6JWR) version of PfHPPK [142].

To get a broad overview of the effect of SC83288 over the activity of kinases in parasites, I measured kinase activity of *P. falciparum* lysates treated with the drug in a range of concentrations up to 10 μ M (Figure 3-5). The results show that there is not a significant effect as a consequence of drug treatment.

However, this does not mean that the molecular target is not a kinase, since this experiment is not specific, and the potential target could be present in the total protein extract in such a small proportion that any effect produced by the drug would be undetectable or masked out. Data from other approaches can provide more information on the relationship between SC83288 and kinases.

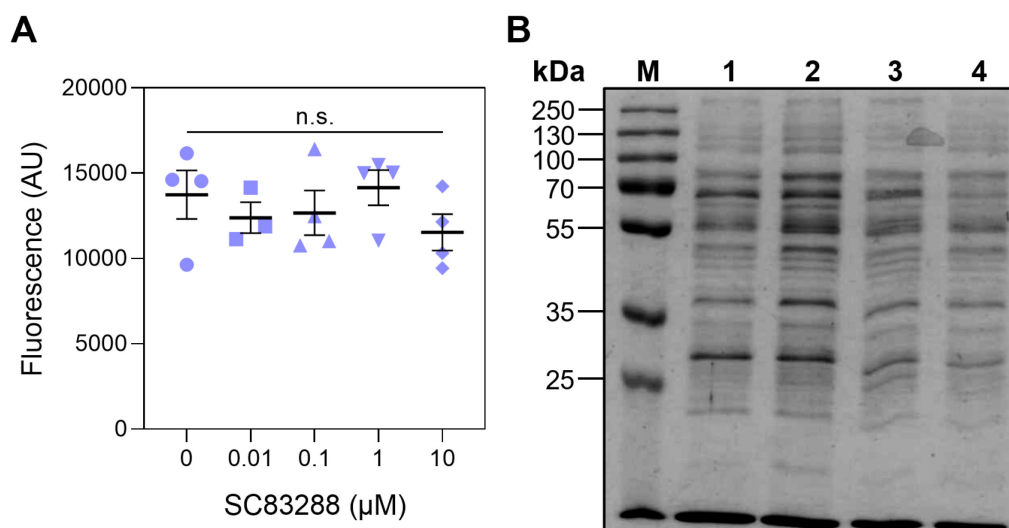


Figure 3-5. Effect of SC83288 over global kinase activity of *P. falciparum* lysates. (A) Kinase enzymatic activity of parasite protein extracts treated with SC83288 ranging from 0 µM (DMSO control) to 10 µM. Activity was measured using the EnzyChrom Kinase assay kit (BioAssay Systems), after thirty minutes of reaction time in presence of drug or solvent. Results from three to four biologically independent replicates, mean ± SEM. There is no significant difference in activity when comparing all treatments together (One Way ANOVA, $P=0.543$) as well as when comparing activity between 0 µM and 10 µM treatments (t-test $P=0.261$). (B) SDS-PAGE of the *P. falciparum* 3D7 WT lysates used for the experiment. Each lane corresponds to a sample originated from an independent parasite culture.

3.3 Untargeted metabolomics analysis shows disruptions in methionine recycling and phospholipids metabolism

In order to gain more insights into the mode of action of SC83288, an untargeted metabolomics study was conducted on *P. falciparum* parasites upon treatment with the drug. Ring-stage cultures were treated for 12 h until extraction of metabolites [81]. The samples prepared by Dr. Maëlle Duffey were analysed then via HILIC-MS (as described in Section 2.2.7) by Erin Manson in the laboratory of Prof. Michael Barrett (University of Glasgow, UK). For the subsequent analysis of the data, I used Z-scores to compare the levels of metabolites in the treated and control samples. A first look at the effects of SC83288 over metabolic pathways or compound categories shows no significant alterations (Figure 3-6, A). However, at the individual metabolite level, a number of metabolites displays a significant change in concentration as a consequence of treatment (Figure 3-6, B). The Z-scores and associated P-values from this analysis can be found in Table 3-3 and Table 3-4.

A second analysis, using a volcano plot, integrates the fold change of the metabolite level as a further parameter to identify the significantly altered compounds (Figure 3-6, C). A summary of the metabolites affected by SC83288-treatment and associated information can be found in Table 3-5.

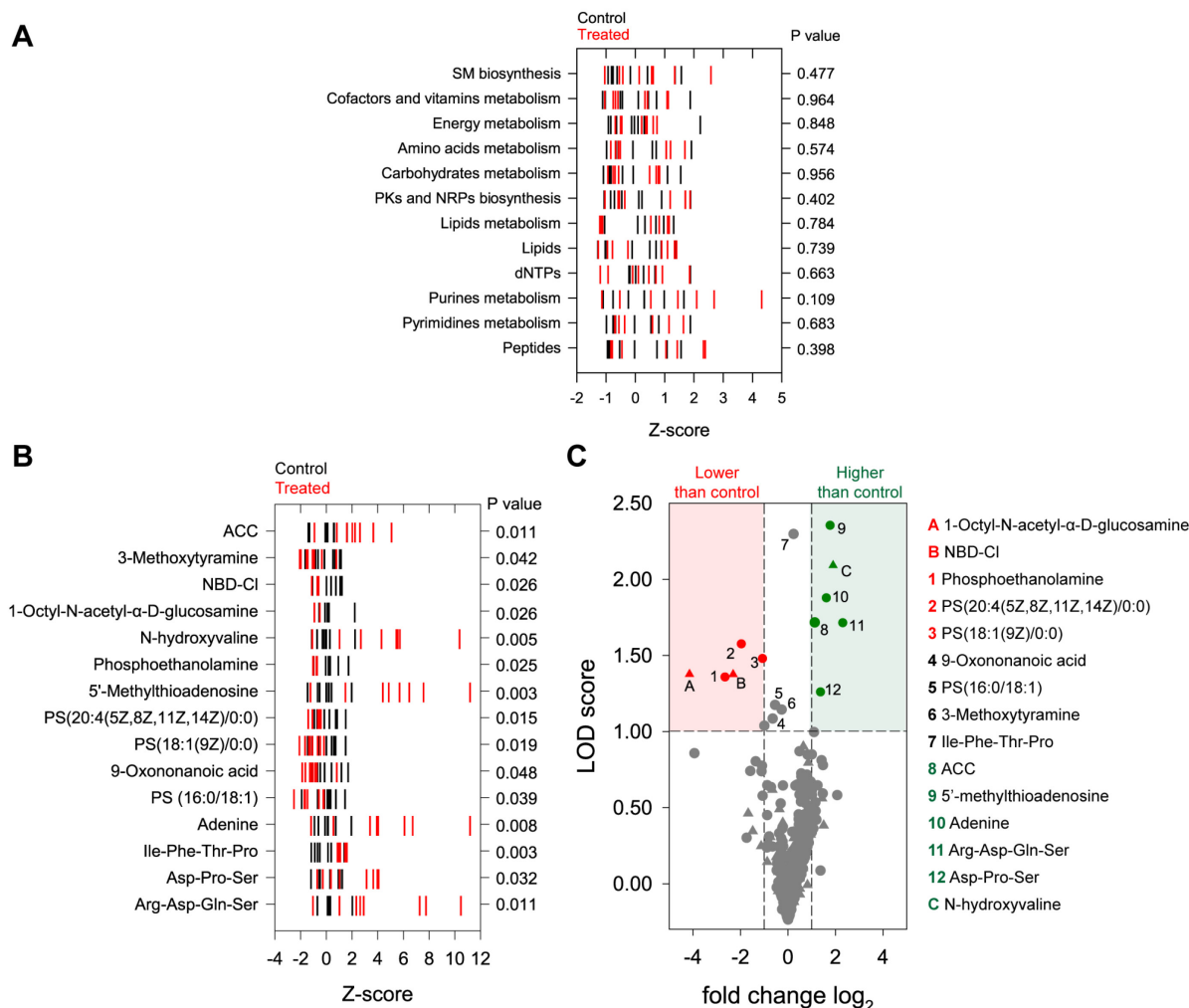


Figure 3-6. Untargeted metabolomics study of *P. falciparum* 3D7 WT parasites treated with SC83288 reveals disruptions of nucleotides metabolism. (A) Z-scores for compound categories in control (black) or samples treated (red) with 40 nM SC83288 for 12 hours from ring to trophozoite stages. Obtention of Z-scores from eight independent replicates is explained in Section 2.2.7, each vertical line corresponds to a replicate. P values shown are the result of a homoscedastic two-tailed t-test. (B) Z-scores for individual metabolites that display a statistically significant difference (P value < 0.05, homoscedastic two-tailed t-test) between levels in control (black) and treated (red) samples as mentioned in (A). (C) Volcano plot, where individual metabolites are represented in accordance with the \log_2 of their fold change between control and treated samples and their LOD score as described in detail in Section 2.2.7. The compounds that are statistically significant altered by the drug treatment (LOD score > 1, fold change \log_2 < -1 or >1) are highlighted according to their concentration in treated samples in relation to the control, i.e. red for lower concentration and green for lower accumulation. Those metabolites without an identified pathway are represented with a triangle instead of a circle, and those significantly altered are indicated with a letter instead of a number. Abbreviations: SM, secondary metabolites; PKs, polyketides; NRPs, non-ribosomal peptides; dNTPs, deoxynucleotides triphosphate; PS (16:0/18:1), 2-Oleoyl-1-palmitoyl-sn-glycero-3-phosphoserine; PS (18:1(9Z)/0:0), 1-O-oleoyl-sn-glycero-3-phosphoserine; PS (20:4(5Z, 8Z, 11Z, 14Z)/0:0), 1-arachidonoyl-sn-glycero-3-phosphoserine; ACC, 1-Aminocyclopropane-1-carboxylate; NBD-Cl, 4-chloro-7-nitrobenzofurazan.

Table 3-3. Z-scores and P-values of compound categories from the analysis of 3D7 WT samples treated with SC83288 versus control samples. Abbreviations: MB, metabolism; dNTPs, deoxyribonucleosides triphosphate; PKs, polyketides; NRPs, non-ribosomal peptides; BS, biosynthesis; SM, secondary metabolites.

Compound Category	Z-score																P value
	3D7 WT Control								3D7 WT Treated								
	r1	r2	r3	r4	r5	r6	r7	r8	r1	r2	r3	r4	r5	r6	r7	r8	
Peptides	-0.541	-0.957	-0.936	-0.895	1.077	-0.036	0.735	1.553	-0.463	-0.839	-0.799	-0.794	1.042	1.429	2.319	2.384	0.398
Pyrimidines MB	-0.713	-0.770	-0.687	-0.995	1.877	0.529	-0.036	0.795	-0.706	-0.696	-0.371	-0.565	1.143	1.634	0.579	0.577	0.683
Purines MB	-0.243	-0.766	-1.119	-1.106	1.655	0.300	0.301	0.979	0.523	0.521	-1.147	-0.535	2.682	4.313	2.090	1.446	0.109
dNTPs	-0.222	-0.193	-1.202	-1.202	1.873	0.277	0.003	0.665	0.097	-0.102	-1.202	-0.935	0.917	1.846	0.694	0.456	0.663
Lipids	-0.116	-1.036	-1.287	-0.972	1.346	0.702	0.487	0.876	-0.262	-0.788	-1.271	-0.957	1.403	1.330	0.894	1.089	0.739
Lipids MB	0.076	-1.125	-1.184	-1.052	1.306	0.321	0.694	0.964	0.519	-1.221	-1.176	-1.120	0.809	1.122	1.097	1.150	0.784
PKs and NRPs BS	-0.470	-0.851	-1.069	-0.721	1.878	0.113	0.222	0.896	-0.364	-0.554	-1.048	-0.595	1.185	1.701	1.699	1.860	0.402
Carbohydrates MB	-0.444	-0.895	-0.838	-1.093	1.547	-0.081	0.709	1.096	-0.575	-0.770	-0.703	-0.943	0.485	0.820	0.779	0.708	0.956
Amino acids MB	-0.673	-0.596	-0.844	-0.992	1.910	0.577	-0.091	0.710	-0.585	-0.841	-0.522	-0.686	1.193	1.692	1.047	1.051	0.574
Energy MB	-0.649	0.084	-0.846	-0.924	-0.038	-0.134	0.294	2.213	-0.689	0.209	-0.508	-0.469	0.604	0.737	0.396	0.353	0.848
Cofactors and vitamins MB	-0.520	-0.445	-1.122	-1.034	1.868	0.716	0.099	0.439	-0.687	-0.760	-0.597	-1.050	1.115	1.078	0.409	0.320	0.964
SM BS	-0.815	0.411	-0.177	-0.766	-0.938	-0.629	1.566	1.349	-1.051	-0.550	0.555	0.606	1.338	-0.436	0.129	2.577	0.477

Table 3-4. Z-scores and P-values of individual metabolites from the analysis of 3D7 WT samples treated with SC83288 versus control samples. The metabolites displayed on the table correspond to those exhibiting a P-value lower than 0.05. Abbreviations: PS (16:0/18:1), 2-Oleoyl-1-palmitoyl-sn-glycero-3-phosphoserine; PS (18:1(9Z)/0:0), 1-O-oleoyl-sn-glycero-3-phosphoserine; PS (20:4(5Z, 8Z, 11Z, 14Z)/0:0), 1-arachidonoyl-sn-glycero-3-phosphoserine; ACC, 1-Aminocyclopropane-1-carboxylate; NBD-Cl, 4-chloro-7-nitrobenzofurazan.

Putative Metabolite	Z-score																P value
	3D7 WT Control								3D7 WT Treated								
	r1	r2	r3	r4	r5	r6	r7	r8	r1	r2	r3	r4	r5	r6	r7	r8	
Arg-Asp-Gln-Ser	-1.058	2.014	-1.058	0.083	0.141	0.303	-0.712	0.288	2.326	7.749	-1.058	1.009	7.248	10.458	2.903	2.620	0.011
Asp-Pro-Ser	-1.203	-1.203	-0.570	-0.499	0.929	0.275	1.046	1.225	1.017	-0.723	-0.291	0.348	3.638	3.961	3.119	4.066	0.032
Ile-Phe-Thr-Pro	1.402	-0.684	0.373	0.122	-1.179	-0.510	1.389	-0.912	1.068	1.448	0.860	1.567	0.979	1.554	1.568	1.590	0.003
Adenine	-0.110	-0.623	-1.194	-0.940	1.935	0.128	0.083	0.722	4.027	3.388	-1.198	0.548	6.709	11.178	6.068	3.917	0.008
PS (16:0/18:1)	-0.690	0.072	-1.927	0.205	1.448	0.317	-0.162	0.736	-1.721	-1.476	-2.531	-1.653	-0.242	-0.586	-0.204	-0.199	0.039
9-Oxononanoic acid	-0.773	-1.152	1.685	1.163	-0.693	-0.477	0.393	-0.146	0.801	-1.286	-1.645	-1.886	-1.214	-0.873	-1.066	-0.747	0.048
PS (18:1(9Z)/0:0)	-1.113	-0.010	-1.457	1.496	0.406	-0.620	0.584	0.714	-2.110	-1.090	-1.668	-0.190	-1.370	-1.271	-0.480	-0.683	0.019
PS (20:4(5Z,8Z,11Z,14Z)/0:0)	-0.947	-0.727	-1.428	1.500	0.228	-0.172	0.720	0.826	-1.428	-1.428	-1.428	-0.439	-1.098	-1.428	-0.670	-0.578	0.015
5'-Methylthioadenosine	0.394	-0.532	-1.471	-0.689	1.965	0.156	-0.017	0.195	7.557	4.850	-1.251	1.478	5.682	11.178	6.451	4.382	0.003
Phosphoethanolamine	-0.058	-1.001	-1.033	-1.004	1.717	0.160	0.292	0.927	-1.017	-1.029	-1.042	-1.034	-0.784	-0.726	-0.764	-0.752	0.025
3-Methoxytyramine	-0.163	-0.661	0.514	0.665	1.127	-1.659	1.034	-0.858	-1.081	-1.547	-0.353	0.771	-2.084	-1.999	-0.955	-1.452	0.042
ACC	0.595	-0.082	-1.326	-1.414	1.598	0.095	0.563	-0.029	3.649	1.582	-0.938	0.803	2.014	5.063	2.603	2.224	0.011
N-hydroxyvaline	0.260	-0.314	-1.143	-0.731	2.224	-0.019	-0.208	-0.069	5.437	4.286	-1.103	1.017	5.717	10.352	5.548	2.671	0.005
1-Octyl-N-Ac- α -D-glucosamine	0.190	-0.944	0.095	-0.567	-0.944	-0.108	2.199	0.079	-0.944	-0.517	-0.944	-0.944	-0.944	-0.944	-0.944	-0.944	0.026
NBD-Cl	0.003	-1.083	-1.136	-1.136	1.202	0.352	0.730	1.069	-1.136	-1.136	-1.136	-1.136	-0.705	-0.697	-0.693	-0.610	0.026

Giving an initial look at the results, the accumulation of adenine and MTA caught my attention. They are intermediates in the purine salvage pathway of *P. falciparum* (Figure 3-7, A; structures of highlighted metabolites in Figure 3-7, B). The first step to understand the meaning of these metabolic alterations was measuring the potential toxicity of MTA accumulation (Figure 3-7, C), but I found that parasite growth levels were not affected by MTA levels of up to 100 μ M. The accumulation of adenine and MTA can be understood in terms of a blockage of the pathway at the level of the enzyme adenosine deaminase (PfADA) (Figure 3-7, A).

This is, however, a hindrance that can be bypassed by the parasite cell with relative ease by importing the key downstream metabolite, hypoxanthine, from the host red blood cell [23]. In order to test if the disruptions observed in the purine salvage pathway are a direct consequence of the action of SC83288 over the metabolic route, I supplemented parasite cultures treated with the drug with hypoxanthine. Therefore, if this were the case, the exogenous hypoxanthine should be able to rescue parasites by providing an easier path to bypass the blockade. Nevertheless, supplementation with up to 500 μM hypoxanthine failed to improve parasite growth of cultures treated with 5 or 10 nM SC83288 (Figure 3-7, D) (5 nM: $P = 0.871$, Kruskal-Wallis one way ANOVA on ranks; 10 nM: $P = 0.971$, one way ANOVA). The limit of 500 μM as the highest tested supplementation was set as a consequence of the low solubility of hypoxanthine at the neutral pH range needed for parasite culture.

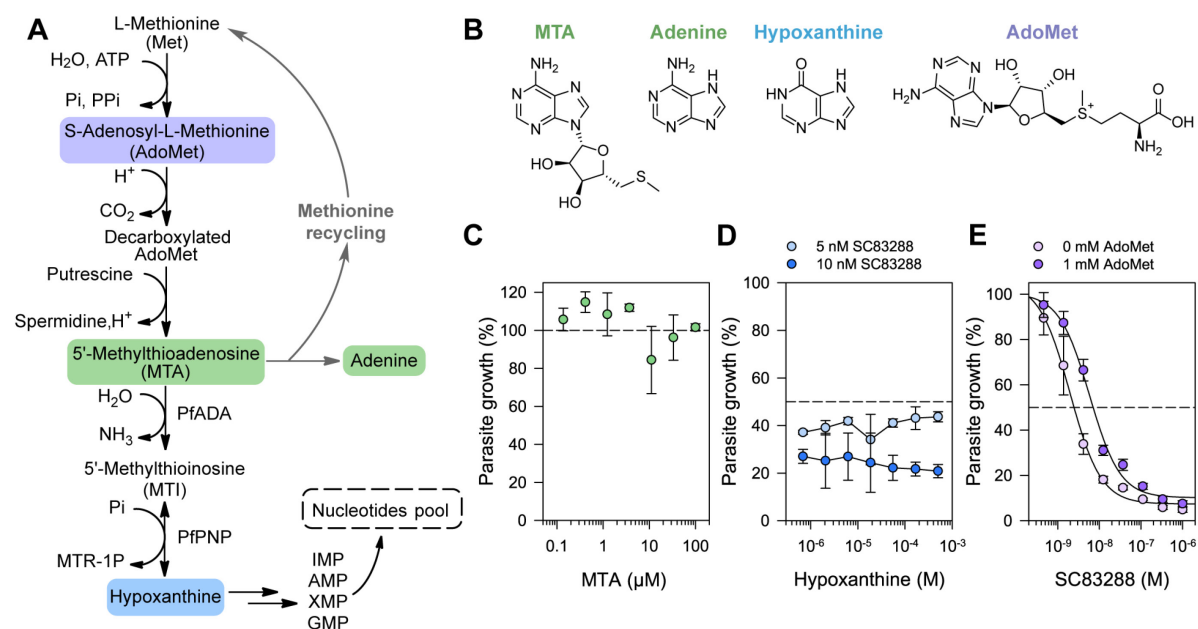


Figure 3-7. The accumulation patterns observed do not originate from a blockage in purine salvage. (A) Fragment of the purine salvage pathway in *P. falciparum*, highlighting key metabolites. Accumulated intermediates (MTA, adenine) are shown in green. (B) Chemical structure of the compounds marked in (A). (C) *In vitro* growth inhibition assay of 3D7 WT *P. falciparum* parasites treated with MTA. Mean \pm SEM of three independent replicates. (D) *In vitro* growth inhibition assay of parasites treated with either 5 nM (light blue) or 10 nM (dark blue) SC83288, under varying concentrations of hypoxanthine. The supplementation with hypoxanthine has no effect over parasite growth, 5 nM SC83288: $P = 0.871$, Kruskal-Wallis one way ANOVA on ranks; 10 nM SC83288: $P = 0.971$, one way ANOVA. Mean \pm SEM of three independent replicates. (E) *In vitro* growth inhibition assay of parasites treated with SC83288 in absence or presence of 1 mM AdoMet. A significant difference in the susceptibility of parasites to the drug is observed, $P = 0.01$, Welch's test. Mean \pm SEM of four independent replicates.

Another key intermediate on the purine recycling route is S-adenosylmethionine (AdoMet), which is located upstream and has a primordial role in *P. falciparum* metabolism. AdoMet acts as an alkyl donor in a variety of reactions: either as a methyl donor with acceptors such as DNA, RNA, proteins, and lipids; or as a propyl donor for the synthesis of polyamines after its decarboxylation [143]. Interestingly, medium supplementation with AdoMet had a mild, but statistically significant, recovery effect on treated parasites (Figure 3-7, E) ($P = 0.01$, Welch's test).

The hypothesis of a disruption of the salvage of purines as the cause for the metabolic alterations in treated cells had to be discarded. The accumulated metabolites are also central to the recycling of methionine, where the sulfur from MTA is salvaged through a series of steps that start with a cleavage to release adenine and either 5'-methylthioribose-1-phosphate (MTR1P) or 5'-methylthioribose (MTR) [144]. The first alternative involves one step catalysed by MTA phosphorylase and is used widely by eukaryotes, although most plants along with prokaryotes have a two-step process that involves the generation of MTR through MTA nucleosidase and a posterior phosphorylation catalysed by MTR kinase to generate MTR1P. However, there are no clear delimitations, and some bacteria use a phosphorylase for this reaction [144, 145]. In *P. falciparum*, genes for the three possible enzymes involved in MTA cleavage were not identified [146], despite previous measurements of MTA nucleosidase and MTR kinase activity in parasite extracts [147]. The simultaneous accumulation of MTA and adenine suggests that the cleavage takes place and could be repressed by the concentration of adenine. The origin of MTA overproduction could be traced back to more than one process. Besides its production during polyamine synthesis, MTA is also generated in plants during ethylene biosynthesis. The first step of this route is catalysed by the pyridoxal phosphate-dependent enzyme 1-aminocyclopropane 1-carboxylic acid synthase (ACC synthase, or ACS), which uses AdoMet to generate ACC and MTA. Then, as MTA is recycled, ACC is further metabolized to the hormone ethylene which regulates various developmental processes. Additionally, it has been shown that ACC acts a signaling molecule itself, beyond its role in ethylene synthesis [148]. Notably, ACC is among the metabolites accumulated in *P. falciparum* cells treated with SC83288 (Figure 3-6, B-C, Table 3-5). The function of this compound in the apicomplexan parasite is unclear. The enzyme ACS has not been identified so far in this organism, although PF3D7_0205200 could play this role, as the corresponding EC number 4.4.1.14 was inferred by orthology in the PlasmoDB database [107].

The increase in MTA and ACC is then generated at the expense of consuming AdoMet which, as mentioned earlier, has a key role in the parasite biology. The fact that the cells direct the use of valuable AdoMet to a potentially worthless plant-inherited metabolic route under SC83288-induced stress does not seem logical at first. However, this could be understood as a response that triggers programmed cell death (PCD). The increase in ethylene production in plant cells has been linked with PCD [149] and responses to stress that lead to cell growth arrest [150]. As mentioned earlier, ACC acts as a signalling molecule independently of its role on ethylene synthesis [151] and its production has been associated with an acute response to perturbation of cell wall growth and consequent reduced cell elongation, although mechanistic details are not understood [152, 153]. Therefore, with the current knowledge of *P. falciparum* biology, it can be speculated that the accumulation of ACC (along with MTA and adenine) is actually a response to imbalances or effects caused by SC83288. Upon AdoMet supplementation, there is a mild reduction on the susceptibility of *P. falciparum* parasites to the drug that could be interpreted as a partial compensation of the metabolite consumed in the synthesis of ACC.

Parasites exposed to SC83288 also present lower levels of phosphoethanolamine, a precursor of the synthesis of glycerophospholipids, as well as three different phosphatidylserine (PS) lipids (Figure 3-6, B-C, Table 3-5). The decrease in concentration of the three PS can be attributed to them being used to replenish the correspondent phosphatidylethanolamine (PE) lipids, whose levels remain comparable between treated and untreated samples, through the decarboxylation of serine (Figure 3-8). The original precursors of the PE lipids are phosphoethanolamine and CDP-ethanolamine, both with reduced levels on parasites treated with SC83288. The alterations in CDP-ethanolamine are, however, not enough to put the decrease in concentration over the significance cut-off (a LOD score over 1 is considered significant, while the value for this metabolite is 0.775). Ethanolamine was not detected among the metabolites. The reason behind the observed decrease in phosphoethanolamine and, consequently, CDP-ethanolamine is not clear, but it could only be explained by a lower ethanolamine kinase (EK) activity since parasites are able to either import ethanolamine from the host or obtain it from the decarboxylation of serine. Serine can, in turn, also be obtained from the host through its direct import or as a product of hemoglobin digestion in the food vacuole. These observations should be contrasted with other results in order to understand the underlying causes. Additionally, there is an accumulation of three peptides, although tracing them back to their origin is practically impossible.

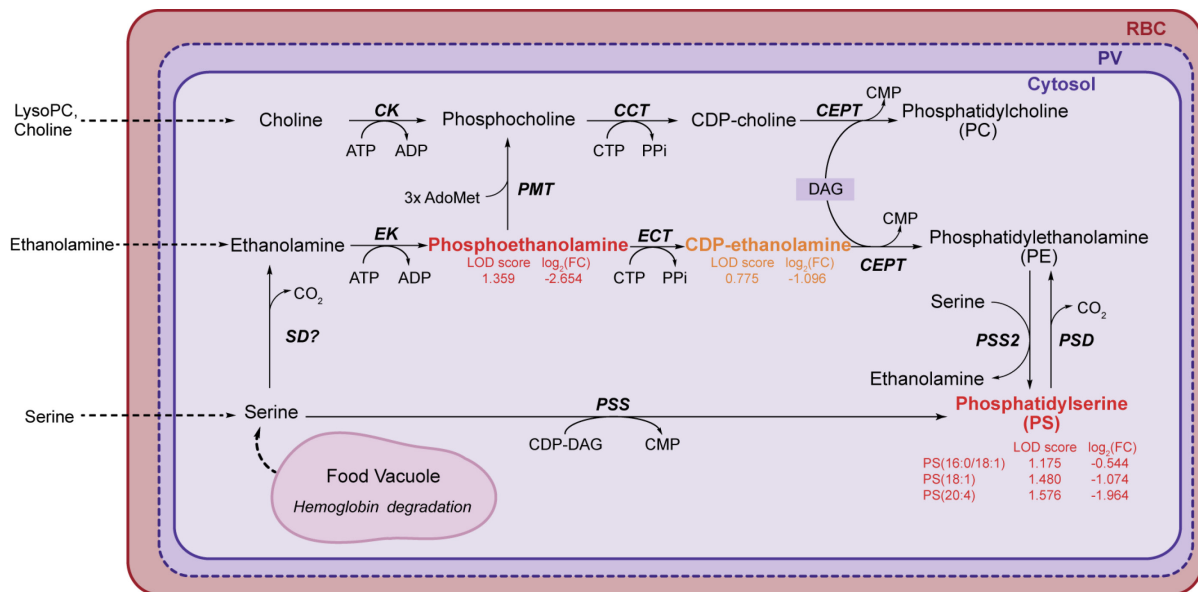


Figure 3-8. Fragment of the glycerophospholipids biosynthesis pathway of *P. falciparum* affected by SC83288. Metabolites with altered levels are shown in red (significantly reduced) or orange (reduced but not over the threshold of significance). The details under or next to the names refer to the LOD score and log₂(fold change) from the treated versus untreated *P. falciparum* 3D7 WT untargeted metabolomics study. LysoPC and choline can be incorporated into the biosynthesis of PC lipids from the iRBC or host serum, as well as ethanolamine and serine. This amino acid can also be obtained from the digestion of hemoglobin in the food vacuole. The question mark next to SD indicates that the enzyme has not been identified yet, although the activity has been observed. Abbreviations: PV, parasitophorous vacuole; CK, choline kinase; CCT, CTP-phosphocholine cytidyltransferase; CEPT, choline/ethanolamine-phosphotransferase; ECT, CTP-phosphoethanolamine cytidyltransferase; EK, ethanolamine kinase; PPI, pyrophosphate; PMT, phosphoethanolamine methyltransferase; SD, serine decarboxylase; PSD, PS decarboxylase; PSS/PSS2 PS synthase; DAG, diacylglycerol; PS (16:0/18:1), 2-Oleoyl-1-palmitoyl-sn-glycero-3-phosphoserine; PS (18:1), 1-O-oleoyl-sn-glycero-3-phosphoserine; PS (20:4), 1-arachidonoyl-sn-glycero-3-phosphoserine. Adapted from the work of Kilian et al. and Wein et al. [154, 155].

Table 3-5. Summary of metabolites disrupted by SC83288. The associated pathways marked in gray correspond to metabolites without an assigned metabolic route. The information gathered in this table, besides the p-value and log₂(FC) derived from the untargeted metabolomics study, was collected through the search for each individual compound on the following databases: PlasmDB [107], KEGG [102], UniProt [112], MetaCyc [103], YMDB [111], and MPMP Project [26]. Abbreviations: MTA, 5'-methylthioadenosine; Etn-P, phosphoethanolamine; AdoMet, S-adenosylmethionine; ACC, 1-aminocyclopropane-1-carboxylic acid; NBD-Cl, 4-chloro-7-nitrobenzofurazan.

Compound	p-value	log ₂ (FC)	Associated pathway	Associated enzymes	Cofactors or dependencies	Localization
ACC	0.011	1.124	Methionine metabolism	1-Aminocyclopropane-1-carboxylate synthase (PF3D7_0205200 inferred by orthology)	Pyridoxal phosphate, AdoMet	Cytosol
3-Methoxytyramine	0.042	-0.270	Tyrosine metabolism, betalain biosynthesis (human and plant metabolite)	catechol O-methyltransferase (human, animals)	The methyl group transferred to dopamine comes from AdoMet	Unknown
NBD-Cl	0.026	-2.305	Not a naturally occurring metabolite	-	-	-
1-Octyl-N-acetyl-α-D-glucosamine	0.026	-4.145	Cell-surface glycoconjugate-linked phosphocholine or phosphonate biosynthesis (in bacteria)	Unknown (2.7.1 Phosphotransferases with an alcohol group as acceptor)	Unknown	Unknown
N-hydroxyvaline	0.005	1.898	Valine metabolism, linamarin biosynthesis	Valine N-monooxygenase (Cyt P450, not identified)	NADPH	Unknown
Etn-P	0.025	-2.654	Synthesis of phosphatidylcholine and phosphatidylserine lipids	Ethanolamine kinase, phosphoethanolamine methyltransferase, phosphoethanolamine cytidyltransferase	ATP, AdoMet, CTP	ER, Golgi
MTA	0.003	1.770	Methionine recycling, purine salvage pathway, polyamine synthesis	1-Aminocyclopropane-1-carboxylate synthase (PF3D7_0205200 inferred by orthology), MTA phosphorylase, MTR kinase, MTA nucleosidase	Pyridoxal phosphate, AdoMet	Cytosol
PS(20:4)	0.015	-1.964	Glycerophospholipids metabolism	choline/ethanolamine-phosphotransferase, phosphatidylserine synthase	-	Cytosol (yeast)
PS(18:1)	0.019	-1.074	Glycerophospholipids metabolism	choline/ethanolamine-phosphotransferase, phosphatidylserine synthase	-	ER, mitochondria (yeast)
9-Oxononanoic acid	0.048	-0.647	alpha-Linolenic acid metabolism	Hydroperoxide lyase	-	Mitochondria
PS (16:0/18:1)	0.039	-0.544	Glycerophospholipids metabolism	choline/ethanolamine-phosphotransferase, phosphatidylserine synthase	-	Membranes
Adenine	0.008	1.610	Purine salvage pathway, methionine recycling	MTA nucleosidase, MTA phosphorylase, purine nucleoside phosphorylase	-	Cytosol
Ile-Phe-Thr-Pro	0.003	0.231	Peptides	-	-	-
Asp-Pro-Ser	0.032	1.363	Peptides	-	-	-
Arg-Asp-Gln-Ser	0.011	2.302	Peptides	-	-	-

3.4 SC83288 does not interact with DNA molecules through binding

In the light of previous results showing that early treated (ring-stages) parasites do not undergo DNA replication [81], I speculated that the mode of action of SC83288 could involve DNA binding. Furthermore, it could be argued that the drug structure resembles that of other molecules with DNA-binding properties, such as diamidines [156]. Therefore, I tested this possibility using two independent experiments. For the first, a trichloroacetic acid (TCA) precipitation assay was carried out, where DNA was incubated with radiolabelled drug (^3H -SC83288) prior to precipitation and filtration. Thus, if there was binding the compound would co-precipitate with the DNA. After the measurement of total counts in the solids and filters, I observed that a minimal proportion of compound had bound (Figure 3-9, A). Across a concentration range from 0 to 5 μg of either salmon sperm or *P. falciparum* DNA, the bound compound fraction stayed at a low binding level, with a maximum of 0.034 ± 0.006 and 0.018 ± 0.001 at 5 μg of the corresponding DNA. These low levels of binding can be attributed to non-specific interactions and to the occlusion of drug molecules within the precipitate. For comparison, in a fluorescence measurement using the same DNA concentration range, the bound fraction of known DNA binding dyes as TP3 (an intercalator [157]) and DAPI (minor groove binder and intercalator [158, 159]) increased up to 0.764 ± 0.002 and 0.81 ± 0.01 , respectively, at 5 μg DNA (Figure 3-9, A). The compound concentrations were 0.5 μM for SC83288 and 1 μM for the binding dyes.

In a second approach, and as part of Anne Lorenz BSc thesis, we carried out a fluorescence quenching-based assay following the work of Williams *et al.* [127]. We used the aforementioned DNA binding dyes DAPI and TP3 (see structures in Figure 3-9, B), and as a first step we characterized them in order to compare their binding parameters with those reported and ensure a correct experimental setup. The binding parameters were obtained as described in Section 2.2.4.4 (Figure 3-9, C-D) and, although they deviate from those reported [127], they remain in an acceptable range. The number of base pairs per bound molecule of dye (N) measured was to 19.3 ± 0.5 for DAPI and 19.1 ± 0.5 for TP3, while the dye-DNA binding constant (K_b) equalled $3.9 \pm 0.1 \mu\text{M}^{-1}$ for DAPI and $3.01 \pm 0.08 \mu\text{M}^{-1}$ for TP3. Fluorescence quenching measurements were then carried out by sequential addition of SC83288 aliquots to a dye solution (Figure 3-9, E) covering a nanomolar and a micromolar range. In the nanomolar range, the addition of the drug had no effect over TP3 fluorescence while it had a booster effect for DAPI, whose relative signal intensity increased. The reason behind this effect remains elusive. In the micromolar range, a small decrease in fluorescence for DAPI and a more marked decrease trend for TP3 can

be observed. This is, however, not comparable with the effects observed by Williams *et al.* with DNA binding drugs that compete with the dyes and could be attributed to other quenching mechanisms besides competition. Moreover, the concentration span in which this quenching effects are observed exceed the relevant antimalarial activity range, which is at low nanomolar concentrations. Together, the results from both experiments show that SC83288 lacks relevant DNA binding properties.

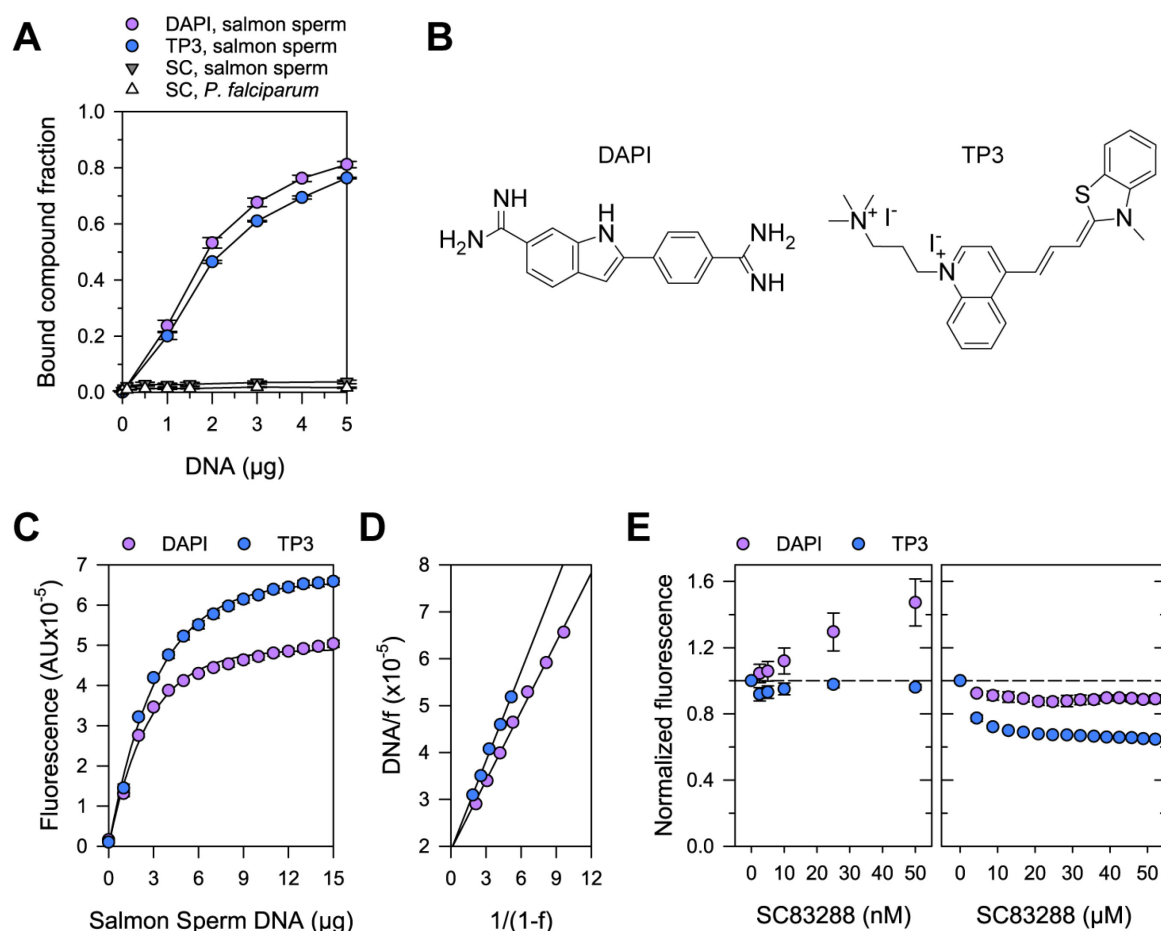


Figure 3-9. SC83288 does not display DNA binding properties. (A) Fraction of SC83288 bound to DNA is derived from the TCA DNA precipitation assay with radiolabelled drug and is calculated in relationship to total counts added to the sample. Fraction of DAPI and TP3 bound to DNA (f) is derived from fluorescence measurements and is calculated from: $f = (F_{corr} - F_D) / (F_{max,corr} - F_D)$, where F_{corr} is the measured fluorescence value at the given DNA amount corrected for sample dilution, F_D is the fluorescence of the free dye and $F_{max,corr}$ is the corrected maximum fluorescence measured when saturation has been reached. Mean \pm SEM of three independent replicates. (B) Structures of DAPI and TP3. (C) Fluorescence of a 1 μ M dye solution upon addition of salmon sperm DNA. (D) Scatchard plot, from which the dye-DNA binding constant (K_b) and the number of base pairs per molecule of dye (N) can be obtained (see Section 2.2.4.4). The fraction of dye bound to DNA (f) is calculated as described in (A). Measured N value was to 19.3 ± 0.5 for DAPI and 19.1 ± 0.5 for TP3, while K_b was $3.9 \pm 0.1 \mu\text{M}^{-1}$ for DAPI and $3.01 \pm 0.08 \mu\text{M}^{-1}$ for TP3 (mean \pm SEM of three independent replicates). (E) Relative fluorescence of a 1 μ M dye and 4 μ g salmon sperm DNA solution upon addition of SC83288 in the nanomolar (left) or micromolar (right) range of concentration. The dashed line corresponds to the fluorescence level of the dye-DNA solution prior to drug addition, to which the signal is then relativized. Experiments carried out jointly with Anne Lorenz.

3.5 Intracellular localization strategies

Taking into consideration results from Dr. Cecilia Sanchez regarding the uptake and accumulation of SC83288 in *P. falciparum* cells (unpublished data), understanding the fate of the compound inside the parasites became a central part of the project. After one hour of incubation with [³H]-SC83288, the concentration of the drug inside the infected red blood cells is almost 100-fold higher than in the medium. Since the SC-compound antimalarial properties are highly sensitive to structural modifications (see SAR study reported by Pegoraro *et al.* [78]), a label-free approach was carried out as presented in the next sections.

3.5.1 SC83288 does not possess relevant fluorescent properties

As a first step, I evaluated the possibility of tracking SC83288 inside parasite cells directly. Therefore, I studied the fluorescent properties of the molecule through the acquisition of absorbance and emission spectra (Figure 3-10). The UV-Vis absorption spectrum of SC83288 presented a peak that located depending on the solvent at 275 nm or 278 nm, for PBS and DMSO. These parameters were used as excitation wavelengths for the record of the emission spectra of the solutions. The fluorescent signal observed was negligible and even when a small peak could be observed for the DMSO solution, this is not an environment that could be reproduced in the context of cell-based experiments due to the toxicity of the solvent. The physiological environment is better represented by the PBS solution, where fluorescence was practically null. Therefore, it was necessary to bind a probe, such as a fluorophore tag, in order to detect SC83288.

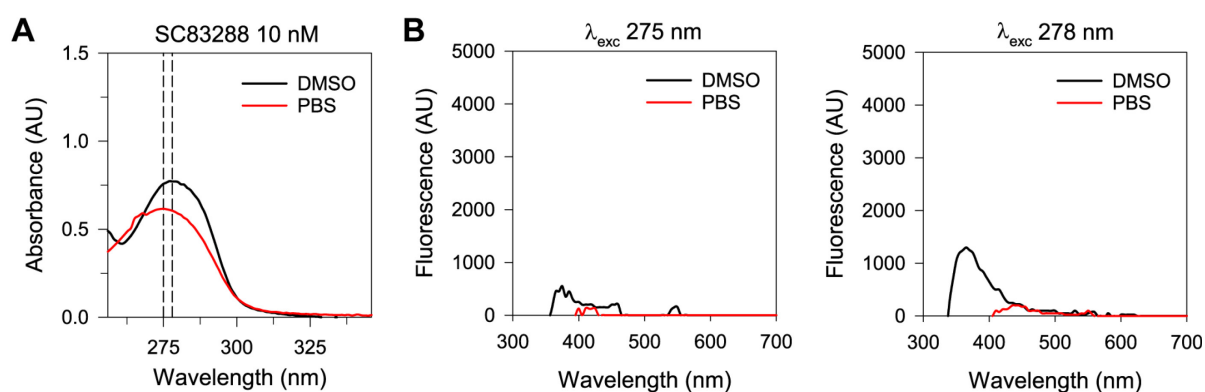


Figure 3-10. SC83288 does not possess relevant fluorescent properties. (A) Absorption spectrum of a 10 nM SC83288 solution in DMSO (black) or PBS (red). Peaks are observed at 278 and 275 nm, respectively. The spectrum was acquired using a UVIKON 923 spectrophotometer (Kontron Instruments). (B) Emission spectra of a 10 nM SC83288 solution in DMSO (black) or PBS (red), using 275 (right) or 278 nm (left) as excitation wavelengths. The spectra were acquired using a Cytation3 plate reader (BioTEK).

3.5.2 Click chemistry-based approach gives clues about resistance mechanism

After ruling out the possibility of using a direct detection method for the intracellular localization of SC83288, a click chemistry-based approach was followed. In general, I refer here with the terms “click reaction” or “click chemistry” to a copper-catalysed azide-alkyne cycloaddition (CuAAC), where the coupling of an azide and a terminal alkyne gives rise to a triazole conjugate [160, 161]. For making use of this tool, it is necessary to introduce structural modifications to the drug, although incorporating a terminal alkyne group has a milder effect than the addition of a fluorescent probe. At the same time this alkyne-tagged drug derivative has higher versatility, given that it could be coupled to azide-tagged probes beyond fluorophores such as gold nanoparticles for electron microscopy (Figure 3-11). Furthermore, it can also be used for target deconvolution through the so-called target fishing with an activity-based protein profiling strategy (enrichment of bound proteins with biotin-azide and posterior identification using mass spectrometry) [162].

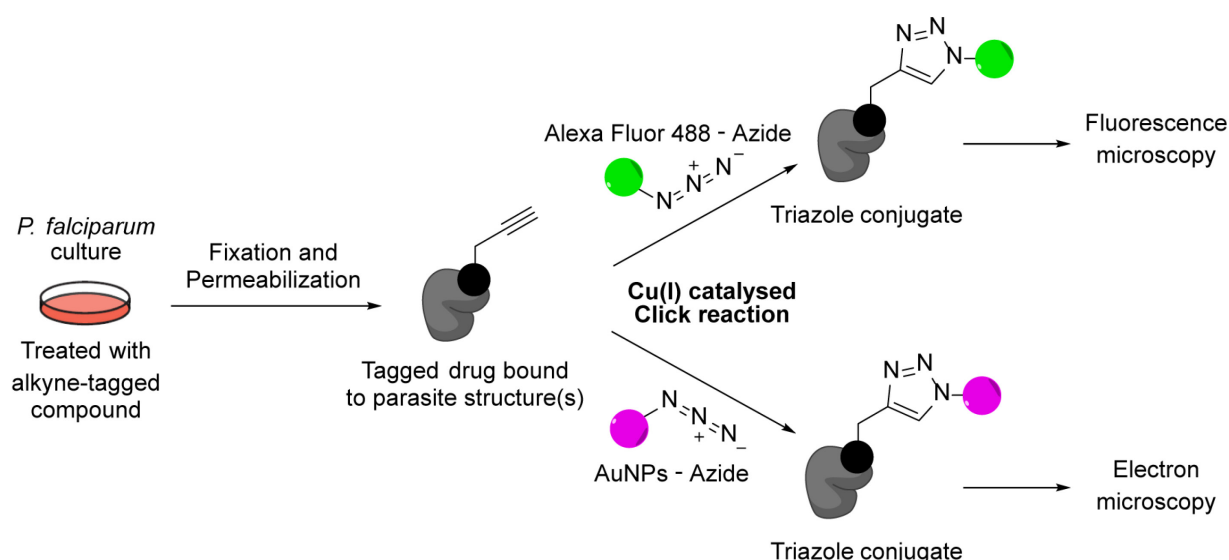


Figure 3-11. Scheme of intracellular localization strategies based on copper-catalysed click reactions. For this approach, a parasite culture is treated with an alkyne-tagged compound. It is worth noting that the alkyne group must be terminal. After fixation and permeabilization of infected red blood cells, the tagged drug is bound to parasite structures at its accumulation site(s). In a subsequent step, the free alkyne can be coupled to an azide-tagged probe, such as the fluorophore Alexa Fluor 488-azide (top, green) for the imaging of the resulting triazole conjugate and its location within cells using fluorescence microscopy. Alternatively, the coupling can be carried out using azide-tagged gold nanoparticles (bottom, magenta) for the visualization using electron microscopy.

An alkyne-tagged derivative of SC83288, named SC106879 (Figure 3-12, A) was synthesized by Dr. Stephanie Fehler (4SC AG). Although it possesses a lower antimalarial activity than SC83288 (74 ± 9 nM, see Figure 3-12, B), I considered that for my purposes they remained comparable.

Moreover, parasites resistant to SC83288 clearly showed no susceptibility to SC106879 in concentrations of up to 1 μM . However, the results of these *in vitro* growth inhibition assays had a high variability and inconsistencies, and therefore are not reported here.

I followed the fluorescence microscopy strategy showed in Figure 3-11 (top). Through several rounds of optimization I encountered difficulties of two types: first, either the fixed and permeabilized cells had membrane perturbations or they were clumping in a way such that imaging of individual infected red blood cells was not possible. After overcoming this issue, the fluorescent signal was low and inconsistent, an obstacle for correct intracellular localization of the compound. This inconsistency can be understood as a consequence of a reduced or absent availability of the alkyne group for the coupling reaction. Such effect may be due to the fixation procedure, the drug being buried inside the target protein(s) structure(s), or a combination of both.

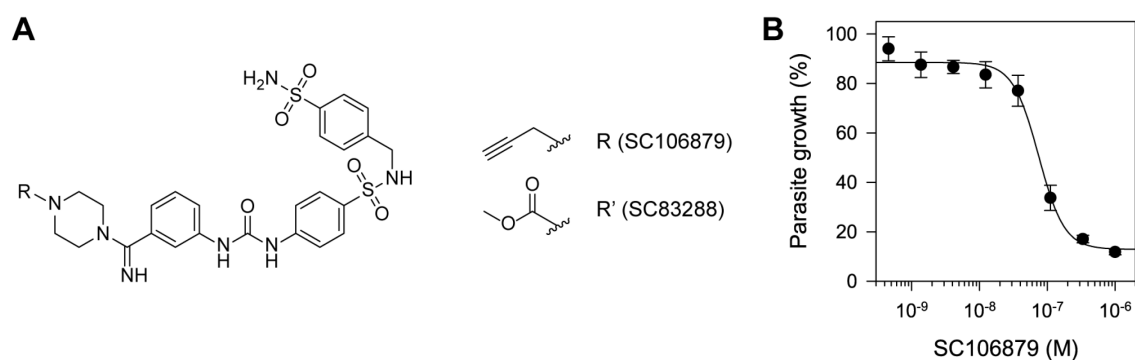


Figure 3-12. SC106879 constitutes a versatile tool for studies on SC83288. (A) Structures of SC83288 and SC106879. They only differ in the R substituent group shown, a propargyl for SC106879 and a methyl ester for SC83288. (B) Results from an *in vitro* growth inhibition assay of *P. falciparum* 3D7 WT parasites treated with SC106879, with an IC_{50} value of 74 ± 9 nM. Mean \pm SEM of five independent replicates.

Further optimisation was carried out by Dr. Cecilia Sanchez, who confirmed that in 3D7 WT *P. falciparum* cells, SC106879 cannot be localized. Interestingly, in 3D7 PfATP6^{F972Y} parasites which are resistant to SC83288 (and presumably to SC106879, as explained before), the fluorescent signal is accumulated in clearly defined cellular compartments or organelles (unpublished data). At the moment of writing this dissertation, said compartments were not yet identified (e.g., using the electron microscopy strategy or by using a co-staining), although it is highly likely that they correspond to the ER lumen.

3.6 SC83288 does not cause a swollen appearance of parasite cells

During the optimization of the protocol for the click chemistry-aided intracellular localization, I noticed that the parasite cells appeared seemingly bigger or swollen after the experiment. A swollen phenotype has been described as an effect of drugs associated with PfATP4 [163], which is a putative Na⁺/H⁺-ATPase located in the parasite plasma membrane, implicated in the regulation of parasite sodium levels [164]. Such swelling can be explained as a consequence of PfATP4 inhibition, which leads to an increase in the cytosolic pH and sodium ions concentration that produces an osmotic imbalance compensated by water incorporation. This, in turn, leads to an increase in cell volume and a swollen appearance. This swelling effect is sodium-dependent and therefore, is not seen when parasites are incubated in sodium-free environments (such as NMDG saline, where sodium is replaced with N-methyl-D-glucamine) [163].

In order to find if the cause of the observations was a true phenotype caused by the drug or an artifact related to the cell fixation process or the click reaction, I carried out a swelling assay as described in Section 2.2.10 (Figure 3-13). Briefly, trophozoite-stages 3D7 WT and PfATP6^{F972Y} *P. falciparum* cultures were incubated in three different media which either contained or not sodium and treated with SC83288 in a range of concentrations from 0 to 15 μM. Microscope slides were imaged before treatment and at three timepoints (15, 30 and 60 minutes). The area of parasite cells was measured and, after normalization to cell size before treatment, compared over time for each drug treatment. The results show, in general, no significant effect of the drug over the course of one hour except in the case of the treatment of the wild-type strain with 15 μM SC83288 in carbonate-free RPMI 1640 medium (P=0.003, Kruskal-Wallis one way ANOVA on ranks). However, this is an extremely high drug concentration. The effect was not seen in the activity-relevant concentration range, nor in the samples treated in physiological saline where I expected the same behaviour due to their analogous sodium levels. As expected, there was no response from the SC-resistant parasites. It is worth mentioning that the original drug concentration that I used for the click chemistry-aided intracellular localization experiment was 10 μM and the parasites were incubated in carbonate-free RPMI 1640 medium, therefore the swelling appearance could have been an artifact or a side effect of the extreme drug quantities. This experiment was carried out with the collaboration of Anne Lorenz and Maren Gehringer, and partial results were part of their BSc theses.

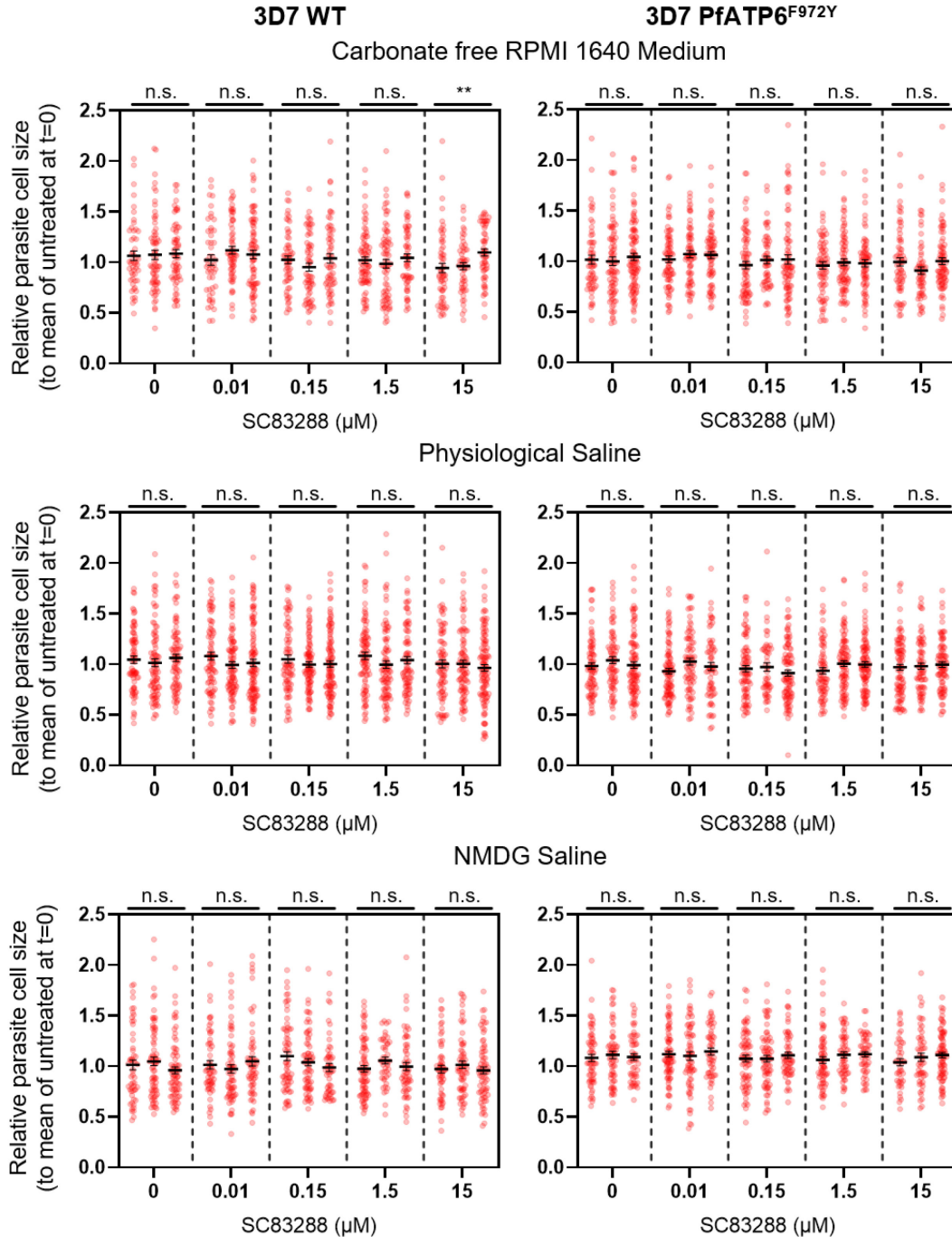


Figure 3-13. SC83288 does not cause a swelling of parasite cells. Swelling assay (see Section 2.2.10) results presented as mean \pm SEM of parasite cell size relative to the mean size of untreated parasite cells before treatment. Individual cell sizes are displayed as red circles. The assay was performed using 3D7 WT (left) and PfATP6^{F972Y} (right) *P. falciparum* cultures incubated in two sodium-containing solutions (RPMI 1640 carbonate free medium and physiological saline, top and middle respectively) and one sodium-free solution (NMDG saline, bottom). Cells were treated with concentrations of SC83288 in the range from 0 to 15 μ M at 37 $^{\circ}$ C and size was measured after 15, 30 and 60 minutes (shown from left to right for each drug treatment). When comparing differences in cell size over time for each drug treatment using a Kruskal-Wallis test (or one way ANOVA, depending on data distribution), the only significant effect is seen for the 3D7 WT strain treated with 15 μ M SC83288, only on carbonate free RPMI 1640 ($P=0.003$, Kruskal-Wallis one way ANOVA on ranks). Where normal distribution (Shapiro-Wilk) test was passed, one way ANOVA was used. Data corresponds to the results of three independent replicates, and the total number of cells measured per incubation medium (for each strain) ranges between 1 036 and 1 426. Some of the results were acquired and partially analysed by Anne Lorenz and Maren Gehringer.

3.7 Untargeted metabolomics analysis of SC83288 resistant parasites

An untargeted metabolomics study was performed with samples from resistant parasites in the same fashion presented earlier for the sensitive 3D7 wild-type strain. As expected, the metabolism of 3D7 PfATP6^{F972Y} parasites did not show alterations as a consequence of treatment with SC83288 (Figure 3-14, Table 3-6). Interestingly, when comparing untreated 3D7 PfATP6^{F972Y} samples with their wild-type counterpart, alterations on a pathway level are not evident (Figure 3-15, A, Table 3-6, Table 3-7), although lower basal levels of orotate and guanine (Figure 3-15, B-C, Table 3-8) can be observed. Other metabolites present alterations, although with a less pronounced fold change, such as indole-3-acetate, uracil, L-isoglutamine, N-carbamoyl-L-aspartate, N-3-oxo-hexanoyl-homoserine lactone, octanoic acid, citronellyl acetate, suberic acid and PS(16:0/18:2). Notably, as the resistance mechanism seems to not be associated with the mode of action of SC83288 [81], the metabolic changes may not be related with the lower susceptibility of parasites to the drug but rather compensate the functional changes associated with the mutation F972Y in PfATP6. The reason behind the lower flow of metabolites through the synthesis of nucleotides, manifested as lower basal levels of orotate and guanine, is unclear but an approach to evaluate its role as a potential advantage against antifolates is described in the next section.

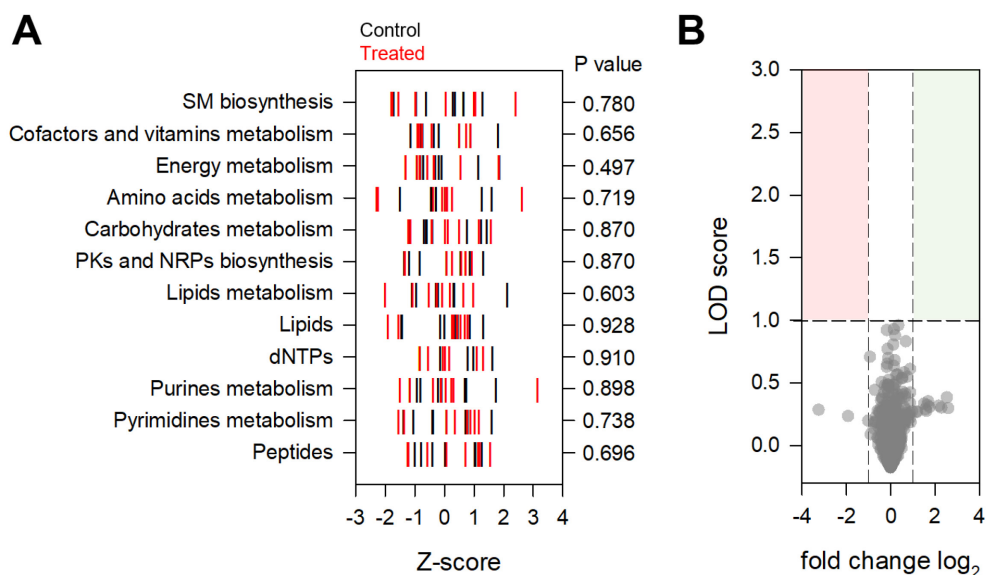


Figure 3-14. The metabolic profile of *P. falciparum* 3D7 PfATP6^{F972Y} parasites is not altered by treatment with SC83288. (A) Z-scores for compound categories in control (black) or samples treated (red) with 40 nM SC83288 for 12 hours from ring to trophozoite stages. Obtention of Z-scores from four to eight independent replicates is explained in Section 2.2.7, each vertical line corresponds to a replicate. P values shown are the result of a homoscedastic two-tailed t-test. **(B)** Volcano plot, where individual metabolites are represented in accordance with the log₂ of their fold change between control and treated samples and their LOD score, as described in Section 2.2.7. The compounds that are statistically significant altered by the drug treatment (LOD score > 1, fold change log₂ < -1 or > 1) will locate in the top right and left, i.e., red for lower concentration and green for accumulation. Abbreviations: SM, secondary metabolites; PKs, polyketides; NRPs, non-ribosomal peptides; dNTPs, deoxynucleotides triphosphate.

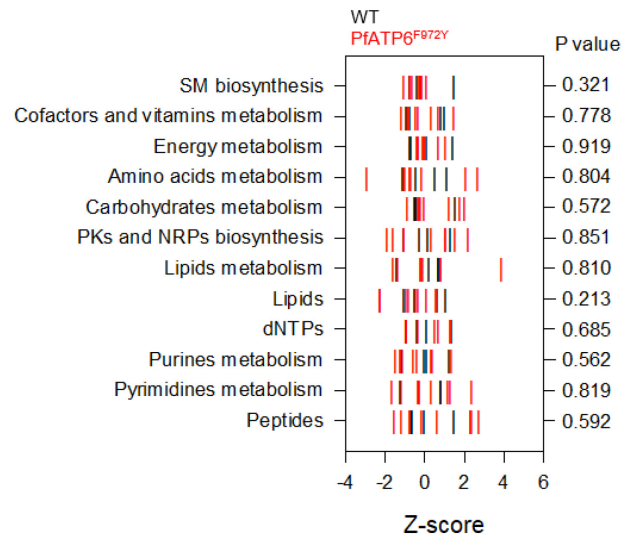
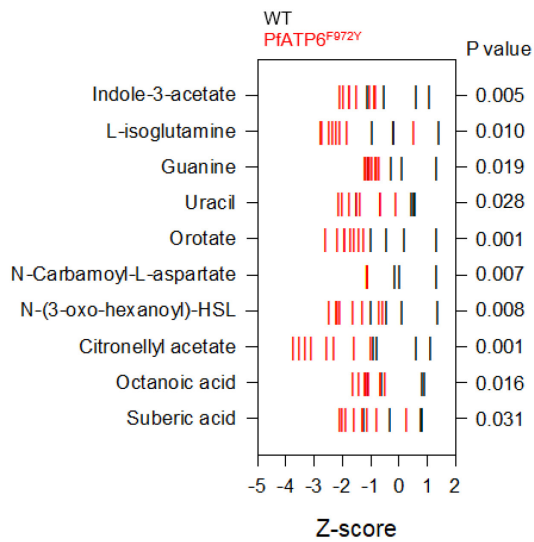
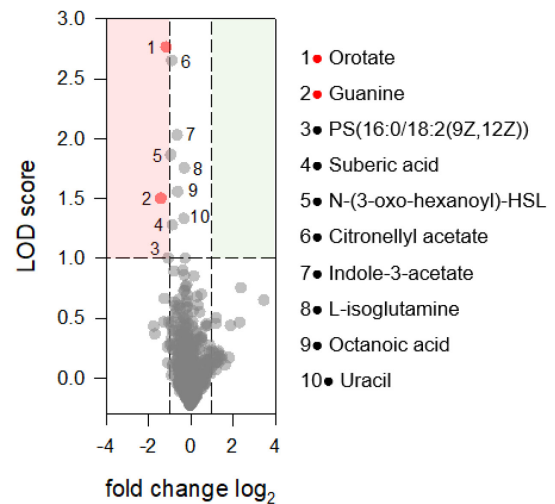
A**B****C**

Figure 3-15. Comparison of the metabolic profile of *P. falciparum* 3D7 WT versus PfATP6^{F972Y} parasites. (A) Z-scores for compound categories in WT (black) or PfATP6^{F972Y} (red) samples, both untreated. Obtention of Z-scores from four to eight independent replicates is explained in Section 2.2.7, each vertical line corresponds to a replicate. P values shown are the result of a homoscedastic two-tailed t-test. (B) Z-scores for individual metabolites that display a statistically significant difference (P value < 0.05, homoscedastic two-tailed t-test) between levels in samples as mentioned in (A). (C) Volcano plot comparing untreated WT and PfATP6^{F972Y} samples, where individual metabolites are represented in accordance with the log₂ of their fold change between control and treated samples and their LOD score as described in Section 2.2.7. The compounds that are statistically significant altered by the drug treatment (LOD score > 1, fold change log₂ < -1 or >1) will locate in the top right and left, i.e., red for lower concentration and green for accumulation. PfATP6^{F972Y} parasites have lower levels of orotate and guanine. Abbreviations: SM, secondary metabolites; PKs, polyketides; NRPs, non-ribosomal peptides; dNTPs, deoxynucleotides triphosphate; N-(3-oxo-hexanoyl)-HSL, N-(3-oxo-hexanoyl)-homoserine lactone; PS(16:0/18:2(9Z,12Z)), 1-hexadecanoyl-2-(9Z,12Z-octadecadienoyl)-glycero-3-phosphoserine.

Table 3-6. Z-scores and P-values of compound categories from the analysis of 3D7 PfATP6^{F972Y} samples treated with SC83288 versus control samples. Abbreviations: MB, metabolism; dNTPs, deoxyribonucleosides triphosphate; PKs, polyketides; NRPs, non-ribosomal peptides; BS, biosynthesis; SM, secondary metabolites.

Compound Category	Z-score																P value
	3D7 PfATP6 ^{F972Y} Control								3D7 PfATP6 ^{F972Y} Treated								
	r1	r2	r3	r4	r5	r6	r7	r8	r1	r2	r3	r4	r5	r6	r7	r8	
Peptides	1.278	-1.208	1.047	-0.396	1.023	-1.005	-0.772	0.032	1.562	-1.207	0.719	0.065	1.200	-1.230	1.149	-0.570	0.696
Lipids	0.356	-1.454	1.327	0.003	0.459	-0.131	-1.423	0.863	0.439	-1.550	0.704	0.556	0.265	-1.906	0.794	0.320	0.928
Lipids MB	-0.948	-0.215	-0.252	0.319	-1.092	0.336	-0.271	1.214	-1.999	-0.518	-0.259	0.197	-1.067	0.650	-0.070	0.987	0.603
Purines MB	0.705	-1.166	1.737	-0.086	0.756	-0.216	-0.921	-0.808	0.234	-1.153	-0.364	-0.115	0.307	-1.492	0.054	3.164	0.898
Pyrimidines MB	0.712	-1.380	1.605	-0.400	0.795	-1.039	0.073	-0.366	1.182	-1.545	0.074	0.362	0.893	-1.359	1.030	0.772	0.738
dNTPs	0.989	-0.819	0.793	-0.819	1.640	-0.819	-0.819	-0.145	1.325	-0.819	0.033	0.171	1.101	-0.819	-0.030	-0.540	0.910
Amino acids MB	-0.420	-1.497	1.614	-0.277	0.042	1.270	-0.273	-0.458	0.033	-2.296	0.264	0.103	-0.056	-2.232	2.641	-0.379	0.719
Carbohydrates MB	1.254	-1.164	0.769	-0.623	1.449	-0.697	-0.597	-0.391	1.576	-1.197	-0.424	0.124	1.176	-1.128	0.039	0.502	0.870
PKs and NRPs BS	0.555	-1.352	1.311	0.079	0.863	-1.184	-0.827	0.555	0.937	-1.320	0.268	0.715	0.724	-1.333	0.579	0.071	0.870
Energy MB	-0.299	-0.084	1.158	-0.721	-0.188	1.869	-0.799	-0.936	-0.924	-0.355	1.838	-1.302	-0.566	-0.834	0.556	-1.305	0.497
SM BS	1.305	-1.714	0.656	0.656	-0.624	0.290	0.373	-0.942	2.425	-1.778	1.065	-0.969	0.060	-1.768	1.003	-1.539	0.780
Cofactors and vitamins MB	0.505	-0.340	-0.193	-0.794	0.891	1.818	-0.740	-1.147	0.892	-0.754	-0.423	-0.892	0.757	-0.851	0.498	-0.862	0.656

Table 3-7. Z-scores and P-values of compound categories from the analysis of 3D7 PfATP6^{F972Y} samples versus 3D7 WT samples. Both samples correspond to untreated parasites. Abbreviations: MB, metabolism; dNTPs, deoxyribonucleosides triphosphate; PKs, polyketides; NRPs, non-ribosomal peptides; BS, biosynthesis; SM, secondary metabolites.

Compound Category	Z-score												P value
	3D7 WT Control				3D7 PfATP6 ^{F972Y} Control								
	r1	r2	r3	r4	r1	r2	r3	r4	r5	r6	r7	r8	
Peptides	1.439	-0.664	-0.695	-0.080	2.720	-1.555	2.322	-0.159	2.281	-1.207	-0.806	0.576	0.592
Lipids	0.613	1.050	-1.097	-0.565	-0.464	-2.312	0.527	-0.824	-0.358	-0.961	-2.280	0.054	0.213
Lipids MB	-1.459	0.633	0.158	0.667	-1.388	-0.136	-0.198	0.776	-1.634	0.806	-0.232	3.860	0.810
Purines MB	1.232	0.033	-1.216	-0.048	0.332	-1.516	1.351	-0.449	0.382	-0.577	-1.274	-1.162	0.562
Pyrimidines MB	0.777	-1.288	0.807	-0.295	1.145	-1.688	2.354	-0.361	1.258	-1.226	0.279	-0.315	0.819
dNTPs	1.352	0.073	-0.988	-0.437	0.662	-0.988	0.483	-0.988	1.255	-0.988	-0.988	-0.372	0.685
Amino acids MB	0.508	1.106	-0.477	-1.137	-1.008	-2.949	2.661	-0.749	-0.175	2.040	-0.742	-1.076	0.804
Carbohydrates MB	1.500	-0.530	-0.496	-0.474	1.746	-0.887	1.218	-0.297	1.958	-0.378	-0.269	-0.045	0.572
PKs and NRPs BS	1.290	-0.296	-1.111	0.117	1.010	-1.896	2.162	0.284	1.479	-1.640	-1.097	1.010	0.851
Energy MB	0.089	1.382	-0.720	-0.751	-0.110	0.001	0.644	-0.329	-0.053	1.013	-0.369	-0.441	0.919
SM BS	-0.442	1.467	-0.766	-0.258	0.090	-1.055	-0.156	-0.156	-0.641	-0.295	-0.263	-0.762	0.321
Cofactors and vitamins MB	0.759	0.964	-0.788	-0.934	0.287	-0.469	-0.337	-0.875	0.633	1.462	-0.827	-1.191	0.778

Table 3-8. Z-scores and P-values of individual metabolites from the analysis of 3D7 PfATP6^{F972Y} samples versus 3D7 WT samples. The metabolites displayed on the table correspond to those exhibiting a P-value lower than 0.05. Abbreviation: N-(3-oxo-hexanoyl)-HSL, N-(3-oxo-hexanoyl)-homoserine lactone.

Putative metabolite	Z-score												P value
	3D7 WT Control				3D7 PfATP6 ^{F972Y} Control								
	r1	r2	r3	r4	r1	r2	r3	r4	r5	r6	r7	r8	
Suberic acid	0.823	-0.329	0.776	-1.270	-1.302	-2.008	0.274	-1.886	-1.611	-2.091	-0.782	-1.118	0.031
Octanoic acid	0.893	-0.609	0.804	-1.088	-1.087	-1.176	-0.667	-1.407	-0.505	-1.646	-1.227	-1.155	0.016
Citronellyl acetate	1.092	-0.779	0.603	-0.916	-2.297	-1.584	-2.556	-3.552	-1.020	-3.763	-3.310	-3.126	0.001
N-(3-oxo-hexanoyl)-HSL	0.070	-0.989	-0.434	1.353	-2.494	-1.291	-2.081	-1.648	-2.164	-0.707	-0.572	-2.235	0.008
N-Carbamoyl-L-aspartate	1.294	-1.138	0.019	-0.175	-1.138	-1.138	-1.138	-1.138	-1.138	-1.138	-1.138	-1.138	0.007
Orotate	-0.470	-1.016	1.310	0.176	-1.612	-1.934	-1.710	-1.413	-1.936	-2.200	-2.598	-1.276	0.001
Uracil	0.492	0.577	0.428	-1.497	-0.676	-0.671	-1.498	-2.158	-1.782	-0.130	-2.003	-1.385	0.028
Guanine	1.301	-0.296	-1.101	0.096	-0.706	-1.176	-0.800	-0.958	-0.823	-1.107	-1.228	-1.035	0.019
L-isoglutamine	-0.205	-0.981	-0.211	1.397	-2.238	0.499	-1.853	-2.714	-2.778	-2.349	-2.099	-2.485	0.010
Indole-3-acetate	-0.528	1.065	0.581	-1.118	-0.830	-1.516	-1.744	-1.053	-1.770	-2.088	-0.887	-1.986	0.006

3.8 Lower orotate basal levels do not constitute a coping mechanism against antifolates

As presented in the previous section, untargeted metabolomics data revealed that untreated resistant parasites have lower basal levels of orotate and guanine than the WT counterpart. The consequent lower flow of carbon downstream of orotate results in more methylenetetrahydrofolate (CH₂-THF) available for other metabolic routes (Figure 3-16, A). This could constitute a coping mechanism that would confer some degree of resistance to antifolates, and in turn contribute to SC83288 resistance, since they have shown to interact in an antagonistic manner and their modes of action can be therefore related in some way.

In order to test if this lower amount of orotate represents an advantage against antifolates in general, I measured the sensitivity of the strain to the antifolate WR99210 (Figure 3-16, B) and compared it with both the known sensitive 3D7 WT strain and a known WR resistant transfectant line. This strain (from here on named 3D7 hDHFR) was generated in the laboratory of Prof. Jude Przyborski and carries a plasmid containing GFP and hDHFR as a selection marker (see Section 2.1.5.5). Meanwhile, the F972Y mutation of the SC-resistant strain 3D7 PfATP6^{F972Y} was introduced using the gene editing tool CRISPR-Cas9, which does not necessarily mean that the parasites carry the *hdhfr* gene. The presence of *hdhfr* in the genomic DNA of the strains used for this experiment was confirmed with PCR (Figure 3-16, C).

As shown in part D of Figure 3-16, if lower orotate levels constituted a coping mechanism against antifolates, a higher IC₅₀ value of WR99210 could be expected from the 3D7 PfATP6^{F972Y} strain than from the 3D7 hDHFR. However, this was not the case, since both strains showed a similar susceptibility level towards the drug, without a statistical difference (P = 1.00, Mann-Whitney rank sum test). Consequently, there is no advantage towards this type of drugs conferred by the lower flow of carbon through the pyrimidine synthesis pathway.

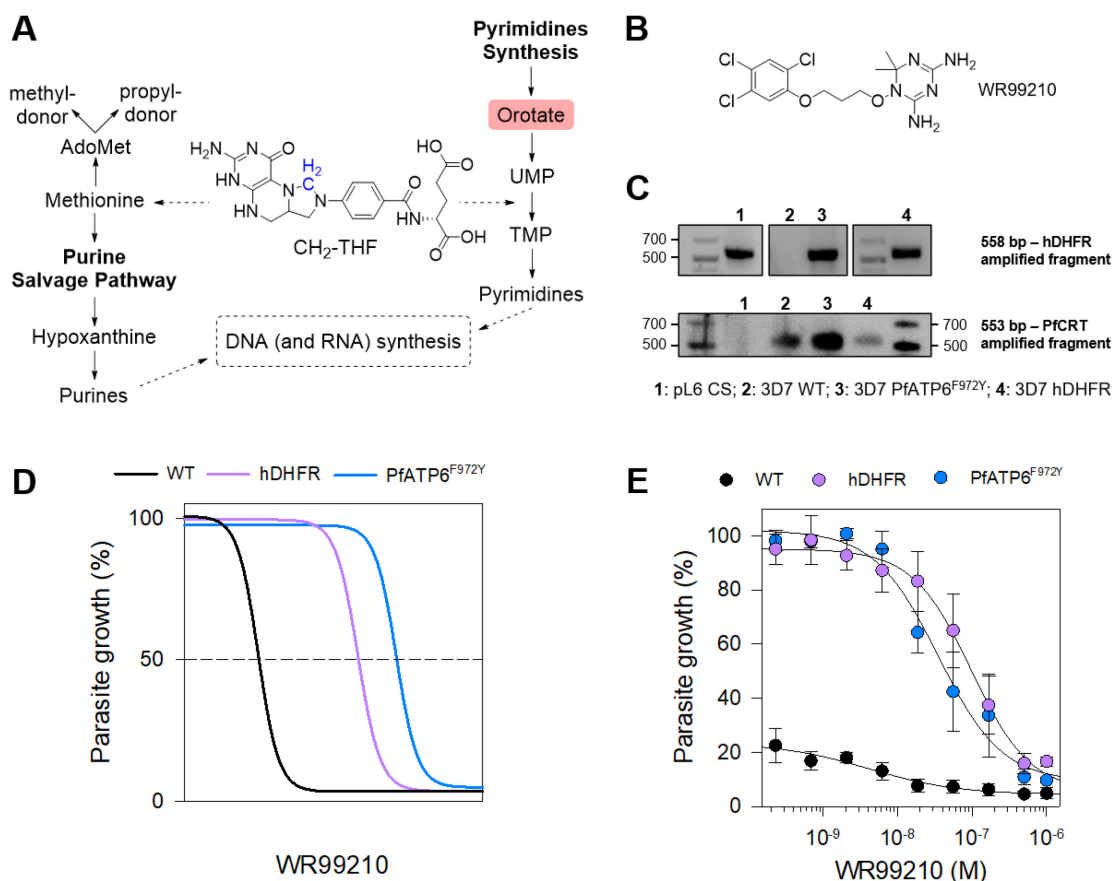


Figure 3-16. Lower orotate in *P. falciparum* 3D7 PfATP6^{F972Y} is not an advantage against antifolates. (A) Fates of methylenetetrahydrofolate in *P. falciparum* cells, based on [27]. (B) Structure of the antifolate WR99210. (C) DNA electrophoresis on agarose gel of samples of a PCR for the amplification of *hdhfr* (top) or *pfcr1* (bottom). Template samples correspond to: 1, pL6 CS (control vector containing *hdhfr*); 2, 3D7 WT genomic DNA; 3, 3D7 PfATP6^{F972Y} genomic DNA; 4, 3D7 parasites carrying a plasmid containing *hdhfr*. While all parasites genomic DNA amplify *pfcr1*, only 3 and 4 are positive for *hdhfr*. (D) Schematic representation of expected results in the case that lower orotate levels constitute an advantage against antifolates. Here, 3D7 PfATP6^{F972Y} parasites (blue) would show a higher IC₅₀ value for WR99210 than 3D7 hDHFR (purple), while WT parasites (black) have of course a much lower value. (E) Susceptibility towards WR99210 of 3D7 WT (black), 3D7 hDHFR (purple) and PfATP6^{F972Y} (blue). There is no significant difference between the last two, P = 1.00, Mann-Whitney rank sum test. Mean ± SEM of four to six independent replicates.

3.9 DBP9 is not a potential target of SC83288

The RNA helicase PF3D7_1241800 was thought to have potential relevance in the mode of action of SC83288. A single mutation was observed in the results of the resistance screening on the position 533, exchanging an aspartic acid for a glutamic acid (D533E) [78]. This residue is located in the middle of a repetitive region between the motifs IV and V. In the light of having a more promising candidate target (the ER Ca²⁺ pump PfATP6) and considering the surrounding residues in the protein sequence, this mutation was deemed irrelevant. However, as later on PfATP6 was found out to be not a molecular target but to play a crucial role in resistance [81], I re-examined PF3D7_1241800 in more depth.

RNA helicases participate in diverse biological processes and are involved in RNA metabolism including transcription, splicing, translation, and ribosome biogenesis [165]. Several families of helicases can be defined based on their sequence. Among them, the “DEAD box” family comprises helicases with nine short, conserved signature motifs (including the DEAD sequence of Asp-Glu-Ala-Asp). These signature fragments are surrounded by sequences that vary in identity but have similar length. However, both terminal regions of these proteins present high diversity in length and sequence. These divergent regions have been linked with the individual protein functions and specificity [166, 167]. Structural studies suggest that the signature motifs are associated with the tertiary structure of the protein and may form a large functional domain [168]. The helicase signature motifs are called Q, I, Ia, Ib, II, III, IV, V and VI (Figure 3-17, A).

In yeast, all helicases are essential and specific. Studies have shown that the absence of a DEAD box protein cannot be replaced by overexpression of another family member [169, 170]. For some viruses, helicases are necessary for proliferation, providing a novel antiviral strategy. Furthermore, several anti-helicase agents have been reported for a range of proteins from different viruses [171-175]. The genome of the apicomplexan parasite *P. falciparum* consists of 14 chromosomes, a linear mitochondrial genome and a circular plastid-like genome [140]. In its sequence, at least 22 full-length putative DEAD box helicases can be found. Helicases have been proposed as potential drug targets against malaria, although extensive validation is still necessary [176-178]. The RNA helicase PF3D7_1241800, also named DBP9 and PFL2010c, is one of the malarial putative DEAD box proteins. It is associated with: (a) several RNA polymerase subunits and other helicases required for transcription; (b) nucleolar GTP-binding proteins, putative GTPases, and BRIX-domain containing proteins for ribosomal biogenesis and maturation; (c) at least three putative U3 snoRNP associated proteins for pre-rRNA processing; (d) a ribosomal subunit export protein for RNA transport; and (e) and eukaryotic initiation factor required for translation. In addition, PF3D7_1241800 is associated with a putative transcription factor (PF3D7_0206600). The correct functioning of the processes linked to DBP9-interacting proteins and DBP9 itself are essential for parasite development [179].

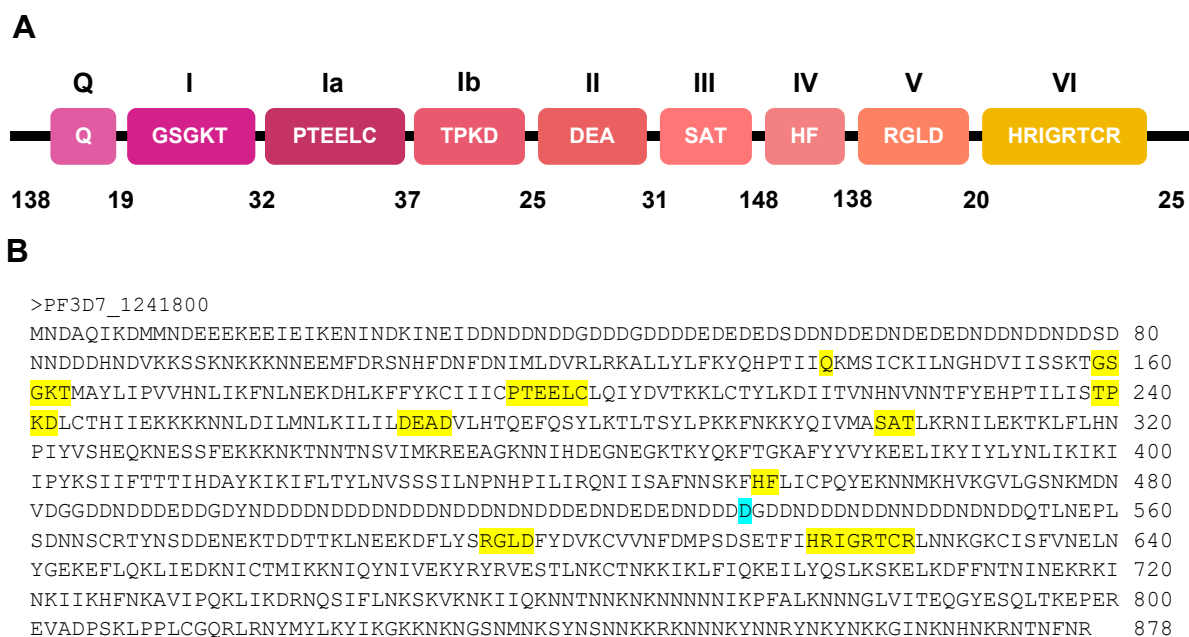


Figure 3-17. Sequence of the malarial RNA helicase PF3D7_1241800. (A) Schematic representation (not to scale), motif sequences are written inside the boxes. The text in black refers to the name of the conserved regions, and the numbers to the residues located between the highlighted fragments as well as the length of N- and C- terminal extensions. (B) Full protein sequence, motif fragments are highlighted in yellow and the mutation D533E present in SC83288-resistant parasites is highlighted in cyan.

If PF3D7_1241800 were a target for SC83288, I would expect the compound binding either to the enzyme active site to inhibit it; or to a protein-protein interaction site, blocking essential associations. As previously mentioned, the mutation observed in the SC-resistant parasites does not seem too relevant: it is surrounded by similar amino acid residues, and it is located away from the helicase functional motifs. However, these fragments between motifs could have a crucial role in supporting the 3D structure and the formation of an active site cavity. To better understand the importance of mutations in this position I analysed the protein structure by means of modelling and prediction methods, using Phyre2 (Protein Homology/analogy Recognition Engine V2.0, Structural Bioinformatics Group, Imperial College, London) [106]. I obtained a structure model for DBP9 and observed through the Phyre Investigation workbench that the sequence fragment around the position 533 is indeed predicted to be disordered. Further analysis using SuSPect (Disease-Susceptibility-based Single Amino acid Variance Phenotype Prediction) shows the predicted phenotypic impact of single amino acid changes in each position [108]. In the case of the position 533 and its surroundings it can be observed that in general all mutations have neutral consequences (Figure 3-18), it is a sequence with low conservation (Jensen-Shannon divergence) predicted to be disordered, as mentioned earlier.

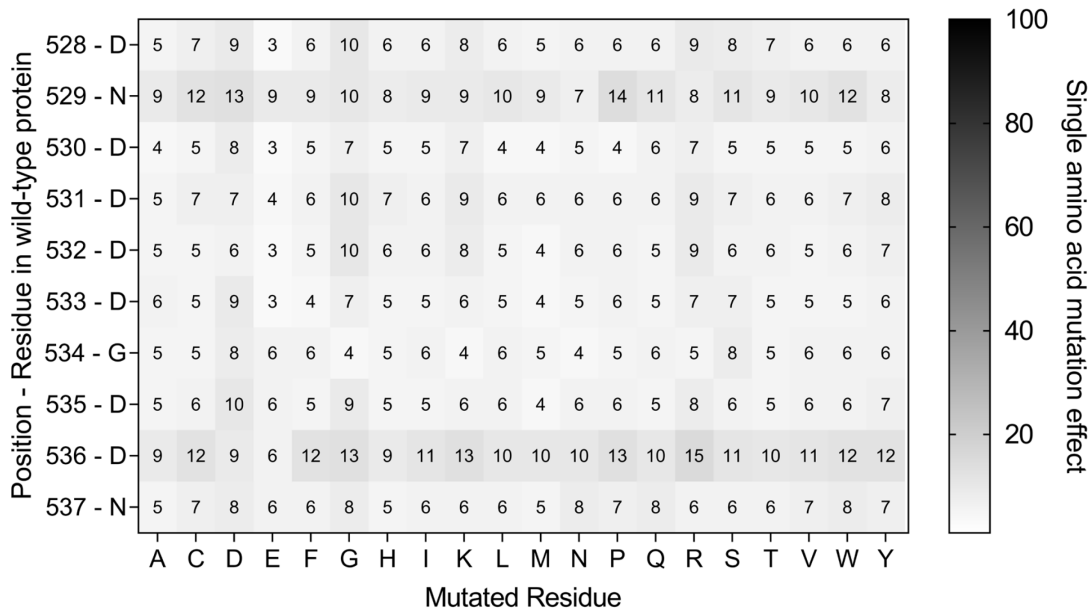


Figure 3-18. Mutation effect predicted for the sequence fragment of PfDBP9 around the mutation D533E. The region is predicted to be disordered and amino acid exchanges are predicted to have little to no effect over the protein function. Data obtained using SuSPeCt software, Structural Bioinformatics Group, Imperial College London [108].

3.10 SC83288 causes membrane disruptions in *P. falciparum* cells

Given that complete inhibition of DNA synthesis was observed after drug treatment during ring-stages and the strength of the effect was found to be dependant of the time of treatment [81], live cell imaging of late trophozoites and schizonts stages was carried out in order to get more insights in to the effect of SC83288 over DNA replication in *P. falciparum* parasites. This experiment was performed in collaboration with Severina Klaus (from the group of Dr. Markus Ganter, CIID Heidelberg), using a *P. falciparum* 3D7 strain that episomally expresses an mCherry-tagged nuclear localization signal (NLS) that is used for the visualization of nuclei and GFP-tagged PCNA1 (proliferating cell nuclear antigen 1). It can be used to detect DNA replication, as it is temporarily accumulated in the nuclei where DNA synthesis is taking place [21]. Following the conditions under which the inhibition of DNA replication was reported, cells were synchronized and treated with 10x IC₅₀ concentration of SC83288 (for 3D7 parasites, this equals 80 nM) at 6 hpi. Parasites were then observed through live cell fluorescence microscopy during 10 hours at 10 min intervals, starting at 28 hpi. A negative control, using 0.1% DMSO for the treatment, was run in the same fashion and for a positive control, a higher concentration of the same solvent was used but with a shorter exposure time, treating parasites right before imaging at approximately 28 hpi with 5% DMSO (Figure 3-19).

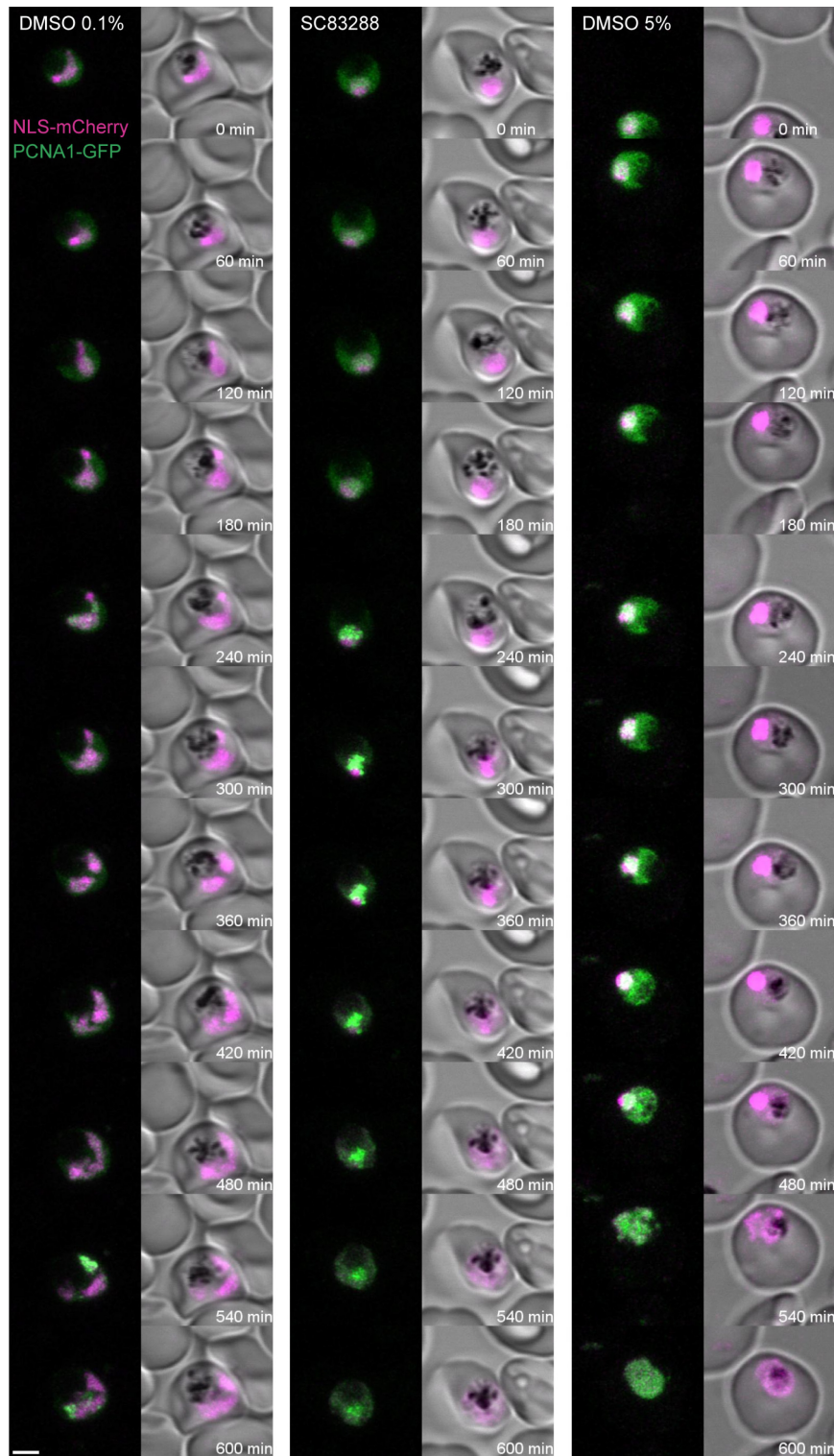


Figure 3-19. Live cell imaging of *P. falciparum* parasites entering schizogony reveals nuclear membrane disruption upon treatment with SC83288. Images of representative cells at 60 min intervals during the 10 hours imaging session. 3D7 parasites episomally expressing NLS-mCherry (magenta) for nuclear localization and PCNA1-GFP (green) as a marker for DNA replication [21] were treated with 0.1% DMSO (vehicle control, left) or 80 nM SC83288 (10X IC₅₀, center) at 6 ± 1 hpi (synchronized cultures), or with 5% DMSO (positive control, right) at ca. 28 hpi (age matched to appearance). Imaging was carried out in a Zeiss Airyscan 2 LSM900 point laser scanning confocal fluorescence microscope with enhanced resolution, starting at 28 hpi and in 10 min intervals. The scale bar on the bottom left represents 2 μm. This experiment was carried out jointly with Severina Klaus.

As expected, parasites treated with 0.1% DMSO progressed through DNA replication and nuclear division without further inconveniences, with only one cell (4.8%) dying during the imaging session. In contrast, cells treated with SC83288 presented major alterations. While 43.3% of all cells remained alive at the end of the imaging session, only 13.3% managed not only to stay alive but also to synthesize DNA. This suggests that a portion of the cells not dying as a result of the treatment could be either in an earlier trophozoite stage or experiencing some delay in the onset of DNA replication and nuclear division. One cell had aberrant morphology, and the rest died either before or during imaging: 10% of total cells were dead prior to the session, of which 83.3% presented nuclear lysis; and the remaining 45% died during imaging, of which 96.3% underwent nuclear lysis (Figure 3-20, A-B). Additionally, 22.2% of the parasites dying during imaging did so after or during DNA replication. Furthermore, right before the nuclear signal extended through the parasite's cytoplasm, the hemozoin crystals that were moving inside the food vacuole suddenly froze in 92.6% of dying parasites.

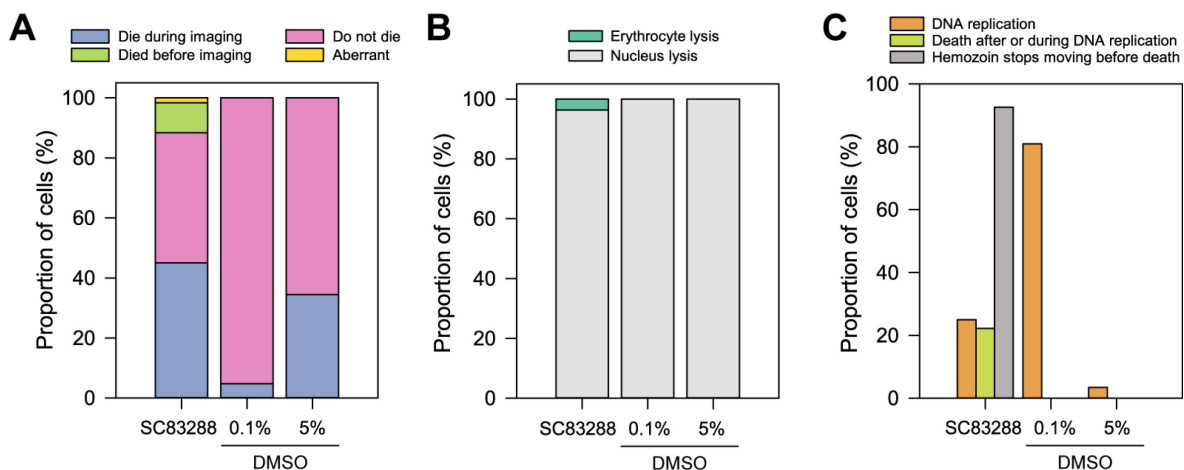


Figure 3-20. Summary of phenotypical observations from live cell imaging of *P. falciparum* parasites treated with SC83288 or DMSO. The observations are derived from the evaluation of 60 parasite cells treated with 80 nM SC83288 in two independent replicates, 21 cells treated with 0.1% DMSO and 29 cells treated with 5% DMSO. (A) Of all cells observed for each condition, the proportion of parasites that died during imaging is shown in purple and those that were already dead at the start of the session are shown in green. The percentage of parasites that continued to be alive by the end of the experiment is shown in pink. Aberrant parasites are shown in yellow. (B) Of the parasites that died during the imaging session, the proportion that died through lysis of the nucleus is shown in light gray and the ones that underwent erythrocyte lysis are shown in teal. It is worth noting that prior to the lysis of the red blood cell, 75% of those cells were already going through nuclear lysis. (C) The proportion of parasites that undergo DNA replication of all the imaged cells is shown in orange, and the percentage of dead parasites that died after or during this process is shown in light green. Out of all parasites dying during the imaging session, those in which hemozoin stopped moving before nuclear lysis are shown in dark grey.

Among parasites treated with 5% DMSO, 34.5% died during imaging due to nuclear lysis. DMSO is an organic polar aprotic solvent with amphipathic properties, widely used to dissolve drugs and for cryopreservation. Although is generally considered safe, its toxicity depends on both in the concentration and the time of exposure, and its mode of action is not fully understood [180, 181]. However, although parasite death in 5% DMSO-treated cells has common features with that of SC83288-treated ones, there are key differences between them. In the positive control sample, no parasites died during or after replication, and only 3.4% of them replicated at all. Moreover, the effect over hemozoin observed in SC83288-treated samples was not present, but hemozoin appears rather to be more condensed in the 5% DMSO-treated sample. The fact that the apparent nuclear lysis or, more concretely, the diffusion of the nuclear localization signal onto the cytoplasm is not only a consequence of treatment with SC83288 but also with DMSO could be an indication of it being a more generic response to high stress or a common mechanism of cell death rather than a specific phenotype. Alternatively, it could be just associated with membrane destabilization or alterations in membrane permeability common to both compounds. However, the one cell that died upon treatment with 0.1% DMSO (50 times less solvent than in the positive control) also showed this effect, as well as other negative controls previously examined with this method (Severina Klaus, personal communication), supporting that it could be a non-specific response.

The observations of hemozoin stopping its movement before parasite death in samples treated with SC83288 are compatible with disruptions on the food vacuole membrane. Moreover, it could be speculated that defects in both the nuclear envelope and the food vacuole membrane are a consequence of oxidative damage or alterations in lipid composition. However, at this point there is not enough evidence to support any hypotheses.

3.11 Proteomics approaches

Cellular Thermal Shift Assay (CETSA), also known as Thermal Proteome Profiling (TPP), is a technique that has become very popular over the last years for the elucidation of molecular targets and mode of action of bioactive molecules both in- and outside of the malaria field [32, 88, 182, 183]. This method allows for the identification proteins that form a complex with a small molecule or drug, and therefore display a differential stability towards heat-induced unfolding as a product of the interaction. For this, either lysates or whole cells are treated with a drug before being subjected to a thermal challenge.

Then, soluble proteins are isolated and analysed using mass spectrometry for their identification and quantification. Depending on the treatment conditions, i.e. a range of drug concentrations and a few temperatures or a range of temperatures and a few drug concentrations, different melting curves can be constructed to measure the effect of the small molecule over the thermal stability of proteins [124].

3.11.1 Thermal proteome profiling of *P. falciparum* lysates

A first approach in collaboration with the group of Dr. Mikhail Savitski (EMBL Heidelberg) using parasite lysates rendered no significant stabilization/destabilization of proteins. The protocol used in these trials (described in Section 2.2.3.5) included a range of temperatures for the thermal challenge of proteins of 37 - 66.3 °C. Some reasons that explain the absence of reliable target candidates are the fact that lysates have non-physiological conditions; since samples are diluted and cell structures are not intact, there is no drug accumulation in the site of action; protein complexes that interact with the drug can be dissociated; the target may be very thermostable; and the target could be non-soluble or associated with cell membranes, therefore absent from analysis. All these factors contribute to having inappropriate conditions for the drug-protein interaction to take place. Some of these limitations could be circumvented by using a whole cell approach, as described in the next section.

3.11.2 Intact-cell CETSA reveals the interaction of SC83288 with *P. falciparum* DNA replication licensing factor MCM2 and fumarase among other proteins

A second approach, this time using intact cells was followed in collaboration with Dr. Jerzy Dziekan (from the group of Prof. Zbynek Bozdech, NTU Singapore), using a ITDR (isothermal dose response) strategy with SC83288 concentrations ranging from 3 µM to 7 pM (using DMSO as vehicle control) and the following thermal challenges: 37, 50, 55 and 60 °C. The resulting protein isothermal curves were then filtered according to the following criteria: (a) the normalized difference in area under the curve (ΔAUC) of the thermal challenges in comparison with the control condition (37 °C) had to be over the median \pm 2 times the median absolute deviation (MAD) of the whole dataset; (b) the goodness of fit (R^2) for the adjustment of the curve of at least one denaturing condition (>37 °C) to a sigmoid curve had to be above 0.8 [124]. While 20 proteins meet these requirements (Figure 3-21), four of them lack a known function. I evaluated further the remaining 16 proteins, in order to assess if they constituted reliable candidate targets and how their interaction with SC83288 could explain previous observations on the mode of action of the drug. For this second analysis, several parameters were taken into account.

The isothermal curves were inspected visually, along with their aspects shown in Table 3-9. The first variable evaluated was the number of unique peptides identified and the peptide spectrum matches for each protein. A higher number of identified peptides increases the confidence for the identification of the protein as a candidate target. However, this number is influenced by the protein abundance, which has to be taken into consideration. Then, the minimal dose threshold (MDT), the minimal drug dose necessary to produce a detectable effect on the protein stabilization, was compared with the drug concentration in which the compound exerts its antimalarial activity. The proximity of these two concentration ranges gives an indication of how relevant this interaction is to the mode of action of the drug. The half-maximal effective concentration (drug dose at which 50% of the total (de-)stabilization effect is achieved) can be analysed in the same fashion. Last but not least, the goodness of fit (R^2) across the different thermal challenges and the sigmoidal curve slope are factors associated with the reliability of the stabilization effect and the confidence to identify a protein as a candidate target. The result of the analysis of the hit proteins and their role in the biology of *P. falciparum* parasites is presented in the sections below, following their order of appearance in Figure 3-21.

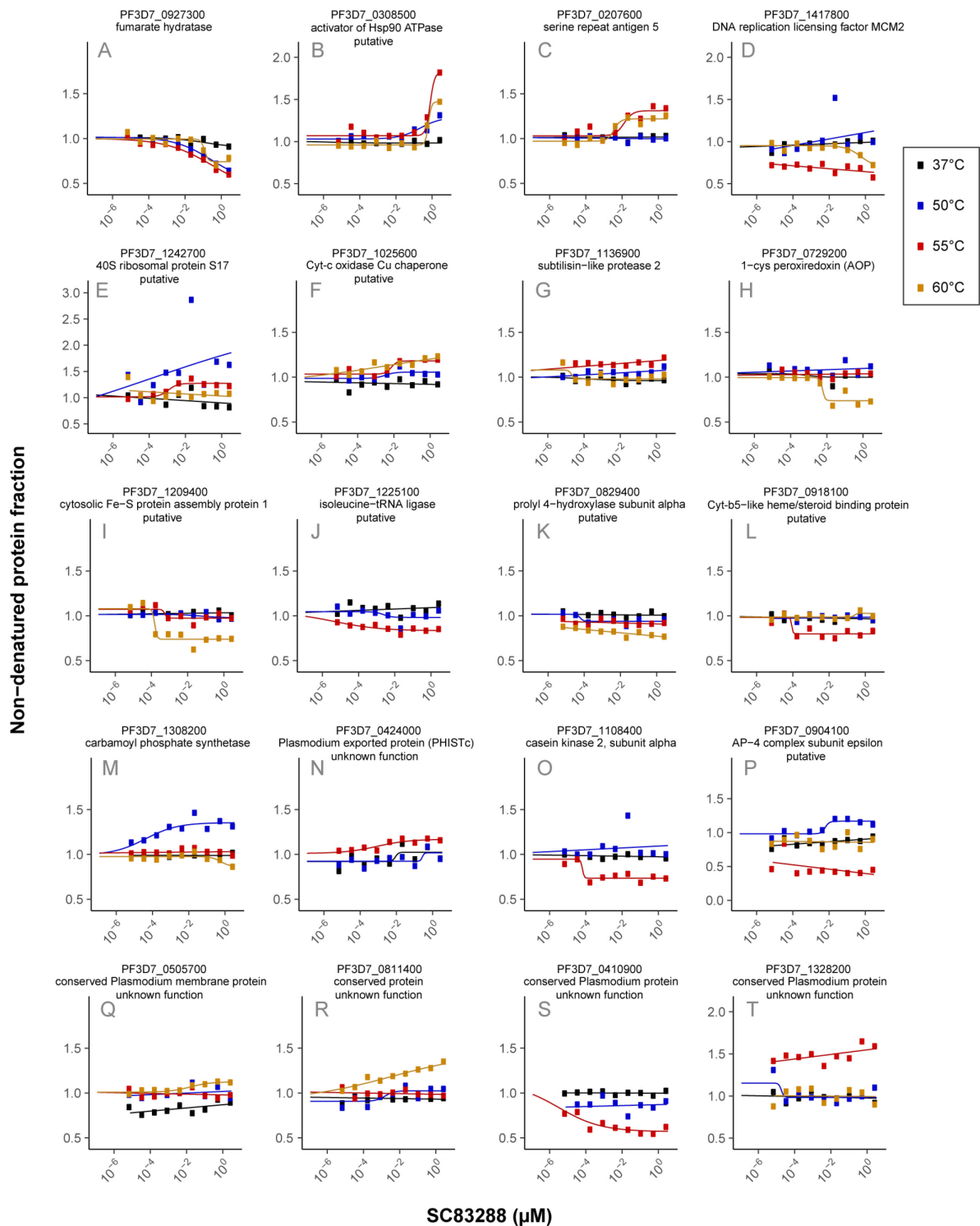


Figure 3-21. Isothermal dose response curves for filtered hit proteins resulting from intact cell CETSA. The proteins included meet the following criteria: (a) the normalized difference in area under the curve (Δ AUC) of the thermal challenges in comparison with the control condition (37 °C) is over the median \pm 2 times the median absolute deviation (MAD) of the whole dataset; (b) the goodness of fit (R2) for the adjustment of the curve of at least one denaturing condition (>37 °C) to a sigmoid curve is above 0.8. Out of the 20 protein hits, four correspond to conserved proteins without a known function. For all the plots, the y-axis corresponds to the normalized non-denatured protein fraction, and the x-axis to the concentration of SC82388 (expressed in μ M). The isothermal curves correspond to 37 °C (black), 50 °C (blue), 55 °C (red) and 60 °C (yellow). Protein names correspond to their annotation in the PlasmoDB database [107].

Table 3-9. Summary of the protein profile parameters of the hits from intact cell ITDR CETSA. The parameters are associated to the curves A to P shown in Figure 3-21. Sum Uni Peps corresponds to the number of unique peptides identified for each protein, and sum PSMs to the number of peptide spectrum matches identified for each protein. MDT is the minimal dose threshold (minimal drug dose to induce an effect on protein stabilization) and EC₅₀ is the half-maximal effective concentration. The last two parameters refer to the adjustment of each isotherm to a sigmoidal curve and correspond the goodness of fit (R²) and its slope.

Protein	Temp.	sum Uni Peps	sum PSMs	MDT	EC ₅₀	R ²	Slope
PF3D7_0927300 fumarate hydratase	37 °C	21	24	2.0055	0.3854	0.6782	-0.5801
	50 °C	16	18	0.0109	0.3081	0.9752	-0.4751
	55 °C	10	12	0.0014	0.2443	0.9786	-0.3510
	60 °C	2	2	0.0995	0.1185	0.8800	-4.4580
PF3D7_0308500 activator of HSP90 ATPase putative	37 °C	3	9	-	4.29x10 ⁴	0.0410	-1.57x10 ⁻⁴
	50 °C	4	11	0.0135	0.1452	0.7721	0.4315
	55 °C	3	6	0.1326	1.3428	0.8989	1.1071
	60 °C	1	2	0.4880	0.6428	0.9271	5.7081
PF3D7_0207600 serine repeat antigen 5	37 °C	57	554	-	1.9156	-0.0419	-0.1636
	50 °C	56	619	-	186.2710	0.0074	-0.1239
	55 °C	55	517	0.0022	0.0241	0.8248	0.5430
	60 °C	51	296	0.0036	0.0042	0.9116	3.8287
PF3D7_1417800 DNA replication licensing factor MCM2	37 °C	36	51	-	0.0285	0.3681	5.4258
	50 °C	21	22	0.0077	0.0071	0.2218	5.2816
	55 °C	2	2	1.06x10 ⁻¹⁹	1.27x10 ⁻⁴	0.8835	-0.0522
	60 °C	2	2	0.0098	0.8853	0.7314	-0.2989
PF3D7_1242700 40S ribosomal protein S17 putative	37 °C	7	17	0.0401	0.0403	0.5408	-16.1351
	50 °C	7	10	8.36x10 ⁻⁵	6.12x10 ⁻⁴	0.3270	1.0936
	55 °C	2	2	4.81x10 ⁻⁴	9.15x10 ⁻⁴	0.8848	1.3385
	60 °C	3	3	3.02x10 ⁻⁵	2.76x10 ⁻⁵	0.2079	-3.8316
PF3D7_1025600 Cyt-c oxidase Cu chaperone putative	37 °C	2	3	-	0.7035	-0.1423	0.4078
	50 °C	4	4	-	0.0044	0.5692	2.5340
	55 °C	4	4	0.0015	0.0069	0.8063	0.3616
	60 °C	2	3	1.55x10 ⁻⁴	0.0032	0.8262	0.2430
PF3D7_1136900 subtilisin-like protease 2	37 °C	7	8	-	1.97x10 ⁻⁴	0.2766	-0.4681
	50 °C	6	6	4.3755	0.0663	0.4936	0.2097
	55 °C	7	8	5.0x10 ⁻²³	6.05x10 ⁻⁶	0.8115	0.0238
	60 °C	9	10	-	1.83x10 ⁻⁵	0.3182	-8.1319
PF3D7_0729200 1-cys peroxiredoxin (AOP)	37 °C	7	10	-	9.38x10 ⁻⁴	0.1352	-1.1516
	50 °C	5	9	0	1.61x10 ⁻⁴	0.2235	1.95x10 ⁻⁵
	55 °C	4	7	-	0.0506	-0.1862	-0.1586
	60 °C	1	1	0.0050	0.0057	0.8929	-6.2493
PF3D7_1209400 cytosolic Fe-S protein assembly protein 1 putative	37 °C	14	19	-	1.97x10 ⁻⁴	0.2076	0.0160
	50 °C	8	13	-	0.2182	0.2433	-4.4496
	55 °C	3	4	-	4.45x10 ⁻⁴	0.4556	-7.9645
	60 °C	1	1	1.38x10 ⁻⁴	1.57x10 ⁻⁴	0.8178	-6.4591
PF3D7_1225100 isoleucine-tRNA ligase putative	37 °C	1	5	-	1.9378	-0.2037	-0.3125
	50 °C	1	3	-	0.0015	0.2009	-1.9768
	55 °C	1	4	1.20x10 ⁻⁵	1.38x10 ⁻⁵	0.8336	-0.3576
	60 °C	-	-	-	-	-	-
PF3D7_0829400 prolyl 4-hydroxylase subunit α putative	37 °C	5	6	-	0.0050	0.0800	-2.2370
	50 °C	4	4	-	8.27x10 ⁻⁵	0.6007	-7.5319
	55 °C	3	3	-	1.20x10 ⁻⁴²	-6.8x10 ⁻⁵	0.0953
	60 °C	2	2	3.31x10 ⁻⁷	7.03x10 ⁻⁷	0.9330	-0.2161
PF3D7_0918100 Cyt-b5-like heme/steroid binding protein putative	37 °C	4	5	-	0.0048	0.0954	-0.0658
	50 °C	3	3	-	0.0104	-0.0808	0.1927
	55 °C	2	3	8.12x10 ⁻⁵	8.48x10 ⁻⁵	0.8060	-9.1858
	60 °C	3	4	-	0.2320	0.1587	7.7254
PF3D7_1308200 carbamoyl phosphate synthetase	37 °C	1	4	-	0.0267	0.0498	-0.5061
	50 °C	24	37	3.60x10 ⁻⁶	4.47x10 ⁻⁵	0.8429	0.4829
	55 °C	17	23	-	0.1529	0.1102	-2.4859
	60 °C	13	17	0.5571	0.4465	0.4313	-1.0253
PF3D7_0424000 Plasmodium exported protein (PHISTc) unknown function	37 °C	4	6	-	0.0096	0.3147	7.6017
	50 °C	3	5	-	0.2421	0.3058	10.0398
	55 °C	3	3	4.50x10 ⁻⁴	6.47x10 ⁻⁴	0.8574	0.3852
	60 °C	-	-	-	-	-	-
PF3D7_1108400 casein kinase 2 subunit α	37 °C	9	22	-	5.24x10 ⁻⁵	0.2502	-1.0995
	50 °C	5	11	0.3725	5593.318	0.0360	0.0473
	55 °C	1	3	4.26x10 ⁻⁵	5.04x10 ⁻⁵	0.8150	-4.8595
	60 °C	-	-	-	-	-	-
PF3D7_0904100 AP-4 complex subunit ε putative	37 °C	11	14	1.2293	1.6763	0.1116	1.0821
	50 °C	8	12	0.0065	0.0065	0.8383	4.4002
	55 °C	4	4	-	-	0.0303	0.0393
	60 °C	4	4	-	-	5.7x10 ⁻⁴	-0.0024

3.11.2.1 Fumarate hydratase (PF3D7_0927300)

The metabolization of fumarate is of importance since it is a by-product of the synthesis of AMP from IMP through the purine salvage pathway (Figure 1-4). As the genome of *Plasmodium* parasites is rich in AT base pairs and the cells undergo multiple rounds of DNA replication, the flow of fumarate is considerably high. This metabolite is not secreted as waste but instead recycled into malate, oxaloacetate, phosphoenolpyruvate and lactate [184]. *P. falciparum* parasites convert fumarate into malate through a reaction catalysed by a class I fumarate hydratase (PffH, PF3D7_0927300, also called fumarase), a mitochondrial enzyme containing an 4Fe-4S cluster [185]. Then, the subsequent metabolization of malate through malate-quinone oxidoreductase generates oxaloacetate and reduced ubiquinone and supplements the mitochondrial electron transport chain at the level of complex III [186]. Fumarase hydratase appears to be essential for parasites, since it has shown to be refractory to genetic deletion [186]. Inhibition of this enzyme could lead to compromises in cell growth and homeostasis in two ways: first, since fumarate would not be metabolized, its accumulation could shift the reversible process catalysed by adenylosuccinate lyase to the inverse reaction that consumes fumarate and AMP to produce adenylosuccinate and lead to AMP depletion in the parasite (Figure 1-4). Second, the excess fumarate could also lead to the succination of cysteine residues in proteins [187] as well as glutathione, which results in the accumulation of reactive oxygen species (ROS) [188]. The effects of AMP depletion were not observed in the untargeted metabolomics study of parasites treated with SC83288, although they are consistent with the previously reported inhibition of DNA replication by this molecule [81]. The dose-response isothermal curves observed (Figure 3-21, A) indicate an interaction of SC83288 with PffH that induces thermal destabilization of the protein. Across the three denaturing conditions, the goodness of fit of the curves is well over the set threshold of 0.80 and the MDT is in the range of 1 to 100 nM, which is in accordance with the range of antimalarial activity of SC83288 (Table 3-9). Additionally, the number of unique peptides identified is equal or above ten for all the curves, with the exception of the 60 °C thermal challenge. However, in untreated samples, at this temperature the non-denatured protein fraction is below 20% of that at 37 °C (see Supplementary data 1, on Dziekan *et al.* [32]) and this could be the cause for the identification of only two unique peptides at 60 °C. Overall, PffH could be considered a candidate target for SC83288, and should be evaluated further.

3.11.2.2 Activator of Hsp90 ATPase, putative (PF3D7_0308500, old name PFC0360w)

The heat shock protein 90 (Hsp90) is a known eukaryotic protein in charge of the regulation of the maturation, activity and stability of a vast range of client or substrate proteins. Among the client proteins, transcription factors and kinases involved in cell cycle regulation can be found [189]. In order to adjust to the needs of different substrates, a functional PfHsp90 homodimer undergoes ATP-dependent conformational changes that are regulated by its so-called co-chaperones. In *P. falciparum*, Hsp90's co-chaperones include PfHop, Pfp23, PfAha1, PfPP5, PFKBP35 and the four-protein complex R2TP [189, 190]. In the genome of these parasites, two putative copies of PfAha1 were identified by homology search. One of them, PF3D7_0308500 (previously known as PFC0360w), is shorter than the other and is less similar to the human and yeast Aha1 homolog, with 140 amino acid residues and 13% identity. Studies on PfAha1 were carried out using the longer putative copy, PF3D7_0306200 (previously known as PFC0270w), and have shown that it stimulates the ATPase activity of PfHsp90 up to 3-fold [191]. However, the shorter PF3D7_0308500 lacks the Aha1 N-terminal domain known to be essential for the interaction with Hsp90. Its function and its ability to bind to PfHsp90 remain unclear [189]. The isothermal curves for this protein (Figure 3-21, B) display a clear stabilization effect, with an MDT ranging from 13.5 nM to 488 nM of SC83288. The goodness of fit is above the threshold for the curves at 55 and 60 °C, while that of the 50 °C curve is quite close with 0.7721 (Table 3-9). The number of unique peptides identified is, however, rather low and below five for all conditions. This, together with the uncertainty of the protein function and no cross-reference with previous data, lead to a rejection of PF3D7_0308500 as a target for SC83288.

3.11.2.3 Serine repeat antigen 5 (PF3D7_0207600)

Plasmodium falciparum serine repeat antigen 5 (PfSERA5, PF3D7_0207600) is a pseudoprotease abundantly expressed, secreted to the parasitophorous vacuole and involved in egress. It is known that before merozoite egress PfSERA5 is proteolytically processed, although the role of the cleavages remains unclear along with the protein function. For a long time it was believed that PfSERA5 was essential for parasite development, although a conditional knock-down revealed that cells lacking the protein undergo a premature schizont rupture resulting in less efficient invasion and lower replication rates [192]. The isothermal dose response curves of PfSERA5 show a stabilization effect as a result of SC83288 treatment (Figure 3-21, C). Due to the abundance of the protein, the number of unique identified peptides is over 50 across all conditions (Table 3-9).

The curve at 50 °C shows no difference to that of the non-denaturing condition (37 °C), as the protein is practically thermostable at this temperature (see Supplementary data 1, on Dziekan *et al.* [32]). At denaturing conditions (55 and 60 °C) the R^2 is over the threshold, and the MDT is in the low nanomolar range, in accordance with the *in vitro* antimalarial activity. Although these results would position PfSERA5 as a reliable candidate target for SC83288, the phenotype observed on parasites treated with the drug differs greatly from that of cells lacking PfSERA5. Therefore, this interaction could be an indicator of the protein being a secondary target.

3.11.2.4 DNA replication licensing factor MCM2 (PF3D7_1417800)

The mini-chromosome maintenance complex (MCM) is composed of six subunits (MCM2-7) and is involved in several cell processes, such as DNA replication, transcription, chromatin remodelling and genome stability [193]. It is a necessary factor for the assembly of the pre-replicative complex, where it unwinds DNA and ensures the progression of the replication fork [194]. The subunits of MCM are present in all asexual development stages of the parasites, although their levels vary throughout the cycle. PfMCM2 (PF3D7_1417800) contains a putative C₄-type zinc finger domain (which may play a role in the interaction with DNA), and is mostly located in the cytosol, but in late schizonts its presence in nuclear fractions increases at the same time that its expression reaches a peak [195]. *Prima facie*, the isothermal curves of PfMCM2 (shown in Figure 3-21, D) do not look reliable. The dose response curve at 60 °C indicates a destabilization effect with an MDT of 9.85 nM and a sufficiently high goodness of fit (Table 3-9). At 50 °C there is no evident effect, although the curve parameters are influenced by an outlier datapoint. At 55 °C, a destabilization effect can be identified, although given that the non-denatured fraction of the lower drug doses is already lower than that of the control, the curve MDT is close to zero. Furthermore, the shape of the curve results in a lower R^2 , that with a value of 0.7315 does not reach the set threshold. When considering the number of unique peptides identified for each condition, in both the non-denaturing condition (37 °C) and the first denaturing one (50 °C) more than 20 can be found. At higher temperatures, however, only two peptides were identified. This can be attributed to PfMCM2 being highly thermolabile (see Supplementary data 1, on Dziekan *et al.* [32]). Despite the unfavorable characteristics of the curves, PfMCM2 is an attractive candidate target because it is in agreement with data on the mode of action of SC83288 originated in diverse and independent approaches. Therefore, other approaches might be useful to either validate or reject this particular protein as a molecular target the compound.

3.11.2.5 Ribosomal protein of the 40S subunit eS17 (PF3D7_1242700)

In the malaria parasite, protein translation is carried out in three places: while the cytoplasm is the principal location, the apicoplast and the mitochondria also possess ribosomes. During the intraerythrocytic development cycle, parasites depend mainly on the cytoplasmic ribosome Pf80S, formed by the subunits Pf40S and Pf60S [196]. PF3D7_1242700 (eS17) is a ribosomal protein of the Pf40S subunit. In other eukaryotes, including yeast and mammalian cells, eS17 interacts with the receptor for activated C-kinase 1 (RACK1) that has a key role in various signaling pathways. However, in *P. falciparum* RACK1 is not bound to Pf40S but functions rather in a free state, while eS17 has shown to be flexible [197]. The role of this protein remains then unclear. The isothermal dose response curves of eS17 (Figure 3-21, E) show a stabilization effect, as the non-denatured protein fraction in the denaturing conditions is higher than that of the 37 °C. However, only one of the non-denaturing conditions meets the requirement of a R^2 higher than 0.80: the 55 °C isothermal curve, which corresponds to only two identified unique peptides and has an MDT of 0.48 nM (Table 3-9). The parameters of the 50 °C curve, which originates from the identification of 7 unique peptides, are influenced by two datapoints that appear to be outliers. Lastly, the 60 °C curve has little difference with the non-denaturing condition, and a shape that is far from being sigmoidal with an R^2 of 0.2079. Overall, the observed effect of SC83288 over the thermal stability of eS17 cannot be considered significant. Moreover, without a clear interaction partner for eS17 arising from previous studies [196, 197], a potential interaction of the ribosomal protein with the drug would not play a critical role that can explain the mode of action of the drug.

3.11.2.6 CCO copper chaperone Cox17 (PF3D7_1025600)

The cytochrome-c oxidase complex (CCO) requires copper to be catalytically active, which is delivered for its assembly by the copper chaperone Cox17 to the accessory proteins (Sco1 and Cox11) that ultimately insert the metal to the two copper sites in CCO. Throughout the intraerythrocytic life cycle of *P. falciparum*, PfCox17 (PF3D7_1025600) is primarily localized in the parasites cytoplasm, and the mechanism through which it transports copper into the mitochondria is not clear [198]. Alterations in copper homeostasis and copper-binding proteins have been linked to arrested early stage cell development, particularly in the transition from rings to trophozoites [199]. The isothermal dose response curves for PfCox17 (Figure 3-21, F) indicate a rather mild stabilization effect, with two of the denaturing conditions (55 and 60 °C) having a goodness of fit sufficiently high (Table 3-9). The MDT for these two curves is 1.517 and 0.155 nM, respectively.

However, the number of unique peptides identified is below five for all tested temperatures. The consequences of the binding of SC83288 to PfCox17 do not explain the mode of action of the drug, since parasites treated at ring stages can develop until late trophozoites and their growth is arrested only in the beginning of the schizont stage. Parasites with compromised mitochondrial function would not be able to display the phenotype observed upon SC83288 treatment. This suggests that the interaction of the copper chaperone and the drug is not significant and can be disregarded.

3.11.2.7 Subtilisin-like protease 2 (PF3D7_1136900)

In order to egress the infected red blood cell, newly formed merozoites tear the host cell membrane with the help of proteins present in their surface. During the invasion of a new erythrocyte, these proteins are shed from the surface as they are cleaved by the subtilisin-like protease 2 (SUB2, PF3D7_1136900). PfSUB2 is released from the merozoite's micronemes and binds to the cell surface prior to, or during, invasion. Disruption of this protease leads to either ineffective invasion with consequent erythrocyte lysis or, abnormal parasitophorous vacuole biogenesis that results in parasite death during ring stages [200]. The isothermal dose response curves of PfSUB2 (Figure 3-21, G) are far from having a sigmoidal shape, with only the one at 55 °C having an R^2 just above 0.80 (Table 3-9), and an MDT is close to zero for this condition. Besides the unfavorable interaction parameters, SUB2 does not constitute a plausible molecular target of SC83288, since the drug exerts its effect during the first asexual development cycle subjected to treatment, that is, before invasion can take place. Therefore, any interaction with SUB2 can be considered irrelevant.

3.11.2.8 1-Cys peroxiredoxin, PfAOP (PF3D7_0729200)

Peroxiredoxins can have different functions in both prokaryotic and eukaryotic cells but they typically reduce hydroperoxides, that have toxic effects. Among the peroxiredoxins present in *P. falciparum*, the antioxidant protein (PfAOP, PF3D7_0729200) can be distinguished by its use of glutathione and glutaredoxin as electron donors for the reduction of hydrophobic hydroperoxides. It is present in both the cytosol and apicoplast of parasites [201]. PfAOP has been characterized as dispensable, since knock-out strains generated using the CRISPR-Cas9 gene editing system did not show alterations in cell development or increased sensitivity to external oxidants [202].

The isothermal dose response curves of PfaOP show no effect of SC83288 on the protein thermal stability (Figure 3-21, H), with the exception of the 60 °C condition, where one unique peptide shows induced destabilization with an MDT of 4.982 nM (Table 3-9). However, since PfaOP is not essential for parasite survival, this interaction can be disregarded.

3.11.2.9 Cytosolic Fe-S protein assembly protein 1 (PF3D7_1209400)

The cytosolic iron-sulfur protein assembly (CIA) machinery is one of various systems used by *P. falciparum* parasites and other eukaryotes for the biogenesis of proteins containing Fe-S clusters, and to date it has not been well studied for the apicomplexan parasite [203]. CIA1, encoded in the malaria parasite by the gene PF3D7_1209400, is a WD domain-containing protein involved in the transfer of Fe-S clusters to target proteins. In yeast, absence of CIA1 is accompanied by the lack of activity of nuclear and cytosolic Fe-S proteins [204]. In eukaryotes, such proteins are involved in diverse processes that include the biosynthesis of amino acids and nucleotides, protein translation, tRNA base modification, as well as DNA synthesis and repair [205]. PfCIA1 exhibits a thermal destabilization effect only for the 60 °C thermal challenge (Figure 3-21, I), with an MDT of 0.138 nM and only one identified unique peptide (Table 3-9). The fact that there is only a significant effect on stability at one of the three denaturing conditions tested puts in doubt the reliability of PfCIA1 as a candidate target for SC83288. At the same time, the consequences of CIA1 disruption in others organisms are compatible with previous data on the mode of action of the drug. Thus, further data from other approaches can be helpful to understand the actual significance of this interaction.

3.11.2.10 Isoleucine tRNA ligase, putative (PF3D7_1225100)

During translation, aminoacyl-tRNAs are in charge of matching a codon with the amino acid that will be incorporated into the nascent protein. The synthesis of aminoacyl-tRNAs is mediated by tRNA ligases (also called tRNA synthetases). PF3D7_1225100 (old name PFL1210w) encodes the apicoplast isoleucine tRNA synthetase (api-IRS) [206]. Mupirocin is an antibiotic that targets api-IRS, causing a delayed death phenotype in which treated parasites are able to complete at least one cell cycle before being unable to produce merozoites that can perform a successful invasion [207, 208]. Each isothermal dose response curve of api-IRS is associated with just one unique peptide, and the protein was not identified in the 60 °C treatment (Figure 3-21, J and Table 3-9). The dose response curve of the 55 °C treatment has a sufficiently high R² value for the consideration of the protein among the hits but its MDT is very low, at 0.012 nM.

Beyond the little significance of the observed interaction, parasites treated with SC83288 undergo an arrest in development in the same cell cycle in which they are exposed to the drug. An inhibitory interaction with api-IRS would cause a delayed death of parasites, which reflects the irrelevance of the protein in the mode of action of the compound.

3.11.2.11 Prolyl 4-hydroxylase subunit α , putative (PF3D7_0829400)

Prolyl 4-hydroxylases (P4Hs) are non-heme Fe(II) enzymes that catalyze the breakage of molecular oxygen for the incorporation of a hydroxyl group into a proline ring giving rise to 4-hydroxyproline, at the time that α -ketoglutarate is decarboxylated oxidatively to take up the other oxygen atom, releasing succinate and CO₂ [209]. The irreversible hydroxylation of protein proline residues can serve the function of a posttranslational modification that alters protein-protein interactions or protein conformation [209]; while it has been shown for other organisms that it plays a role in oxygen sensing [210]. Studies of P4Hs in *Toxoplasma gondii* have shown that the enzyme TgPhyB has critical differences with its *Plasmodium* homolog, suggesting that they may not share a common function or mechanism [211]. A study using *piggyBac* transposon insertional mutagenesis has shown that the gene encoding P4H in *P. falciparum* (PF3D7_0829400) is dispensable for intraerythrocytic asexual development of parasites [212]. The fact that P4H is not essential for parasite growth in blood stages adds to the lack of plausibility of it being a target of SC83288 displayed by its isothermal dose response curves (Figure 3-21, K). The curve for the treatment at 60 °C fulfills the requirement of having a R² value higher than 0.80, but it does so with an extremely low MDT (Table 3-9). This apparent destabilization effect is not enough for further consideration of this protein in target deconvolution studies.

3.11.2.12 Cyt-b₅-like heme/steroid binding protein (PF3D7_0918100)

PF3D7_0918100 (previously known as PFI0885w) encodes what that has been denominated cytochrome b₅-like heme/steroid binding protein, which has shown to be non-mutable in the study of *piggyBac* transposon insertional mutagenesis reported by Zhang *et al.* [212] and can therefore be considered indispensable for parasite growth during asexual blood stages. It has internal homology with PF3D7_1232300 (cytochrome b₅, putative) and PF3D7_1428700 (heme/steroid binding domain-containing protein, putative), it does not contain an apicoplast targeting signal and it is also not included in the *P. falciparum* mitochondrial proteome [213]. There is evidence of a *P. falciparum* putative cytochrome b₅ located in the membrane of the food vacuole, that is involved in nitric oxide generation for the solubilization of heme inside the digestive vacuole [214].

The protein encoded by PF3D7_0918100 could be related to this process but remains understudied, and its function and localization are unknown. The isothermal dose response curves for this protein show no stabilization effect resulting from the presence of SC83288 (Figure 3-21, L), with the exception of the 55 °C condition where the drug-protein interaction induces thermal destabilization. However, this curve is just above the threshold of significance with an R^2 of 0.8060, and has an MDT of 0.081 nM (Table 3-9). These results do not position the so-called cyt- b_5 -like heme/steroid binding protein as a candidate target of SC83288.

3.11.2.13 Carbamoyl phosphate synthetase (PF3D7_1308200)

Carbamoyl phosphate synthetase (PfCPS, PF3D7_1308200) is an essential enzyme for *P. falciparum*, as it catalyzes the first step of the *de novo* pyrimidines synthesis pathway (Figure 1-5) and the parasites are unable to salvage pyrimidines for nucleotides synthesis [27, 215]. The isothermal dose response curves display no thermal stabilization of PfCPS, with the exception of the 50 °C denaturing condition (Figure 3-21, M), where the curve fulfills the requirement of a R^2 value over 0.80 but with an extremely low MDT at 0.004 nM (Table 3-9). Although PfCPS constitutes an attractive target for an antimalarial drug, the results from the untargeted metabolomics study of parasites treated with SC83288 did not show significant alterations in the metabolism of pyrimidines (i.e., reduced levels of pathway intermediates). This, in addition to the unreliable stabilization pattern resulting from the CETSA, lead to the rejection of PfCPS as a candidate target for SC83288.

3.11.2.14 *Plasmodium* exported protein PHISTc (PF3D7_0424000)

The *Plasmodium* helical interspersed subtelomeric (PHIST) protein family is composed of at least 89 proteins and is part of the proteins exported by the parasite into the host red blood cell for its remodeling [216]. PF3D7_0424000 (previously known as PFD1140w) encodes a PHIST protein belonging to a subgroup called PHISTc. Although its function is unknown, a number of PHISTc proteins have shown to be associated with Maurer's clefts and exosome vesicles, which lead to the hypothesis that they may be involved in protein trafficking [216]. Interestingly, PF3D7_0424000 is upregulated in parasites from samples of infected pregnant women: it is expressed in higher level (two- to four-fold) in placental parasites than in samples derived from infected children, and it is co-expressed with *var2csa* [217]. However, PF3D7_0424000 has proved to be dispensable for *in vitro* blood stages development as it was possible to generate knock down parasite strains [218], as well as through a *piggyBac* transposon insertion mutagenesis study [212].

Despite showing a mild thermal stabilization effect in samples subjected to 55 °C thermal treatment due to interaction with SC83288 (Figure 3-21, N), no peptides belonging to PF3D7_0424000 were identified at 60 °C. Moreover, the MDT associated with the 55 °C curve is on the lower side, at 0.45 nM (Table 3-9). Since PF3D7_0424000 is not essential for the asexual life cycle of *in vitro* cultured parasites, none of the effects associated with the mode of action of SC83288 could be attributed to its interaction with the protein or protein disruption caused by the drug. Therefore, this protein cannot be considered as a potential target for SC83288.

3.11.2.15 Casein kinase 2 subunit α (PF3D7_1108400)

P. falciparum protein kinase PfCK2 (previously known as casein kinase 2) is a protein localized in both the cytoplasm and nucleus of the parasite [219] and plays an essential role in its asexual development [220]. The quaternary structure of PfCK2 is formed by the catalytic subunit PfCK2 α and the two regulatory subunits PfCK2 β 1 and PfCK2 β 2 [219]. In other organisms, CK2 has been shown to play a role in DNA and RNA metabolism, DNA damage response and cell cycle regulation [221, 222]. A study on *P. falciparum* suggests that it may have a similar range of substrates in the parasites [219]. Although PfCK2 α could be a candidate target for SC83288 from the perspective of previous data on the drug's mode of action, the isothermal dose response curves (Figure 3-21, O) put it in doubt. At 50 °C, no effect over the thermal stability of the protein can be seen, while at 55 °C there is a destabilization profile that surpasses the set minimum value for R² but has a considerably low MDT, at 0.043 nM (Table 3-9). There were no peptides identified for the 60 °C condition, although this could be due to a combination of the protein being around 90% denatured at that temperature and the drug having a destabilization effect that reduces even more the non-denatured fraction of the protein. Despite not observing a convincing effect on thermal stability of PfCK2 α upon treatment with SC83288, it would be worth to consider this protein in other approaches that could allow for a clearer distinction of this protein kinase as a target (or not) for the drug.

3.11.8.16 AP-4 complex subunit ϵ , putative (PF3D7_0904100)

The adaptor protein complexes (AP-1 to -5) are heterotetrameric complexes involved in vesicular trafficking. The role of AP-4 is not clear, but it is known that it does not interact with clathrin [223, 224]. The subunit ϵ from the AP-4 complex (encoded by PF3D7_0904100) has shown to be essential for *P. falciparum* intraerythrocytic development in a *piggyBac* transposon insertion mutagenesis study [212].

The isothermal dose response curves of PF3D7_0904100 resulting from CETSA are rather chaotic and do not exhibit a clear effect in the protein thermal stability upon treatment with SC83288 (Figure 3-21, P). While at 50 °C a stabilization effect with a goodness of fit over 0.80 and an MDT of 6.45 nM filters the protein as a hit and potential candidate target, at 55 °C the fraction of soluble protein is not only unaltered by increasing concentrations of SC83288 but also considerably lower than that of the non-denaturing condition. In addition, at 60 °C the curve overlaps completely with the one at 37 °C. Overall, these results are not a reliable indicator of an interaction of the protein with the molecule and therefore they will not be considered further.

3.12 SC83288 induces major downregulation of transcription

Upon treatment with small molecules, cells can regulate gene expression to reduce the negative effects or toxicity induced. This can be done in more than one way, as both overexpression and downregulation of the drug target can lead to this result. Downregulation, however, may not be the best option when there is no alternative pathway that can cover up the function of the target. The transcriptional response of cells upon being treated with a compound can then aid in the elucidation of its mode of action and is of importance as it can lead to tolerance development [225]. However, when a drug has multiple targets, overlapping regulatory effects lead to a complex landscape of differentially expressed genes which makes interpretation difficult.

Although initial studies with antifolates showed no regulation of gene expression in *P. falciparum* upon treatment [226], recent work with panels of antimalarial drugs has proved that specific transcriptional responses can be associated to the mode of action of drugs [227, 228]. However, the variety of targets covered so far remain limited.

With the aim of getting more insights into the *P. falciparum* cellular processes affected by SC83288 and comparing its effect with those of other antimalarials, a drug-dose response transcriptional profiling (DRTP) study was carried out in collaboration with Dr. Jerzy Dziekan and Michal Kucharski (from the group of Prof. Zbynek Bozdech, NTU Singapore). From about 5 300 protein-encoding genes identified in the genome of *P. falciparum* [229], 4 295 were recognized in our analysis. Parasites treated with different concentrations of SC83288 exhibit major downregulation of transcription, in comparison with untreated samples (Figure 3-22, A). Across the three drug treatments (5, 10 and 20 nM), an increasing number of genes with a relative abundance of 80% or less of that in untreated samples can be found (2 032, 2 095 and 2 801, respectively).

However, for the 10 nM drug treatment, only 173 genes pass the filter of having a LOD score higher than 1.30 (that is, having a false discovery rate (FDR), or Benjamini-Hochberg corrected p-value, lower than 0.05), which can be appreciated from the spread of the data points in the volcano plot shown in Figure 3-22 (B, middle plot), and 166 of them belong to those with relative abundances of 80% and below (inside red rectangle in the top left of volcano plot). The number of differentially expressed genes is then lower than that of the 5 nM treatment, where of 396 differentially expressed genes, 370 are significantly downregulated. For the 20 nM treatment, 1 019 genes fulfil the requirement of having an FDR below 0.05, of which 356 have an FDR below 0.01. In the volcano plot for this treatment (Figure 3-22, B, right plot), 997 genes can be found among those significantly downregulated in the top left of the volcano plot (red background).

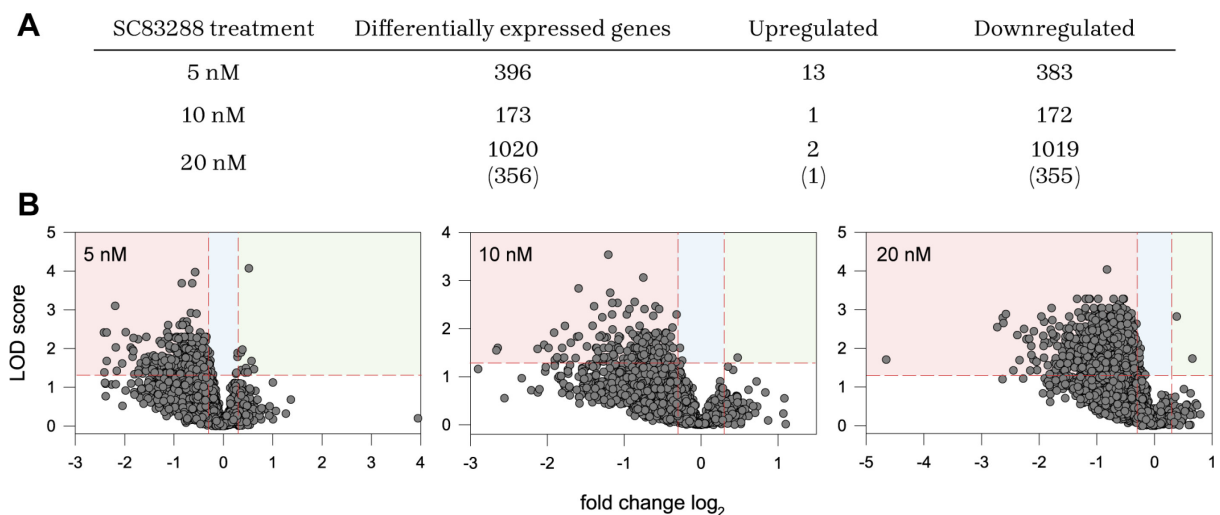


Figure 3-22. SC83288 induces downregulation of gene transcription in *P. falciparum* parasites. (A) Summary of the number of differentially expressed genes in parasites treated with various concentrations of SC83288. The criterion for significance is an FDR (Benjamini-Hochberg corrected p-value) below 0.05. The values between brackets indicate the number of genes with an FDR below 0.01. **(B)** Volcano plots showing the distribution of the 4295 identified genes (gray circles) according to their $\log_2(\text{fold change})$ and LOD score ($-\log(\text{FDR})$). The dashed red lines show the significance thresholds: $-0.3 < \log_2(\text{fold change}) > 0.3$ and LOD score > 1.3 (corresponding to FDR < 0.05). Significantly downregulated genes locate within the red rectangle, and significantly upregulated ones within the green rectangle. Those genes that only fulfil the requirement of a LOD score > 1.3 locate within the light blue area. The plots correspond to treatment of cells with 5 nM (left), 10 nM (middle) or 20 nM (right) SC83288.

For a first overview of the results, the genes that were found to be differentially expressed as a result of each drug treatment (DEG) were subjected to a search for enriched Gene Ontology (GO) terms. Three analyses were carried out for the different ontologies (biological processes, cellular components and molecular functions) using PlasmoDB with a p-value cut-off of 0.05. The results were further filtered by selecting GO terms with at least five genes from the DEG list and the selection was visualized through interactive graphs using Revigo [230].

Tables with the results of GO enrichment analysis and their associated interaction graphs can be found in Appendix I. For all doses of drug treatment, the major downregulations are focused on RNA-processing related genes. In a second place, for the 5 and 20 nM treatments, ribonuclear complex biogenesis is enriched along with mitochondrial transport and organization. Consequentially, both the nucleus and nucleolus are main enriched terms among GO terms for cellular components.

Then, DEGs were examined individually. In order to do this, downregulated genes were selected if they consistently appeared across all drug treatments since then they are more likely to be associated with the mode of action [227]. This allowed me to summarize the DEGs as presented in Table 3-10 and Table 3-11. Among the downregulated transcripts, we can distinguish genes involved in transcription (transcription factor TFIIB, AP2 domain transcription factor), in protein synthesis (eukaryotic translation initiation factor eIF2A, ribosome biogenesis protein TSR3), RNA processing and DNA repair (exosome complex exonuclease RRP6), metabolism of purines (AMP deaminase) and Fe/S cluster assembly (SufA), among others, although it is worth noting that several remain uncharacterized. With transcription being downregulated, most of the upregulated genes are only observed in cells treated with the lowest drug concentration (5 nM) and, even when statistically significant, show mild increases in concentration. Interestingly, the transcriptional coactivator ADA2 is upregulated, which may be an attempt of the cells to counteract the downregulation at lower drug doses. This is also the case of the ribosome biogenesis GTPase A and a ribonuclease. The overexpression of aconitate hydratase and the so-called apoptosis-related protein are also observed.

In a comparative analysis with other antimalarials assayed in parallel with out drug, the transcriptional response towards SC83288 showed correlation with that of methylene blue (Dr. Jerzy Dziekan and Michal Kucharski, preliminary unpublished results). Although methylene blue has proven to have a polypharmacological profile and while some targets and mode of action may remain unknown [231], this can bring some insights into the mechanisms through which SC83288 exerts its antiplasmodial activity.

Table 3-10. Summary of genes downregulated upon treatment with SC83288. Data presented originated from the transcriptional profiling or was gathered from the following databases: PlasmoDB [107], KEGG [102], UniProt [112], TDR Targets [109], PhenoPlasm [105], and MPMP Project [26]. Abbreviations: P, P-value; FC, log₂(fold change); ADC, asexual development cycle; IL, intracellular localization; BP, biological processes; MF, molecular functions.

Gene	Product	5 nM		10 nM		20 nM		Essential for ADC	IL	Process or pathway associated	GO terms associated (BP are prioritized over MF)
		P	FC	P	FC	P	FC				
PF3D7_0110800	transcription initiation factor TFIB, putative	0.024	-0.919	0.044	-0.918	0.049	-0.739	Yes	Nucleus	Transcription	DNA-templated transcription, initiation, transcription initiation from mRNA polymerase II promoter, transcription preinitiation complex assembly
PF3D7_0206300	pentafunctional AROM polypeptide, putative, pseudogene	0.036	-0.796	0.025	-0.923	0.005	-0.984	No	Cytosol or apicoplast	Shikimate biosynthesis	-
PF3D7_0522700	iron-sulfur cluster assembly protein SufA	0.033	-0.859	0.015	-0.736	0.004	-0.702	Yes	Cytosol	Fe-S cluster assembly	iron-sulfur cluster assembly, protein maturation by iron-sulfur cluster transfer (BP), 2Fe-2S cluster binding (MF)
PF3D7_0622300	vacuolar transporter chaperone, putative	0.005	-1.565	0.015	-1.229	0.006	-1.547	Yes	integral component of membrane	Unknown	integral to membrane, ATP binding, transport (MF)
PF3D7_0705200	conserved Plasmodium protein, unknown function	0.017	-1.351	0.038	-1.131	0.033	-1.021	Yes	Unknown	Unknown	Unknown
PF3D7_0919700	pyridoxal phosphate homeostasis protein, putative	0.004	-1.144	0.015	-0.864	0.014	-0.910	No	Unknown	Unknown	pyridoxal phosphate binding (MF)
PF3D7_1134200	conserved Plasmodium protein, unknown function	0.025	-0.866	0.029	-0.960	0.003	-1.206	Yes	Unknown	Unknown	Unknown
PF3D7_1210300	conserved Plasmodium protein, unknown function	0.045	-1.340	0.044	-0.890	0.025	-1.001	Yes	Unknown	Unknown	Unknown
PF3D7_1220500	ribosome biogenesis protein TSR3, putative	0.001	-2.195	0.022	-1.169	0.001	-1.788	Yes	Cytosol	Ribosome biogenesis, rRNA processing	enzyme-directed rRNA pseudouridine synthesis, maturation of SSU-rRNA (BP), 18S rRNA aminocarboxypropyl-transferase activity, AdoMet binding (MF)
PF3D7_1222800	conserved Plasmodium protein, unknown function	0.005	-1.825	0.003	NA	0.030	-0.960	No	Unknown	Unknown	Unknown
PF3D7_1224400	WD repeat-containing protein, putative	0.027	-0.988	0.027	-1.133	0.010	-1.166	Yes	Nucleolus	Unknown	Protein binding, nucleotide binding (MF)
PF3D7_1239000	HD superfamily phosphohydrolase protein, putative	0.046	-0.656	0.038	-0.782	0.019	-0.839	No	Nucleus	Purine metabolism	dGTP catabolic process (BP), 3',5'-cyclic-nucleotide phosphodiesterase activity, dGTPase activity (MF)
PF3D7_1305200	AP2 domain transcription factor, putative	0.005	-1.119	0.017	-0.829	0.022	-1.314	No	Nucleus	Transcription	regulation of transcription, DNA-dependent, transcription factor activity (MF)
PF3D7_1329400	AMP deaminase	0.015	-0.656	0.042	-0.474	0.039	-0.368	No	Cytosol	Purine metabolism	AMP catabolic process, AMP metabolic process, IMP biosynthetic process, IMP salvage
PF3D7_1403700	translocation associated membrane protein, putative	0.042	-0.582	0.003	-1.158	0.011	-0.976	No	Membrane	Sphingolipid <i>de novo</i> biosynthesis	Ceramide biosynthetic process (BP), N-acyltransferase activity, sphingosine N-acyltransferase activity
PF3D7_1438000	eukaryotic translation initiation factor eIF2A, putative	0.029	-0.710	0.025	-0.835	0.047	-0.808	No	Cytosol	Protein translation	mRNA binding, ribosome binding, translation initiation factor activity, tRNA binding (MF)
PF3D7_1449700	exosome complex exonuclease RRP6	0.017	-0.767	0.026	-0.761	0.017	-0.932	Yes	Nuclear periphery, nuclear exosome, nucleolus	RNA processing, DNA repair	exonucleolytic trimming to generate mature 3'-end of 5.8S rRNA from tricistronic rRNA transcript (SSU-rRNA, 5.8S rRNA, LSU-rRNA), histone mRNA catabolic process, nuclear polyadenylation-dependent antisense transcript catabolic process, nuclear polyadenylation-dependent CUT catabolic process, nuclear polyadenylation-dependent rRNA catabolic process, nuclear polyadenylation-dependent snoRNA catabolic process, nuclear polyadenylation-dependent snRNA catabolic process, nuclear polyadenylation-dependent tRNA catabolic process, nuclear retention of unspliced pre-mRNA at the site of transcription, polyadenylation-dependent snoRNA 3'-end processing

Table 3-11. Summary of genes upregulated upon treatment with SC83288. Data presented originated from the transcriptional profiling or was gathered from the following databases: PlasmoDB [107], KEGG [102], UniProt [112], TDR Targets [109], PhenoPlasm [105], and MPMP Project [26]. Abbreviations: P, P-value; FC, log₂(fold change); ADC, asexual development cycle; IL, intracellular localization; BP, biological processes; MF, molecular functions; Etn-P, ethanolamine phosphate; PE, phosphatidylethanolamine; PS, phosphatidylserine.

Gene	Product	5 nM		10 nM		20 nM		Essential for ADC	IL	Process or pathway associated	GO terms associated (BP are prioritized over MF)
		P	FC	P	FC	P	FC				
PF3D7_0303900	Etn-P-binding protein, putative	0.942	0.052	0.564	-0.546	0.018	0.653	No	ER and mitochondria associated membrane (yeast, mammals)	PE and PS metabolism	Unknown
PF3D7_0312400	glycogen synthase kinase 3	0.016	0.281	0.481	0.161	0.720	0.041	Yes	Cytosol, Maurer's cleft	Signal transduction	Signal transduction (BP), ATP-binding, protein serine/threonine kinase activity, tau-protein kinase activity (MF)
PF3D7_0410700	ribosome biogenesis GTPase A, putative	0.036	0.362	0.933	0.024	0.128	-0.383	Yes	Mitochondria, apicoplast	Ribosome biogenesis	G protein activity, GTPase activity, GTP binding (MF)
PF3D7_0615400	ribonuclease, putative	0.032	0.453	0.268	0.263	0.791	-0.051	Yes	Exosome, P-body	RNA processing	mRNA catabolic process, RNA processing
PF3D7_0709100	Cg1 protein	8.45E-05	0.513	0.252	0.466	0.001	0.381	No	Unknown	Unknown, predicted chromatin binding domain	Protein binding, DNA binding (MF)
PF3D7_0821800	protein transport protein SEC61 subunit beta, putative	0.034	0.618	0.504	0.544	0.350	0.263	No	ER membrane	Protein translocation in the ER	Intracellular protein transport, posttranslational protein targeting to membrane, translocation, SRP-dependent cotranslational protein targeting to membrane, translocation
PF3D7_0909300	apoptosis-related protein	0.042	0.437	0.958	0.031	0.116	-0.373	Yes	Cytosol, nucleus	Apoptosis mechanism	DNA binding (MF)
PF3D7_1014600	transcriptional coactivator ADA2	0.013	0.286	0.704	0.097	0.198	0.178	Yes	Nucleus	Transcription	Chromatin remodeling, positive regulation of histone acetylation, regulation of transcription, DNA-templated, regulation of transcription by RNA polymerase II
PF3D7_1032500	DER1-like protein, putative	0.041	0.491	0.502	0.181	0.527	-0.079	Yes	ER membrane	Degradation of misfolded proteins in ER lumen	ER unfolded protein response, ubiquitin-dependent ERAD pathway
PF3D7_1128400	bifunctional farnesyl-geranylgeranyl diphosphate synthase	0.013	0.354	0.495	0.352	0.613	0.081	Yes	Cytosol	Cholesterol biosynthesis	farnesyl diphosphate biosynthetic process, isoprenoid biosynthetic process
PF3D7_1341900	V-type proton ATPase subunit D, putative	0.044	0.253	0.941	0.025	0.690	-0.080	Yes	Vacuolar membrane	Oxidative phosphorylation	proton transmembrane transport (BP), ATP synthesis coupled proton transport, ATPase activity, coupled to transmembrane movement of substances, vacuolar proton-transporting V-type ATPase, V0 domain
PF3D7_1342100	aconitate hydratase	0.011	0.382	0.554	0.176	0.951	-0.017	No	Mitochondria, cytosol, food vacuole	CAC	citrate metabolic process, regulation of translational initiation by iron, tricarboxylic acid cycle
PF3D7_1360000	ATP synthase-associated protein, putative	0.021	0.565	0.612	0.233	0.948	0.248	Yes	Mitochondria	Oxidative phosphorylation	Unknown
PF3D7_1471800	conserved Plasmodium protein, unknown function	0.845	-0.218	0.040	0.474	0.128	-0.621	No	Unknown	Unknown	Unknown

4. Discussion

The fight against malaria needs the discovery of new medicines with different modes of action, refractory to the development of resistance, to ensure the supply of compounds into the development pipeline. This is essential to counteract the stalling of progress in malaria elimination observed in recent years, widely influenced by resistance to antimalarial drugs and vector resistance to insecticides [11]. SC83288 has shown to be a promising candidate for the treatment of severe malaria [78]. The mechanism through which this this compound acts on *P. falciparum* parasites remained elusive over several years. The understanding of the molecular details behind the biological activity of a compound is not a decisive factor for its clinical testing and introduction to the market, especially in the case of a disease like malaria, for which current therapies have shown an increasing degree of failure due to resistance. In fact, safety concerns can be addressed with sufficient data covering the absence of potentially undesired side effects and favourable results from animal models [232]. Nevertheless, pursuing the investigation of the mode of action has relevance beyond the molecule of interest. First, because novel targets may be discovered, which can be exploited for the development of improved medicines. And second, this research can result as well in a better knowledge of parasite biology.

From the results of this work, it can be hypothesized that the effects of SC83288 over *P. falciparum* parasites are a product of its interaction with the parasite fumarate hydratase (PfhF, PF3D7_0927300), the enzyme responsible for the metabolization of fumarate to malate within the citric acid cycle (CAC) [184]. The use of CETSA for the target identification of SC83288 yielded a number of candidates with differential thermal stability in the presence of the drug, with three proteins presenting the most reliable profiles: PfhF, PfSERA5, and a putative activator of Hsp90 ATPase activity. The last one is one of two putative copies of the co-chaperone Aha1, but as it lacks the N-terminus functional domain it has not been thoroughly studied and its role is unclear [189, 191]. While PfSERA5 could be a target, parasites lacking this protein have shown defects in parasite egress that do not prevent their replication [192], and this is not consistent with the phenotypes observed in treated cells.

Fumarate is a by-product of the purine salvage pathway, generated along with AMP in the reversible reaction catalysed by adenylosuccinate lyase, and is imported to the mitochondrion for its incorporation to the CAC. Inhibition of PfhF would lead to the accumulation of fumarate which has three major cytotoxic consequences (Figure 4-1).

First, high concentrations of this metabolite can shift the direction of the reaction of adenylosuccinate lyase, consuming the excess fumarate as well as depleting the AMP reserves of the parasite [185]. Second, increased fumarate concentrations can lead to succination of protein cysteine residues through an irreversible non-enzymatic Michael addition producing S-(2-succinyl)cysteine (2SC). This reaction has been observed preferentially in catalytic cysteine residues (as they have lower pKa values), therefore having an impact in the biological functions of the cells paired with the consumption of fumarate [233]. Furthermore, the succination can extend to glutathione (GSH), constituting the third effect, which impacts the antioxidant capacity of the cell. In cancer cells, excess fumarate binds GSH to yield succinated glutathione (GSF) reducing the antioxidant capacity of the cell provided by GSH. The enzyme glutathione reductase (GR) recycles the antioxidant capacity of cells by reducing glutathione dimers (GSSG) back into GSH, and it was observed that it is also able to break GSF into GSH and fumarate, at the expense of consuming NADPH. As GSF is formed again spontaneously, the fumarate that can no longer be removed by fumarase enters a cycle that consumes NADPH and exploits the activity GR for this futile cycle. Ultimately, the reduction in NADPH levels results in higher ROS and oxidative damage [188]. This effect has also been described in *Mycobacterium tuberculosis* [234] and has been proposed as possible for *P. falciparum* [185]. Additionally, lower availability of NADPH limits other biological processes, such as the activation of ribonucleotide reductase for DNA replication as well as the synthesis of pyrimidines. There, NADPH is necessary for the recycling of dihydrofolate into tetrahydrofolate, that is then transformed again to methylenetetrahydrofolate [27, 235]. As *Plasmodium* parasites go through schizogony they require a steady supply of high amounts of nucleotides to support the synthesis of up to 20 copies of their genome [236]. Additionally, as their genome is extremely rich in A+T pairs [237], providing the necessary amounts of dATP implies giving rise to high concentrations of fumarate. Furthermore, in order to successfully carry out DNA replication (as well as transcription and translation) ATP is required as a source of energy by numerous proteins involved in the process [238]. A peak in demand of ATP and dATP can then be expected around 30 hpi, with the onset of the S-phase and therefore DNA replication. In this situation, the AMP depletion defect caused by fumarate accumulation would have catastrophic consequences. Even when the cell manages to increase the metabolic flow through glycolysis to obtain ATP and tries to recover to some extent, the damage caused by cysteine succination would have a devastating impact on the parasite.

Moreover, deficiencies in nucleotides supply hinder the correct gene expression and translation, and insufficient amounts of certain proteins, or their complete absence, can also stop the development of parasites through the cell cycle.

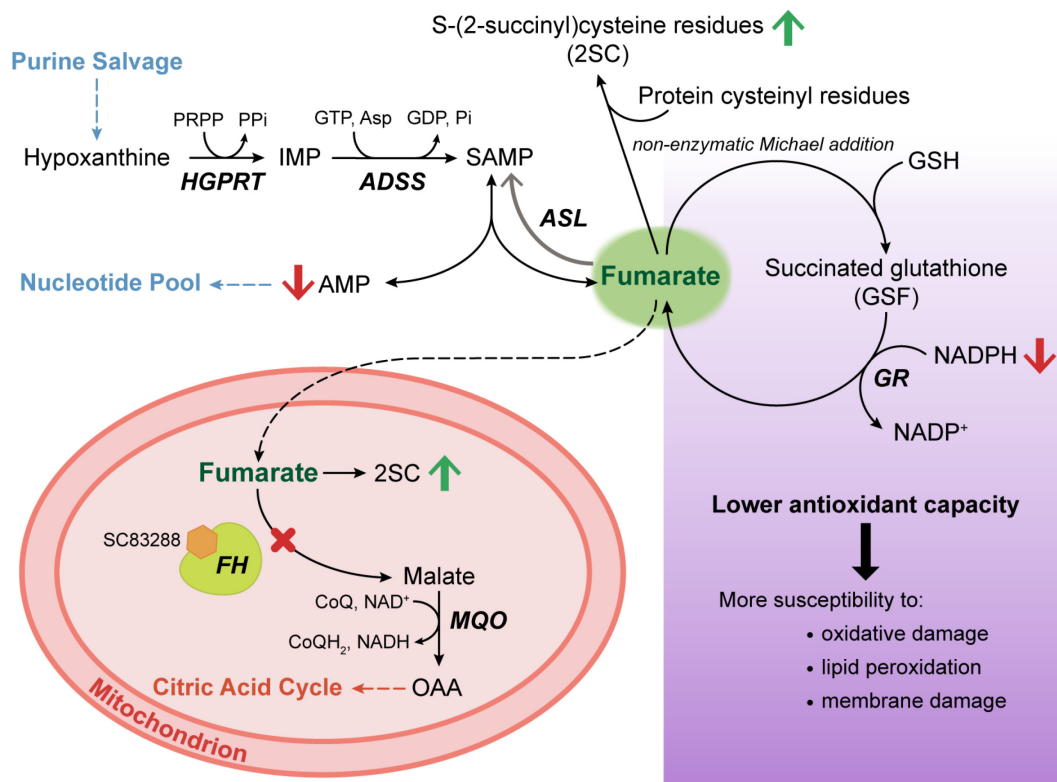


Figure 4-1. Schematic representation of the main predicted effects of SC83288 over *P. falciparum* as a consequence of its action over the mitochondrial enzyme fumarate hydratase. Black dashed arrows represent metabolite transport, and blue- or orange-colored dashed arrows point towards a metabolic route where the intermediate is further processed. The arrows next to the metabolite name indicate expected accumulation (green) or depletion (red) after treatment with SC83288. Abbreviations: HGPRT, hypoxanthine-guanine phosphoribosyltransferase; PRPP, phosphoribosyl pyrophosphate; P_i, pyrophosphate; ADSS, adenylosuccinate synthase; SAMP, adenylosuccinate; ASL, adenylosuccinate lyase; GSH, glutathione; GR, glutathione reductase; FH, fumarate hydratase; MQO, malate:quinone oxidoreductase; OAA, oxaloacetate.

Pulse treatments with SC83288 during the course of six hours over the three main stages of asexual development revealed a differential susceptibility to the drug [78]. The observed almost seventy-five-fold higher IC₅₀ for ring-stages than for trophozoites can be explained by two main reasons. In first place, the uptake of SC83288 by parasite cells has been shown to occur to a large extent through NPPs (Dr. Cecilia Sanchez, unpublished data), which are only fully established at a later development point, approximately 18 hpi. Then, either the lower proportion of compound incorporated into the apicomplexans could be insufficient to fully block the fumarase activity, or the parasites could have enough time to counteract the effect by producing more enzyme or excreting the small molecule, once the pulse treatment is over and they are no longer under drug pressure. In contrast, older parasites are more permeable to SC83288, and are not able to circumvent the drug effect.

However, at schizont stages (35-37 hpi) parasites are currently undergoing schizogony and some cells could have successfully completed the process before reaching a critical point in fumarate accumulation. This explains the almost three-fold higher IC₅₀ observed for schizonts in comparison with trophozoites. Similarly, different degrees of DNA replication inhibition were observed in *P. falciparum* cultures exposed to 10X the IC₅₀ of SC83288 depending on the parasite age at the treatment starting time [81]. They were able to increase their DNA content to some extent the later they were exposed to the drug, although they showed no evidence of merozoite egress. The results from live cell imaging support the observations that parasites subjected to treatment with SC83288 from ring-stages onwards are not able to successfully carry out DNA replication. Additionally, it was evident that at the moment of cell death the nuclear marker diffused to the cytoplasm and hemozoin movement stopped, both indicators of membrane damage and increased permeation.

An untargeted metabolomics study revealed that parasites treated with SC83288 from ring- to trophozoite-stages accumulate ACC, MTA and adenine, while they have lower levels of phosphoethanolamine, PS(20:4), PS(18:1) and PS(16:0/18:1). The accumulation of ACC is a puzzling result, since it is a plant metabolite that has not been reported so far in *P. falciparum*. While it is consistent with the concomitant increase in MTA and adenine concentrations, given that it is generated through the metabolization of AdoMet into ACC and MTA, and adenine is the by-product of the posterior cleavage of MTA, it is not clear why ACC is being synthesized. In plants, ACC is a signalling molecule that has been associated with growth arrest [152] and is the first intermediate of the ethylene biosynthesis pathway, which in some cases is linked to programmed cell death (PCD) [149]. Although there are reports of PCD in *P. falciparum*, and evidence of these pathways in other protozoa, it has been a controversial topic [239, 240]. Furthermore, the production of ACC implies the consumption of AdoMet, which is generated at the expense of ATP. In the recycling of MTA to methionine yet another ATP equivalent is used, as the only evidence of MTA cleavage in *P. falciparum* suggests that it is mediated by a nucleosidase and a kinase [147]. Energy-wise, this recycling process is unfavourable and likely just a futile cycle, as it only produces an apparently dead-end metabolite as ACC. A recent study of non-canonical metabolic pathways has found new metabolites and reactions in *P. falciparum* which were not predicted from genomic reconstructions. This included the identification of the aforementioned GSF, but their results did not present ACC as a parasite intermediate [241]. This supports the idea of the synthesis of ACC being an acute stress response mechanism.

The observed reduced levels of intermediates of phospholipids metabolism could represent a compensatory mechanism. Parasite growth during the asexual development cycle requires a 6-fold increase in phospholipids, the main component of parasite membranes. Among them, PS lipids one of the least abundant after PC and PE [154]. During development, it has been shown that PE content grows, while PS slightly decreases [242]. As PS and PE can be interconverted [154], and stable levels of the PE correspondent to the affected PS can be observed, it can be speculated that the PS are being transformed to compensate lower levels of PE and maintain membrane integrity. It is interesting that the PS are then not replenished by synthesis from serine [155], but as PS levels normally decrease during parasite development, the parasites could be less disturbed by this imbalance. As the three depleted PS contain unsaturated acyl chains, they could be replacing PE affected by oxidative damage. However, there is no sufficient evidence to support this claim so far. Additionally, parasites treated with SC83288 have lower levels of other intermediates of the Kennedy pathway for PE synthesis: phosphoethanolamine, CDP-ethanolamine, and phosphodimethylethanolamine. The last two compounds, despite showing a significant $\log_2(\text{fold change})$ of -1.096 and -1.590, do not pass the significance cut-off of a LOD score over 1, although they are close with values of 0.775 and 0.742, respectively. This depletion is consistent with a lower PfEK activity, and although there is no further evidence of SC83288 interaction with this particular enzyme, the drug has shown certain affinity with another kinases (namely, PfCK2 and PfHPPK). The metabolism of phosphatidylcholines is not affected since parasites can scavenge choline from the host for its incorporation to the Kennedy pathway [155].

There is a chance that a second untargeted metabolomics study, either concentration- or time-resolved (or at least with shorter exposure times), can provide better information to distinguish primary and secondary effects [243] and initial metabolic responses to the drug that are more closely related to its mode of action.

One of the consequences of deficient fumarase activity, AMP depletion, leads to insufficient nucleotides levels, which do not only block DNA replication, but also disrupt the metabolism of RNA, gene transcription and consequently translation. This was observed in a dose-response transcriptional profiling, where the exposure of trophozoite stage parasites to 5 to 20 nM of SC83288 for 4.5 h led to the downregulation of the expression of several hundreds of genes, including transcription and translation initiation factors.

An analysis of the gene ontology terms enriched among differentially expressed genes showed RNA processing and metabolism as the main process affected by drug treatment, followed by ribonuclear complex biogenesis and mitochondrial transport and organization. Notably, AMP deaminase (PF3D7_1329400) can be found among the genes downregulated across all drug treatments. The reaction catalysed by this enzyme reverses the synthesis of AMP, transforming it back to IMP, a process that can be useful to interconvert purine nucleotides and generate GMP. This is an irreversible reaction, with the same effect as the reaction catalysed by adenylosuccinate lyase that depletes AMP for fumarate detoxification. It is logical in the scenario of fumarate accumulation that the parasite can dispense of AMP deaminase and consequently downregulates its expression.

The transcriptional response of *P. falciparum* parasites to SC83288 shows a correlation with the one elicited by methylene blue (Dr. Jerzy Dziekan and Michal Kucharski, unpublished data). Methylene blue (MB) is a compound with antimalarial activity attributed to a polypharmacological mode of action. Among the known targets of MB, hemozoin formation and the redox metabolism of the parasite were found [244]. This compound acts as a subversive redox-cycling substrate, reversing the action of enzymes in charge of sustaining the reduced environment of the parasite cytoplasm and using them to generate peroxide molecules [245, 246]. A parallel can be established between this antimalarial mechanism and one of the consequences of fumarate accumulation. Both MB and fumarate exploit the parasite glutathione reductase to induce oxidative stress, although the later does it in a more indirect fashion through GSF [188]. Additional contributions to the similarities could be driven by downstream effects of secondary targets. A key feature of MB is the lack of both cross-resistance with other antimalarials and resistance development, commonly attributed to the diverse effects it has on parasites and its multiple targets, including potentially still unknown modes of action [231, 247-249]. This is another similarity with SC83288 that, besides displaying no cross-resistance with common antimalarials, had to be used continuously to keep *P. falciparum* cultures under increasing drug pressure *in vitro* for approximately eight months in order to obtain mutant parasites exhibiting resistance to the compound [78]. Resistance to SC83288 is mediated by the ER calcium pump PfATP6 (PF3D7_0106300) [81] which, due to the mutation F972Y, is able to transport the drug into the ER lumen (Dr. Cecilia Sanchez, unpublished data). This sequestration of the drug allows the parasite to isolate the compound from its molecular targets but is not directly related with the antimalarial mode of action.

Additionally, the mutation that introduces this compensatory effect represents a fitness cost for the parasites, and co-culture experiments have shown that cells containing wild-type PfATP6 displace the mutant population after the course of around thirty life cycles [81].

From a logical point of view, resistance to a drug that targets an enzyme is likely to arise from mutations in the protein that limit or eliminate the interaction between the biomolecule and such a ligand. However, when the active compound has multiple targets, the chances of developing these mutations in each target are rather low. In these cases cells are more refractory to the development of resistance, or secondary mechanisms of resistance arise such as the one mediated by PfATP6. It has been shown that *P. falciparum* parasites can adapt to suboptimal activity of PffH, as this induces changes in their metabolism that allow them to ultimately survive without the enzyme [250]. This is mainly achieved through excretion of fumarate to the host red blood cell, where it can be processed by the human enzyme from the urea cycle argininosuccinate lyase which can catalyse the reverse reaction in which fumarate binds to arginine through a Michael addition to produce argininosuccinate [251]. A homologous enzyme has not been characterized so far in *Plasmodium* cells. These results from Rajaram *et al.* [250] imply that parasites would be able to develop resistance to SC83288 relatively fast if PffH were the unique molecular target of the drug. However, it was not only seen that the generation of resistant parasite lines is difficult but also that the drug interacts with a number of *P. falciparum* proteins. Thus, parasites that are able to survive due to metabolic rewiring would be then killed through secondary modes of action.

The complex landscape of effects of SC83288 makes the interpretation of drug-drug interaction profiles, such as the antagonism observed with pyrimethamine, a difficult task. As they can be understood through the use of different and sometimes even conflicting hypotheses [252], these results are neither support nor disprove PffH as the main target of SC83288.

Besides PffH, at least three other enzymes can be considered as potential targets for SC83288 among the interacting proteins found through whole-cell CETSA: the DNA replication licensing factor MCM2 (PF3D7_1417800), the cytosolic Fe-S protein assembly protein 1 (CIA1, PF3D7_1209400) and the casein kinase 2 alpha subunit (CK2, PF3D7_1108400). The existence of multiple modes of action, also referred to as polypharmacology, has historically been considered a negative feature of drugs in development.

However, this kind of drugs have proven to be effective in complex diseases [253]. As mentioned for MB, this multi-target profile is associated with a lower risk of resistance development. This is undoubtedly an attractive feature once safety has been demonstrated. Some of the effects observed in parasites treated with SC83288 can be explained through the action of the compound over the aforementioned proteins. For instance, disruption of MCM2 would block DNA replication of parasites with enough nucleotide levels, as it is necessary for the correct formation of the MCM complex, the pre-replicative complex and the progression of the replication fork [194]. Additionally, hCK2 has been shown to have a wide range of substrate proteins, of which more than one third are involved in gene expression and translation [254]. Despite having a different quaternary structure, the catalytic subunit of PfCK2 has a similar amino acid sequence to that of the human enzyme [255], and it has also been linked with chromatin assembly and DNA repair [219]. Silmitasertib (CX- 4945) is a potent inhibitor of hCK2 [256] in clinical trials for the treatment of advanced cholangiocarcinoma (ClinicalTrials.gov Identifier: NCT02128282) and proposed as well for the treatment of hematological tumors [257]. It has also shown activity against PfCK2, albeit lower, suggesting a different binding mode for the inhibition of the parasite enzyme [255]. Last but not least, an interaction with CIA1 could also contribute to the mode of action of SC83288, as its disruption would block the complete synthesis of a number of proteins containing [Fe-S] clusters. On one hand, the absence of [Fe-S] would interfere with the processes in which they participate, such as DNA replication, DNA repair, protein synthesis, among others [205]. On the other hand, the disruption on CIA1 function could result in the exposure of [Fe-S] clusters, which cannot be delivered to the corresponding apoprotein, to oxidative damage. Then, Fe²⁺ released from the damaged cluster could propagate damage through the Fenton reaction and induce lipid peroxidation and membrane damage. However, there is no evidence that the clusters are indeed more likely to be damaged upon disruption of CIA1. There should be already a source of oxidative stress in the cell, and repair systems have been observed in other organisms [258]. In a scenario where PffH and CIA1 are simultaneously disrupted by SC83288, the consequences presented earlier could set the right environment for an increased susceptibility of [Fe-S] clusters to oxidative damage given the reduced antioxidant capacity of the parasite. Furthermore, among the differentially expressed genes (DEG) upon treatment with 5 nM SC83288, aconitate hydratase is upregulated. This enzyme does not only have a role in the CAC but also in iron regulation [259, 260]. It is worth noting that FH is a [Fe-S] protein itself, and that upon disruption of assembly, its activity would also be impaired from the absence of newly synthesized protein. Interestingly, another observed DEG is *SufA*, which encodes a protein involved

in the assembly of [Fe-S] proteins in the apicoplast that is probably used as the scaffold for the cluster assembly [203] and its expression is downregulated across all concentrations of SC83288 treatment. Overall, while the interaction with CIA1 seems to be part of the mode of action of SC83288, the mechanistic details are more complex to explain than those arising from the interaction with FH, partly due to the CIA system being understudied in *P. falciparum*. Additionally, since the interaction of the drug with the proteins has only been evidenced through CETSA, the reliability of the ITDR curves favours the hypothesis of FH being the main target.

5. Conclusion and outlook

SC83288 is a leading candidate for a new class of antimalarials and it has consistently showed to be a promising candidate for the treatment of severe malaria. Preclinical studies position it in a favourable place for future clinical trials [78, 80, 81]. So far, although a possible mechanism of resistance has been characterised, there were no clear insights into the mode in which the drug exerts its antiplasmodial activity.

The aim of this doctoral thesis was to shed light into the mode of action and the molecular targets of SC83288. From the results obtained, I was able to formulate a hypothesis that positions the enzyme fumarate hydratase as the main target of the compound. However, the data suggests that the drug has multiple targets, among which MCM2, CK2 and CIA1 can be found. This hypothesis needs further experimental evidence and validation that supports it.

The first and obvious test to carry out, is the measurement of PfFH activity inhibition by SC83288. Besides that, it would be beneficial to further explore the metabolomic response of parasites to the drug in a more systematic approach by either approximating the treatment conditions to those of other approaches already employed, such as CETSA or transcriptomics, or by the use of a time- or concentration-resolved experiment [243].

A key observation that deserves further investigation is the apparent membrane damage evident from the live cell imaging results. The combination of electron microscopy and the distribution of the Ca^{2+} dye Fluo-4-AM observed through fluorescent microscopy has been used before to evaluate the integrity of the food vacuolar membrane [240] and could be applied for the same purpose here. Additionally, the potential lipid peroxidation can be detected through the measurement of malondialdehyde formation [261], readily analysed nowadays in cell extracts or in a cell-based assay by using commercially available kits [262, 263].

The interaction of SC83288 with the four candidate targets can be validated through the use of DARTS [87]. Moreover, molecular docking approaches can support the hypothesized interaction with CK2 (whose structure has been characterized [256]) as well as with other proteins, in case a structural model of sufficient quality can be built for them. Additionally, the interaction with CK2 can be confirmed through the measurement of the protein enzymatic activity of CK2 in the presence of SC83288 [256].

The identification of proteins that interact with SC83288 through CETSA may be affected not only by the underrepresentation of membrane-bound proteins but also to false negatives due to the fact that not all protein interactions have an effect over thermal stability [85]. In order to obtain a more complete picture of the interactions partners and potential targets of SC83288 in *P. falciparum*, an antibody-based strategy could be followed. The generation of anti-SC83288 antibodies would represent an alternative to the modification of the drug structure for introduction of probes. Although it is a cost-intensive method and there is a risk of only obtaining antibodies with low affinity for the small molecule [264], anti-hapten antibodies have been successfully developed for the detection of toxins [265]. These anti-SC83288 molecules would not only allow the implementation of immunofluorescence-based assays but also the possibility of a pull-down strategy in the form of co-immunoprecipitation for the identification of interacting proteins [266].

Intracellular localization of SC83288 (through its alkyne tagged derivative SC106879) in WT parasites using a click chemistry-based approach on fixed samples proved unsuccessful. However, an analogous strategy can be followed in a live cell setting to eliminate the protein crosslinking caused by fixation, a probable cause of coupling reaction failure due to the alkyne group being shielded by protein structures. The alternative is the use of a copper-free live cell compatible click reaction, which requires the functionalization of SC83288 with an azide tag instead of the propargyl present in SC106879 and the use of a DIFO-fluorophore (difluorinated cyclooctyne) [267].

Overall, despite the need of further experimental evidence for the validation of my hypothesis, the results presented in this work constitute a substantial leap towards the elucidation of the mode of action of SC83288.

6. References

1. Cox, F.E.G., *History of the discovery of the malaria parasites and their vectors*. Parasites & Vectors, 2010. **3**(1): p. 5.
2. Bruce-Chwatt, L.J., *Alphonse Laveran's discovery 100 years ago and today's global fight against malaria*. J R Soc Med, 1981. **74**(7): p. 531-6.
3. Alphonse Laveran, C.L., *A Newly Discovered Parasite in the Blood of Patients Suffering from Malaria. Parasitic Etiology of Attacks of Malaria*. Reviews of Infectious Diseases, 1982. **4**(4): p. 908-911.
4. Ross, R., *On some Peculiar Pigmented Cells Found in Two Mosquitos Fed on Malarial Blood*. Br Med J, 1897. **2**(1929): p. 1786-8.
5. Manson, P., *SURGEON-MAJOR RONALD ROSS'S RECENT INVESTIGATIONS on the MOSQUITO-MALARIA THEORY*. Br Med J, 1898. **1**(1955): p. 1575-7.
6. Ross, R., *The role of the mosquito in the evolution of the malarial parasite: the recent researches of Surgeon-Major Ronald Ross, I.M.S. 1898*. Yale J Biol Med, 2002. **75**(2): p. 103-5.
7. Nobel Prize Organization AB, *All Nobel Prizes in Physiology or Medicine*. [07-05-2022]; Available from: <https://www.nobelprize.org/prizes/lists/all-nobel-laureates-in-physiology-or-medicine>.
8. Kantele, A. and T.S. Jokiranta, *Review of cases with the emerging fifth human malaria parasite, Plasmodium knowlesi*. Clin Infect Dis, 2011. **52**(11): p. 1356-62.
9. Sutherland, C.J., et al., *Two Nonrecombining Sympatric Forms of the Human Malaria Parasite Plasmodium ovale Occur Globally*. The Journal of Infectious Diseases, 2010. **201**(10): p. 1544-1550.
10. WHO, *World malaria report 2018*. 2018: WHO Press, Geneva
11. WHO, *World Malaria Report 2021*. 2021: WHO Press, Geneva.
12. Moxon, C.A., et al., *New Insights into Malaria Pathogenesis*. Annu Rev Pathol, 2020. **15**: p. 315-343.
13. Ashley, E.A., A. Pyae Phyo, and C.J. Woodrow, *Malaria*. The Lancet, 2018. **391**(10130): p. 1608-1621.
14. *Severe Malaria*. Tropical Medicine & International Health, 2014. **19**(s1): p. 7-131.
15. WHO, *World malaria report 2020: 20 years of global progress and challenges*. 2020, Geneva: World Health Organization.
16. Weiss, D.J., et al., *Mapping the global prevalence, incidence, and mortality of Plasmodium falciparum, 2000-17: a spatial and temporal modelling study*. The Lancet, 2019. **394**(10195): p. 322-331.
17. Malaria Atlas Project. [07-05-2022]; Available from: <https://malariaatlas.org/>.

18. WHO, *Global technical strategy for malaria 2016–2030*. 2021 update ed. 2021, Geneva: World Health Organization.
19. Cowman, A.F., et al., *Malaria: Biology and Disease*. Cell, 2016. **167**(3): p. 610-624.
20. Matthews, H., C.W. Duffy, and C.J. Merrick, *Checks and balances? DNA replication and the cell cycle in Plasmodium*. Parasites & Vectors, 2018. **11**(1): p. 216.
21. Klaus, S., et al., *Asynchronous nuclear cycles in multinucleated Plasmodium falciparum facilitate rapid proliferation*. Science Advances, 2022. **8**(13): p. eabj5362.
22. Arnot, D.E., E. Ronander, and D.C. Bengtsson, *The progression of the intraerythrocytic cell cycle of Plasmodium falciparum and the role of the centriolar plaques in asynchronous mitotic division during schizogony*. International Journal for Parasitology, 2011. **41**(1): p. 71-80.
23. Quashie, Neils B., et al., *A comprehensive model of purine uptake by the malaria parasite Plasmodium falciparum: identification of four purine transport activities in intraerythrocytic parasites*. Biochemical Journal, 2008. **411**(2): p. 287-295.
24. Cassera, M.B., et al., *Erythrocytic Adenosine Monophosphate as an Alternative Purine Source in Plasmodium falciparum*. Journal of Biological Chemistry, 2008. **283**(47): p. 32889-32899.
25. Frame, I.J., et al., *Malaria parasite type 4 equilibrative nucleoside transporters (ENT4) are purine transporters with distinct substrate specificity*. Biochemical Journal, 2012. **446**(2): p. 179-190.
26. Ginsburg, H. and A.M. Abdel-Haleem, *Malaria Parasite Metabolic Pathways (MPMP) Upgraded with Targeted Chemical Compounds*. Trends in Parasitology, 2016. **32**(1): p. 7-9.
27. Ginsburg, H., *The biochemistry of Plasmodium falciparum*, in *Advances in Malaria Research*. 2016. p. 219-290.
28. Phillips, M.A. and P.K. Rathod, *Plasmodium dihydroorotate dehydrogenase: a promising target for novel anti-malarial chemotherapy*. Infectious disorders drug targets, 2010. **10**(3): p. 226-239.
29. Achan, J., et al., *Quinine, an old anti-malarial drug in a modern world: role in the treatment of malaria*. Malaria Journal, 2011. **10**(1): p. 144.
30. *Quinine*, in *Classical Methods in Structure Elucidation of Natural Products*. 2018. p. 151-165.
31. Renslo, A.R., *Antimalarial Drug Discovery: From Quinine to the Dream of Eradication*. ACS Medicinal Chemistry Letters, 2013. **4**(12): p. 1126-1128.
32. Dziekan, J.M., et al., *Identifying purine nucleoside phosphorylase as the target of quinine using cellular thermal shift assay*. Science Translational Medicine, 2019. **11**(473): p. eaau3174.
33. WHO, *World Health Organization model list of essential medicines: 22nd list (2021)*. 2021, World Health Organization: Geneva.

34. Greenwood, D., *Conflicts of interest: the genesis of synthetic antimalarial agents in peace and war*. Journal of Antimicrobial Chemotherapy, 1995. **36**(5): p. 857-872.
35. Oien, D.B., et al., *Repurposing quinacrine for treatment-refractory cancer*. Semin Cancer Biol, 2021. **68**: p. 21-30.
36. Loeb, F., et al., *ACTIVITY OF A NEW ANTIMALARIAL AGENT, CHLOROQUINE (SN 7618): Statement Approved by the Board for Coordination of Malarial Studies*. Journal of the American Medical Association, 1946. **130**(16): p. 1069-1070.
37. Payne, D., *Spread of chloroquine resistance in Plasmodium falciparum*. Parasitology Today, 1987. **3**(8): p. 241-246.
38. Olafson, K.N., et al., *Antimalarials inhibit hematin crystallization by unique drug-surface site interactions*. Proceedings of the National Academy of Sciences, 2017. **114**(29): p. 7531-7536.
39. Saliba, K.J., P.I. Folb, and P.J. Smith, *Role for the Plasmodium falciparum Digestive Vacuole in Chloroquine Resistance*. Biochemical Pharmacology, 1998. **56**(3): p. 313-320.
40. Yayon, A., Z.I. Cabantchik, and H. Ginsburg, *Identification of the acidic compartment of Plasmodium falciparum-infected human erythrocytes as the target of the antimalarial drug chloroquine*. The EMBO Journal, 1984. **3**(11): p. 2695-2700.
41. Lakshmanan, V., et al., *A critical role for PfCRT K76T in Plasmodium falciparum verapamil-reversible chloroquine resistance*. The EMBO Journal, 2005. **24**(13): p. 2294-2305.
42. Sanchez, C.P., et al., *Differences in trans-stimulated chloroquine efflux kinetics are linked to PfCRT in Plasmodium falciparum*. Molecular Microbiology, 2007. **64**(2): p. 407-420.
43. Martin, R.E., et al., *Chloroquine Transport via the Malaria Parasite Chloroquine Resistance Transporter*. Science, 2009. **325**(5948): p. 1680-1682.
44. Paguio, M.F., M. Cabrera, and P.D. Roepe, *Chloroquine Transport in Plasmodium falciparum. 2. Analysis of PfCRT-Mediated Drug Transport Using Proteoliposomes and a Fluorescent Chloroquine Probe*. Biochemistry, 2009. **48**(40): p. 9482-9491.
45. Sanchez, C.P., et al., *Phosphomimetic substitution at Ser-33 of the chloroquine resistance transporter PfCRT reconstitutes drug responses in Plasmodium falciparum*. Journal of Biological Chemistry, 2019. **294**(34): p. 12766-12778.
46. Kim, J., et al., *Structure and drug resistance of the Plasmodium falciparum transporter PfCRT*. Nature, 2019. **576**(7786): p. 315-320.
47. Croft, A.M., *A lesson learnt: the rise and fall of Lariam and Halfan*. Journal of the Royal Society of Medicine, 2007. **100**(4): p. 170-174.
48. Tse, E.G., M. Korsik, and M.H. Todd, *The past, present and future of anti-malarial medicines*. Malaria Journal, 2019. **18**(1): p. 93.

49. Preechapornkul, P., et al., *Plasmodium falciparum pfmdr1 Amplification, Mefloquine Resistance, and Parasite Fitness*. Antimicrobial Agents and Chemotherapy, 2009. **53**(4): p. 1509-1515.
50. Price, R.N., et al., *Mefloquine resistance in Plasmodium falciparum and increased pfmdr1 gene copy number*. Lancet (London, England), 2004. **364**(9432): p. 438-447.
51. Schlagenhauf, P., et al., *The position of mefloquine as a 21st century malaria chemoprophylaxis*. Malar J, 2010. **9**: p. 357.
52. Nevin, R.L. and A.M. Croft, *Psychiatric effects of malaria and anti-malarial drugs: historical and modern perspectives*. Malaria Journal, 2016. **15**(1): p. 332.
53. Cosgriff, T.M., et al., *Evaluation of the antimalarial activity of the phenanthrenemethanol halofantrine (WR 171,669)*. Am J Trop Med Hyg, 1982. **31**(6): p. 1075-9.
54. Wang, J., et al., *Artemisinin, the Magic Drug Discovered from Traditional Chinese Medicine*. Engineering, 2019. **5**(1): p. 32-39.
55. Faurant, C., *From bark to weed: the history of artemisinin*. Parasite, 2011. **18**(3): p. 215-8.
56. White, N.J., T.T. Hien, and F.H. Nosten, *A Brief History of Qinghaosu*. Trends in Parasitology, 2015. **31**(12): p. 607-610.
57. Müller, O., G.Y. Lu, and L. von Seidlein, *Geographic expansion of artemisinin resistance*. Journal of Travel Medicine, 2019. **26**(4).
58. Phuc, B.Q., et al., *Treatment Failure of Dihydroartemisinin/Piperaquine for Plasmodium falciparum Malaria, Vietnam*. Emerging infectious diseases, 2017. **23**(4): p. 715-717.
59. Thanh, N.V., et al., *Rapid decline in the susceptibility of Plasmodium falciparum to dihydroartemisinin–piperaquine in the south of Vietnam*. Malaria Journal, 2017. **16**(1): p. 27.
60. Ashley, E.A., et al., *Spread of artemisinin resistance in Plasmodium falciparum malaria*. The New England journal of medicine, 2014. **371**(5): p. 411-423.
61. Dondorp, A.M., et al., *Artemisinin resistance in Plasmodium falciparum malaria*. The New England journal of medicine, 2009. **361**(5): p. 455-467.
62. O'Neill, P.M., V.E. Barton, and S.A. Ward, *The molecular mechanism of action of artemisinin--the debate continues*. Molecules (Basel, Switzerland), 2010. **15**(3): p. 1705-1721.
63. Wang, J., et al., *Haem-activated promiscuous targeting of artemisinin in Plasmodium falciparum*. Nat Commun, 2015. **6**: p. 10111.
64. Tilley, L., et al., *Artemisinin Action and Resistance in Plasmodium falciparum*. Trends Parasitol, 2016. **32**(9): p. 682-696.

65. Mok, S., et al., *Drug resistance. Population transcriptomics of human malaria parasites reveals the mechanism of artemisinin resistance*. *Science*, 2015. **347**(6220): p. 431-5.
66. Ariey, F., et al., *A molecular marker of artemisinin-resistant Plasmodium falciparum malaria*. *Nature*, 2014. **505**(7481): p. 50-55.
67. Talman, A.M., et al., *Artemisinin Bioactivity and Resistance in Malaria Parasites*. *Trends in Parasitology*, 2019. **35**(12): p. 953-963.
68. Cui, L. and X.-z. Su, *Discovery, mechanisms of action and combination therapy of artemisinin*. *Expert Review of Anti-infective Therapy*, 2009. **7**(8): p. 999-1013.
69. Croft, S.L., et al., *Review of pyronaridine anti-malarial properties and product characteristics*. *Malaria Journal*, 2012. **11**(1): p. 270.
70. Eastman, R.T. and D.A. Fidock, *Artemisinin-based combination therapies: a vital tool in efforts to eliminate malaria*. *Nature Reviews Microbiology*, 2009. **7**(12): p. 864-874.
71. Sirima, S.B. and A. Gansané, *Artesunate–amodiaquine for the treatment of uncomplicated malaria*. *Expert Opinion on Investigational Drugs*, 2007. **16**(7): p. 1079-1085.
72. Davis, T.M., et al., *Piperaquine: a resurgent antimalarial drug*. *Drugs*, 2005. **65**(1): p. 75-87.
73. Nzila, A., *The past, present and future of antifolates in the treatment of Plasmodium falciparum infection*. *Journal of Antimicrobial Chemotherapy*, 2006. **57**(6): p. 1043-1054.
74. Patel, S.N. and K.C. Kain, *Atovaquone/proguanil for the prophylaxis and treatment of malaria*. *Expert Rev Anti Infect Ther*, 2005. **3**(6): p. 849-61.
75. Burrows, J.N., et al., *New developments in anti-malarial target candidate and product profiles*. *Malaria Journal*, 2017. **16**(1): p. 26.
76. *MMV-supported drug development projects*. Last updated March 2022 [03-05-2022]; Available from: <https://www.mmv.org/research-development/mmv-supported-projects>.
77. Wells, T.N.C., R.H. van Huijsduijnen, and W.C. Van Voorhis, *Malaria medicines: a glass half full?* *Nature Reviews Drug Discovery*, 2015. **14**(6): p. 424-442.
78. Pegoraro, S., et al., *SC83288 is a clinical development candidate for the treatment of severe malaria*. *Nat Commun*, 2017. **8**: p. 14193.
79. Leban, J., et al., *Sulfonyl-phenyl-ureido benzamidines; a novel structural class of potent antimalarial agents*. *Bioorg Med Chem Lett*, 2004. **14**(8): p. 1979-82.
80. Duffey, M., C.P. Sanchez, and M. Lanzer, *Profiling of the anti-malarial drug candidate SC83288 against artemisinins in Plasmodium falciparum*. *Malaria Journal*, 2018. **17**(1): p. 121.

81. Duffey, M., *Characterization of amicarbalide derivatives as new antimalarial compounds: Investigation of the mode of action and the mechanism of resistance*. 2018, Ruperto-Carola University of Heidelberg.
82. Wiedemar, N., D.A. Hauser, and P. Mäser, *100 Years of Suramin*. *Antimicrobial agents and chemotherapy*, 2020. **64**(3): p. e01168-19.
83. Ziegler, S., et al., *Target Identification for Small Bioactive Molecules: Finding the Needle in the Haystack*. *Angewandte Chemie International Edition*, 2013. **52**(10): p. 2744-2792.
84. Luth, M.R., et al., *Using in Vitro Evolution and Whole Genome Analysis To Discover Next Generation Targets for Antimalarial Drug Discovery*. *ACS Infectious Diseases*, 2018. **4**(3): p. 301-314.
85. Li, J., et al., *Label-free technologies for target identification and validation*. *MedChemComm*, 2016. **7**(5): p. 769-777.
86. Park, H., J. Ha, and S.B. Park, *Label-free target identification in drug discovery via phenotypic screening*. *Current Opinion in Chemical Biology*, 2019. **50**: p. 66-72.
87. Lomenick, B., et al., *Target identification using drug affinity responsive target stability (DARTS)*. *Proceedings of the National Academy of Sciences*, 2009. **106**(51): p. 21984.
88. Mateus, A., T.A. Määttä, and M.M. Savitski, *Thermal proteome profiling: unbiased assessment of protein state through heat-induced stability changes*. *Proteome Science*, 2017. **15**(1): p. 13.
89. Davis, R.L., *Mechanism of Action and Target Identification: A Matter of Timing in Drug Discovery*. *iScience*, 2020. **23**(9): p. 101487.
90. Walliker, D., et al., *Genetic analysis of the human malaria parasite Plasmodium falciparum*. *Science*, 1987. **236**(4809): p. 1661-6.
91. Doherty, J.P., et al., *Escherichia coli host strains SURETM and SRB fail to preserve a palindrome cloned in lambda phage: improved alternate host strains*. *Gene*, 1993. **124**(1): p. 29-35.
92. Przyborski, J.M., et al., *Trafficking of STEVOR to the Maurer's clefts in Plasmodium falciparum-infected erythrocytes*. *The EMBO Journal*, 2005. **24**(13): p. 2306-2317.
93. Ghorbal, M., et al., *Genome editing in the human malaria parasite Plasmodium falciparum using the CRISPR-Cas9 system*. *Nat Biotechnol*, 2014. **32**(8): p. 819-21.
94. Quinlan, A.R. and I.M. Hall, *BEDTools: a flexible suite of utilities for comparing genomic features*. *Bioinformatics*, 2010. **26**(6): p. 841-2.
95. Yamanishi, Y., et al., *DINIES: drug-target interaction network inference engine based on supervised analysis*. *Nucleic Acids Research*, 2014. **42**(W1): p. W39-W45.
96. Schindelin, J., et al., *Fiji: an open-source platform for biological-image analysis*. *Nature Methods*, 2012. **9**(7): p. 676-682.

97. Friesner, R.A., et al., *Extra Precision Glide: Docking and Scoring Incorporating a Model of Hydrophobic Enclosure for Protein–Ligand Complexes*. Journal of Medicinal Chemistry, 2006. **49**(21): p. 6177-6196.
98. Halgren, T.A., et al., *Glide: A New Approach for Rapid, Accurate Docking and Scoring. 2. Enrichment Factors in Database Screening*. Journal of Medicinal Chemistry, 2004. **47**(7): p. 1750-1759.
99. Friesner, R.A., et al., *Glide: A New Approach for Rapid, Accurate Docking and Scoring. 1. Method and Assessment of Docking Accuracy*. Journal of Medicinal Chemistry, 2004. **47**(7): p. 1739-1749.
100. Kim, D., et al., *Graph-based genome alignment and genotyping with HISAT2 and HISAT-genotype*. Nat Biotechnol, 2019. **37**(8): p. 907-915.
101. Creek, D.J., et al., *IDEOM: an Excel interface for analysis of LC-MS-based metabolomics data*. Bioinformatics, 2012. **28**(7): p. 1048-9.
102. Kanehisa, M., et al., *KEGG: integrating viruses and cellular organisms*. Nucleic acids research, 2021. **49**(D1): p. D545-D551.
103. Caspi, R., et al., *The MetaCyc database of metabolic pathways and enzymes - a 2019 update*. Nucleic Acids Res, 2020. **48**(D1): p. D445-d453.
104. Scheltema, R.A., et al., *PeakML/mzMatch: A File Format, Java Library, R Library, and Tool-Chain for Mass Spectrometry Data Analysis*. Analytical Chemistry, 2011. **83**(7): p. 2786-2793.
105. Sanderson, T. and J. Rayner, *PhenoPlasm: a database of disruption phenotypes for malaria parasite genes [version 1; peer review: 2 approved]*. Wellcome Open Research, 2017. **2**(45).
106. Kelley, L.A., et al., *The Phyre2 web portal for protein modeling, prediction and analysis*. Nature Protocols, 2015. **10**(6): p. 845-858.
107. Amos, B., et al., *VEuPathDB: the eukaryotic pathogen, vector and host bioinformatics resource center*. Nucleic Acids Research, 2021.
108. Yates, C.M., et al., *SuSPect: enhanced prediction of single amino acid variant (SAV) phenotype using network features*. J Mol Biol, 2014. **426**(14): p. 2692-701.
109. Urán Landaburu, L., et al., *TDR Targets 6: driving drug discovery for human pathogens through intensive chemogenomic data integration*. Nucleic acids research, 2020. **48**(D1): p. D992-D1005.
110. Babraham Bioinformatics, *Trim Galore!* [03-05-2022]; Available from: https://www.bioinformatics.babraham.ac.uk/projects/trim_galore/.
111. Ramirez-Gaona, M., et al., *YMDB 2.0: a significantly expanded version of the yeast metabolome database*. Nucleic Acids Res, 2017. **45**(D1): p. D440-d445.
112. Consortium, T.U., *UniProt: the universal protein knowledgebase in 2021*. Nucleic Acids Research, 2020. **49**(D1): p. D480-D489.

113. Smith, C.A., et al., *XCMS: Processing Mass Spectrometry Data for Metabolite Profiling Using Nonlinear Peak Alignment, Matching, and Identification*. Analytical Chemistry, 2006. **78**(3): p. 779-787.
114. Trager, W. and J.B. Jensen, *Human Malaria Parasites in Continuous Culture*. Science, 1976. **193**(4254): p. 673-675.
115. Silamut, K., et al., *A quantitative analysis of the microvascular sequestration of malaria parasites in the human brain*. The American journal of pathology, 1999. **155**(2): p. 395-410.
116. Radfar, A., et al., *Synchronous culture of Plasmodium falciparum at high parasitemia levels*. Nature Protocols, 2009. **4**(12): p. 1899-1915.
117. Lambros, C. and J.P. Vanderberg, *Synchronization of Plasmodium falciparum erythrocytic stages in culture*. J Parasitol, 1979. **65**(3): p. 418-20.
118. Coronado, L.M., C.T. Nadovich, and C. Spadafora, *Malarial hemozoin: From target to tool*. Biochimica et Biophysica Acta (BBA) - General Subjects, 2014. **1840**(6): p. 2032-2041.
119. Ribaut, C., et al., *Concentration and purification by magnetic separation of the erythrocytic stages of all human Plasmodium species*. Malaria Journal, 2008. **7**(1): p. 45.
120. Paul, F., et al., *Separation of malaria-infected erythrocytes from whole blood: use of a selective high-gradient magnetic separation technique*. Lancet, 1981. **2**(8237): p. 70-1.
121. M. Ausubel, R.B., R.E. Kingston, D.D. Moore, J.G. Seidman, J.A. Smith, and K. Struhl, *Current protocols in molecular biology*. 1991, New York: John Wiley and Sons.
122. Bradford, M.M., *A rapid and sensitive method for the quantitation of microgram quantities of protein utilizing the principle of protein-dye binding*. Analytical Biochemistry, 1976. **72**(1): p. 248-254.
123. Franken, H., et al., *Thermal proteome profiling for unbiased identification of direct and indirect drug targets using multiplexed quantitative mass spectrometry*. Nat Protoc, 2015. **10**(10): p. 1567-93.
124. Dziekan, J.M., et al., *Cellular thermal shift assay for the identification of drug-target interactions in the Plasmodium falciparum proteome*. Nature Protocols, 2020. **15**(6): p. 1881-1921.
125. Kamchonwongpaisan, S., et al., *Inhibitors of multiple mutants of Plasmodium falciparum dihydrofolate reductase and their antimalarial activities*. J Med Chem, 2004. **47**(3): p. 673-80.
126. Sambrook, J. and D.W. Russell, *Fragmentation of DNA by Sonication*. Cold Spring Harbor Protocols, 2006. **2006**(4): p. pdb.prot4538.
127. Williams, A.K., et al., *Determination of the drug-DNA binding modes using fluorescence-based assays*. Analytical Biochemistry, 2012. **422**(2): p. 66-73.

128. Smilkstein, M., et al., *Simple and Inexpensive Fluorescence-Based Technique for High-Throughput Antimalarial Drug Screening*. *Antimicrobial Agents and Chemotherapy*, 2004. **48**(5): p. 1803-1806.
129. Wang, P., et al., *Sulfadoxine resistance in the human malaria parasite Plasmodium falciparum is determined by mutations in dihydropteroate synthetase and an additional factor associated with folate utilization*. *Mol Microbiol*, 1997. **23**(5): p. 979-86.
130. Wang, P., P.F. Sims, and J.E. Hyde, *A modified in vitro sulfadoxine susceptibility assay for Plasmodium falciparum suitable for investigating Fansidar resistance*. *Parasitology*, 1997. **115** (Pt 3): p. 223-30.
131. Fivelman, Q.L., I.S. Adagu, and D.C. Warhurst, *Modified fixed-ratio isobologram method for studying in vitro interactions between atovaquone and proguanil or dihydroartemisinin against drug-resistant strains of Plasmodium falciparum*. *Antimicrob Agents Chemother*, 2004. **48**(11): p. 4097-102.
132. Gabryszewski, S.J., et al., *Evolution of Fitness Cost-Neutral Mutant PfCRT Conferring P. falciparum 4-Aminoquinoline Drug Resistance Is Accompanied by Altered Parasite Metabolism and Digestive Vacuole Physiology*. *PLOS Pathogens*, 2016. **12**(11): p. e1005976.
133. Grüring, C. and T. Spielmann, *Chapter five - Imaging of Live Malaria Blood Stage Parasites*, in *Methods in Enzymology*, P.M. Conn, Editor. 2012, Academic Press. p. 81-92.
134. Kucharski, M., et al., *A comprehensive RNA handling and transcriptomics guide for high-throughput processing of Plasmodium blood-stage samples*. *Malaria Journal*, 2020. **19**(1): p. 363.
135. Li, H., et al., *The Sequence Alignment/Map format and SAMtools*. *Bioinformatics*, 2009. **25**(16): p. 2078-9.
136. Patel, P.H., et al., *Omecamtiv Mecarbil: A Novel Mechanistic and Therapeutic Approach to Chronic Heart Failure Management*. *Cureus*, 2021. **13**(1): p. e12419.
137. Morgan, B.P., et al., *Discovery of omecamtiv mecarbil the first, selective, small molecule activator of cardiac Myosin*. *ACS Med Chem Lett*, 2010. **1**(9): p. 472-7.
138. Müller, I.B. and J.E. Hyde, *Folate metabolism in human malaria parasites—75 years on*. *Molecular and Biochemical Parasitology*, 2013. **188**(1): p. 63-77.
139. Xavier, J.B. and C. Sander, *Principle of System Balance for Drug Interactions*. 2010. **362**(14): p. 1339-1340.
140. Bahl, A., et al., *PlasmoDB: the Plasmodium genome resource. A database integrating experimental and computational data*. *Nucleic Acids Res*, 2003. **31**(1): p. 212-5.
141. Kasekarn, W., et al., *Molecular characterization of bifunctional hydroxymethyldihydropterin pyrophosphokinase-dihydropteroate synthase from Plasmodium falciparum*. *Molecular and Biochemical Parasitology*, 2004. **137**(1): p. 43-53.

142. Chitnumsub, P., et al., *The structure of Plasmodium falciparum hydroxymethyldihydropterin pyrophosphokinase-dihydropteroate synthase reveals the basis of sulfa resistance*. The FEBS Journal, 2020. **287**(15): p. 3273-3297.
143. Sturm, N., et al., *Identification of Proteins Targeted by the Thioredoxin Superfamily in Plasmodium falciparum*. PLOS Pathogens, 2009. **5**(4): p. e1000383.
144. Albers, E., *Metabolic characteristics and importance of the universal methionine salvage pathway recycling methionine from 5'-methylthioadenosine*. IUBMB Life, 2009. **61**(12): p. 1132-1142.
145. Sekowska, A., H. Ashida, and A. Danchin, *Revisiting the methionine salvage pathway and its paralogues*. Microbial biotechnology, 2019. **12**(1): p. 77-97.
146. Ting, L.-M., et al., *Targeting a Novel Plasmodium falciparum Purine Recycling Pathway with Specific Immucillins*. Journal of Biological Chemistry, 2005. **280**(10): p. 9547-9554.
147. Riscoe, M.K., A.J. Ferro, and J.H. Fitchen, *Analogs of 5-methylthioribose, a novel class of antiprotozoal agents*. Antimicrobial agents and chemotherapy, 1988. **32**(12): p. 1904-1906.
148. Polko, J.K. and J.J. Kieber, *1-Aminocyclopropane 1-Carboxylic Acid and Its Emerging Role as an Ethylene-Independent Growth Regulator*. Frontiers in Plant Science, 2019. **10**.
149. Vendrell, M., *Biology and Biotechnology of the Plant Hormone Ethylene III*. 2003: IOS Press.
150. Dubois, M., L. Van den Broeck, and D. Inzé, *The Pivotal Role of Ethylene in Plant Growth*. Trends in Plant Science, 2018. **23**(4): p. 311-323.
151. Li, D., et al., *Something old, something new: Conservation of the ethylene precursor 1-amino-cyclopropane-1-carboxylic acid as a signaling molecule*. Current Opinion in Plant Biology, 2022. **65**: p. 102116.
152. Tsang, D.L., et al., *Cell Wall Integrity Controls Root Elongation via a General 1-Aminocyclopropane-1-Carboxylic Acid-Dependent, Ethylene-Independent Pathway* Plant Physiology, 2011. **156**(2): p. 596-604.
153. Van de Poel, B. and D. Van Der Straeten, *1-aminocyclopropane-1-carboxylic acid (ACC) in plants: more than just the precursor of ethylene!* Frontiers in Plant Science, 2014. **5**.
154. Wein, S., et al., *Contribution of the precursors and interplay of the pathways in the phospholipid metabolism of the malaria parasite*. Journal of lipid research, 2018. **59**(8): p. 1461-1471.
155. Kilian, N., et al., *Role of phospholipid synthesis in the development and differentiation of malaria parasites in the blood*. The Journal of biological chemistry, 2018. **293**(45): p. 17308-17316.

156. Purfield, A.E., R.R. Tidwell, and S.R. Meshnick, *The diamidine DB75 targets the nucleus of Plasmodium falciparum*. *Malaria Journal*, 2009. **8**(1): p. 104.
157. Rampal, S., M.-S. Liu, and F.-T.A. Chen, *Characterization of TO-PRO-3 as an intercalator for double-stranded DNA analysis with red diode laser-induced fluorescence detection*. *Journal of Chromatography A*, 1997. **781**(1): p. 357-365.
158. Wilson, W.D., et al., *Binding of 4',6-diamidino-2-phenylindole (DAPI) to GC and mixed sequences in DNA: intercalation of a classical groove-binding molecule*. *Journal of the American Chemical Society*, 1989. **111**(13): p. 5008-5010.
159. Biancardi, A., et al., *An investigation of the photophysical properties of minor groove bound and intercalated DAPI through quantum-mechanical and spectroscopic tools*. *Physical Chemistry Chemical Physics*, 2013. **15**(13): p. 4596-4603.
160. Rostovtsev, V.V., et al., *A Stepwise Huisgen Cycloaddition Process: Copper(I)-Catalyzed Regioselective "Ligation" of Azides and Terminal Alkynes*. *Angewandte Chemie International Edition*, 2002. **41**(14): p. 2596-2599.
161. Tornøe, C.W., C. Christensen, and M. Meldal, *Peptidotriazoles on Solid Phase: [1,2,3]-Triazoles by Regiospecific Copper(I)-Catalyzed 1,3-Dipolar Cycloadditions of Terminal Alkynes to Azides*. *The Journal of Organic Chemistry*, 2002. **67**(9): p. 3057-3064.
162. Martell, J. and E. Weerapana, *Applications of Copper-Catalyzed Click Chemistry in Activity-Based Protein Profiling*. *Molecules*, 2014. **19**(2): p. 1378-1393.
163. Dennis, A.S.M., et al., *Cell Swelling Induced by the Antimalarial KAE609 (Cipargamin) and Other PfATP4-Associated Antimalarials*. *Antimicrobial Agents and Chemotherapy*, 2018. **62**(6): p. e00087-18.
164. Spillman, N.J. and K. Kirk, *The malaria parasite cation ATPase PfATP4 and its role in the mechanism of action of a new arsenal of antimalarial drugs*. *Int J Parasitol Drugs Drug Resist*, 2015. **5**(3): p. 149-62.
165. Linder, P., *Dead-box proteins: a family affair--active and passive players in RNP-remodeling*. *Nucleic Acids Res*, 2006. **34**(15): p. 4168-80.
166. Cordin, O., et al., *The DEAD-box protein family of RNA helicases*. *Gene*, 2006. **367**: p. 17-37.
167. Rocak, S. and P. Linder, *DEAD-box proteins: the driving forces behind RNA metabolism*. *Nat Rev Mol Cell Biol*, 2004. **5**(3): p. 232-41.
168. Linder, P., et al., *Birth of the D-E-A-D box*. *Nature*, 1989. **337**(6203): p. 121-122.
169. Kessler, M.M., et al., *Hrp1, a sequence-specific RNA-binding protein that shuttles between the nucleus and the cytoplasm, is required for mRNA 3'-end formation in yeast*. *Genes & development*, 1997. **11**(19): p. 2545-2556.
170. Linder, P., E. Gasteiger, and A. Bairoch, *A comprehensive web resource on RNA helicases from the baker's yeast Saccharomyces cerevisiae*. *Yeast*, 2000. **16**(6): p. 507-9.

171. Frick, D.N., *Helicases as antiviral drug targets*. Drug News Perspect, 2003. **16**(6): p. 355-62.
172. Frick, D.N. and A.M. Lam, *Understanding helicases as a means of virus control*. Curr Pharm Des, 2006. **12**(11): p. 1315-38.
173. Borowski, P., et al., *Characterization of imidazo[4,5-d]pyridazine nucleosides as modulators of unwinding reaction mediated by West Nile virus nucleoside triphosphatase/helicase: evidence for activity on the level of substrate and/or enzyme*. Antimicrob Agents Chemother, 2002. **46**(5): p. 1231-9.
174. Kleymann, G., *New antiviral drugs that target herpesvirus helicase primase enzymes*. Herpes, 2003. **10**(2): p. 46-52.
175. Kwong, A.D., B.G. Rao, and K.T. Jeang, *Viral and cellular RNA helicases as antiviral targets*. Nat Rev Drug Discov, 2005. **4**(10): p. 845-53.
176. Tuteja, R. and A. Pradhan, *Unraveling the 'DEAD-box' helicases of Plasmodium falciparum*. Gene, 2006. **376**(1): p. 1-12.
177. Tuteja, R., *Helicases - feasible antimalarial drug target for Plasmodium falciparum*. Febs j, 2007. **274**(18): p. 4699-704.
178. Pradhan, A. and R. Tuteja, *Bipolar, Dual Plasmodium falciparum helicase 45 expressed in the intraerythrocytic developmental cycle is required for parasite growth*. J Mol Biol, 2007. **373**(2): p. 268-81.
179. Cai, H., et al., *Predicting and exploring network components involved in pathogenesis in the malaria parasite via novel subnetwork alignments*. BMC Syst Biol, 2015. **9 Suppl 4**(Suppl 4): p. S1.
180. De Abreu Costa, L., et al., *Dimethyl Sulfoxide (DMSO) Decreases Cell Proliferation and TNF- α , IFN- γ , and IL-2 Cytokines Production in Cultures of Peripheral Blood Lymphocytes*. Molecules, 2017. **22**(11): p. 1789.
181. Brayton, C.F., *Dimethyl sulfoxide (DMSO): a review*. Cornell Vet, 1986. **76**(1): p. 61-90.
182. Becher, I., et al., *Thermal profiling reveals phenylalanine hydroxylase as an off-target of panobinostat*. Nature Chemical Biology, 2016. **12**: p. 908.
183. Savitski, M.M., et al., *Tracking cancer drugs in living cells by thermal profiling of the proteome*. Science, 2014. **346**(6205): p. 1255784.
184. Bulusu, V., V. Jayaraman, and H. Balaram, *Metabolic Fate of Fumarate, a Side Product of the Purine Salvage Pathway in the Intraerythrocytic Stages of Plasmodium falciparum*. Journal of Biological Chemistry, 2011. **286**(11): p. 9236-9245.
185. Jayaraman, V., et al., *Biochemical characterization and essentiality of Plasmodium fumarate hydratase*. Journal of Biological Chemistry, 2018. **293**(16): p. 5878-5894.
186. Ke, H., et al., *Genetic Investigation of Tricarboxylic Acid Metabolism during the Plasmodium falciparum Life Cycle*. Cell Reports, 2015. **11**(1): p. 164-174.

187. Alderson, N.L., et al., *S-(2-Succinyl)cysteine: A novel chemical modification of tissue proteins by a Krebs cycle intermediate*. Archives of Biochemistry and Biophysics, 2006. **450**(1): p. 1-8.
188. Sullivan, Lucas B., et al., *The Proto-oncometabolite Fumarate Binds Glutathione to Amplify ROS-Dependent Signaling*. Molecular Cell, 2013. **51**(2): p. 236-248.
189. Chua, C.-S., H. Low, and T.-S. Sim, *Co-chaperones of Hsp90 in Plasmodium falciparum and their concerted roles in cellular regulation*. Parasitology, 2014. **141**(9): p. 1177-1191.
190. Seraphim, T.V., et al., *Plasmodium falciparum R2TP complex: driver of parasite Hsp90 function*. Biophysical Reviews, 2019. **11**(6): p. 1007-1015.
191. Chua, C.S., et al., *Molecular analysis of Plasmodium falciparum co-chaperone Aha1 supports its interaction with and regulation of Hsp90 in the malaria parasite*. The International Journal of Biochemistry & Cell Biology, 2012. **44**(1): p. 233-245.
192. Collins, C.R., et al., *The Plasmodium falciparum pseudoprotease SERA5 regulates the kinetics and efficiency of malaria parasite egress from host erythrocytes*. PLOS Pathogens, 2017. **13**(7): p. e1006453.
193. Ansari, A. and R. Tuteja, *Genome wide comparative comprehensive analysis of Plasmodium falciparum MCM family with human host*. Communicative & Integrative Biology, 2012. **5**(6): p. 607-615.
194. Mitra, P., A.S. Deshmukh, and S.K. Dhar, *DNA replication during intra-erythrocytic stages of human malarial parasite Plasmodium falciparum*. Current Science, 2012. **102**(5): p. 725-740.
195. Patterson, S., et al., *Pre-replication complex organization in the atypical DNA replication cycle of Plasmodium falciparum: Characterization of the mini-chromosome maintenance (MCM) complex formation*. Molecular and Biochemical Parasitology, 2006. **145**(1): p. 50-59.
196. Wong, W., et al., *Cryo-EM structure of the Plasmodium falciparum 80S ribosome bound to the anti-protozoan drug emetine*. eLife, 2014. **3**: p. e03080.
197. Sun, M., et al., *Dynamical features of the Plasmodium falciparum ribosome during translation*. Nucleic Acids Research, 2015. **43**(21): p. 10515-10524.
198. Choveaux, D.L., et al., *Identification and initial characterisation of a Plasmodium falciparum Cox17 copper metallochaperone*. Experimental Parasitology, 2015. **148**: p. 30-39.
199. Asahi, H., et al., *Copper Homeostasis for the Developmental Progression of Intraerythrocytic Malarial Parasite*. Current topics in medicinal chemistry, 2016. **16**(27): p. 3048-3057.
200. Collins, C.R., et al., *The malaria parasite sheddase SUB2 governs host red blood cell membrane sealing at invasion*. eLife, 2020. **9**: p. e61121.

201. Djuika, C.F., et al., *Prokaryotic ancestry and gene fusion of a dual localized peroxiredoxin in malaria parasites*. Microbial cell (Graz, Austria), 2015. **2**(1): p. 5-13.
202. Djuika, C.F., et al., *Knockout of the peroxiredoxin 5 homologue PFAOP does not affect the artemisinin susceptibility of Plasmodium falciparum*. Scientific Reports, 2017. **7**(1): p. 4410.
203. Ali, V. and T. Nozaki, *Chapter One - Iron–Sulphur Clusters, Their Biosynthesis, and Biological Functions in Protozoan Parasites*, in *Advances in Parasitology*, D. Rollinson, Editor. 2013, Academic Press. p. 1-92.
204. Tsaousis, A.D., et al., *Evolution of the Cytosolic Iron-Sulfur Cluster Assembly Machinery in Blastocystis Species and Other Microbial Eukaryotes*. Eukaryotic Cell, 2014. **13**(1): p. 143-153.
205. Netz, D.J.A., et al., *Maturation of cytosolic and nuclear iron–sulfur proteins*. Trends in Cell Biology, 2014. **24**(5): p. 303-312.
206. Pino, P., et al., *Mitochondrial translation in absence of local tRNA aminoacylation and methionyl tRNAMet formylation in Apicomplexa*. Molecular Microbiology, 2010. **76**(3): p. 706-718.
207. Uddin, T., G.I. McFadden, and C.D. Goodman, *Validation of Putative Apicoplast-Targeting Drugs Using a Chemical Supplementation Assay in Cultured Human Malaria Parasites*. Antimicrobial Agents and Chemotherapy, 2018. **62**(1): p. e01161-17.
208. Istvan, E.S., et al., *Validation of isoleucine utilization targets in Plasmodium falciparum*. Proceedings of the National Academy of Sciences, 2011. **108**(4): p. 1627-1632.
209. Gorres, K.L. and R.T. Raines, *Prolyl 4-hydroxylase*. Critical Reviews in Biochemistry and Molecular Biology, 2010. **45**(2): p. 106-124.
210. West, C.M. and I.J. Blader, *Oxygen sensing by protozoans: how they catch their breath*. Current Opinion in Microbiology, 2015. **26**: p. 41-47.
211. Florimond, C., et al., *A Toxoplasma Prolyl Hydroxylase Mediates Oxygen Stress Responses by Regulating Translation Elongation*. mBio, 2019. **10**(2): p. e00234-19.
212. Zhang, M., et al., *Uncovering the essential genes of the human malaria parasite Plasmodium falciparum by saturation mutagenesis*. Science, 2018. **360**(6388): p. eaap7847.
213. van Esveld, S.L., et al., *A Prioritized and Validated Resource of Mitochondrial Proteins in Plasmodium Identifies Unique Biology*. mSphere, 2021. **6**(5): p. e0061421.
214. Ostera, G., et al., *Plasmodium falciparum: Nitric oxide modulates heme speciation in isolated food vacuoles*. Experimental Parasitology, 2011. **127**(1): p. 1-8.
215. Flores, M.V.C., W.J. O'Sullivan, and T.S. Stewart, *Characterisation of the carbamoyl phosphate synthetase gene from Plasmodium falciparum*. Molecular and Biochemical Parasitology, 1994. **68**(2): p. 315-318.

216. Warncke, J.D., I. Vakonakis, and H.-P. Beck, *Plasmodium Helical Interspersed Subtelomeric (PHIST) Proteins, at the Center of Host Cell Remodeling*. Microbiology and Molecular Biology Reviews, 2016. **80**(4): p. 905-927.
217. Francis, S.E., et al., *Six Genes Are Preferentially Transcribed by the Circulating and Sequestered Forms of Plasmodium falciparum Parasites That Infect Pregnant Women*. Infection and Immunity, 2007. **75**(10): p. 4838-4850.
218. Maier, A.G., et al., *Exported Proteins Required for Virulence and Rigidity of Plasmodium falciparum-Infected Human Erythrocytes*. Cell, 2008. **134**(1): p. 48-61.
219. Dastidar, E.G., et al., *Involvement of Plasmodium falciparum protein kinase CK2 in the chromatin assembly pathway*. BMC Biology, 2012. **10**(1): p. 5.
220. Holland, Z., et al., *Functional Analysis of Protein Kinase CK2 of the Human Malaria Parasite Plasmodium falciparum*. Eukaryotic Cell, 2009. **8**(3): p. 388-397.
221. Filhol, O. and C. Cochet, *Protein Kinase CK2 in Health and Disease*. Cellular and Molecular Life Sciences, 2009. **66**(11): p. 1830-1839.
222. Bibby, A.C. and D.W. Litchfield, *The multiple personalities of the regulatory subunit of protein kinase CK2: CK2 dependent and CK2 independent roles reveal a secret identity for CK2beta*. International journal of biological sciences, 2005. **1**(2): p. 67-79.
223. Mayer, D.C.G., *Protein Sorting in Plasmodium Falciparum*. Life, 2021. **11**(9): p. 937.
224. Henrici, R.C., et al., *The Plasmodium falciparum Artemisinin Susceptibility-Associated AP-2 Adaptin μ Subunit is Clathrin Independent and Essential for Schizont Maturation*. mBio, 2020. **11**(1): p. e02918-19.
225. Iskar, M., et al., *Drug-Induced Regulation of Target Expression*. PLOS Computational Biology, 2010. **6**(9): p. e1000925.
226. Ganesan, K., et al., *A Genetically Hard-Wired Metabolic Transcriptome in Plasmodium falciparum Fails to Mount Protective Responses to Lethal Antifolates*. PLOS Pathogens, 2008. **4**(11): p. e1000214.
227. Siwo, G.H., et al., *An integrative analysis of small molecule transcriptional responses in the human malaria parasite Plasmodium falciparum*. BMC Genomics, 2015. **16**(1): p. 1030.
228. van Heerden, A., R. van Wyk, and L.-M. Birkholtz, *Machine Learning Uses Chemo-Transcriptomic Profiles to Stratify Antimalarial Compounds With Similar Mode of Action*. Frontiers in Cellular and Infection Microbiology, 2021. **11**.
229. Gardner, M.J., et al., *Genome sequence of the human malaria parasite Plasmodium falciparum*. Nature, 2002. **419**(6906): p. 498-511.
230. Supek, F., et al., *REVIGO Summarizes and Visualizes Long Lists of Gene Ontology Terms*. PLOS ONE, 2011. **6**(7): p. e21800.
231. Müller, O., et al., *How worthwhile is methylene blue as a treatment of malaria? Expert Review of Anti-infective Therapy*, 2019. **17**(7): p. 471-473.

232. Moffat, J.G., et al., *Opportunities and challenges in phenotypic drug discovery: an industry perspective*. Nature Reviews Drug Discovery, 2017. **16**(8): p. 531-543.
233. Lin, H., X. Su, and B. He, *Protein lysine acylation and cysteine succination by intermediates of energy metabolism*. ACS chemical biology, 2012. **7**(6): p. 947-960.
234. Ruecker, N., et al., *Fumarase Deficiency Causes Protein and Metabolite Succination and Intoxicates Mycobacterium tuberculosis*. Cell Chemical Biology, 2017. **24**(3): p. 306-315.
235. Berg, J.M., et al., *Biochemistry*. 2015: Macmillan Learning.
236. Simon, C.S., V.S. Stürmer, and J. Guizetti, *How Many Is Enough? - Challenges of Multinucleated Cell Division in Malaria Parasites*. Frontiers in cellular and infection microbiology, 2021. **11**: p. 658616-658616.
237. Weber, J.L., *Analysis of sequences from the extremely A + T-rich genome of Plasmodium falciparum*. Gene, 1987. **52**(1): p. 103-9.
238. Ortega, C., et al., *A Global Survey of ATPase Activity in Plasmodium falciparum Asexual Blood Stages and Gametocytes **. Molecular & Cellular Proteomics, 2018. **17**(1): p. 111-120.
239. Engelbrecht, D., P.M. Durand, and T.L. Coetzer, *On Programmed Cell Death in Plasmodium falciparum: Status Quo*. Journal of Tropical Medicine, 2012. **2012**: p. 646534.
240. Ch'Ng, J.H., et al., *Drug-induced permeabilization of parasite's digestive vacuole is a key trigger of programmed cell death in Plasmodium falciparum*. Cell Death & Disease, 2011. **2**(10): p. e216-e216.
241. Cobbold, S.A., et al., *Non-canonical metabolic pathways in the malaria parasite detected by isotope-tracing metabolomics*. Molecular Systems Biology, 2021. **17**(4): p. e10023.
242. Gulati, S., et al., *Profiling the Essential Nature of Lipid Metabolism in Asexual Blood and Gametocyte Stages of Plasmodium falciparum*. Cell Host & Microbe, 2015. **18**(3): p. 371-381.
243. Cobbold, S.A. and M.J. McConville, *Determining the Mode of Action of Antimalarial Drugs Using Time-Resolved LC-MS-Based Metabolite Profiling*, in *Microbial Metabolomics: Methods and Protocols*, E.E.K. Baidoo, Editor. 2019, Springer New York: New York, NY. p. 225-239.
244. Atamna, H., et al., *Mode of antimalarial effect of methylene blue and some of its analogues on Plasmodium falciparum in culture and their inhibition of P. vinckei petteri and P. yoelii nigeriensis in vivo*. Biochemical Pharmacology, 1996. **51**(5): p. 693-700.
245. Lu, G., et al., *Efficacy and safety of methylene blue in the treatment of malaria: a systematic review*. BMC Medicine, 2018. **16**(1): p. 59.

246. Buchholz, K., et al., *Interactions of Methylene Blue with Human Disulfide Reductases and Their Orthologues from Plasmodium falciparum*. *Antimicrobial Agents and Chemotherapy*, 2008. **52**(1): p. 183-191.
247. Gendrot, M., et al., *Absence of Association between Methylene Blue Reduced Susceptibility and Polymorphisms in 12 Genes Involved in Antimalarial Drug Resistance in African Plasmodium falciparum*. *Pharmaceuticals*, 2021. **14**(4): p. 351.
248. Schirmer, R.H., et al., *Methylene blue as an antimalarial agent*. *Redox Report*, 2003. **8**(5): p. 272-275.
249. Thurston, J.P., *The chemotherapy of Plasmodium berghei. I. Resistance to drugs*. *Parasitology*, 1953. **43**(3-4): p. 246-252.
250. Rajaram, K., et al., *Metabolic changes accompanying the loss of fumarate hydratase and malate-quinone oxidoreductase in the asexual blood stage of Plasmodium falciparum*. *Journal of Biological Chemistry*, 2022: p. 101897.
251. Zheng, L., et al., *Reversed argininosuccinate lyase activity in fumarate hydratase-deficient cancer cells*. *Cancer & Metabolism*, 2013. **1**(1): p. 12.
252. Bell, A., *Antimalarial drug synergism and antagonism: mechanistic and clinical significance*. *FEMS Microbiol Lett*, 2005. **253**(2): p. 171-84.
253. Hopkins, A.L., *Network pharmacology*. *Nature Biotechnology*, 2007. **25**(10): p. 1110-1111.
254. Meggio, F. and L.A. Pinna, *One-thousand-and-one substrates of protein kinase CK2?* *The FASEB Journal*, 2003. **17**(3): p. 349-368.
255. Ruiz-Carrillo, D., et al., *The protein kinase CK2 catalytic domain from Plasmodium falciparum: crystal structure, tyrosine kinase activity and inhibition*. *Scientific Reports*, 2018. **8**(1): p. 7365.
256. Siddiqui-Jain, A., et al., *CX-4945, an Orally Bioavailable Selective Inhibitor of Protein Kinase CK2, Inhibits Prosurvival and Angiogenic Signaling and Exhibits Antitumor Efficacy*. *Cancer Research*, 2010. **70**(24): p. 10288-10298.
257. Chon, H.J., et al., *The casein kinase 2 inhibitor, CX-4945, as an anti-cancer drug in treatment of human hematological malignancies*. *Frontiers in Pharmacology*, 2015. **6**.
258. Djaman, O., F.W. Outten, and J.A. Imlay, *Repair of Oxidized Iron-Sulfur Clusters in Escherichia coli*. *Journal of Biological Chemistry*, 2004. **279**(43): p. 44590-44599.
259. Hodges, M., et al., *An iron regulatory-like protein expressed in Plasmodium falciparum displays aconitase activity*. *Molecular and Biochemical Parasitology*, 2005. **143**(1): p. 29-38.
260. Loyevsky, M., et al., *Expression of a recombinant IRP-like Plasmodium falciparum protein that specifically binds putative plasmodial IREs*. *Molecular and Biochemical Parasitology*, 2003. **126**(2): p. 231-238.
261. Smith, M.T., et al., *The measurement of lipid peroxidation in isolated hepatocytes*. *Biochemical Pharmacology*, 1982. **31**(1): p. 19-26.

262. Eleftheriadis, T., et al., *Factors that May Protect the Native Hibernator Syrian Hamster Renal Tubular Epithelial Cells from Ferroptosis Due to Warm Anoxia-Reoxygenation*. *Biology*, 2019. **8**(2): p. 22.
263. Qiu, J., et al., *Transferrin Receptor Functionally Marks Thermogenic Adipocytes*. *Frontiers in Cell and Developmental Biology*, 2020. **8**.
264. Basta, P.V., et al., *Preparation of monoclonal antibodies reactive to the endogenous small molecule, anandamide*. *Journal of Immunological Methods*, 2004. **285**(2): p. 181-195.
265. Wang, Y., et al., *Preparation and Characterization of Monoclonal Antibodies with High Affinity and Broad Class Specificity against Zearalenone and Its Major Metabolites*. *Toxins*, 2021. **13**(6): p. 383.
266. Smith, B.J., et al., *Co-immunoprecipitation for Deciphering Protein Interactomes*, in *Proteomic Methods in Neuropsychiatric Research*, P.C. Guest, Editor. 2017, Springer International Publishing: Cham. p. 229-236.
267. Baskin, J.M., et al., *Copper-free click chemistry for dynamic in vivo imaging*. *Proceedings of the National Academy of Sciences*, 2007. **104**(43): p. 16793-16797.
268. Consortium, T.G.O., *The Gene Ontology resource: enriching a GOLD mine*. *Nucleic Acids Research*, 2020. **49**(D1): p. D325-D334.
269. Ashburner, M., et al., *Gene ontology: tool for the unification of biology*. *The Gene Ontology Consortium*. *Nature genetics*, 2000. **25**(1): p. 25-29.

7. Appendix I: Results from GO enrichment analysis

The following tables and figures are the results from a GO enrichment analysis carried out using PlasmoDB [107, 140] and Revigo [230] using the DEG from a dose-response transcriptional profiling as explained below.

The list of DEG was uploaded to the Workspace section in PlasmoDB (Release 56: 15 February 2022) for each drug treatment condition (5, 10 and 20 nM), and subsequently enriched GO terms were searched for each ontology: biological processes, cellular components, and molecular functions [268, 269], with a p-value cut-off set at 0.05. *P. falciparum* 3D7 was chosen as the organism for the search, and both computed and curated evidence were selected. The results were collected as a table and those GO terms that with less than five associated genes in the DEG list were filtered out. Each new GO term list (presented in this section in tables 1 to 7) was used as input for visualization (and removal of redundant terms) in Revigo. The terms were associated to their p-values and the size of results was set as medium (0.7). Obsolete GO terms were removed, and the species *P. falciparum* 3D7 – 36329 was selected. Interactive maps were chosen for visualization, where GO terms are represented as bubbles with a size and color corresponding to their LogSize value and p-value, respectively. The LogSize is the \log_{10} (number of annotations for the GO term ID in the selected species in the EBI GOA database¹). The color scale shows more intense shades of red with increasing p-values.

The GO term for some GO IDs in the PlasmoDB results tables is shown as “not yet available” without modification from the original results, but in each table description they are clarified according to their name in the EBI GOA database. The columns in the tables refer to: background count, number of genes with this term in the background (genome); result count, number of genes with this term in the input list of DEG; % of background in result, percentage of genes in input list of DEG with this term in relation to those of the background; fold enrichment, percentage of genes with this term in the input list of DEG divided the percentage of genes with this term in the background; odds ratio, odds ratio statistic from Fisher’s exact test; p-value, derived from Fisher’s exact test.

¹ European Bioinformatics Institute’s Gene Ontology Annotation database

Table 7-1. GO enrichment analysis of biological processes among genes altered in *P. falciparum* upon treatment with 5 nM SC83288. Terms labeled as “not yet available” correspond to: GO:0010467, gene expression; GO:0044085, cellular component biogenesis; GO:0034660, ncRNA metabolic process; GO:0022607, cellular component assembly.

ID	Process name	Background count	Result count	% of background in result	Fold enrichment	Odds ratio	P-value
GO:0006396	RNA processing	362	56	15.5	2.09	2.53	3.71E-08
GO:0016070	RNA metabolic process	408	58	14.2	1.92	2.28	4.33E-07
GO:0010467	Not yet available	451	61	13.5	1.83	2.15	1.22E-06
GO:0006364	rRNA processing	130	25	19.2	2.6	3.13	6.60E-06
GO:0034470	ncRNA processing	200	33	16.5	2.23	2.62	7.49E-06
GO:0022613	ribonucleoprotein complex biogenesis	248	38	15.3	2.07	2.41	9.14E-06
GO:0044085	Not yet available	250	38	15.2	2.05	2.39	1.11E-05
GO:0016072	rRNA metabolic process	134	25	18.7	2.52	3.01	1.15E-05
GO:0034660	Not yet available	247	37	15	2.02	2.34	2.04E-05
GO:0042254	ribosome biogenesis	194	31	16	2.16	2.51	2.77E-05
GO:0000470	maturation of LSU-rRNA	22	8	36.4	4.92	7.29	1.06E-04
GO:0008380	RNA splicing	129	21	16.3	2.2	2.52	4.32E-04
GO:0006626	protein targeting to mitochondrion	23	7	30.4	4.11	5.56	9.93E-04
GO:0072655	establishment of protein localization to mitochondrion	24	7	29.2	3.94	5.24	1.31E-03
GO:0070585	protein localization to mitochondrion	24	7	29.2	3.94	5.24	1.31E-03
GO:0009156	ribonucleoside monophosphate biosynthetic process	14	5	35.7	4.83	7.04	2.47E-03
GO:0000460	maturation of 5.8S rRNA	20	6	30	4.06	5.44	2.50E-03
GO:0042274	ribosomal small subunit biogenesis	49	10	20.4	2.76	3.27	2.62E-03
GO:0009451	RNA modification	85	14	16.5	2.23	2.53	3.44E-03
GO:0009161	ribonucleoside monophosphate metabolic process	15	5	33.3	4.51	6.33	3.48E-03
GO:0006839	mitochondrial transport	29	7	24.1	3.26	4.04	4.29E-03
GO:0009124	nucleoside monophosphate biosynthetic process	16	5	31.3	4.22	5.76	4.76E-03
GO:0022618	ribonucleoprotein complex assembly	98	15	15.3	2.07	2.32	5.13E-03
GO:0042273	ribosomal large subunit biogenesis	62	11	17.7	2.4	2.75	5.13E-03
GO:0009123	nucleoside monophosphate metabolic process	17	5	29.4	3.98	5.27	6.34E-03
GO:0071826	ribonucleoprotein complex subunit organization	101	15	14.9	2.01	2.23	6.82E-03
GO:0016071	mRNA metabolic process	185	23	12.4	1.68	1.83	8.95E-03
GO:0006397	mRNA processing	145	19	13.1	1.77	1.94	9.83E-03
GO:0044237	cellular metabolic process	576	57	9.9	1.34	1.45	1.12E-02
GO:0043933	protein-containing complex subunit organization	222	25	11.3	1.52	1.63	2.15E-02
GO:0007005	mitochondrion organization	48	8	16.7	2.25	2.54	2.30E-02
GO:0022607	Not yet available	249	27	10.8	1.47	1.56	2.69E-02
GO:0030490	maturation of SSU-rRNA	32	6	18.8	2.53	2.92	2.75E-02
GO:0071806	protein transmembrane transport	24	5	20.8	2.82	3.33	2.84E-02
GO:0034622	cellular protein-containing complex assembly	176	20	11.4	1.54	1.64	3.44E-02
GO:0000375	RNA splicing, via transesterification reactions	104	13	12.5	1.69	1.82	4.18E-02
GO:0065003	protein-containing complex assembly	192	21	10.9	1.48	1.57	4.39E-02
GO:0006400	tRNA modification	45	7	15.6	2.1	2.33	4.52E-02

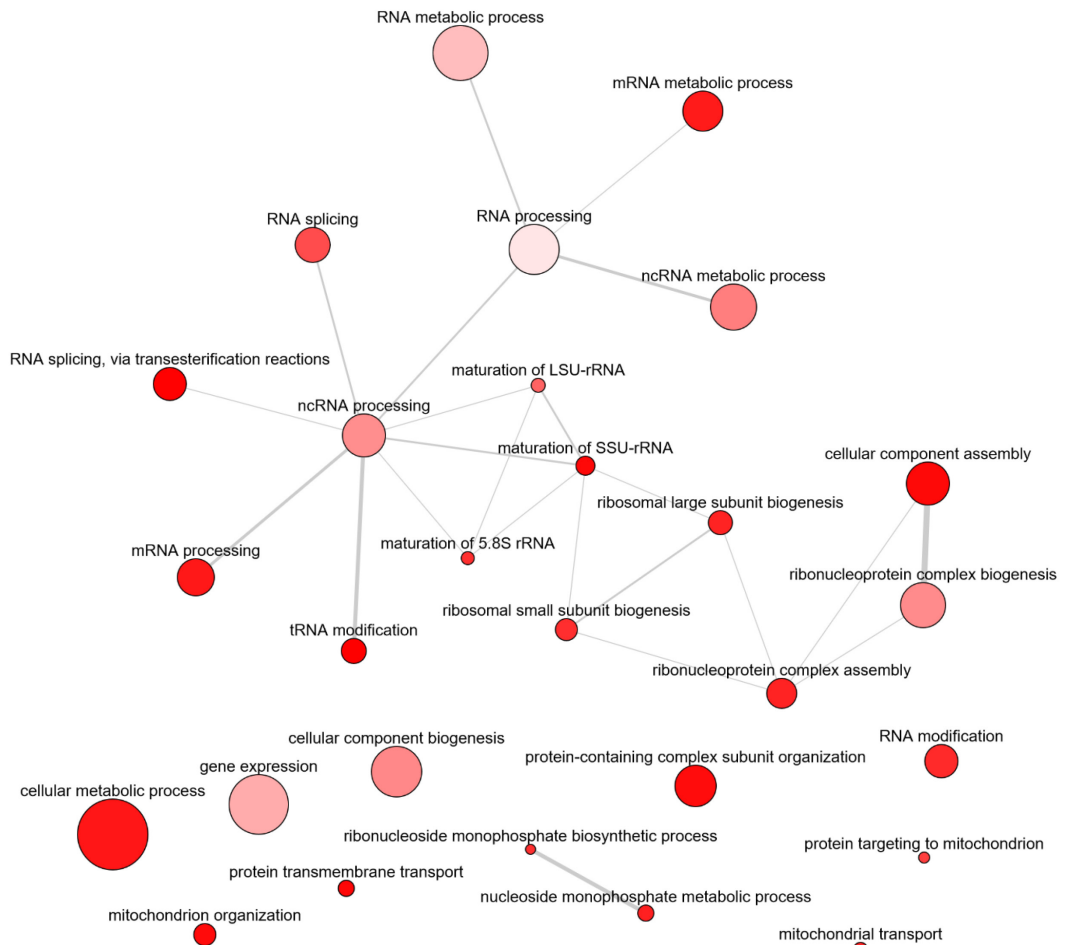


Figure 7-1. Interaction map of biological processes enriched among genes altered in *P. falciparum* upon treatment with 5 nM SC83288.

Table 7-2. GO enrichment analysis of cellular components among genes altered in *P. falciparum* upon treatment with 5 nM SC83288. Terms labeled as “not yet available” correspond to: GO:0043229, intracellular organelle.

ID	Component name	Background count	Result count	% of background in result	Fold enrichment	Odds ratio	P-value
GO:0005730	nucleolus	126	23	18.3	2.47	2.92	3.75E-05
GO:0070013	intracellular organelle lumen	366	47	12.8	1.74	1.97	9.19E-05
GO:0043233	organelle lumen	367	47	12.8	1.73	1.96	9.84E-05
GO:0031974	membrane-enclosed lumen	367	47	12.8	1.73	1.96	9.84E-05
GO:0030684	preribosome	77	16	20.8	2.81	3.39	1.21E-04
GO:0030686	90S preribosome	24	8	33.3	4.51	6.38	2.13E-04
GO:0031981	nuclear lumen	268	36	13.4	1.82	2.05	2.67E-04
GO:0044428	obsolete nuclear part	104	18	17.3	2.34	2.71	5.19E-04
GO:0005634	nucleus	915	91	9.9	1.34	1.51	9.73E-04
GO:0032991	protein-containing complex	1020	99	9.7	1.31	1.48	1.28E-03
GO:0097526	spliceosomal tri-snRNP complex	25	7	28	3.78	4.94	1.71E-03
GO:0032040	small-subunit processome	34	8	23.5	3.18	3.92	2.73E-03
GO:1990234	transferase complex	139	20	14.4	1.94	2.17	2.80E-03
GO:0046540	U4/U6 x U5 tri-snRNP complex	21	6	28.6	3.86	5.07	3.28E-03
GO:0140534	endoplasmic reticulum protein-containing complex	52	10	19.2	2.6	3.04	4.14E-03
GO:1990904	ribonucleoprotein complex	381	42	11	1.49	1.62	4.85E-03
GO:0140513	nuclear protein-containing complex	326	37	11.3	1.53	1.67	5.04E-03
GO:0005681	spliceosomal complex	100	14	14	1.89	2.08	1.46E-02
GO:0098827	endoplasmic reticulum subcompartment	113	14	12.4	1.67	1.8	3.79E-02
GO:0005789	endoplasmic reticulum membrane	113	14	12.4	1.67	1.8	3.79E-02
GO:0030687	preribosome, large subunit precursor	26	5	19.2	2.6	3.01	3.90E-02
GO:0042175	nuclear outer membrane-endoplasmic reticulum membrane network	114	14	12.3	1.66	1.78	4.04E-02
GO:0030176	integral component of endoplasmic reticulum membrane	35	6	17.1	2.32	2.62	4.10E-02
GO:0031227	intrinsic component of endoplasmic reticulum membrane	35	6	17.1	2.32	2.62	4.10E-02
GO:0043229	Not yet available	920	81	8.8	1.19	1.27	4.30E-02

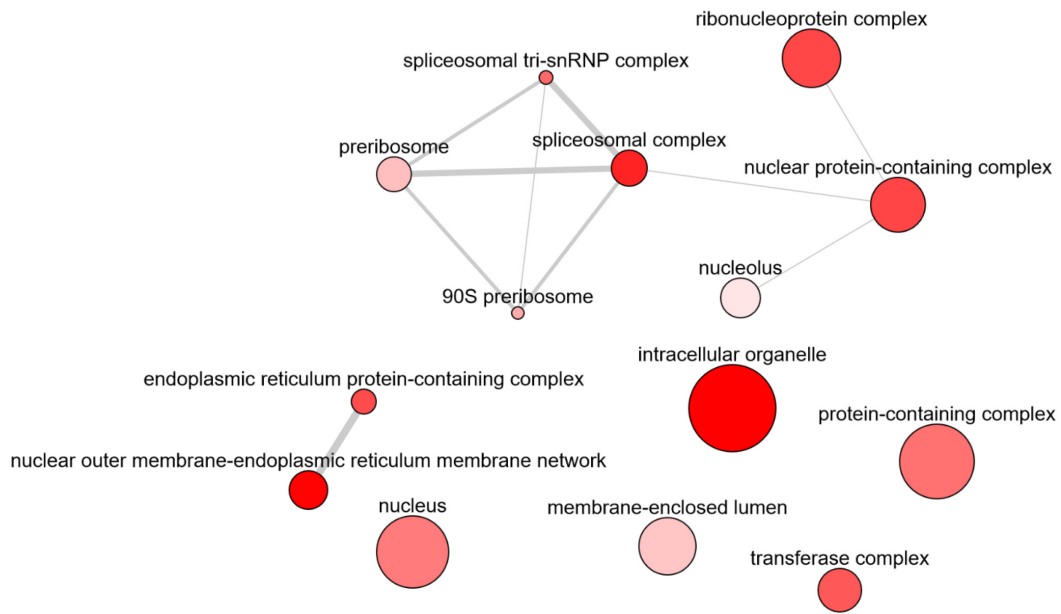


Figure 7-2. Interaction map of cellular components enriched among genes altered in *P. falciparum* upon treatment with 5 nM SC83288.

Table 7-3. GO enrichment analysis of molecular functions among genes altered in *P. falciparum* upon treatment with 5 nM SC83288. Terms labeled as “not yet available” correspond to: GO:0045182, translation regulator activity.

ID	Molecular function	Background count	Result count	% of background in result	Fold enrichment	Odds ratio	P-value
GO:0008649	rRNA methyltransferase activity	20	6	30	4.06	5.44	0.002
GO:0140102	catalytic activity, acting on a rRNA	20	6	30	4.06	5.44	0.002
GO:0016740	transferase activity	299	35	11.7	1.58	1.73	0.004
GO:0003743	translation initiation factor activity	63	11	17.5	2.36	2.7	0.006
GO:0003723	RNA binding	629	61	9.7	1.31	1.41	0.013
GO:0140098	catalytic activity, acting on RNA	249	28	11.2	1.52	1.64	0.016
GO:0008135	translation factor activity, RNA binding	94	13	13.8	1.87	2.05	0.020
GO:0016757	glycosyltransferase activity	30	6	20	2.7	3.17	0.020
GO:0045182	Not yet available	96	13	13.5	1.83	2	0.023
GO:0090079	translation regulator activity, nucleic acid binding	96	13	13.5	1.83	2	0.023
GO:0000287	magnesium ion binding	40	7	17.5	2.37	2.69	0.025
GO:0004518	nuclease activity	68	10	14.7	1.99	2.19	0.027
GO:0003684	damaged DNA binding	24	5	20.8	2.82	3.33	0.028
GO:0008408	3'-5' exonuclease activity	25	5	20	2.7	3.16	0.033
GO:0004527	exonuclease activity	43	7	16.3	2.2	2.46	0.036
GO:0140640	catalytic activity, acting on a nucleic acid	291	30	10.3	1.39	1.48	0.037
GO:0003676	nucleic acid binding	702	64	9.1	1.23	1.31	0.038

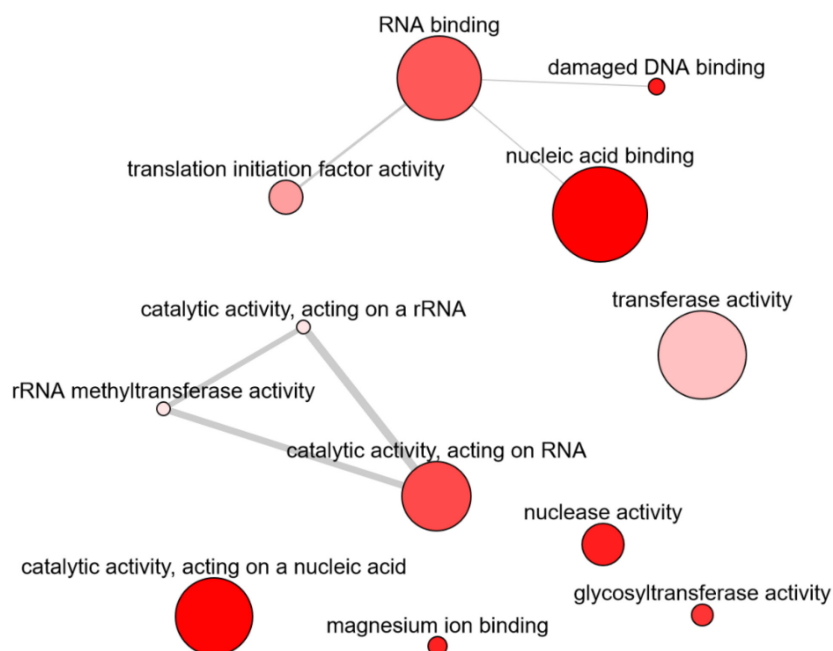


Figure 7-3. Interaction map of molecular functions enriched among genes altered in *P. falciparum* upon treatment with 5 nM SC83288.

Table 7-4. GO enrichment analysis of biological processes among genes altered in *P. falciparum* upon treatment with 10 nM SC83288. Terms labeled as “not yet available” correspond to: GO:0010467, gene expression.

ID	Process name	Background count	Result count	% of background in result	Fold enrichment	Odds ratio	P-value
GO:0010467	Not yet available	451	23	5.1	1.72	1.91	0.006
GO:0006396	RNA processing	362	19	5.2	1.77	1.94	0.010
GO:0006400	tRNA modification	45	5	11.1	3.75	4.21	0.010
GO:0046394	carboxylic acid biosynthetic process	48	5	10.4	3.52	3.91	0.013
GO:0042274	ribosomal small subunit biogenesis	49	5	10.2	3.45	3.82	0.014
GO:0016053	organic acid biosynthetic process	50	5	10	3.38	3.74	0.015
GO:0016070	RNA metabolic process	408	19	4.7	1.57	1.69	0.031
GO:0034470	ncRNA processing	200	11	5.5	1.86	1.98	0.034
GO:0009451	RNA modification	85	6	7.1	2.39	2.56	0.039
GO:0008033	tRNA processing	66	5	7.6	2.56	2.75	0.045

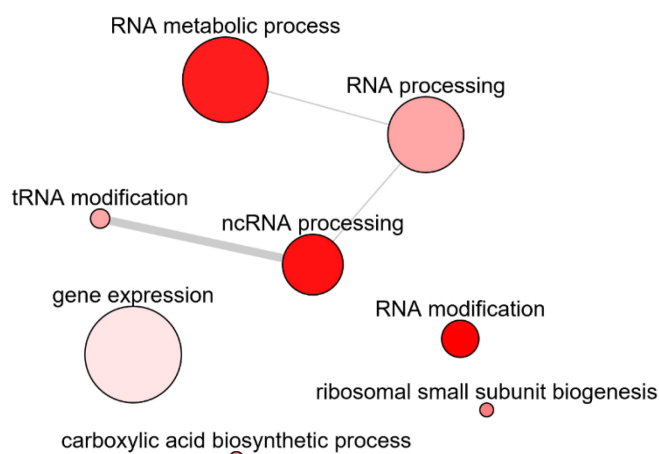


Figure 7-4. Interaction map of biological processes enriched among genes altered in *P. falciparum* upon treatment with 10 nM SC83288.

Table 7-5. . GO enrichment analysis of cellular components and molecular functions among genes altered in *P. falciparum* upon treatment with 10 nM SC83288 .

A	ID	Component name	Background count	Result count	% of background in result	Fold enrichment	Odds ratio	P-value
	GO:0030684	preribosome	77	6	7.8	2.63	2.85	0.026
	GO:0005730	nucleolus	126	8	6.3	2.15	2.3	0.032
	GO:0044428	obsolete nuclear part	104	7	6.7	2.27	2.44	0.034

B	ID	Molecular function	Background count	Result count	% of background in result	Fold enrichment	Odds ratio	P-value
	GO:0016747	acyltransferase activity, transferring groups other than amino-acyl groups	57	5	8.8	2.96	3.23	0.026

Table 7-6. GO enrichment analysis of biological processes among genes altered in *P. falciparum* upon treatment with 20 nM SC83288. Terms labeled as “not yet available” correspond to: GO:0010467, gene expression; GO:0044085, cellular component biogenesis; GO:0034660, ncRNA metabolic process; GO:0022607, cellular component assembly; GO:0043414, macromolecule methylation.

ID	Process name	Background count	Result count	% of background in result	Fold enrichment	Odds ratio	P-value
GO:0016070	RNA metabolic process	408	133	32.6	1.74	2.28	1.96E-12
GO:0006396	RNA processing	362	120	33.1	1.76	2.32	7.96E-12
GO:0010467	Not yet available	451	140	31	1.65	2.12	2.91E-11
GO:0022613	ribonucleoprotein complex biogenesis	248	88	35.5	1.89	2.52	1.28E-10
GO:0034470	ncRNA processing	200	75	37.5	2	2.74	1.74E-10
GO:0044085	Not yet available	250	88	35.2	1.87	2.49	2.07E-10
GO:0034660	Not yet available	247	87	35.2	1.88	2.49	2.55E-10
GO:0042254	ribosome biogenesis	194	72	37.1	1.98	2.68	7.12E-10
GO:0006364	rRNA processing	130	52	40	2.13	3	9.74E-09
GO:0016072	rRNA metabolic process	134	52	38.8	2.07	2.85	3.28E-08
GO:0009451	RNA modification	85	30	35.3	1.88	2.4	2.13E-04
GO:0034622	cellular protein-containing complex assembly	176	52	29.5	1.57	1.86	2.87E-04
GO:0022618	ribonucleoprotein complex assembly	98	33	33.7	1.79	2.24	2.89E-04
GO:0042273	ribosomal large subunit biogenesis	62	23	37.1	1.97	2.59	5.10E-04
GO:0071826	ribonucleoprotein complex subunit organization	101	33	32.7	1.74	2.14	5.38E-04
GO:0007005	mitochondrion organization	48	19	39.6	2.11	2.87	6.10E-04
GO:0090305	nucleic acid phosphodiester bond hydrolysis	45	18	40	2.13	2.92	7.28E-04
GO:0065003	protein-containing complex assembly	192	54	28.1	1.5	1.74	8.34E-04
GO:0016071	mRNA metabolic process	185	52	28.1	1.5	1.73	1.05E-03
GO:0000154	rRNA modification	29	13	44.8	2.39	3.55	1.14E-03
GO:0006399	tRNA metabolic process	114	35	30.7	1.63	1.95	1.32E-03
GO:0006397	mRNA processing	145	42	29	1.54	1.8	1.66E-03
GO:0001510	RNA methylation	37	15	40.5	2.16	2.98	1.70E-03
GO:0022607	Not yet available	249	65	26.1	1.39	1.57	2.17E-03
GO:0043933	protein-containing complex subunit organization	222	59	26.6	1.41	1.6	2.20E-03
GO:0042255	ribosome assembly	46	17	37	1.97	2.56	2.81E-03
GO:0006379	mRNA cleavage	7	5	71.4	3.8	10.86	3.47E-03
GO:0000470	maturation of LSU-rRNA	22	10	45.5	2.42	3.63	3.75E-03
GO:0032259	methylation	36	14	38.9	2.07	2.78	3.80E-03
GO:0006520	cellular amino acid metabolic process	87	27	31	1.65	1.97	3.83E-03
GO:0031167	rRNA methylation	19	9	47.4	2.52	3.92	4.23E-03
GO:0044743	protein transmembrane import into intracellular organelle	10	6	60	3.19	6.52	4.55E-03
GO:0030150	protein import into mitochondrial matrix	10	6	60	3.19	6.52	4.55E-03
GO:0006626	protein targeting to mitochondrion	23	10	43.5	2.31	3.35	5.54E-03
GO:0006400	tRNA modification	45	16	35.6	1.89	2.41	5.75E-03
GO:0008033	tRNA processing	66	21	31.8	1.69	2.04	7.44E-03
GO:0090501	RNA phosphodiester bond hydrolysis	31	12	38.7	2.06	2.75	7.51E-03
GO:0043414	Not yet available	58	19	32.8	1.74	2.13	7.57E-03

Table 7-7. GO enrichment analysis of biological processes among genes altered in *P. falciparum* upon treatment with 20 nM SC83288, continuation. Terms labeled as “not yet available” correspond to: GO:0016043, cellular component organization; GO:0043604, amide biosynthetic process.

ID	Process name	Background count	Result count	% of background in result	Fold enrichment	Odds ratio	P-value
GO:0072655	establishment of protein localization to mitochondrion	24	10	41.7	2.22	3.11	7.93E-03
GO:0070585	protein localization to mitochondrion	24	10	41.7	2.22	3.11	7.93E-03
GO:0000463	maturation of LSU-rRNA from tricistronic rRNA transcript (SSU-rRNA, 5.8S rRNA, LSU-rRNA)	11	6	54.5	2.9	5.22	8.43E-03
GO:0000027	ribosomal large subunit assembly	28	11	39.3	2.09	2.82	9.12E-03
GO:0042274	ribosomal small subunit biogenesis	49	16	32.7	1.74	2.12	1.41E-02
GO:0031124	mRNA 3'-end processing	12	6	50	2.66	4.35	1.42E-02
GO:0009069	serine family amino acid metabolic process	12	6	50	2.66	4.35	1.42E-02
GO:0043631	RNA polyadenylation	9	5	55.6	2.96	5.43	1.49E-02
GO:1901605	alpha-amino acid metabolic process	38	13	34.2	1.82	2.27	1.73E-02
GO:0006575	cellular modified amino acid metabolic process	16	7	43.8	2.33	3.38	1.90E-02
GO:0070475	rRNA base methylation	13	6	46.2	2.46	3.72	2.23E-02
GO:0042398	cellular modified amino acid biosynthetic process	10	5	50	2.66	4.34	2.53E-02
GO:0031123	RNA 3'-end processing	32	11	34.4	1.83	2.28	2.66E-02
GO:0140694	non-membrane-bounded organelle assembly	61	18	29.5	1.57	1.83	2.77E-02
GO:0016043	Not yet available	323	74	22.9	1.22	1.31	3.14E-02
GO:0008380	RNA splicing	129	33	25.6	1.36	1.5	3.28E-02
GO:0140053	mitochondrial gene expression	29	10	34.5	1.84	2.29	3.31E-02
GO:0006839	mitochondrial transport	29	10	34.5	1.84	2.29	3.31E-02
GO:0043604	Not yet available	11	5	45.5	2.42	3.62	3.93E-02
GO:0000398	mRNA splicing, via spliceosome	100	26	26	1.38	1.53	4.51E-02
GO:0000377	RNA splicing, via transesterification reactions with bulged adenosine as nucleophile	100	26	26	1.38	1.53	4.51E-02

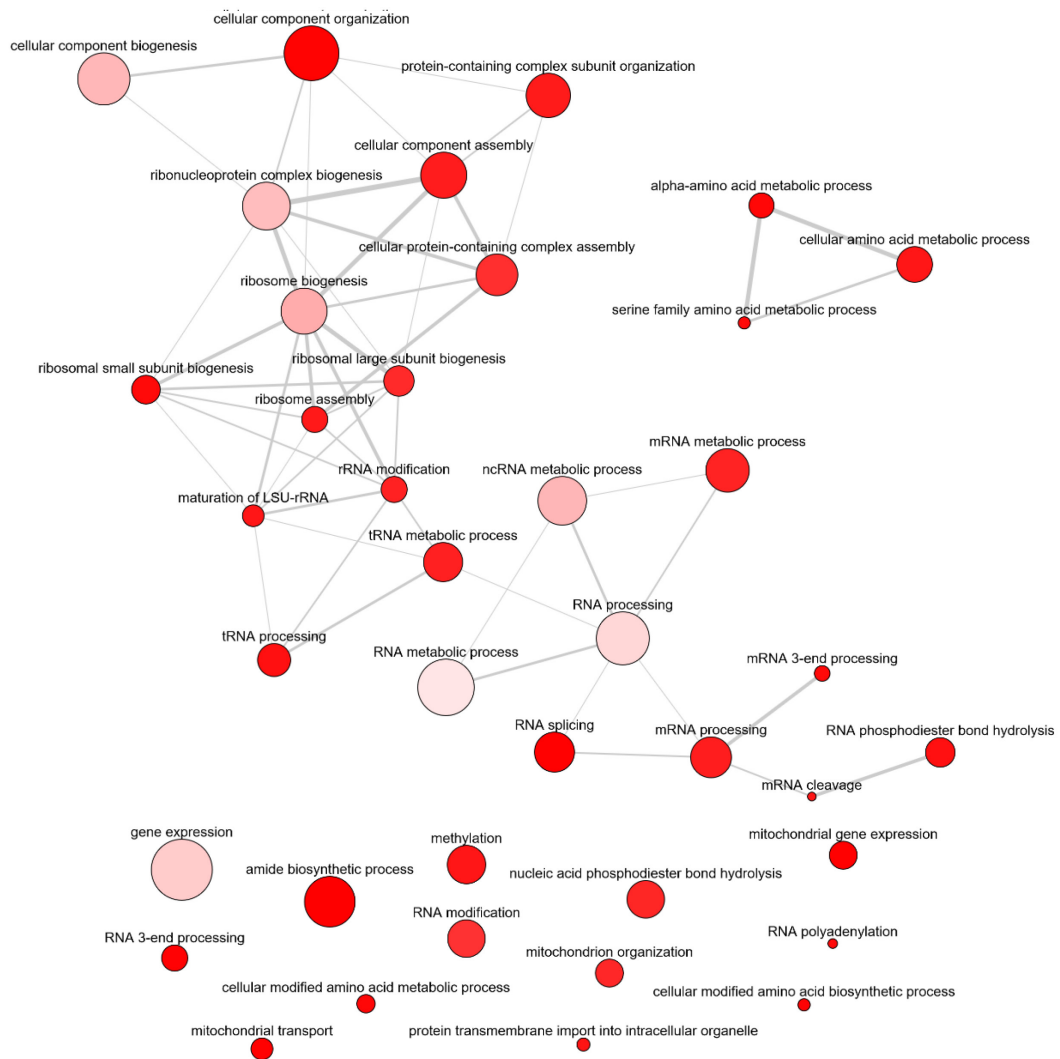


Figure 7-5. Interaction map of biological processes enriched among genes altered in *P. falciparum* upon treatment with 20 nM SC83288.

Table 7-8. GO enrichment analysis of cellular components among genes altered in *P. falciparum* upon treatment with 20 nM SC83288. Terms labeled as “not yet available” correspond to: GO:0034708, methyltransferase complex.

ID	Component name	Background count	Result count	% of background in result	Fold enrichment	Odds ratio	P-value
GO:0005730	nucleolus	126	52	41.3	2.2	3.16	2.66E-09
GO:0030684	preribosome	77	37	48.1	2.56	4.13	3.96E-09
GO:0044428	obsolete nuclear part	104	45	43.3	2.3	3.42	5.49E-09
GO:0005634	nucleus	915	233	25.5	1.36	1.64	1.57E-08
GO:0030686	90S preribosome	24	16	66.7	3.55	8.78	3.44E-07
GO:0032040	small-subunit processome	34	18	52.9	2.82	4.94	7.57E-06
GO:1990904	ribonucleoprotein complex	381	105	27.6	1.47	1.73	8.13E-06
GO:0031981	nuclear lumen	268	78	29.1	1.55	1.85	1.62E-05
GO:0070013	intracellular organelle lumen	366	100	27.3	1.45	1.7	2.03E-05
GO:0043233	organelle lumen	367	100	27.2	1.45	1.7	2.29E-05
GO:0031974	membrane-enclosed lumen	367	100	27.2	1.45	1.7	2.29E-05
GO:0140513	nuclear protein-containing complex	326	88	27	1.44	1.66	1.06E-04
GO:0005847	mRNA cleavage and polyadenylation specificity factor complex	5	5	100	5.32	inf	2.32E-04
GO:0005849	mRNA cleavage factor complex	7	6	85.7	4.56	26.11	2.55E-04
GO:0034708	Not yet available	29	13	44.8	2.39	3.55	1.14E-03
GO:0030687	preribosome, large subunit precursor	26	12	46.2	2.46	3.74	1.29E-03
GO:0005681	spliceosomal complex	100	30	30	1.6	1.88	4.17E-03
GO:0005684	U2-type spliceosomal complex	34	13	38.2	2.04	2.7	6.18E-03
GO:0005740	mitochondrial envelope	103	29	28.2	1.5	1.72	1.25E-02
GO:0005739	mitochondrion	316	75	23.7	1.26	1.38	1.37E-02
GO:0005744	TIM23 mitochondrial import inner membrane translocase complex	9	5	55.6	2.96	5.43	1.49E-02
GO:0031966	mitochondrial membrane	96	27	28.1	1.5	1.71	1.58E-02
GO:0032991	protein-containing complex	1020	215	21.1	1.12	1.2	2.02E-02
GO:0044429	obsolete mitochondrial part	13	6	46.2	2.46	3.72	2.23E-02
GO:0005732	sno(s)RNA-containing ribonucleoprotein complex	28	10	35.7	1.9	2.42	2.59E-02
GO:0019866	organelle inner membrane	91	25	27.5	1.46	1.66	2.62E-02
GO:0005743	mitochondrial inner membrane	88	24	27.3	1.45	1.64	3.15E-02
GO:0071010	prespliceosome	14	6	42.9	2.28	3.26	3.29E-02
GO:0071004	U2-type prespliceosome	14	6	42.9	2.28	3.26	3.29E-02
GO:0030688	preribosome, small subunit precursor	14	6	42.9	2.28	3.26	3.29E-02
GO:0031970	organelle envelope lumen	11	5	45.5	2.42	3.62	3.93E-02
GO:0005758	mitochondrial intermembrane space	11	5	45.5	2.42	3.62	3.93E-02
GO:0036464	cytoplasmic ribonucleoprotein granule	30	10	33.3	1.77	2.17	4.16E-02
GO:0035770	ribonucleoprotein granule	30	10	33.3	1.77	2.17	4.16E-02

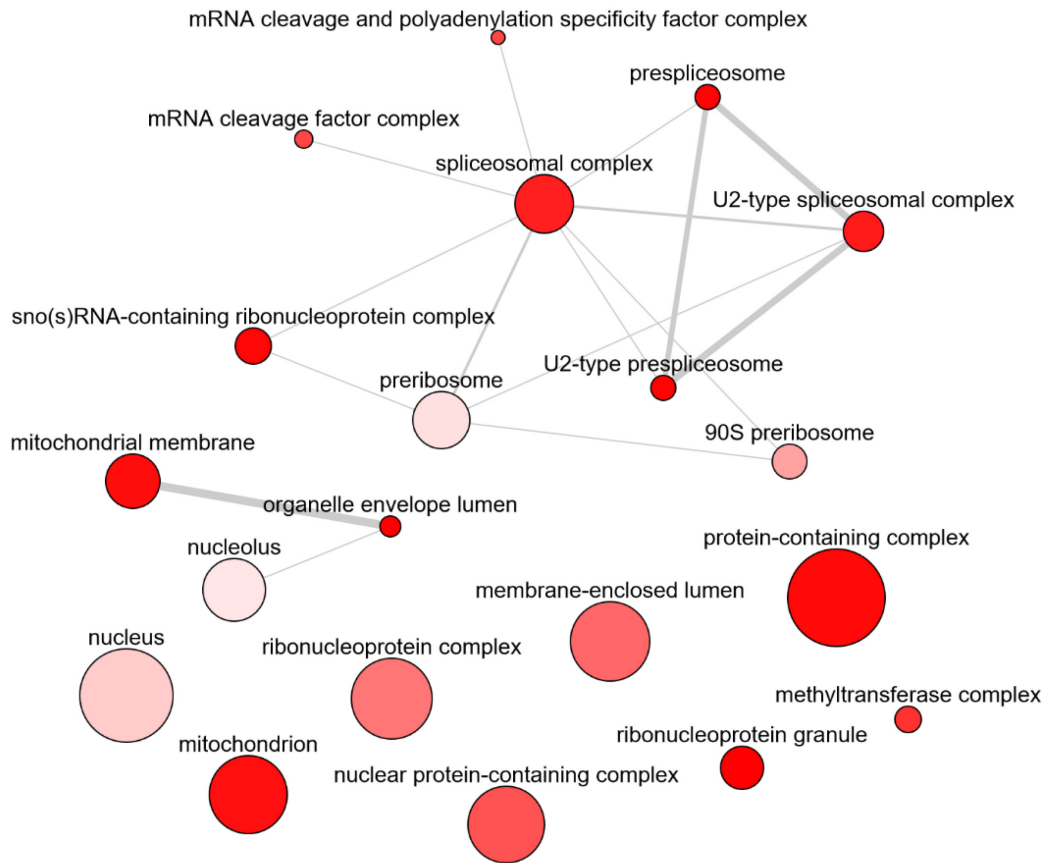


Figure 7-6. Interaction map of cellular components enriched among genes altered in *P. falciparum* upon treatment with 20 nM SC83288.

Table 7-9. GO enrichment analysis of molecular functions among genes altered in *P. falciparum* upon treatment with 20 nM SC83288. Terms labeled as “not yet available” correspond to: GO:0097159, organic cyclic compound binding; GO:0036094, small molecules binding; GO:1901363, heterocyclic compound binding.

ID	Molecular function	Background count	Result count	% of background in result	Fold enrichment	Odds ratio	P-value
GO:0140098	catalytic activity, acting on RNA	249	77	30.9	1.65	2.02	1.50E-06
GO:0003676	nucleic acid binding	702	172	24.5	1.3	1.5	2.76E-05
GO:0140640	catalytic activity, acting on a nucleic acid	291	82	28.2	1.5	1.77	3.63E-05
GO:0003724	RNA helicase activity	55	23	41.8	2.23	3.16	6.10E-05
GO:0003723	RNA binding	629	154	24.5	1.3	1.48	8.32E-05
GO:0008186	ATP-dependent activity, acting on RNA	56	23	41.1	2.19	3.07	8.54E-05
GO:0008168	methyltransferase activity	105	35	33.3	1.77	2.21	2.39E-04
GO:0016741	transferase activity, transferring one-carbon groups	107	35	32.7	1.74	2.15	3.60E-04
GO:0016645	oxidoreductase activity, acting on the CH-NH group of donors	6	5	83.3	4.44	21.73	1.17E-03
GO:0140102	catalytic activity, acting on a rRNA	20	10	50	2.66	4.36	1.54E-03
GO:0008649	rRNA methyltransferase activity	20	10	50	2.66	4.36	1.54E-03
GO:0000049	tRNA binding	30	12	40	2.13	2.91	5.53E-03
GO:0016772	transferase activity, transferring phosphorus-containing groups	246	62	25.2	1.34	1.49	6.44E-03
GO:0030515	snoRNA binding	17	8	47.1	2.51	3.87	7.32E-03
GO:0016740	transferase activity	299	73	24.4	1.3	1.43	7.48E-03
GO:0004518	nuclease activity	68	21	30.9	1.64	1.95	1.08E-02
GO:0004386	helicase activity	99	28	28.3	1.51	1.73	1.31E-02
GO:0016779	nucleotidyltransferase activity	74	22	29.7	1.58	1.85	1.46E-02
GO:0043167	ion binding	1081	228	21.1	1.12	1.21	1.61E-02
GO:0008173	RNA methyltransferase activity	47	15	31.9	1.7	2.04	2.13E-02
GO:0008170	N-methyltransferase activity	35	12	34.3	1.83	2.27	2.14E-02
GO:0097159	Not yet available	836	178	21.3	1.13	1.21	2.42E-02
GO:0036094	Not yet available	828	176	21.3	1.13	1.21	2.66E-02
GO:1901363	Not yet available	834	177	21.2	1.13	1.2	2.77E-02
GO:0008757	S-adenosylmethionine-dependent methyltransferase activity	70	20	28.6	1.52	1.75	2.95E-02
GO:0043168	anion binding	720	154	21.4	1.14	1.21	3.08E-02
GO:0043021	ribonucleoprotein complex binding	49	15	30.6	1.63	1.92	3.09E-02
GO:0005524	ATP binding	570	124	21.8	1.16	1.23	3.18E-02
GO:0140657	ATP-dependent activity	268	62	23.1	1.23	1.32	3.87E-02
GO:0004683	calmodulin-dependent protein kinase activity	11	5	45.5	2.42	3.62	3.93E-02
GO:0030554	adenyl nucleotide binding	582	125	21.5	1.14	1.21	4.45E-02
GO:0000166	nucleotide binding	810	170	21	1.12	1.18	4.48E-02
GO:1901265	nucleoside phosphate binding	810	170	21	1.12	1.18	4.48E-02
GO:0004527	exonuclease activity	43	13	30.2	1.61	1.89	4.71E-02
GO:0003824	catalytic activity	1047	216	20.6	1.1	1.16	4.71E-02
GO:0140101	catalytic activity, acting on a tRNA	96	25	26	1.39	1.54	4.79E-02

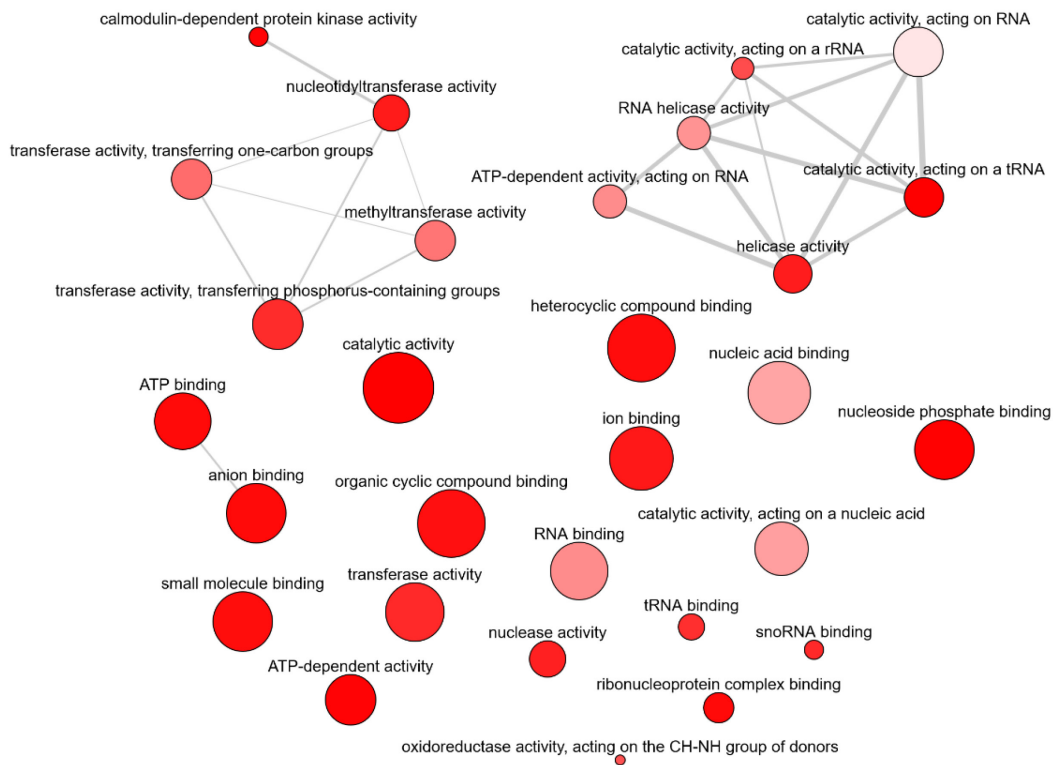


Figure 7-7. Interaction map of molecular functions enriched among genes altered in *P. falciparum* upon treatment with 20 nM SC83288.